# Deformation and seismic style of oceanic transform faults: Evidence from the Southern Troodos Transform Fault Zone, Cyprus

Sophie Cox


submitted for the degree of

Doctor of Philosophy

at Cardiff University

Wales

28/07/2021

**Abstract**

Oceanic transform faults are considered relatively weak structures and are dominantly aseismic, but occasionally host larger earthquakes (Mw >6.0) that occur quasiperiodically. The seismic behaviour varies along-strike, down-dip and between different oceanic transforms. Several mechanisms have been proposed to explain this mechanical weakness and observed variability in seismic behaviour. These include: (1) hydration and alteration of mafic and ultramafic minerals to frictionally weaker phases; (2) elevated fluid pressure; (3) fluid-driven weakening mechanisms and strain localisation and (4) spatial variation in fault zone damage and mechanical properties. There is, however, limited direct geological evidence on the mechanical properties of creeping and locked portions of oceanic transforms. This thesis investigates the geological controls on the seismic behaviour and strength of oceanic transforms using the exhumed Southern Troodos Transform Fault Zone (STTFZ) in Cyprus as an analogue for active oceanic transforms.

Deformation in the STTFZ took place within the thermally-defined seismogenic zone ($T$ <600°C). Within serpentinite shear zones, ubiquitous fractures and macroscopically ductile serpentinite fabrics are mutually cross-cutting. These serpentinite fabrics developed progressively from lizardite-rich mesh-textured serpentinite to intensely-foliated, chrysotile-rich phyllonitic serpentinite with increased strain. Dissolution-precipitation is considered an important fabric-forming mechanism during this transition. Within the mafic crust, jointed dolerite dykes were progressively deformed to generate fault breccias and chlorite-rich fault zones, and brittle fracture and gouge formation were important deformation processes. Direct-shear friction experiments on natural samples show that chlorite-rich faults are weak ($\mu$ <0.3) and velocity-strengthening, while less deformed dolerite crust is strong ($\mu$ ∼0.7) and velocity-weakening.

The geological data indicate that variable deformation and alteration can control the weakness and seismic style of oceanic transforms. In this model, foliated serpentinites and chlorite-rich fault gouges represent weak and dom-

inantly creeping portions. In contrast, less deformed and altered sections remain strong and represent locked patches where earthquakes may nucleate.

**Acknowledgements**

Firstly, I would like to thank my supervisors, Dr Ake Fagereng and Prof. Chris MacLeod, for providing me with the opportunity to carry out this research. Their help, advice and continuous support over the years has been invaluable. I am thankful to NERC and the GW4+ Doctoral Training Partnership for their financial support (Grant agreement NE/L002434/1) to cover fieldwork, analytical costs, conferences and training throughout my PhD. Thanks to the support from the Director, Costas Constantinou, and staff of the Cyprus Geological Survey Department.

Thank you to Matt Ikari and his research group from Bremen, who hosted me on my visit and taught me invaluable skills. Tony Oldroyd helped with sample preparation and never complained when I brought down some fussy serpentinite samples, so thank you! And thanks to Duncan Muir, who is responsible for scanning electron microscope training.

The EARTH PhD community has helped make the last few years enjoyable, but I would especially like to acknowledge Harry, Chris, Christian, Jack, Adam, Lucy and definitely, Sara, with whom I spent too much time drinking coffee and chatting.

Outside of academia, I would like to thank Robyn, who has been by my side for well over a decade. She has put up with me through our swimming days and now my PhD. I have been lucky enough to have you as my friend. A heartfelt thank you goes out to Chris, who has continued to cheer me on continually throughout this project and for being up for many adventures (even if some were Type II fun...). These distractions have helped keep me sane. I would like to thank my brother, Dan, who knows from first-hand experience exactly what it is like to be going through this and dispensed some sage advice when the going got tough. I also appreciate all the support and encouragement I have received from my parents.

Diolch yn fawr iawn pawb!

# Contents

# List of Figures

# Chapter 1

# Introduction

## 1.1 Introduction to oceanic transform faults

Oceanic transform faults are large, dominantly strike-slip plate boundaries that offset mid-ocean ridge segments by up to hundreds of kilometres (Fig. 1.1; Wolfson-Schwehr and Boettcher, 2019). As recognised by Wilson (1965), transform faults are a consequence of plate tectonics and transfer displacement between zones of crustal growth and/or destruction. Their sense of shear is therefore opposite to what would be expected from 'transcurrent' faulting. Oceanic transform faults strike parallel to spreading vectors between mid ocean ridges, playing a key role in accommodating lateral slip that is induced by the creation of new oceanic crust. Consequently, they juxtapose oceanic lithosphere of contrasting ages. Oceanic transforms usually continue for hundreds or even thousands of kilometres along strike, typically including an inactive 'fracture zone' that extends beyond the active segment that separates the mid-ocean ridges (Fig. 1.1; Hensen *et al.*, 2019; Wolfson-Schwehr and Boettcher, 2019). The active portion of oceanic transforms commonly records large offsets between adjacent tectonic plates; for example, the Romanche Fracture Zone, Central Atlantic, spans more than 5000 km in length (the active transform fault being 878 km long) and reaches ∼950 km displacement (e.g. Wolfson-Schwehr and Boettcher, 2019). In this sense, oceanic transforms differ to 'transcurrent' faults, where material is conserved, in that their displacement can exceed the length of the active fault.

Oceanic transforms cut lithosphere of relatively homogeneous composition with a limited tectonic history compared with continental crust, and have his-

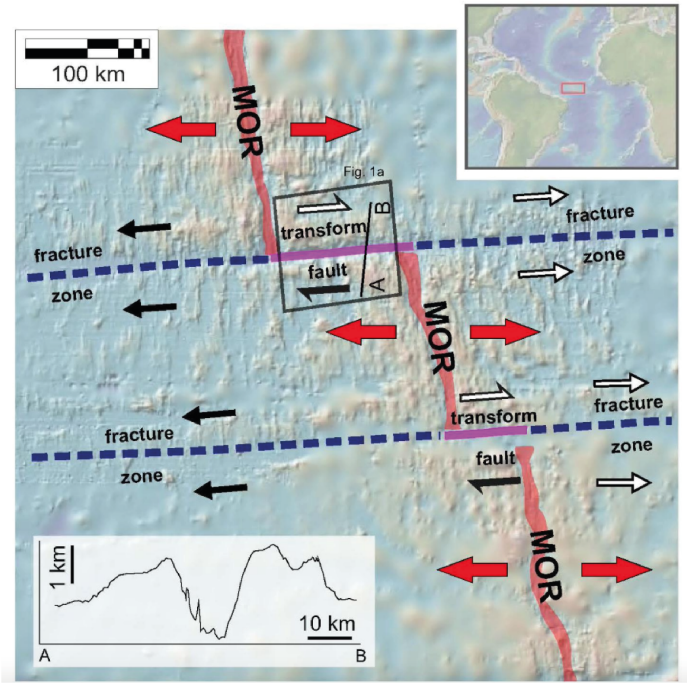


**Figure 1.1:** Map of the Central Atlantic (inset top right) showing the main features of an oceanic transform fault along a Mid Ocean Ridge (MOR) (from Hensen *et al.*, 2019). The cross section (bottom left) highlights that oceanic transform faults can have a strong relief with wide valleys and steep sides that can reach >2 km.

torically been assumed to have an olivine-controlled rheology (e.g. Turcotte and Schubert, 2002). However, while they were once considered relatively simple structures based on their lithology, geometry, thermal structure, known fault lengths and slip rates, they remain largely enigmatic in terms of their origin, evolution, detailed internal structure, geometry and seismic style (e.g. Hensen *et al.*, 2019; Wolfson-Schwehr and Boettcher, 2019). Morphologically, oceanic transforms are complex and defined by seafloor valleys that are usually a few kilometres wide (frequently >5 km) (e.g. Embley and Wilson, 1992; Fox and Gallo, 1984; MacDonald *et al.*, 1986; Pockalny *et al.*, 1988; Searle, 1981, 1983), with steep sides that can reach >2 km of relief (Fig. 1.1). Individual oceanic transforms are not composed of a single fault plane, but rather they involve a series of anastomosing fault surfaces that can be connected by transtensional basins and/or transpressional ridges. Additional complexities can also occur within the oceanic transform domain including detachment faulting (e.g. Karson and Dick, 1983) and intratransform magmatism (Hekinian *et al.*, 1995).

Over the last ∼20 years, there has been substantial discussion surrounding the strength and seismic behaviour of oceanic transform faults - generally

based around observations that require a dominantly aseismic behaviour and relatively weak faults. Explanations for these observations depend on the active deformation mechanisms and style of deformation that are active during oceanic transform faulting, and both the observations and the current explanations are reviewed in this introduction, before outlining the key aims of the thesis.

## 1.2 Brittle and ductile deformation

Before discussing transform faults specifically, it is useful to define some terms and general concepts. In an observational, objective approach, deformation structures can be either described as brittle or ductile (e.g. Byerlee, 1978). Brittle deformation refers to structures that are macroscopically discontinuous, while ductile structures are those that are macroscopically continuous. The scale of observation is important when describing structures, particularly since structures that are ductile on the macroscale may be brittle at the microscale. This structural definition of ductile differs from its mechanical definition, where ductile has been defined as deformation without a stress drop (e.g. Jaeger *et al.*, 2007).

Brittle deformation is the result of fracture and frictional sliding, while ductile structures can result from a range of fracturing, frictional and viscous processes (Rutter, 1986). Frictional mechanisms include processes such as fracturing or sliding along planes/discontinuities. In contrast, viscous processes describe mechanisms that produce a strength dependent on strain rate (e.g. diffusion and dislocation creep). At the grain-scale, deformation mechanisms can be subdivided into (e.g. Knipe, 1989): (1) fracturing and frictional sliding, (2) diffusion creep and (3) dislocation creep. The transition between frictional (1) to viscous deformation (2-3) is referred to as the frictional-viscous transition. Although, rocks are often made up of multiple minerals that can deform either by frictional or viscous mechanisms under various conditions, meaning different deformation mechanisms can be active contemporaneously (e.g. Bos and Spiers, 2002). This makes the transition from frictional to viscous deformation gradual and a wide range of conditions exist where brittle and viscous mechanisms coexist (Fig. 1.2; Sibson, 1984).

Within the crust, frictional mechanisms are important in the upper few kilo-

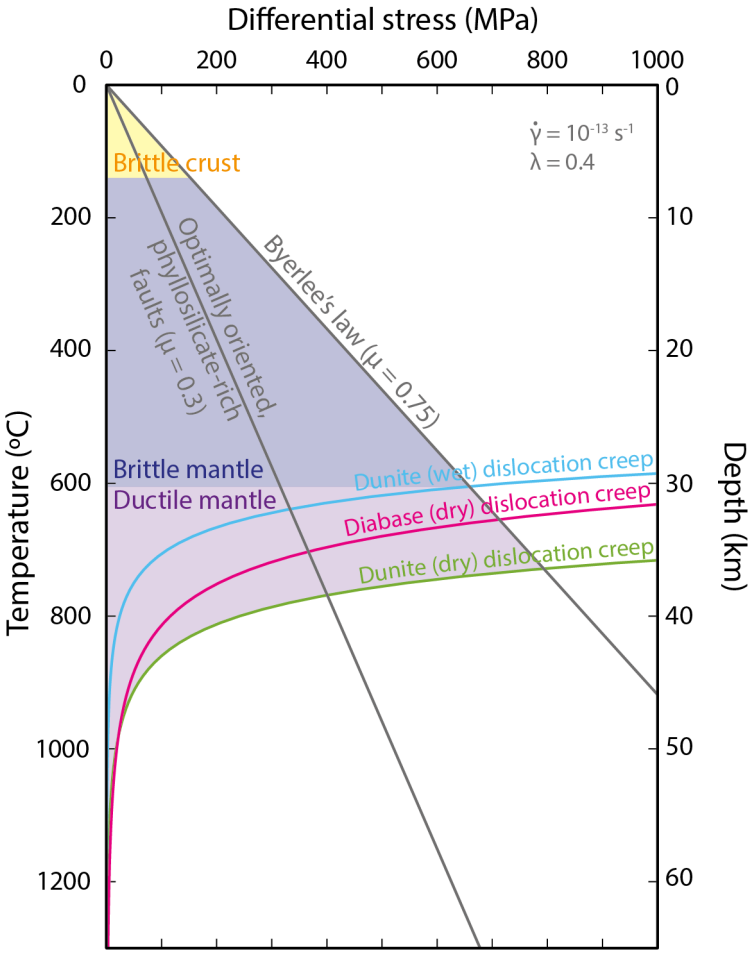


**Figure 1.2:** Strength profile for the oceanic lithosphere. At shallow depths, strength increases with depth, until temperature-dependent viscous deformation mechanisms become more efficient than frictional mechanisms. The strength curves plotted suggest a frictional-viscous transition in the oceanic lithosphere near the 600 °C isotherm. Grey curves show Byerlee friction and the frictional strength of phyllosilicates (e.g. chlorite or serpentine; $\mu$ = 0.3). Dislocation creep flow laws for dunite are from Chopra and Paterson (1984) and the diabase flow law is from Mackwell and Kohlstedt (1998).

metres where pressures and temperatures are low (Fig. 1.2). Frictional failure is typically independent of temperature but dependent on confining pressure, so becomes increasingly difficult with depth, assuming a constant fluid pressure gradient (Byerlee, 1978; Suppe, 2014). However, with increasing temperature, depth and confining pressure, viscous processes (i.e. dislocation and diffusion creep) are more efficient, particularly at lower strain rates, and strength decreases with increasing depth below the 'frictional-viscous' transition (Fig. 1.2; Brace and Kohlstedt, 1980). Composition, grain size, strain rate, fluid availability and differential stress also play a role in the favoured mechanism

(Bürgmann and Dresen, 2008; Knipe, 1989; Sibson, 1984) and the weakest deformation style will be dominant. Diffusion creep is particularly dependent on grain size, becoming substantially more efficient at smaller grain sizes (Rutter, 1976). Fracturing and frictional sliding, and diffusion (dissolution-precipitation) processes are most relevant to the work in this study and described in more detail below.

## 1.3 Fracture and friction

### 1.3.1 Macroscopic failure criteria

In the oceanic lithosphere, a portion of transform fault slip occurs by earthquakes and therefore frictional processes (Reid, 1910). Therefore, it is important to understand fracture criteria in order to understand the rheology of oceanic transform faults. In Chapters 3 and 4, which describe the deformation of the lithospheric mantle and mafic crust, respectively, observations suggest that a substantial portion of the deformation occurred by brittle deformation. The stress conditions for brittle failure are outlined below.

A Mohr diagram can be used to represent the stress state of an intact, homogeneous rock in 2D (Fig. 1.3), where the horizontal and vertical axes represent the effective normal stress ($\sigma_n^{'}$ = $\sigma_n$ - *Pf*, where *Pf* is pore fluid pressure) and shear stress ($\tau$), respectively. The maximum ($\sigma_1$) and minimum ($\sigma_3$) principal compressive stresses are plotted on the horizontal axis and $\sigma_1 - \sigma_3$ (defining the diameter of the Mohr circle) is equal to the differential stress. The Mohr circle is centred at $((\sigma_1 + \sigma_3)/2,0)$. Failure of a rock occurs when the Mohr circle intersects the Griffith-Coulomb failure envelope, at which point the rupture strength of the rock is reached (Fig. 1.3).

The rupture strength of a rock under compression can be described by the Coulomb failure criterion:

$$\tau_f = \sigma_n^{'}\mu + C_0 \tag{1.1}$$

where $\tau_f$ = shear strength; $\mu$ = friction coefficient; $C_0$ = cohesion. If a rock is intact, $\mu$ represents the angle of internal friction ($\mu_i$, sliding resistance on a new plane that is yet to form) rather than the angle of sliding friction (resistance to sliding along an existing plane under a given $\sigma_n$). Rocks can also

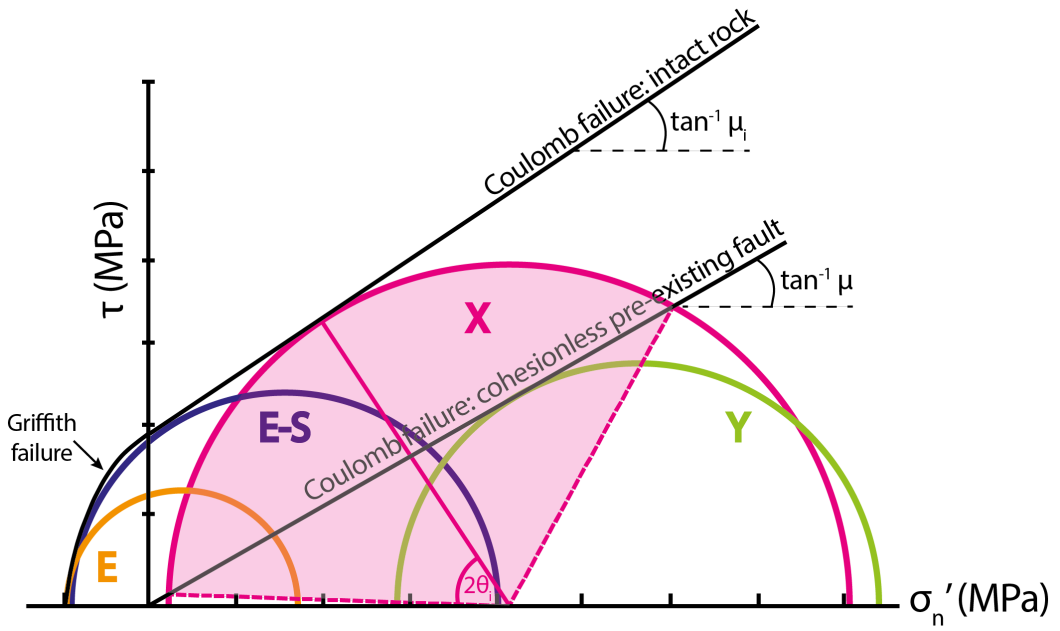


**Figure 1.3:** Mohr diagram sketch showing the Griffith-Coulomb failure criterion for intact rock and a pre-existing fault ($C_0 = 0$) and assuming $\mu = \mu_i$. Mohr circle X represents the stress field where shear failure of intact rock will occur. The solid pink line indicates the orientation of new faults at angle $\theta_1$ to $\sigma_1$. The area between the dashed pink lines represents the range of orientations of pre-existing faults that would be activated in the same stress field as formation of new, optimally-oriented faults. Mohr circle Y indicates the conditions for reactivation of a cohesionless, pre-existing fault. Extension (E) and extension-shear (E-S) failure occur where the Mohr circles intersect the Griffith failure criterion at $\tau = 0$, or $\sigma_3 < 0$ but $\tau > 0$, respectively. The addition of pore fluid pressure would drive the effective normal stress down, and move the Mohr circles to the left.

fail in the tensile regime and a composite failure criterion can be constructed for intact rock (Fig. 1.3) from applying the Griffith criterion for tensile failure:

$$\tau_f = \sqrt{4\sigma_n' T_0 + 4T_0^2} \tag{1.2}$$

where $T_0$ = tensile strength. To fail in the tensile regime, $\sigma_3$ needs to be negative, a condition that is made easier with elevated fluid pressures. Additionally, to fail in the tensile regime, the differential stress $(\sigma_1 - \sigma_3)$ is required to be very low, to prevent shear failure occurring (Fig. 1.3).

Faults represent a record of brittle shear failure, and Anderson (1951) defined three fault regimes based on the orientation of principal compressive stresses $(\sigma_1 \geq \sigma_2 \geq \sigma_3)$ at the time of fault initiation and the assumption that one of the principal stresses must be vertical (the other two, horizontal). The

three regimes are based on which principal stress is vertical ($\sigma_v$): $\sigma_v = \sigma_1$ for normal faults, $\sigma_v = \sigma_2$ for strike-slip faults and $\sigma_v = \sigma_3$ for thrust faults. In an isotropic rock, faults form as planes containing $\sigma_2$ and at an angle of $\theta$ to $\sigma_1$, where $\theta$ depends on the slope of the Coulomb failure criterion, $tan^{-1}\mu_i$ (Fig. 1.3 Anderson, 1951) so that $\theta = 0.5\ tan^{-1}(1/\mu_i)$. Experimentally determined values of $\mu_i$ typically fall in the range 0.5-1 making $\theta = 27\pm5°$ (Jaeger *et al.*, 2007). As a consequence, reverse faults are considered to initiate at a dip of 27±5°, normal faults at dips of 63±5° and strike-slip faults are expected to be sub-vertical. $\mu_i$ may be considered the same as the coefficient of sliding friction as the strength of an incipient rupture plane has been shown to depend on the frictional resistance of pre-existing microcracks (Savage *et al.*, 1996).

Most earthquakes occur from the reactivation of pre-existing faults, where the cohesive strength is commonly approximated to be zero (Fig. 1.3; Marone, 1995). The $\mu$ of a fault is defined as the ratio of shear to normal stress. Byerlee (1978) showed that $\mu$ for most minerals typical of the crust is ∼0.6-0.85, except for some phyllosilicate minerals whose $\mu$ ≈0.3. The frictional strength of a rock is therefore relatively independent of rock type, and shear stress increases linearly with normal stress ($\tau = 0.85\ \sigma_n$ for $<$ 200 MPa, and $\tau = 0.5 + 0.6\ \sigma_n$ for $>$ 200 MPa; Byerlee, 1978). Once a fault has formed, the sum of its cohesion and frictional strength is commonly less than the intact rock. Existing planes can therefore act as planes of weakness, and depending on their strength relative to intact rock, can be reactivated in stress-fields that may not be optimally oriented for their reactivation (Fig. 1.3; Sibson, 1985).

According to Anderson's theory of faulting, the minimum principal stress ($\sigma_3$) is considered perpendicular to mid-ocean ridges to allow spreading, making it approximately parallel to the strike of the oceanic transforms. Consequently, $\sigma_1$ is approximately perpendicular to the transform, as $\sigma_2$ is vertical. Therefore, the principal stress orientations of oceanic transform faults are not favourable. Many plate boundary transform faults such as the San Andreas Fault (e.g. Townend and Zoback, 2004; Zoback, 1991) and Tjörnes Fracture Zone, Iceland (e.g. Angelier *et al.*, 2000; Homberg *et al.*, 2010) are poorly oriented relative to $\sigma_1$, and slip has been explained by frictional weakness ($\mu <<$0.6) by these studies.

### 1.3.2 Frictional stability

Brittle failure can occur as earthquake slip or may also occur by stable frictional sliding (e.g. Dieterich, 1979; Scholz, 1998). The seismic style of a fault therefore depends on its frictional stability, which can be defined by a rate-and-state friction law as introduced by Dieterich (1979). The mathematical framework for rate-and-state friction relates the friction coefficient, sliding velocity and a "state parameter". The most commonly applied rate-and-state friction law is the Dieterich-Ruina law (Dieterich, 1979; Ruina, 1983):

$$\frac{\tau}{\sigma_n^{'}} = \mu = \left[\mu_0 + a \ln\left(\frac{V}{V_0}\right) + b_1 \ln\left(\frac{V_0\theta_1}{Dc_1}\right) + b_2 \ln\left(\frac{V_0\theta_2}{Dc_2}\right)\right] \tag{1.3}$$

where $\tau$ is the shear stress, $\sigma_n^{'}$ is the effective normal stress, $\mu_0$ is steady state friction at reference velocity $V_0$, $V$ is slip velocity, $Dc$ is the critical slip distance over which $\mu$ evolves before reaching a steady-state, $\theta$ is a state variable that describe ageing, and $a$ and $b$ ($b = b_1 + b_2$) are dimensionless constants (Blanpied *et al.*, 1998; Dieterich, 1981; Marone, 1998). In cases where the friction response to the velocity change are well described by a single state variable, $b_2$ and $Dc_2$ are considered zero.

The evolution of friction to a steady-state at a new velocity can be described using one of two evolution laws: (1) the ageing law (Dieterich, 1979; 1981) and (2) the slip law (Ruina, 1983). The ageing law can be described by the relation:

$$\frac{\partial\theta}{\partial t} = 1 - \frac{V\sigma}{D_c} \tag{1.4}$$

where $t$ is time. This law explicitly considers that friction can evolve as a function of time and not necessarily slip (Dieterich and Kilgore, 1994) and is the preferred law in Chapter 5. The slip law, which considers friction can evolve with slip can be described by the relation (Ruina, 1983):

$$\frac{\partial\theta}{\partial t} = \frac{V\sigma}{D_c} ln\left(\frac{V\sigma}{D_c}\right) \tag{1.5}$$

The frictional stability of a material depends on the material parameters $a$, $b$ and $Dc$ (Dieterich, 1979, 1981; Marone, 1998; Scholz, 1998) that can be expressed as the rate-and-state friction parameter $a$-$b$ (Scholz, 1998):

$$a - b = \frac{\partial\mu_{ss}}{\partial[\ln(V)]} \tag{1.6}$$

where $\mu_{ss}$ is the steady-state coefficient of friction. The parameter $a$-$b$ is important in predicting fault slip behaviour. Values of $a$-$b$ >0 indicate velocity-strengthening behaviour as friction increases with increasing slip velocity. Materials with a positive $a$-$b$ are associated with stable fault creep (Dieterich, 1979; Scholz, 1998). $a$-$b$ <0 indicates velocity-weakening behaviour, where the rock friction decreases with increasing slip velocity, characteristic of unstable fault slip and required for earthquake nucleation (Dieterich, 1979, 1981; Marone, 1998; Scholz, 1998). Earthquakes cannot nucleate in, but may propagate into, velocity-strengthening material if the slip velocity is sufficiently high but would be met by a negative stress drop resulting in the rapid termination of the propagating earthquake (Scholz, 1998). A material with $a$-$b$ <0 is frictionally unstable if the effective normal stress is greater than a critical value, dependent on $Dc$. However, if this is not the case, a material can be considered as conditionally unstable, within which unstable sliding occurs under a load of sufficient velocity or if length-scale of the slipping patch reaches a nucleation length (e.g. conditionally stable nature of serpentine discussed in section 1.6.3 and considered in Chapter 3).

### 1.3.3 Microscopic brittle processes

Brittle fracture and frictional mechanisms include intergranular fracturing, intragranular fracturing, frictional sliding on fractures or grain boundaries and grain rotation. The combination of these mechanisms, which occur at the microscale but can give rise to fabrics that are macroscopically ductile, is called cataclasis (Fig. 1.4). Cataclasis typically occurs in fault cores and reduces grain size. Grain size reduction as a result of fracturing during cataclasis can be observed in breccias from the Southern Troodos Transform Fault Zone (Fig. 1.4b; Chapter 4). It is particularly common in the shallow crust in rocks that have a low phyllosilicate content, well-sorted grains and low pore-fluid pressure (Fossen, 2016). However, fracturing of grains during cataclasis promotes hydration and alteration such that progressive cataclasis may aid the formation of a foliated gouge, comprising clays and phyllosilicates that have much lower frictional strengths, $\mu$ <0.3 (e.g. Collettini *et al.*, 2019; Fagereng and Ikari, 2020; Ikari *et al.*, 2011). Within foliated gouges, basal sliding dominates (e.g. Kronenberg *et al.*, 1990; Mariani *et al.*, 2006; Van Diggelen *et al.*, 2010). Additionally, Collettini *et al.* (2009) have shown that a pre-existing

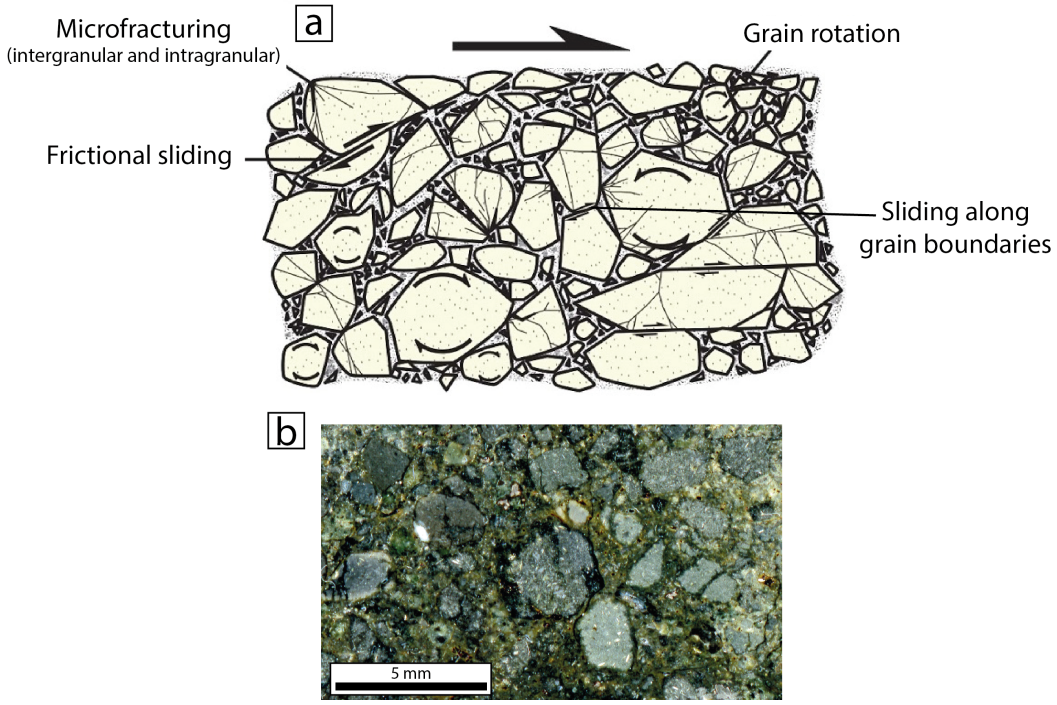


**Figure 1.4:** (a) Sketch of brittle deformation mechanisms including microfracturing, frictional sliding and grain rotation culminating in cataclasis. After Fossen (2016). (b) Photomicrograph (reflected light) of a breccia (18CS25) created by cataclasis.

fabric (e.g. a foliation) greatly reduces the frictional strength of a rock ($\Delta\mu$ ~-0.3) compared to a rock of the same composition but lacking a fabric. These results suggest that mature, phyllosilicate-bearing faults can slide, frictionally, at shear stresses much lower than those expected for $\mu$ = 0.6-0.85, even with a low phyllosilicate content (~20%), as long as the phyllosilicates are well interconnected (Handy, 1990; Niemeijer, 2018).

## 1.4 Viscous deformation

### 1.4.1 Dissolution-precipitation creep

Dissolution-precipitation is considered an important deformation mechanism of fine-grained olivine in oceanic transform faults (e.g. Kohli and Warren, 2020; Warren and Hirth, 2006). Dissolution-precipitation creep is a fluid-assisted diffusion creep process that involves the transfer of dissolved material from high normal stress sites (e.g. surfaces oriented perpendicular to $\sigma_1$) to low normal stress sites (e.g. surfaces oriented perpendicular to $\sigma_3$), usually along grain

boundaries (Fig. 1.5). For example, in serpentinites from the Southern Troodos Transform Fault Zone, chrysotile, formed from the breakdown of lizardite (Chapter 3), forms in stress shadows behind lizardite clasts (Fig. 1.5b). To accommodate movement between grains that change shape during diffusion creep, grain boundary sliding occurs, allowing grains to slide past one another and prevent voids opening up.

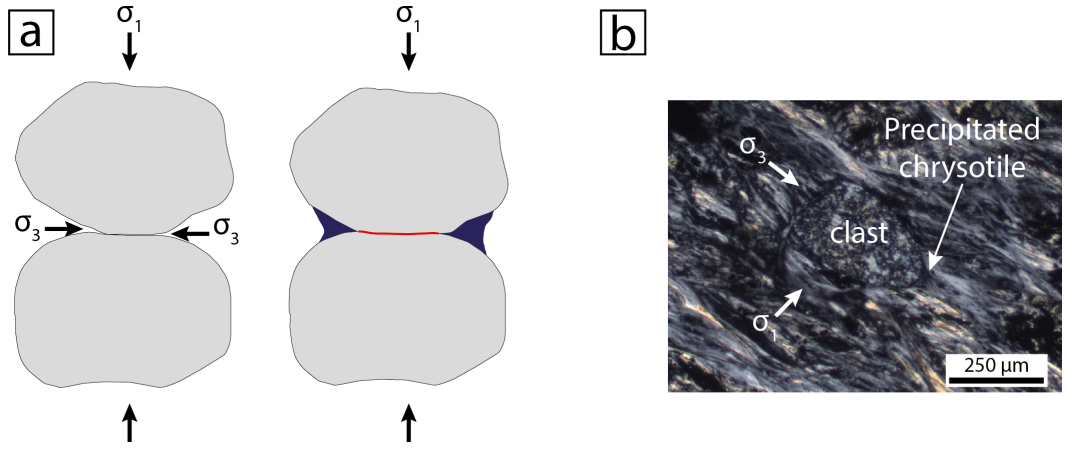


**Figure 1.5:** (a) Sketch of dissolution precipitation consisting of the removal of material from high stress sites by pressure solution (red) and precipitation of new material in low stress sites (blue). (b) Photomicrograph (cross-polarised light) showing chrysotile precipitated within a stress shadow behind serpentinite clast within a highly sheared serpentinite (17CS20).

The dissolution, or "pressure solution", part of dissolution-precipitation is what is considered the driver for dissolution-precipitation creep (Durney, 1972; Gratier *et al.*, 2013). Pressure solution is driven by the chemical potential associated with a normal stress gradient (Paterson, 1973). Dissolution-precipitation creep is a grain-size sensitive process and small grain sizes and warm temperatures under fluid-present conditions favour dissolution-precipitation creep (Rutter, 1976), especially at low strain rates.

### 1.4.2 Dislocation creep

Dislocation creep involves the movement of dislocations through the crystal lattice of a material. It is an important viscous deformation mechanism at elevated temperatures (e.g. Brace and Kohlstedt, 1980; Ramsay, 1967; Rutter, 1974). The onset of dislocation creep, where crystal plastic flow becomes more efficient than brittle deformation mechanisms, is important in controlling the location of the base of the thermally-defined seismogenic zone (Fig. 1.2; e.g.

Sibson, 1977, 1984). The flow law for dislocation creep can be expressed in the form:

$$\dot{\gamma} = A(\sigma_1 - \sigma_3)^n exp\left(-\frac{Q}{RT}\right) \tag{1.7}$$

where $\dot{\gamma}$ is strain rate, $A$ is a material constant, $n$ is a stress exponent, $Q$ is the activation energy, $R$ the gas constant and $T$ is temperature. Therefore, the strain rate of materials undergoing dislocation creep is controlled by differential stress, temperature and composition ($A$, $n$ and $Q$ are parameters dependent on the deforming material). For mafic rocks, dislocation creep in olivine becomes efficient at geological strain rates at ∼600-750 °C (Fig. 1.2).

## 1.5 Strength and rheology of the oceanic lithosphere

The theory behind the rheology of the lithosphere has been introduced in sections 1.2-1.4. This section specifically considers how this theory has been applied to the oceanic lithosphere in general and more specifically to oceanic transforms. In a simplified summary, the oceanic lithosphere is made up of a mafic crust (with a dolerite rheology) and a variably serpentinised, ultramafic lithospheric mantle (simplified to an olivine rheology where not serpentinised).

At mid-ocean ridges, freshly formed mafic crust is dry and strong (at upper to mid crustal conditions; Fig. 1.2). Friction experiments at a range of temperature and pressure conditions show that the dolerite crust has approximately Byerlee friction ($\mu$ = 0.6-0.85; Cox, 1990; He *et al.*, 2007; Phillips *et al.*, 2020; Violay *et al.*, 2014, 2012; Zhang *et al.*, 2017). The lithospheric mantle comprises ultramafic lithologies that, if controlled by olivine rheology, are also considered strong (e.g. Boettcher *et al.*, 2007). The strength of the oceanic lithosphere increases linearly with depth where strength is given by the Byerlee friction law, however, with increasing temperature and depth within the mantle, the strength decreases as dislocation creep becomes more efficient (section 1.2; Fig. 1.2).

Hydrothermal alteration of the oceanic lithosphere is common (e.g. Alt *et al.*, 1986; Cann *et al.*, 1997) due to fracturing and faulting creating abundant permeability. Alteration of the mafic crust at greenschist facies conditions gives

chlorite, albite and amphibole mineralogies while alteration of the ultramafic mantle gives serpentine (+ talc + brucite + magnetite + chlorite + tremolite). Serpentine ($\mu$ ~0.2; Tesei *et al.*, 2018) and chlorite ($\mu = 0.3$; Fagereng and Ikari, 2020; Okamoto *et al.*, 2019) are phyllosilicate minerals that are considered to be far weaker than Byerlee friction under upper crustal conditions (Fig. 1.2). The presence of chlorite would reduce the friction of crustal faults compared with unaltered crust, while the presence of serpentine in altered lithospheric mantle would reduce its frictional strength compared with olivine (Fig. 1.2). Chlorite and serpentine are known to allow strain localisation that can result in weak shear zones, if these minerals form well interconnected networks (e.g. Handy, 1990; Niemeijer, 2018). Therefore, where present, these weak phases can have a big influence of the overall strength, style and localisation of deformation within the oceanic lithosphere (sections 3.6, 4.5 and 5.5).

## 1.6 Serpentinisation and effects on rheology

Serpentinisation occurs during fluid circulation, where olivine and pyroxene in mafic and ultramafic rocks are hydrated to form serpentine ± brucite ± magnetite ± hydrogen. Serpentinisation occurs in a wide range of tectonic settings, but is particularly common in the oceanic mantle lithosphere, and commonly associated with major fault zones that provide adequate pathways for fluids. For example, serpentinites are common along oceanic transforms (e.g. Cox *et al.*, 2021; Irwin and Barnes, 1975; Mével, 2003, Chapter 3), and along detachment faults and oceanic core complexes at slow and ultra-slow spreading ridges (e.g. the Mid Atlantic Ridge, SW Indian Ridge and Gakkel Ridge; Cann *et al.*, 1997; Cannat, 1993; Dick, 1989; Escartín *et al.*, 2003; Rüpke and Hasenclever, 2017). Serpentinites are also documented within subduction zones in normal faults associated with plate bending (e.g. Grevemeyer *et al.*, 2018), and at the slab-mantle interface in the mantle wedge (e.g. Hyndman and Peacock, 2003; Peacock and Hyndman, 1999). Serpentinites are also documented in some continental transform faults such as the San Andreas Fault (Moore and Rymer, 2007). Serpentinisation is an important process as it can induce significant physical, rheological and chemical changes within the oceanic lithosphere (e.g. Escartín *et al.*, 1997a,b, 2001; Guillot *et al.*, 2015; Raleigh and Paterson, 1965) (Fig. 1.2).

### 1.6.1 Chemistry and conditions of serpentinisation

Serpentinisation involves the hydration of mainly olivine and orthopyroxene, and less commonly, clinopyroxene. In the case of the Southern Troodos Transform Fault Zone, however, the mantle peridotites are pervasively serpentinised (MacLeod and Murton, 1993, Chapter 3). Olivine is the first mineral to react during serpentinisation, in particular, its Mg end-member, which reacts to form brucite and serpentine (e.g. Bach *et al.*, 2006; Klein *et al.*, 2013; Rouméjon *et al.*, 2015):

$$2Mg_2SiO_4 + 3H_2O = Mg(OH)_2 + Mg_3Si_2O_5(OH)_4$$
$$Olivine + water = brucite + serpentine$$

The serpentinisation of pyroxene leads to the release of silica in the reactive fluid and formation of serpentine (Bach *et al.*, 2006; Malvoisin, 2015; Rouméjon *et al.*, 2015):

$$3MgSiO_3 + 2H_2O = SiO_{2(aq)} + Mg_3Si_2O_5(OH)_4$$
$$Orthopyroxene + water = aqueous\ silica + serpentine$$

The aqueous silica can react with olivine to form more serpentine:

$$3Mg_2SiO_4 + SiO_{2(aq)} + 4H_2O = 2Mg_3Si_2O_5(OH)_4$$
$$Olivine + aqueous\ silica + water = serpentine$$

The alteration of the Fe end-member of olivine and pyroxene results in the formation of magnetite:

$$3Fe_2SiO_4 + 2H_2O = SiO_{2(aq)} + 2Fe_3O_4 + 2H_2$$
$$Olivine + water = aqueous\ silica + magnetite + hydrogen$$

and:

$$3FeSiO_3 + H_2O = 3SiO_{2(aq)} + Fe_3O_4 + H_2$$
$$Orthopyroxene + water = aqueous\ silica + magnetite + hydrogen$$

The formation of serpentine at the expense of olivine and pyroxene leads to a

change in the density of the affected rocks with water uptake around 13-15% by weight (density decrease from ∼3.3 to ∼2.6 g/cm$^3$) as well as a volume increase of ∼40-50% (Klein and Le Roux, 2020; MacDonald and Fyfe, 1985; O'Hanley, 1992; Shervais *et al.*, 2005).

Serpentinisation occurs under a large range of conditions, from temperatures below 100 °C through to temperatures >500 °C (Evans, 2004; Malvoisin, 2015; Mével, 2003) (Fig. 1.6), i.e. throughout the proposed seismogenic zone in olivine-dominated oceanic lithosphere (Fig. 1.2). Pressure is not a limiting factor for most serpentine stability, however, a decrease in temperature and/or pressure favours serpentine nucleation and growth as these reduce silica solubility (Andreani *et al.*, 2007). Serpentinisation is also influenced by fluid composition, composition of the primary peridotite and redox state.

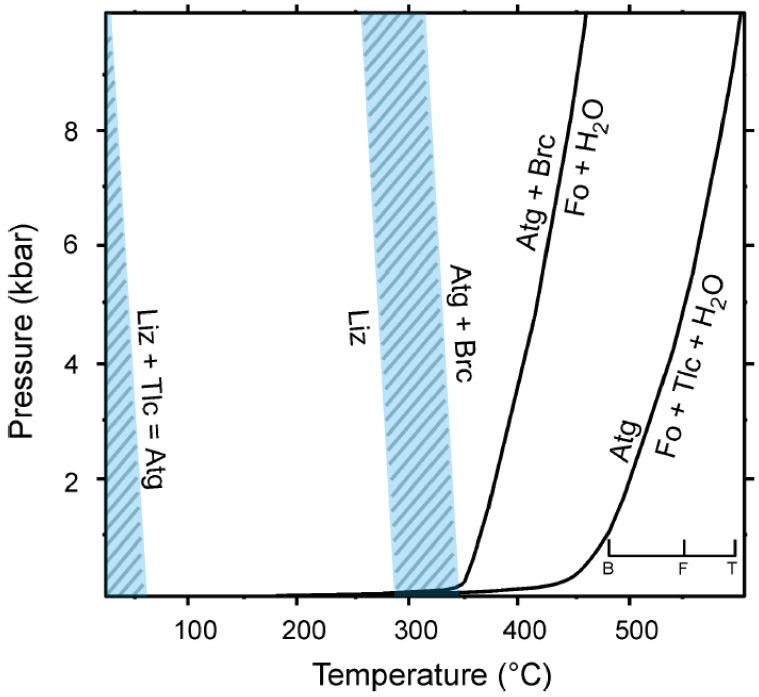


**Figure 1.6:** Stable phase diagram after Evans (2004) for the three main serpentine types; lizardite (Liz), antigorite (Atg) and chrysotile (metastable with respect to lizardite and antigorite). Brucite (Brc), talc (Tlc) and forsterite (Fo) are also shown.

The rate of serpentinisation depends on the evolution of fluid pathways and the reactive surface area (i.e. grain size). Fluid pathways initially form from tectonic deformation, such as during nucleation and growth of transform faults (Rouméjon *et al.*, 2015) or by thermal cracking (Boudier *et al.*, 2010) and during the reaction, fluid pathways can evolve as a consequence of the positive

change in volume which can generate stresses sufficient to fracture the rock (e.g. Jamtveit *et al.*, 2008; Kelemen and Hirth, 2012; Malvoisin *et al.*, 2017; Plümper *et al.*, 2013). Serpentinisation is a fast reaction on geological time scales and is largely controlled by the dissolution rates of olivine and pyroxene as the precipitation of serpentine is a faster process (Malvoisin *et al.*, 2012).

### 1.6.2 Serpentine types

Serpentine is a tri-octahedral sheet silicate ($Mg_3Si_2O_5(OH)_4$) that comprises alternating tetrahedral (T: $Si_2O_5$) and octahedral (O: $Mg_3O_2(OH)_4$) sheets (Fig. 1.7). T and O layers share oxygen atoms that hold the layers together and each TO group of layers is held to one another by hydrogen bonds. Different crystal structures arise from how T and O sheets fit together resulting in three main serpentine types (lizardite, chrysotile and antigorite; Fig. 1.7). Despite a limited chemical difference between the serpentine types, differences in their crystal structure have strong effects on the overall mechanical behaviour (see section 1.6.3 and 3.6.3). This thesis considers direct observation of lizardite and chrysotile, but antigorite is mentioned here for completion and later discussion and extrapolation of results (Chapter 3). Serpentine identification via common methods such as optical microscopy, X-ray powder diffraction and scanning electron microscopy combined with energy dispersive spectroscopy can fail at confidently differentiating the various serpentine types, particularly lizardite and antigorite (Rooney *et al.*, 2018; Tarling *et al.*, 2018). Therefore, techniques such as Raman spectroscopy and TEM are commonly needed to identify the polytypes.

#### Lizardite

Lizardite is the low temperature (most stable at $T$ <300 °C; Evans, 2004), low pressure serpentine mineral (Fig. 1.6). It is the most common variety in the oceanic lithosphere (e.g. at slow spreading ridges and along oceanic transform faults; Mével, 2003; Reinen *et al.*, 1994) and favours relatively low fluid:rock environments (Evans, 2004). Its crystal structure consists of planar or platy layers (Fig. 1.7a).

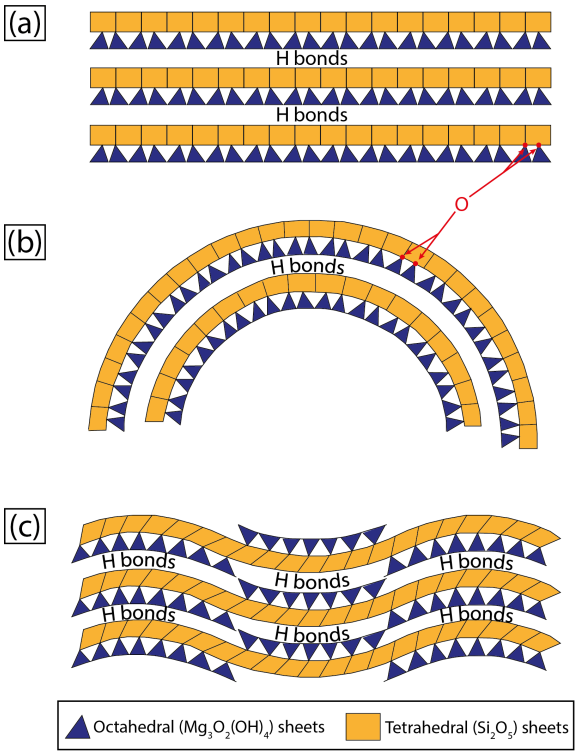


**Figure 1.7:** Crystallographic structures of (a) lizardite, (b) chrysotile and (c) antigorite. After Mével (2003).

### Chrysotile

Chrysotile is thermodynamically stable under the same pressure-temperature conditions as lizardite, and so commonly found occurring with lizardite (e.g. as in serpentinites along the San Andreas Fault; Andreani *et al.*, 2005). Chrysotile growth favours open spaces and higher fluid:rock ratios (Evans, 2004) promoting its occurrance in faults that facilitate localised fluid flow (i.e. high strain zones in oceanic transforms; Chapter 3). Although lizardite is more thermodynamically stable, the formation of chrysotile can be favoured by kinetics (Evans, 2004). Chrysotile is also favoured if the grain size of the original material is small enough to not limit the rate of reaction (Malvoisin *et al.*, 2012). Chrysotile consists of a cylindrical structure, which gives it a fibrous texture (Fig. 1.7b).

### Antigorite

Antigorite has a corrugated structure that forms from TO layers periodically reversing (Fig. 1.7c). This structure makes antigorite stable at higher pressures

and temperatures than lizardite ($T$ ~350-600 °C and <10 kbar; Evans, 2004) (Figs. 1.6 and 1.8). Antigorite can form directly from olivine hydration in relatively high temperature, high pressure conditions such as the mantle wedge (e.g. Smith and Faulkner, 2010) and at spreading ridges (Rouméjon *et al.*, 2019).

### 1.6.3 Serpentine rheology

There have been many studies that provide data on the frictional and rheological properties of the various serpentine types over a wide range of pressure and temperature conditions because of their occurrence in many major fault zones, including oceanic transforms (e.g. Amiguet *et al.*, 2012; Auzende *et al.*, 2015; Brantut *et al.*, 2016; Escartín *et al.*, 1997a,b, 2001; Kohli *et al.*, 2011; Moore and Lockner, 2011; Moore *et al.*, 1996; Okazaki and Katayama, 2015; Reinen *et al.*, 1994; Tesei *et al.*, 2018). Tesei *et al.* (2018) complied much of this experimental data (Fig. 1.8) to show that the frictional properties of the three main serpentine types varies greatly with effective normal stress and fluid presence at pressure-temperature conditions relevant for brittle faulting.

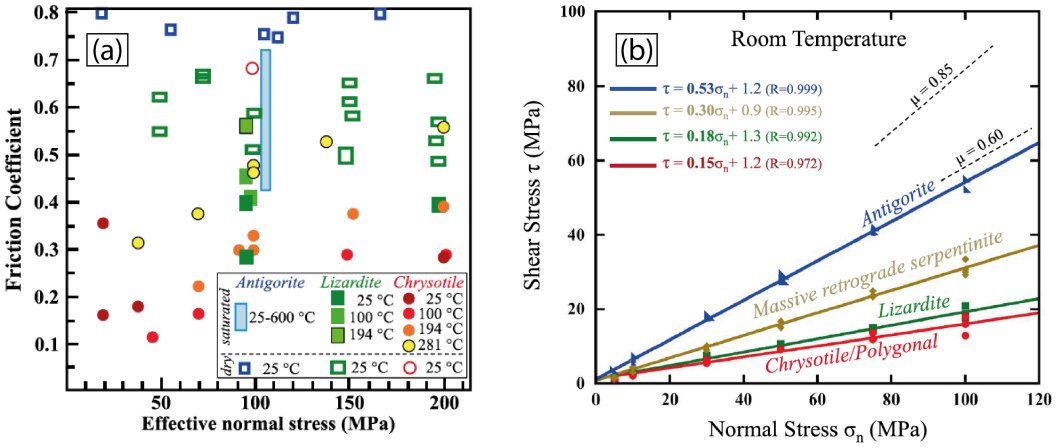


**Figure 1.8:** (a) Compilation of experimental friction coefficient data vs. effective normal stress for the three main serpentine types from Tesei *et al.* (2018). (b) Coulomb failure envelopes for serpentine samples studied at room temperature in Tesei *et al.* (2018). For comparison, typical friction of crust is shown (dashed lines; $\mu$ = 0.6-0.85).

Antigorite has been reported as relatively strong with a frictional strength, $\mu$ = 0.5-0.85 (Moore *et al.*, 1997; Reinen *et al.*, 1994), comparable to Byerlee friction ($\mu$ = 0.6-0.85; Byerlee, 1978). Experiments also indicate a decrease in

$\mu$ with increasing temperature with $\mu$ = 0.5-0.85 at room temperature (Reinen *et al.*, 1994), $\mu$ = 0.4-0.6 at 25-194 °C (Moore *et al.*, 1996) and $\mu$ = 0.1-0.35 at temperatures of 400-550 °C (Chernak and Hirth, 2010). In contrast, experimental studies, simulating conditions from the shallow crust to depths equivalent to ∼8 GPa and 800 °C, indicate a low frictional strength for both lizardite ($\mu$ = 0.29-0.56; Moore and Lockner, 2011; Moore *et al.*, 1997) and chrysotile ($\mu$ = 0.1-0.55; Moore and Lockner, 2004; Moore *et al.*, 1997), however, their strength increases with increasing temperature ($T$ >100 °C; Moore *et al.*, 1997). Both lizardite and chrysotile have $\mu$ ∼0.2 from room temperature up to ∼200 °C and effective normal stresses of 5-120 MPa (Tesei *et al.*, 2018), that is, conditions consistent with those in the brittle upper lithosphere and within the thermally-defined seismogenic zone of oceanic transform faults.

Comparing the frictional data of different serpentine minerals and experiments is difficult since natural serpentine samples are rarely monomineralic, and so experiments are rarely conducted on pure serpentine types (e.g. Viti *et al.*, 2018). They also have very fine grain sizes and complex textures (e.g. Rooney *et al.*, 2018; Tarling *et al.*, 2018; Wicks and Whittaker, 1977). Nevertheless, Tesei *et al.* (2018) reported $\mu$ <0.3 for serpentinites comprising dominantly lizardite and chrysotile and ∼0.5 for antigorite samples that were carefully mineralogically and microstructurally defined (for temperatures of 25 °C and 170 °C, effective normal stress of 5-120 MPa and water-saturated conditions), consistent with the previous studies mentioned above (Fig. 1.8b). It has been suggested that as little as ∼10-15% serpentinisation can reduce rock strength to that of 'pure' serpentine (Escartín *et al.*, 2001), which results in big consequences in fault rheology as in most cases this will decrease strength compared to the unserpentinised protolith (e.g. Bickert *et al.*, 2020).

The limitation to all of these experiments is that they are conducted at strain rates where deformation takes place entirely in the frictional regime (largely through fracturing, crystal bending and folding, and frictional sliding; Tesei *et al.*, 2018). It is known that dissolution-precipitation, in addition to frictional sliding, plays an important role in controlling serpentinite rheology in natural serpentinite shear zones (e.g. Cox *et al.*, 2021; Viti *et al.*, 2018, Chapter 3). At higher temperatures associated with antigorite stability, dislocation creep may become an important mechanism in serpentinite deformation (Amiguet *et al.*, 2014; Auzende *et al.*, 2015; Hilairet *et al.*, 2007;

Padrón-Navarta *et al.*, 2012), however, the temperature of antigorite stability is greater than that expected in oceanic transforms and considered in this thesis.

As well as being frictionally weak minerals, laboratory studies at slow slip rates ($\sim 10^{-9}$ m/s) and $T$ <600 °C show that serpentine minerals behave with a velocity-strengthening behaviour, meaning they favour aseismic creep (Andreani *et al.*, 2005; Kohli *et al.*, 2011; Moore *et al.*, 1997, 1996; Moore and Rymer, 2007; Reinen, 2000; Reinen *et al.*, 1994, Chapter 3). However, at elevated slip rates ($\sim$0.1 m/s), lizardite-rich serpentinites deformed in the laboratory display velocity-weakening, seismogenic behaviour (Kohli *et al.*, 2011) meaning that serpentine has a conditionally stable nature that depends on strain rate (Kaproth and Marone, 2013). This conditionally stable nature of serpentine means that fast earthquake slip and steady creep may occur on the same fault segment resulting in a multimode behaviour of faults (Kaproth and Marone, 2013; Leeman *et al.*, 2016). In contrast to lizardite, chrysotile exhibits a velocity-independent behaviour, remaining velocity-strengthening at all laboratory strain rates under hydrothermal conditions (Moore *et al.*, 1997, 1996; Reinen, 2000). In summary, where hydration occurs, the rheology of the oceanic lithosphere may not be controlled by an olivine rheology, but rather by a serpentine (or chlorite-rich) rheology that is potentially sensitive to slip velocity (as considered in Chapters 3-5).

## 1.7 Oceanic transform faults

### 1.7.1 Depth of seismicity in oceanic lithosphere

It has long been considered, from earthquake focal depths (Abercrombie and Ekström, 2001; Braunmiller and Nábělek, 2008; Roland *et al.*, 2010) and results from laboratory friction experiments (Boettcher *et al.*, 2007), that the base of the seismogenic zone, defined as the depth range where earthquakes can nucleate, can be approximated by the 600 °C isotherm for the oceanic lithosphere in absence of substantial alteration (Fig. 1.2). Furthermore, peridotite mylonite microstructures show localised viscous deformation occurs at 600-800 °C (e.g. within samples dredged from the Shaka Fracture Zone; Warren and Hirth, 2006); suggesting a change from brittle to ductile deformation in this tem-

perature range. A change from velocity-weakening to velocity-strengthening behaviour in olivine is also expected at these temperatures, by extrapolation from laboratory experiments (Fig. 1.2; Boettcher *et al.*, 2007).

More recent studies suggest that a correlation between the seismic-aseismic transition and the 600 °C isotherm is too simple. For example, an observed dominantly aseismic behaviour at shallow crustal conditions ($T$ <600 °C) is not consistent with the velocity-weakening behaviour expected from olivine under these conditions (Boettcher *et al.*, 2007). Additionally, the spatial distribution in seismic behaviour also varies along-strike (Fig. 1.9) (e.g. Braunmiller and Nábělek, 2008; Froment *et al.*, 2014), down-dip (Fig. 1.9b) (some studies recording earthquakes corresponding to depths >1000 °C; e.g. Abercrombie and Ekström, 2001; Kuna *et al.*, 2019; McGuire *et al.*, 2012) and between oceanic transform faults (Boettcher and Jordan, 2004). These observations are inconsistent with an exclusively thermal control on the depth-extent of the seismogenic zone. Studies by Prigent *et al.* (2020) and Kohli and Warren (2020), based on dredged samples, concluded that seawater percolation and mantle hydration occurred at temperatures >850-875 °C along the Shaka and Prince Edward oceanic transforms. Considering hydrothermal cooling in numerical models can explain some of the deeper seismicity by a cooler geotherm than otherwise expected (e.g. Prigent *et al.*, 2020; Roland *et al.*, 2010). The depth to the base of the seismogenic zone has also been suggested to vary during the seismic cycle. For example, the Gofar transform fault displays large mainshock events and associated aftershocks at depths corresponding to $T$ <600 °C, while foreshocks extend to depths corresponding with $T$ ∼1100 °C (Roland *et al.*, 2012).

In addition to the occurrence of seismicity below the seismogenic zone, abundant creep (∼85% of the global slip Boettcher and Jordan, 2004) occurs within the thermally-defined seismogenic zone. Several hypotheses attempt to explain this relatively shallow aseismic behaviour of oceanic transforms, including: (1) The hydration and alteration of mafic and ultramafic minerals to weak phyllosilicates and serpentine, which can favour velocity-strengthening creep (section 1.6.3; Boettcher and Jordan, 2004; Moore *et al.*, 1997; Reinen *et al.*, 1994). (2) A role of elevated fluid pressure that acts to lower the effective normal stress and enable velocity-strengthening creep (Scholz, 1998). (3) Deep fluid flow leading to fluid-driven weakening and strain localisation in weak my-

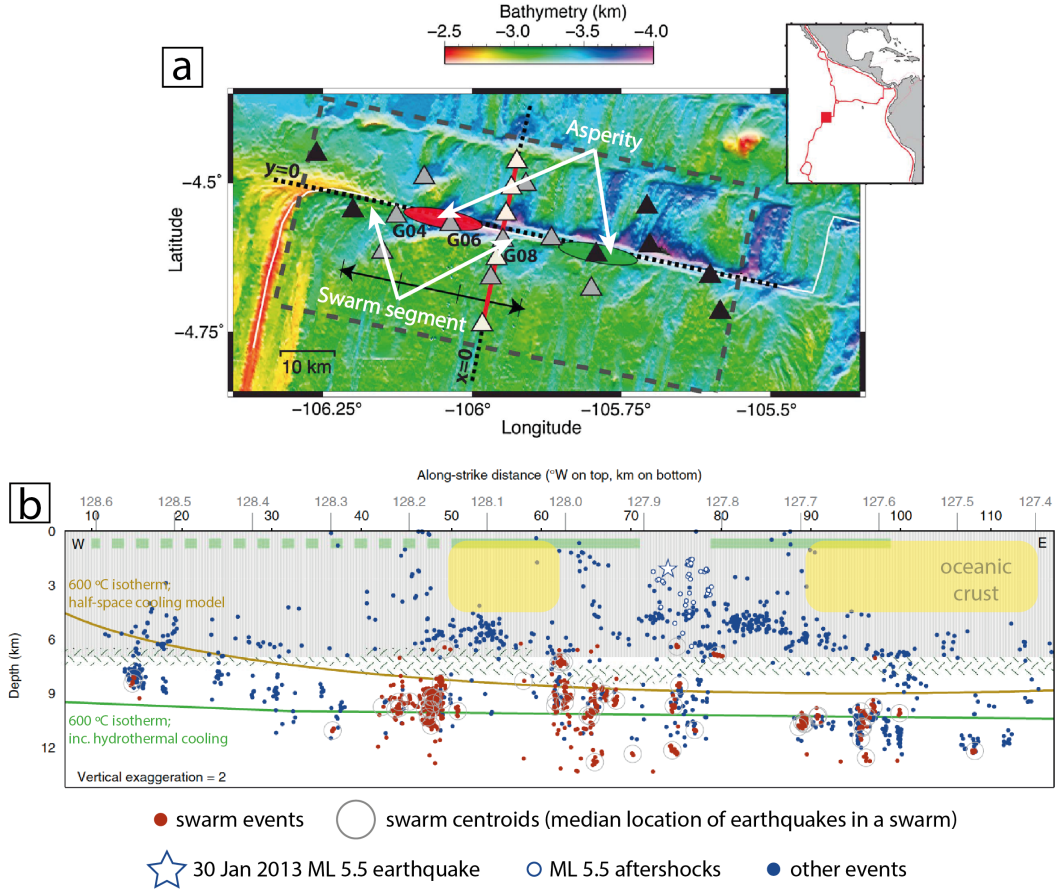


**Figure 1.9:** Examples showing the spatial variation in seismic behaviour along two oceanic transform faults on the East Pacific Rise. (a) Along-strike segmentation of seismic behaviour along the Gofar transform fault into locked asperity regions (red patch is centred on the location of the 2008 Mw 6.0 earthquake, green patch is centred on the 2007 Mw 6.2 earthquake) and swarm segments (after Froment *et al.*, 2014). Triangles show locations of ocean bottom seismometers. (b) The along-strike and down-dip distribution of seismicity along the Blanco ridge transform fault (after Kuna *et al.*, 2019). Notice that there are regions of shallow aseismic behaviour within the oceanic crust (e.g. between 50-60 km and 90-110 km; yellow shaded boxes) and seismic behaviour that extends beyond the 600 °C isotherms, into the mantle.

lonitic shear zones at higher temperatures within the lithospheric mantle (Kohli and Warren, 2020; Prigent *et al.*, 2020) and, (4) spatial variation in fault zone damage, resulting in heterogeneous permeability and subsequently spatial variation in rock properties, possibly favouring swarms of microseismicity or creep (Froment *et al.*, 2014; McGuire *et al.*, 2012; Roland *et al.*, 2012). However, to date, it remains unclear which, or what combination of these processes are responsible for change from seismic to aseismic slip within the seismogenic zone.

As well, the deformation mechanisms active within oceanic transform faults are poorly constrained. This is because the vast majority of work conducted on oceanic transforms seismic behaviour is limited to remote and ocean floor seismological observations, observations made on sea floor samples obtained from dredges, dives and 1D boreholes, and inferences drawn from laboratory experiments and numerical models.

Some recent studies have tried to address some of these observational gaps using samples dredged from modern oceanic transform faults (Kohli and Warren, 2020; Prigent *et al.*, 2020) and samples collected from the exhumed Massif du Sud ophiolite in New Caledonia (Chatzaras *et al.*, 2020). However, these studies largely focused on relatively high-temperature deformation, $T$ >600 °C, and therefore relate to deformation occurring deeper than the base of the thermally-defined seismogenic zone. This thesis seeks to provide an insight into the geological controls on the seismic behaviour of active oceanic transform faults using observations from the Southern Troodos Transform Fault Zone in the Troodos Ophiolite in Cyprus. At this site, micro- to kilometre-scale observations of an exhumed oceanic transform fault can be made where deformation has been inferred to have occurred at $T$ <600 °C. The the Southern Troodos Transform Fault Zone is a unique example of an intact oceanic transform preserved on-land, and hence presents a unique 3D opportunity to characterise the deformation and rheology of an oceanic transform within the seismogenic zone (details on the geological setting can be found in Chapter 2).

### 1.7.2 Seismic coupling of oceanic transform faults

Because earthquake moment magnitude (Mw) scales with rupture length (Kanamori and Anderson, 1975; Wells and Coppersmith, 1994), oceanic transforms are expected to produce relatively frequent, large earthquakes. Given the relatively fast displacement on many oceanic transforms, these large earthquakes should have sufficiently short repeat times to have been recorded in instrumental time (Molnar, 1979). Yet, despite this, it has been recognised that they host relatively few recorded earthquakes, and these are typically of smaller magnitude (rarely > Mw 7.0) than predicted by this scaling relationship (e.g. Bird *et al.*, 2002; Boettcher and Jordan, 2004; Brune, 1968). This section considers scaling relations surrounding oceanic transform fault seismicity.

The fraction of plate motion within the seismogenic zone that is accom-

modated by seismic slip is described as the seismic coupling coefficient, $\chi$. Seismic coupling can be defined by the equation $\chi = \Sigma M_{obs}/\Sigma M_{ref}$ (Scholz, 2002), where $\Sigma M_{obs}$ is the sum of the observed seismic moment, and $\Sigma M_{ref}$ is the sum of the expected seismic moment for a given fault assuming all displacement within a defined depth range occurs in earthquakes. Seismic moment, $M$, is defined by $GAu$, where $G$ is the shear modulus, $A$ is the rupture area and $u$ is the average slip. Moment relates to earthquake magnitude following the relation Mw = (2/3)$\log_{10}M$-6 ($M$ measured in Nm). $\Sigma M_{ref}$ is the moment release expected from a plate tectonic model and can be specified in terms of the thermal area of contact, $A_t$. $A_t$ is calculated as the fault area above a reference isotherm (Fig. 1.10; $T_{ref}$) chosen as the base of the seismogenic zone (taken as 600 °C for oceanic transform faults) using a half space cooling model (Boettcher and Jordan, 2004) and follows the scaling relation $A_t \propto L^{3/2}V^{-1/2}$, where $L$ is fault length and $V$ is slip velocity. The average "thermal thickness" for the reference isotherm is defined by $W_t = A_t/L$. The cumulative seismic moment is $\Sigma M_{ref} = GA_tV\Delta t_{cat}$, where $\Delta t_{cat}$ is the length of the earthquake catalogue (Boettcher and Jordan, 2004). Observed moment, assuming that $L$ and $V$ are as for the fault as a whole, can be cast in terms of the effective seismogenic width, $W_E$ (Fig. 1.10) as $W_E = \Sigma M_{obs}/GLV\Delta t_{cat}$, (Brune, 1968). Following this, $\chi$ is the ratio of $W_E$ and $W_t$ and low values of $\chi$ imply a small effective width of the seismic zone (Boettcher and Jordan, 2004). The concept of $W_E$ implies that seismicity is distributed equally along-strike. However, observations from active oceanic transform faults and conclusions in Chapters 3 and 4 suggest this assumption may not be reasonable.

$\chi$ can vary significantly along a single fault; areas that creep have $\chi = 0$, while locked segments capable of hosting seismic slip with no aseismic creep within the seismogenic zone have $\chi = 1$. A fault with $0 < \chi < 1$ suggests that it comprises both locked and creeping segments or where a fault has no fully coupled segments, i.e. where a fault accommodates slip by creep at a rate less than the plate velocity, and therefore also requires some earthquake moment (e.g. van den Ende *et al.*, 2020).

Oceanic transforms generally have low $\chi$ (Boettcher and Jordan, 2004; Brune, 1968; Okal and Langenhorst, 2000). The global average, assuming the base of the seismogenic zone is controlled by the 600 °C isotherm, is $\chi \sim 0.15$ (Boettcher and Jordan, 2004), suggesting that only ∼15% of slip occurring on

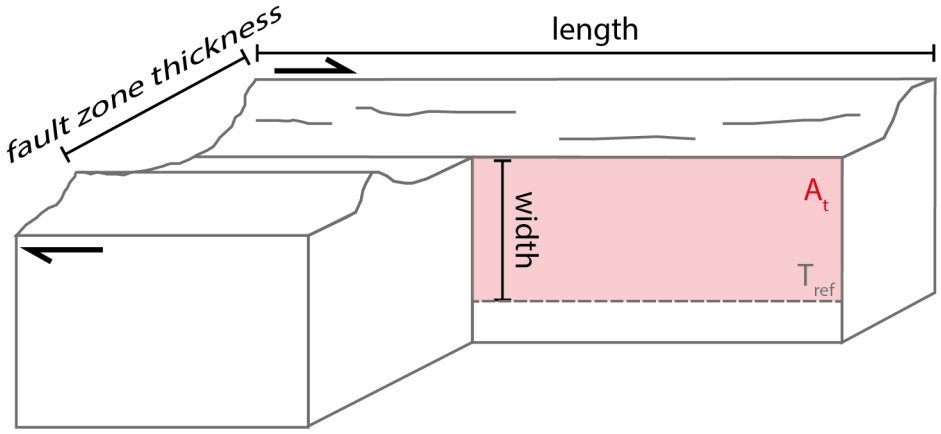


**Figure 1.10:** Block diagram of an oceanic transform fault defining fault length, width and thickness as well as the thermal area of contact, $A_t$ and a reference isotherm $T_{ref}$.

oceanic transforms is accommodated by seismic slip while 85% occurs aseismically. A closer look at $\chi$ of oceanic transform faults reveals that although the global average is $\chi = 0.15$, this varies between faults, and along-strike and down-dip on single fault systems (e.g. McGuire, 2008) (Fig. 1.9). For example, along the East Pacific Rise, most oceanic transforms accommodate displacement almost entirely aseismically, with $\chi$ <0.2 (Boettcher and Jordan, 2004), while the Charlie-Gibbs transform on the Mid Atlantic Ridge can have a $\chi$ ∼0.88 (Aderhold and Abercrombie, 2016). The Eltanin Transform System (comprising the Heezen, Tharp and Hollister transform faults in an en echelon array) in the SE Pacific has a very low $\chi$ with an average of ∼0.1 (Stewart and Okal, 1983). Some parts of the Heezen and Tharp transform faults within this system slip in quasiperiodic large magnitude (Mw <6.4) earthquakes, while the majority of the system creeps aseismically (Molnar *et al.*, 1975; Sykes and Ekström, 2012).

The along-strike variation in $\chi$ seen on oceanic transform faults is reflected in the distribution of quasi-repeating, Mw >6.0, earthquakes along fast-spreading East Pacific Rise transform faults (e.g. Fig. 1.9; McGuire *et al.*, 2005). A year-long ocean-bottom seismometer study of the Gofar transform fault identified a 10 km-long section that hosted a swarm of ∼20 000 foreshocks preceding a Mw 6.0 earthquake (McGuire *et al.*, 2012). The main Mw 6.0 shock was confined to the crust, while the microseismically active foreshock zone extended a few kilometres into the upper mantle. The foreshock zone acted as a "rupture barrier" region to the main earthquake rupture, which did not prop-

agate laterally into the surrounding microseismically active, creeping regions of the crust, or down-dip into the mantle (McGuire *et al.*, 2012). The rupture barrier regions in this location have been associated with high porosity from an observed ∼3% reduction in average shear-wave velocity (Roland *et al.*, 2012). Distinct rupture patches that also fail in Mw ∼6.0 and are restricted to the crust have been identified on the Discovery transform fault (McGuire, 2008). These patches are also punctuated along-strike by zones (≤10 km long) that are rich in microseismicity (Wolfson-Schwehr *et al.*, 2014). Much like as along Gofar, the distinct rupture patches on the Discovery transform appear to be fully coupled, while patches containing a lot of microseismicity are not well coupled (low $\chi$).

Additionally, the Blanco Ridge segment, north Pacific, that connects the Juan de Fuca and Gorda Ridges, has an average $\chi$ of 0.25 suggesting considerable amounts of aseismic creep (Braunmiller and Nábělek, 2008), but also varies substantially along-strike. Here long, straight mature segments have a higher $\chi$, while less mature zones are geometrically more complex with lower $\chi$ (Braunmiller and Nábělek, 2008). Additionally, the Blanco Ridge segment hosts quasirepeating earthquakes (Mw > 6.0) on two distinct patches that are fully coupled and devoid of microseismicity (Braunmiller and Nábělek, 2008; Kuna *et al.*, 2019). In contrast, regions surrounding these locked patches appear to have low $\chi$ (Boettcher and McGuire, 2009; Braunmiller and Nábělek, 2008) and abundant microseismicity that is driven by aseismic loading (Kuna *et al.*, 2019).

Along the slower-spreading Mid Atlantic Ridge, the Charlie-Gibbs transform fault also displays repeating earthquake sequences (Aderhold and Abercrombie, 2016). In 2015 a Mw 7.1 earthquake ruptured the same fault patch as a similar magnitude earthquake in 1974 and a Mw 6.8 event ruptured another fault patch in 1998 that previously hosted an earthquake in 1967. Aderhold and Abercrombie (2016) calculated that the seven main earthquakes that occurred along the Charlie-Gibbs transform fault over the last 92 years accounts for a maximum of 88% fault motion, or a $\chi$ of 0.88, which is much higher than the global average when considering two main events as the start and end period of the calculation and a 600 °C isotherm. Even when adding 15 years to this duration, $\chi$ only reduced to 0.75, which would decrease further if an 800 °C isotherm was used, however, these values still remain much higher

than the global average ($\chi = 0.15$; Boettcher and Jordan, 2004).

### 1.7.3 Oceanic transform fault models

Detailed microseismic studies of oceanic transform faults (e.g. Fig. 1.9) reveal the seismic heterogeneity experienced by these faults and have led to a number of conceptual models for oceanic transforms. Boettcher and Jordan (2004) proposed a set of scaling relations for oceanic transform faults that related thermal structure and seismicity (described in 1.7.2 above). The result from their study, and a later study by Boettcher and McGuire (2009) who added new scaling relations for the expected duration of seismic cycles on oceanic transform faults, show there is a large seismic deficit along oceanic transform faults and that the largest earthquakes do not rupture the entire fault area. They proposed four models for the oceanic transform fault seismogenic zone (Fig. 1.11):

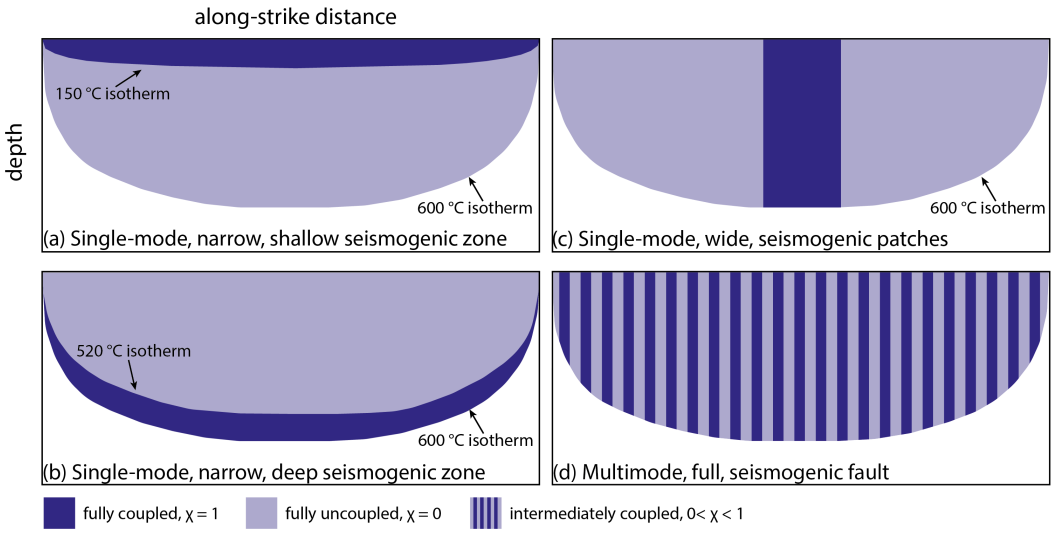


**Figure 1.11:** The four conceptual models of oceanic transform fault seismicity. Adapted from Boettcher and Jordan (2004). (a) Single-mode, thin, shallow seismogenic zone, (b) single-mode, thin, deep seismogenic zone, (c) single-mode, thick, seismogenic patches and (d) multimode, full seismogenic fault. The seismogenic zone in these models is bounded by the 600 °C isotherm.

#### Single-mode, narrow, shallow seismogenic zone

Narrow seismogenic zone with each part of the fault either fully seismically coupled or fully aseismic. As the name of this model suggests, the top part

(shallow portion) of the fault is a fully coupled seismogenic zone while the remainder of the fault below is fully aseismic. This is based on early hypotheses surrounding oceanic transform seismicity (e.g. Brune, 1968). Since $\chi$ implies low values of $W_E$, to account for low values of $\chi$ a narrow seismogenic zone is required. Boettcher and Jordan's (2004) scaling relations constrain the down-dip limit of this seismogenic zone to the ∼100 °C isotherm (for a fault of $L$ = 300 km and $V$ = 40 mm/yr) if the upper boundary of the seismogenic zone is taken as the seafloor; an implausible model since earthquakes nucleate down to >600 °C (e.g. Abercrombie and Ekström, 2001; Braunmiller and Nábělek, 2008; McGuire *et al.*, 2012; Roland *et al.*, 2010).

**Single-mode, narrow, deep seismogenic zone**

Like the model above, this model involves a narrow seismogenic zone that is fully coupled, while the rest of the fault is fully aseismic. Except here, the seismogenic zone is deep. If the deeper limit is fixed to the 600 °C isotherm for the same fault as above, then the upper limit of the seismogenic zone would sit at ∼520 °C (Boettcher and Jordan, 2004). This model is also unlikely since many ocean-bottom seismometer studies document earthquake focal depths far shallower than this temperature range allows, and throughout a multi-kilometre depth range incompatible with this small range in temperatures (e.g. Roland *et al.*, 2012).

**Single-mode, wide seismogenic patches**

This model considers faults being segmented along-strike into patches that are either fully coupled or fully aseismic, rather than segmented with depth. These patches can extend from the seafloor to the 600 °C isotherm (full width of $A_t$), explaining shallow and deeper earthquakes. There is increasing amounts of evidence that oceanic transform faults are segmented into locked asperities and creeping portions along-strike and so this model can explain some observations from some oceanic transform faults (e.g. McGuire *et al.*, 2005).

**Multimode fault**

Seismic slip or aseismic creep is not limited to any portion of the fault shallower than the 600 °C isotherm (e.g. Bird *et al.*, 2002). Fault patches where

creep and microseismic activity occurs (McGuire *et al.*, 2012) and large earthquakes occurring in moderate to low $\chi$ zones (e.g. along the western portion of the Blanco Transform Fault where Mw 6.0 earthquakes occur infrequently; Braunmiller and Nábělek, 2008) provide evidence for multimode behaviour. Additionally, 3D strike-slip rate-and-state models (Liu *et al.*, 2012) suggest oceanic transform fault segments can transition between seismic and aseismic slip over many earthquake cycles. In other words, oceanic transforms may be regarded as comprising small seismogenic patches within a predominately aseismic fault, much like what is proposed for the asperity model for dominantly creeping subduction thrusts (Lay and Kanamori, 1981).

### 1.7.4 Current fit of observations to models

As previously discussed by Fagereng and MacLeod (2019), based on the existing geophysical data, oceanic transforms appear to follow a combination of behaviours that best fit "single-mode, wide seismogenic patches" and "multimode" (Fig. 1.11c-d) models of Boettcher and Jordan (2004). Generally, fully coupled patches rupture during the largest events, but are separated by zones that accommodate slip by creep and/or microseismicity (eg. Braunmiller and Nábělek, 2008; McGuire *et al.*, 2005, 2012). However, it also seems possible in places that segments can temporally change between large earthquake and aseismic/microseismic behaviours, such as along the Charlie-Gibbs transform fault (Aderhold and Abercrombie, 2016) where despite having $\chi$ as high as 0.88, it is suggested that to account for the remaining fault slip along the Charlie-Gibbs transform, aseismic slip must occur during the interseismic period. Therefore, implying that it has a multimode behaviour.

Connections between $\chi$, fault maturity, geometry and/or material properties are likely, but the geological nature of locked and creeping zones is not well constrained, and the spatial and temporal nature of fault segmentation needs further investigation. In particular, multimode behaviour has not been considered until relatively recently, although it has been documented in other tectonic settings, including along the Parkfield section of the San Andreas Fault (Custódio and Archuleta, 2007) and within subduction zones (Ide *et al.*, 2011). Multimode behaviour on oceanic transforms may arise from a number of reasons (Fagereng and MacLeod, 2019) including the velocity-dependence of friction (section 1.3.2; Dieterich, 1992), dynamic weakening by thermal pres-

surization (Noda and Lapusta, 2013), or from the behaviour of a wide range of materials of different rheological and frictional properties coexisting in tabular fault zones (Collettini *et al.*, 2011; Fagereng and Sibson, 2010).

Several factors, based off geophysical observations, have been proposed to influence the seismic coupling of oceanic transforms including increased fault damage, porosity and alteration (e.g. Froment *et al.*, 2014; McGuire *et al.*, 2012; Roland *et al.*, 2012), increased fluid flow lowering the effective normal stress (Roland *et al.*, 2010) and fault geometry (Wolfson-Schwehr *et al.*, 2014). For example, fault bends of a few kilometres have been observed at the end-points of Mw 6.0 earthquakes in continental transforms (e.g. Wesnousky, 2006). Small-scale geometrical complexities have been identified on East Pacific Rise transform faults including a ∼600 m fault bend on Gofar (Froment *et al.*, 2014) and further geometrical complexities offset the main asperity and rupture barrier regions on the western Discovery fault (Wolfson-Schwehr *et al.*, 2014). These observations raise the possibility that fault zone geometry influences the segmentation of East Pacific Rise faults. Even though fault bends observed on Gofar are far smaller than those observed in continental transforms, Froment *et al.* (2014) suggest they may still play a role in perturbing local rupture dynamics by reducing rupture velocity. However, even if these fault bends alone were responsible for terminating Mw 6.0 ruptures on Gofar, they do not explain the overall seismic deficit observed globally along oceanic transform faults (e.g. Boettcher and Jordan, 2004; Froment *et al.*, 2014).

The anomalously low P- and S-wave velocities detected in microseismically active creeping segments could be explained by high porosity and/or increased fluid pressure within these zones (Froment *et al.*, 2014; McGuire *et al.*, 2012; Roland *et al.*, 2012). Increased porosity within rupture barrier regions would make these zones prone to dilatant strengthening and prevent rupture propagation (Fagereng and MacLeod, 2019; Liu *et al.*, 2020). Dilatant strengthening is related to the tendency for pore space to increase and therefore effective normal stress to decrease during earthquake propagation in porous media. Therefore, it can act to suppress dynamic slip (Segall *et al.*, 2010). Alternatively, because aseismic slow-sliding of fluid-overpressured faults prevents elastic loading that is required for seismic slip, highly damaged regions with increased porosity may prevent seismic rupture (Segall and Rice, 1995). The strength and frictional behaviour of the oceanic crust is explored further from field data in Chapter

4 and experiment data in Chapter 5.

The presence of serpentine along oceanic transforms is one explanation for the multimode behaviour, because serpentine is observed to have velocity-strengthening characteristics at slow velocities but velocity-weakening behaviour at fast sliding velocities (Moore and Rymer, 2007; Reinen, 2000; Reinen *et al.*, 1991) allowing for both stable and unstable slip (section 1.3.2). Furthermore, serpentinisation can explain some of the reduced seismic velocities observed along oceanic transform faults (e.g. Froment *et al.*, 2014). Similarly, within the mafic crust, aseismic creep could be explained by the presence of chlorite-rich fault zones where hydration reactions lead to chlorite growth rather than serpentinisation. Chlorite is known to be weak ($\mu \sim 0.3$) and velocity strengthening under almost all experimental conditions from room $T$ and 10 MPa pressure (Fagereng and Ikari, 2020, Chapter 5), up to 400 MPa and 600 °C (Okamoto *et al.*, 2019). Therefore, where the volume of chlorite is sufficient to create an interconnected network (Handy, 1990; Niemeijer, 2018), chlorite-rich faults along oceanic transform faults could explain some aseismic creep that occurs within the oceanic crust, particularly at low slip rates (<1 $\mu$m/s; Niemeijer, 2018; Niemeijer and Spiers, 2006). According to laboratory experiments, at higher sliding velocities (>1 $\mu$m/s), fault gouges can allow velocity-weakening behaviour and the propagation of earthquakes (Niemeijer, 2018; Niemeijer and Spiers, 2006), suggesting that chlorite-rich faults could also explain multimode behaviour of crustal faults.

## 1.8 Main research aims and questions

The review above has highlighted many hypotheses that attempt to explain the weakness and low-$T$ (<600 °C) aseismic behaviour of oceanic transform faults, including increased damage zone fracturing and/or porosity, the alteration to frictionally-weak phyllosilicates and serpentine, and a role of fluid pressure lowering effective normal stress. However, most studies addressing the strength and seismic behaviour of oceanic transform faults are based on remote sensing and ocean floor seismological observations, dredged samples, 1D borehole observations, and inferences from lab experiments and numerical models with little direct geological evidence. The novelty and overall aim of this thesis is to understand the geological controls on the seismic behaviour

of oceanic transform faults. To address this, I conducted fieldwork involving mapping and whole-rock sampling of variably deformed fault and shear zone rocks within the mafic oceanic crust and serpentinised lithospheric mantle from the exhumed Southern Troodos Transform Fault Zone in Cyprus. I carried out mapping at a range of scales including individual outcrops and areas of 1-2 $km^2$ in size, within both the crust and mantle sections of the exhumed ophiolite, to understand the spatial heterogeneity and geometrical controls on deformation. Fieldwork and sampling were followed by microstructural analysis using optical and scanning electron microscopy (Chapters 3-5) including mineral chemistry (energy dispersive spectroscopy) (Chapter 3-4), Raman analysis (Chapter 3), and grain-size analysis (Chapter 4). Direct-shear friction experiments were conducted on sampled fault rocks from Cyprus and intact dolerite from the East Pacific Rise in collaboration with the University of Bremen (Chapter 5). Details of the methods used are given in the appropriate chapters.

The main research questions are:

Q1: How does deformation evolve within the thermally-defined seismogenic zone of oceanic transform faults and what are the deformation mechanisms responsible?

Q2: What is the role of fluids within oceanic transform faults?

Q3: What is the geological nature of the locked and creeping patches along oceanic transform faults?

Q4: How weak are oceanic transform faults?

## 1.9 Thesis outline

This thesis is divided into five main parts: The general introduction in this current chapter, covering the subjects that are discussed in this thesis, including geophysical observations from oceanic transform faults, numerical models relating to their mechanical behaviour, the serpentinisation process, and laboratory experiments on mafic and phyllosilicate materials. The first part ends with an introduction to the geological setting of Cyprus and a review of the

Southern Troodos Transform Fault Zone (Chapter 2). There are three scientific chapters presenting original data, analysis, and interpretation (Chapters 3-5). Two of these chapters present observations from the Southern Troodos Transform Fault Zone to investigate controls on the rheology of the lithospheric mantle (Chapter 3) and mafic oceanic crust (Chapter 4). The third science chapter presents rock deformation experiments that explore variation in strength and seismic behaviour of variably deformed fault rocks from the mafic oceanic crust (Chapter 5). A concluding chapter discusses the findings of Chapters 3-5, by addressing my earlier questions and suggesting ideas for future research.

Chapter 3 investigates the development of serpentinite shear zones within a pervasively serpentinised lithospheric mantle, and how their structure and rheology may evolve with continued deformation (at $T$ <600°C). This study is based on mapping and whole-rock sampling that was followed by microstructural, geochemical and Raman analysis.

Chapter 4 considers the progressive deformation of the shallow mafic oceanic crust along oceanic transforms, based on field mapping and whole-rock sampling on the South Troodos Transform Fault Zone. Microstructures and grain size analyses were used to understand the progressive deformation that occurred during predominantly brittle deformation.

Chapter 5 follows on from Chapter 4, testing a selection of variably deformed mafic fault rocks (and intact dolerite from the Mid-Atlantic Ridge) in direct-shear friction experiments. Experimental observations and rate-and-state frictional modelling are coupled with microstructural observations. The experiments were designed to investigate how variable amounts of brittle damage, and associated alteration, affects the strength and seismic behaviour of crustal faults within an oceanic transform fault setting.

Chapter 3 is derived from a published manuscript (Cox *et al.*, 2021), while Chapters 4 and 5 have been derived from manuscripts prepared for submission. I conducted fieldwork and laboratory analysis with supervision from Ake Fagereng and Chris MacLeod. Raman analysis was conducted by Matt Tarling and Chris Tulley at the University of Otago. I performed the experiments under guidance from Matt Ikari at the university of Bremen. I led the writing for the research conducted in this thesis with input from Ake Fagereng, Christopher MacLeod and Matt Ikari where appropriate. Detailed author con-

tributions are listed at the start of each chapter.

# Chapter 2

# Geological setting of the Troodos Ophiolite and Southern Troodos Transform Fault Zone

## 2.1 Troodos Ophiolite

The Troodos Massif is a fragment of Late Cretaceous-age (91.6 ±1.4 Ma; Mukasa and Ludden, 1987) oceanic lithosphere formed as a consequence of the closure of the Palaeotethys ocean (Fig. 2.1) (e.g. Gass, 1968; Robertson, 1977). The geology and tectonic evolution of the Troodos ophiolite is described briefly in this chapter, with a focus on the Southern Troodos Transform Fault Zone (STTFZ).

The Troodos Ophiolite, along with many Eastern Mediterranean ophiolite terranes, has played an important role in our understanding of plate tectonics (e.g. Gass, 1968, 1980; Moores and Vine, 1971). In 1959, Wilson realised that what is called the Sheeted Dyke Complex (described section 2.2.3) today represents an area of vertical dykes intruding other dykes. In 1963, Vine and Matthews recognised that consistent linear magnetic anomalies, of alternating positive and negative polarity, are evidence for the creation and spreading of new seafloor at mid-ocean ridges and the mechanism by which continental drift takes place. Following these findings, Ian Gass (1968) made the conceptual link between the Sheeted Dyke Complex in Cyprus and seafloor spreading, deducing that ophiolites are representative of on-land fragments of oceanic lithosphere.

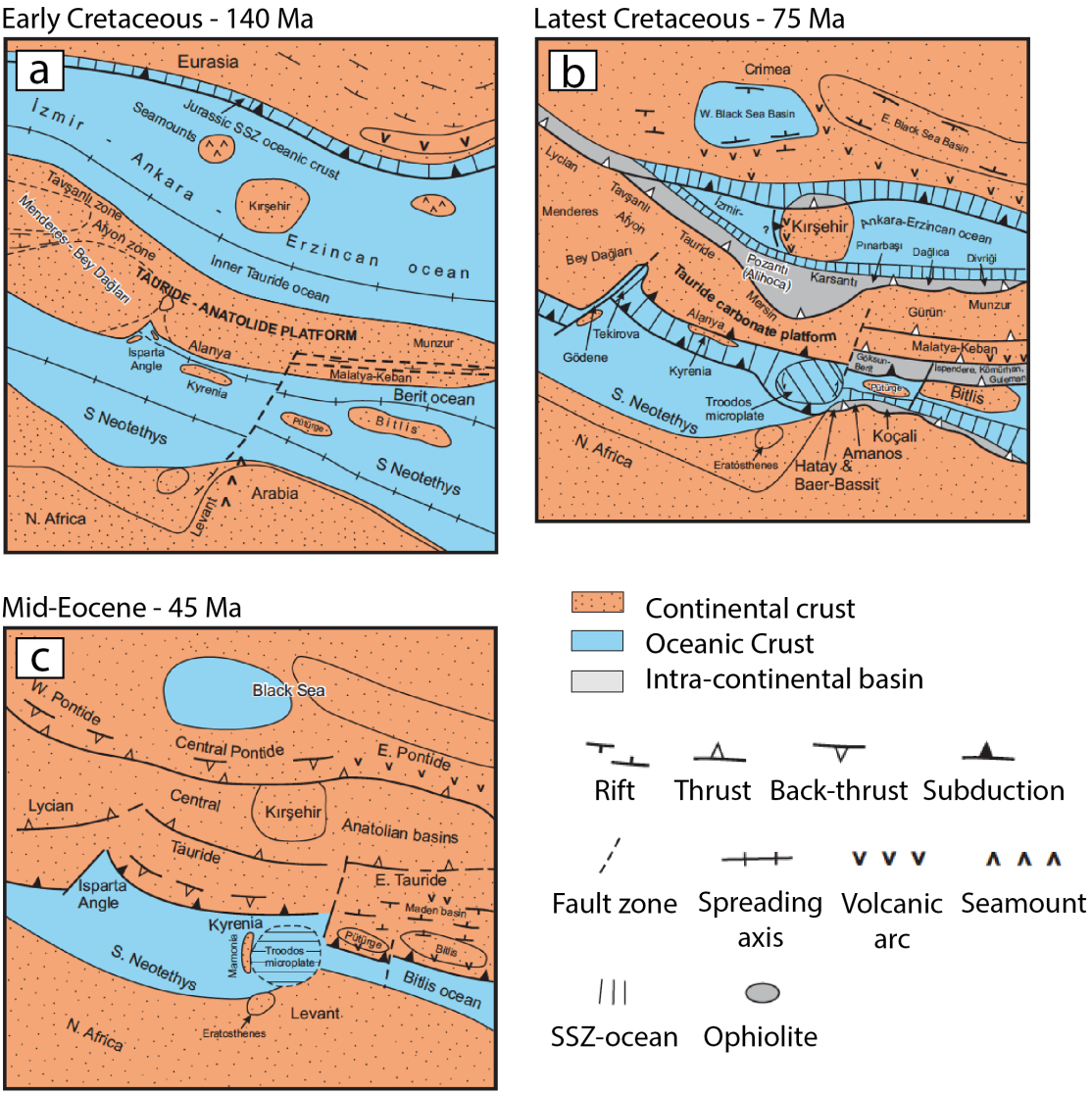


**Figure 2.1:** (a) Early Cretaceous. Southern Neotethys reached its maximum width with subduction to the north below the Eurasian margin closing the Izmir-Ankara-Erzincan Ocean. (b) Latest Cretaceous. Continued closure of the Izmir-Ankara-Erzincan Ocean. Southward subduction along the Arabian continental margin and obduction of ophiolites. Subduction was accompanied by arc volcanism. (c) Mid-Eocene. Final closure of the Izmir-Ankara-Erzincan Ocean. Continued northward subduction of the Southern Neotethys causing it to narrow and resulting in volcanism in SE Turkey. Adapted from Robertson *et al.* (2012).

### 2.1.1 Formation and emplacement of the Troodos ophiolite

The evolution of the eastern Mediterranean is complex, but can be summarised by the opening and closing of several Mesozoic oceanic basins associated with the breakup of Pangaea, and the collision of Africa with Eurasia. Many Eastern Mediterranean ophiolites are located throughout Croatia, Albania, Greece, Turkey and Cyprus, and similar ophiolites extend east and west along the Alpine-Himalayan belt. Almost all of the preserved ophiolites are of Late Cretaceous age and believed to have formed as distinct episodes of spreading within the Neotethys - a large ocean separating Africa and Eurasia (e.g. Moores *et al.*, 1984; Robertson and Mountrakis, 2006; Robertson *et al.*, 2012). The closure of this ocean was driven largely by northwards subduction of the African plate below the Eurasian continent throughout the Mesozoic-Cenozoic, resulting in the emplacement of these ophiolites, and is summarised below (Robertson *et al.*, 2012).

The southern Neotethys reached its maximum width in the Early Cretaceous (∼140 Ma), at which time the Palaeotethys (now replaced by the Izmir-Ankara-Erzincan Ocean) had begun to close along the Eurasian margin further to the north (Fig. 2.1a; Robertson *et al.*, 2012). By the latest Cretaceous, two subparallel belts, trending NE-SW, of Upper Cretaceous ophiolites had formed (Robertson, 2002). The most southern of these two belts includes the Troodos ophiolite of Cyprus (Fig. 2.1b; Robertson *et al.*, 2012). The southern ophiolites are inferred to have formed above a northward dipping subduction zone to the south of Cyprus (Fig. 2.1b; Pearce *et al.*, 1984; Robertson, 2002; Robertson and Mountrakis, 2006; Robertson *et al.*, 2012) at 91.6 ±1.4 Ma, according to U-Pb dating of zircons (Mukasa and Ludden, 1987). In the latest Cretaceous, southward obduction of supra-subduction zone ophiolites onto the Arabian continental margin occurred, as well as the continued subduction of the Palaeotethys northwards beneath Eurasia (Robertson and Mountrakis, 2006; Robertson *et al.*, 2012). Closure of the Izmir-Ankara-Erzincan Ocean, driven by the northward subduction of the African plate beneath the Eurasian plate, was complete by the Mid Eocene (∼45 Ma) (Fig. 2.1c). This closure was coupled with the continued northward subduction of the Southern Neotethys. Continued regional compression led to the closure of the Eastern

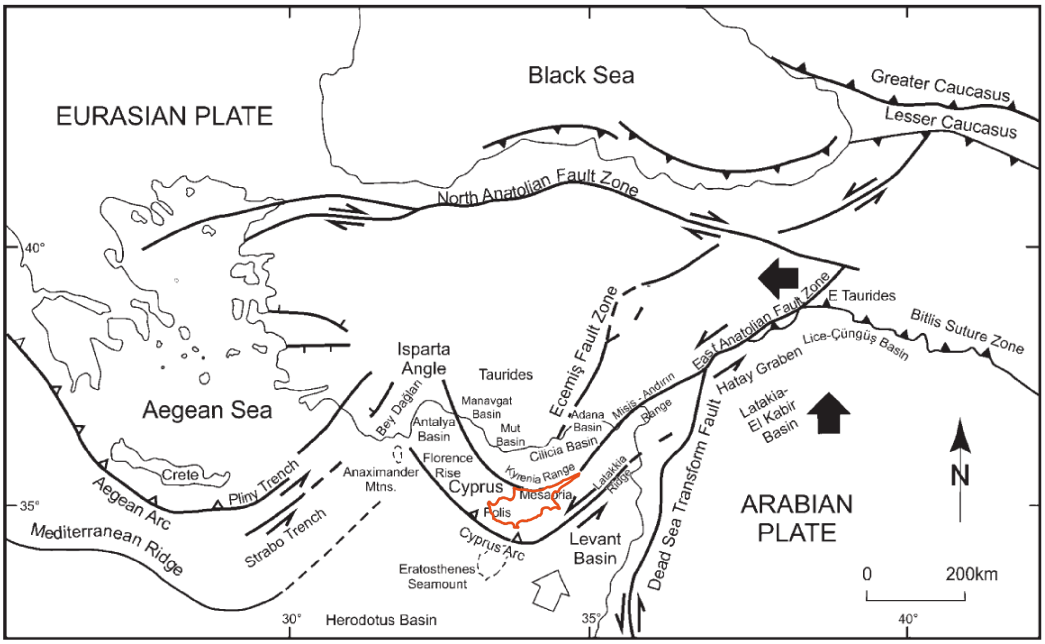


**Figure 2.2:** Map of the present day setting of the Eastern Mediterranean and Cyprus (from Robertson *et al.*, 2012). The Eastern Mediterranean is a region that remains dominated by compression tectonics relating to the continued convergence between Africa and Eurasia. Continued subduction along the Cyprus Arc to the south of Cyprus accounts for the continued seismicity in Cyprus.

Tethys separating it from the Arabian Gulf/Gulf of Oman and formation of the modern-day Mediterranean Sea by the mid Miocene (∼15 Ma; Robertson *et al.*, 2012). More recently, it has been instead suggested that the subduction beneath Cyprus occurred along a ∼NNE/SSW subduction zones within the Neotethys during the late Cretaceous (Maffione *et al.*, 2017), rather than the northward-dipping subduction along an ∼E-W subduction zone discussed above.

Today, Cyprus remains located in the north-eastern Mediterranean Sea (Fig. 2.2). Continued convergence between the African and Eurasian plates (Fig. 2.2; e.g. Feld *et al.*, 2017) means Cyprus remains seismically active (Fig. 2.3; Jackson and McKenzie, 1984; Robertson, 1990). This includes seismicity (e.g. Mw 5.6 in 1999) along the Yerasa Fold and Thrust Belt (section 2.4.3) to the SW of, and on the Arakapas Fault Belt at the northern limit of, the Southern Troodos Transform Fault Zone (introduced in section 2.3) (Cyprus Geological Survey Department, 2017).

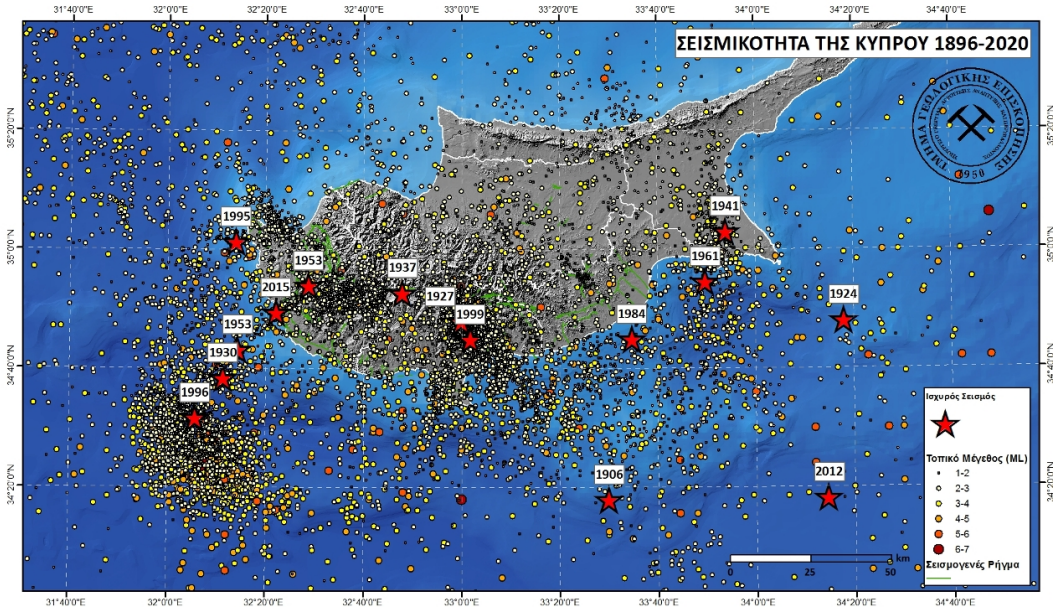


**Figure 2.3:** Seismic activity in Cyprus between 1986 and 2020. (Cyprus Geological Survey Department, 2020).

### 2.1.2 Evidence for a suprasubduction zone setting

The Troodos ophiolite was initially viewed as having formed in a mid-ocean ridge setting (Gass, 1968, 1980). However, geochemical studies suggest the lavas within the Troodos ophiolite's extrusive sequence are more comparable to those erupted within island arcs than those erupted at mid ocean ridges (e.g. Miyashiro, 1973; Pearce and Cann, 1973). The geochemical evidence from the lavas suggests that the magmas were fluid-enriched (e.g. Fonseca *et al.*, 2017; Miyashiro, 1973; Pearce and Robinson, 2010; Pearce, 2003; Pearce *et al.*, 1984; Robinson *et al.*, 1983), demonstrating an affinity for arc tholeiites and boninites, rather than typical N-MORB (e.g. Miyashiro, 1973; Pearce *et al.*, 1984; Robinson *et al.*, 1983). This evidence supports Troodos having formed within a short-lived spreading centre above a subduction zone. However, despite it now being accepted that Troodos formed above a supra-subduction zone, its exact geodynamic setting remains debated (e.g. Gass *et al.*, 1975; Maffione *et al.*, 2017; Pearce and Robinson, 2010; Pearce, 1975; Robertson *et al.*, 2012), with the only broadly agreed conclusion being that it formed at a submarine volcanic spreading centre associated with or immediately following intraoceanic subduction initiation. Formation of the Troodos lithosphere had occurred $\geq$10 Myr before evidence for any arc-type volcanism in the region,

which started in the Campanian (Chen and Robertson, 2020, 2019; Robertson, 1977).

### 2.1.3 Spreading structure of the Troodos ophiolite

The presence of extensive sub-vertical ∼N-S striking sheeted dykes within the main Troodos ophiolite (Fig. 2.4) is evidence of high degrees of extension in an E-W extensional stress field (in present coordinates; Gass, 1968; Moores and Vine, 1971). The dykes formed parallel to a N-S to NNW-SSE trending spreading ridge. In the north of the ophiolite, three structural grabens, the Solea, Mitsero and Larnaca grabens (from west to east), have been identified from ∼N-S striking listric and planar normal faulting within the sheeted dyke complex (Fig. 2.4; e.g. Allerton and Vine, 1987, 1990, 1991; Varga and Moores, 1985). As a result of this extensional faulting, dykes rotated about a sub-horizontal axis parallel to the ridge, and dip towards the graben axis (Allerton and Vine, 1987, 1991; Hurst *et al.*, 1994; Robertson, 1993). These grabens were interpreted as candidates for fossil ridge axes preserved by successive eastward 'ridge jumping' (Moores *et al.*, 1990; Varga and Moores, 1985), though Allerton and Vine (1990, 1991); MacLeod *et al.* (1990) and van Everdingen and Cawood (1995) suggested the Mitsero graben may instead have formed by off-axis stretching. Most authors agree that the Solea graben represents the locus of an abandoned spreading axis (e.g. Allerton and Vine, 1990, 1991), with a ridge-transform intersection preserved where the Solea graben axis intersects the western projection of the Southern Troodos Transform Fault Zone (Fig. 2.4; MacLeod *et al.*, 1990).

The general N-S strike of the Sheeted Dyke Complex (section 2.2.3) throughout Troodos changes in the vicinity of the Southern Troodos Transform Fault Zone (Arakapas Fault Belt) where they instead curve to strike with a more E-W orientation (Fig. 2.4). This clockwise change of dyke strike occurs progressively over a distance of ∼5-10 km as the transform is approached (e.g. Simonian and Gass, 1978). The origin of this rotation has been controversial (discussed in section 2.3.1), with some authors interpreting it as a primary curvature of the original seafloor spreading fabric adjacent to a sinistrally-slipping transform (e.g. Varga and Moores, 1985). However, palaeomagnetic studies have instead shown the curvature is secondary, imparted by large-magnitude vertical-axis tectonic rotations associated with drag along a dextral-slipping

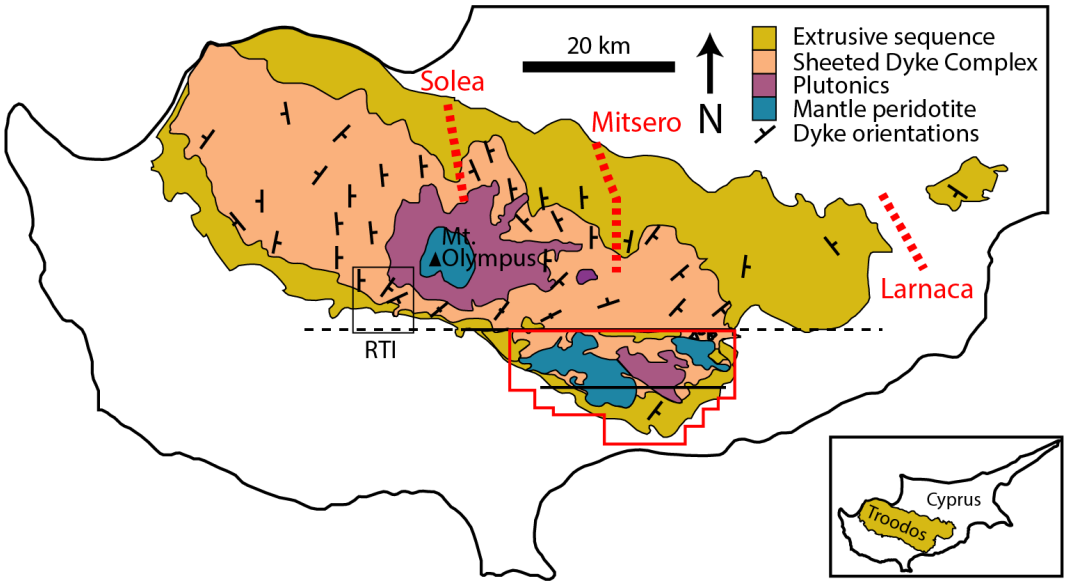


**Figure 2.4:** Simplified geological map of the Troodos ophiolite, Cyprus showing deeper stratigraphic levels exposed in the centre of the ophiolite (Mt Olympus) (after Fagereng and MacLeod, 2019). The Southern Troodos Transform Fault Zone is at the southern margin of the ophiolite (red box). Dyke orientations are shown within the ophiolite highlighting the clockwise rotation of dykes, east of the ridge-transform intersection (RTI). Dashed red lines show graben axes from Allerton and Vine (1991).

transform fault zone (e.g. Allerton and Vine, 1990; Bonhommet *et al.*, 1988; MacLeod *et al.*, 1990; Morris *et al.*, 1990). Most of this rotational strain was imparted at the inside corner of the Solea ridge-transform intersection (MacLeod *et al.*, 1990). Deformation associated with this rotation is considered in this thesis, based on new geological maps around the village of Moniatis, where comparisons are made to deformation in the Southern Troodos Transform Fault Zone (Chapter 4).

## 2.2 Troodos Ophiolite Stratigraphy

The main Troodos Massif preserves a regular layer-cake stratigraphy from which the 'Penrose' model was defined (Penrose conference participants, 1972) (Fig. 2.5): submarine volcanics (Extrusive Sequence) overlie sheeted dykes (Sheeted Dyke Complex) that in turn overlie upper plutonics (gabbros) that overlie lower plutonics (mafic and ultramafic plutonic rocks) and mantle peridotites. This stratigraphy also makes up the building blocks of the Southern Troodos Transform Fault Zone, the main focus of this thesis. The details of

this stratigraphy are discussed below in order of deepest to shallowest.

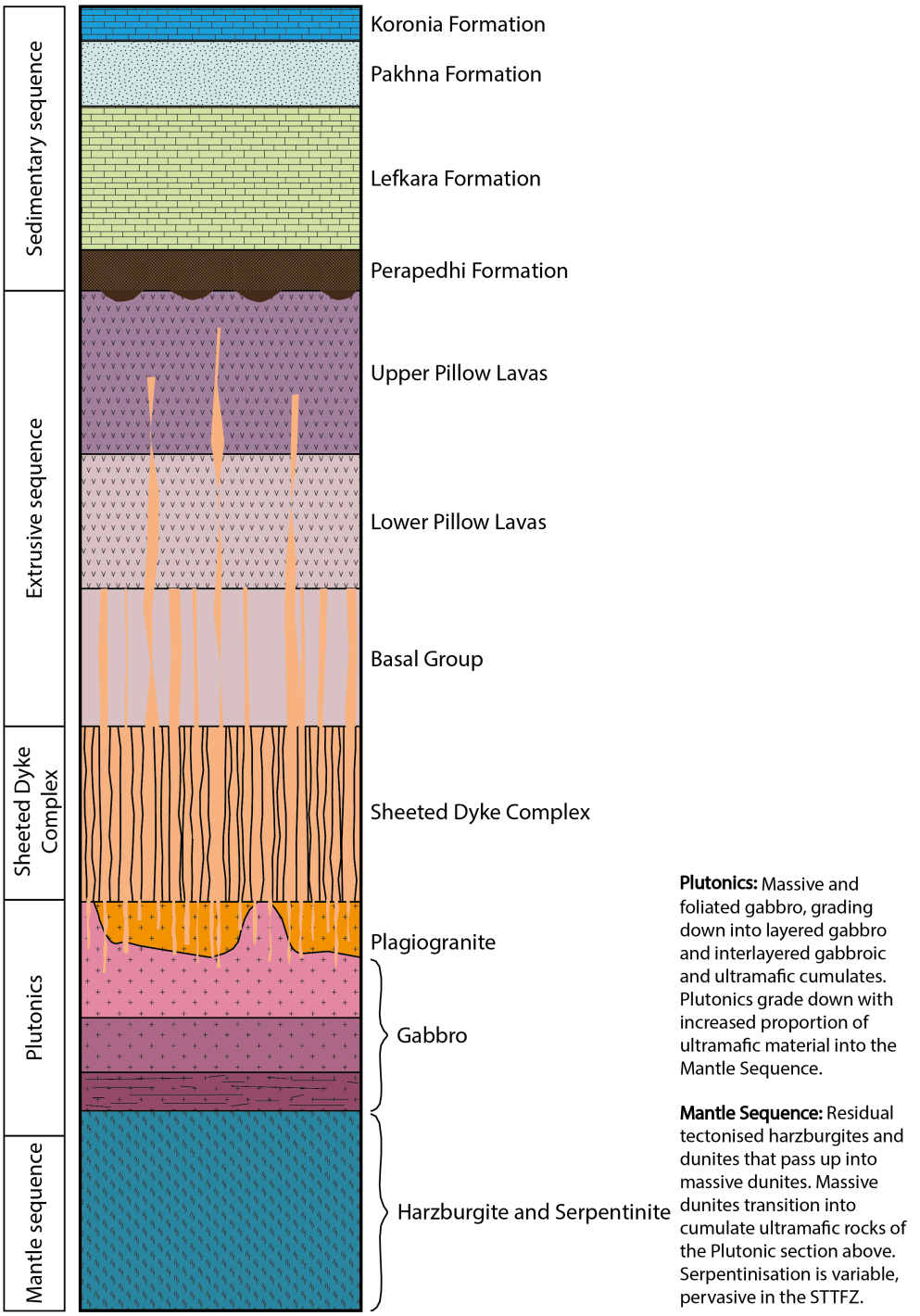


**Figure 2.5:** Simplified (not to scale) stratigraphic section of the Troodos ophiolite stratigraphy (from Robertson and Xenophontos, 1993 and Constantinou, 1980). Magmatic crustal thickness is approximated to 4 km total (Gass *et al.*, 1994)

### 2.2.1 Mantle Sequence

The mantle sequence of the Troodos ophiolite crops out at the highest topographic levels of the Troodos mountains, in and around Mt Olympus (1952 m elevation; Fig. 2.4). The sequence consists mainly of harzburgite (>90%; Wilson, 1959) with dunite, lherzolite and gabbro-pyroxenites (Gass, 1980). Dunite is present in the form of m- to 10-m-scale pods, or as massive dunite (100s-m-thickness) towards the western side of the Troodos mantle sequence outcrop, in places containing concentrations of chromitite (e.g. Greenbaum, 1977; Wilson, 1959). Such massive dunites, probably equating to the crust-mantle transition zone, are also found in the NE Limassol Forest Complex (Gass *et al.*, 1994).

Much of the mantle sequence, particularly within the central eastern Mantle Sequence and within the Limassol Forest Complex (associated with the Southern Troodos Transform Fault Zone), has experienced pervasive or near-pervasive serpentinisation (Fig. 2.6a, Chapter 3; e.g. Gass and Masson-Smith, 1963; Magaritz and Taylor Jr, 1974; Wilson, 1959). Although now pervasively, or near-pervasively serpentinised, the original lithologies can be recognised where shearing is absent. Orthopyroxene in harzburgite is replaced by bastite (serpentine pseudomorph), which may be elongated and generally outline an original, steeply-dipping, high-temperature (1000-1200 °C) tectonite fabric (Fig. 2.6b; e.g. Gass, 1980; Gass *et al.*, 1994). In the Limassol Forest Complex, however, serpentinite deformation (Chapter 3) obscures evidence for these earlier fabrics in many outcrops of mantle rocks. These pre-serpentinisation porphyroclastic fabrics, also observed on Mt Olympus and generally NNW-striking (George, 1978; Wilson, 1959), were interpreted as remnants of high-temperature plastic deformation in the convecting asthenosphere (Allen, 1975; George, 1978; Wilson, 1959). They are comparable to L-S tectonic fabrics found in most mantle peridotites (e.g. Nicolas and Violette, 1982). Within the western Limassol Forest Complex, these asthenospheric fabrics strike predominantly NE/NNE on the kilometre scale, and document a clockwise rotation towards E-W (Gass *et al.*, 1994; Murton, 1986b). Dunite is completely serpentinised and can be distinguished from a harzburgite protolith by the absence of bastites (i.e. lack of orthopyroxene grains in the dunite protolith) and a higher proportion of Cr-spinel.

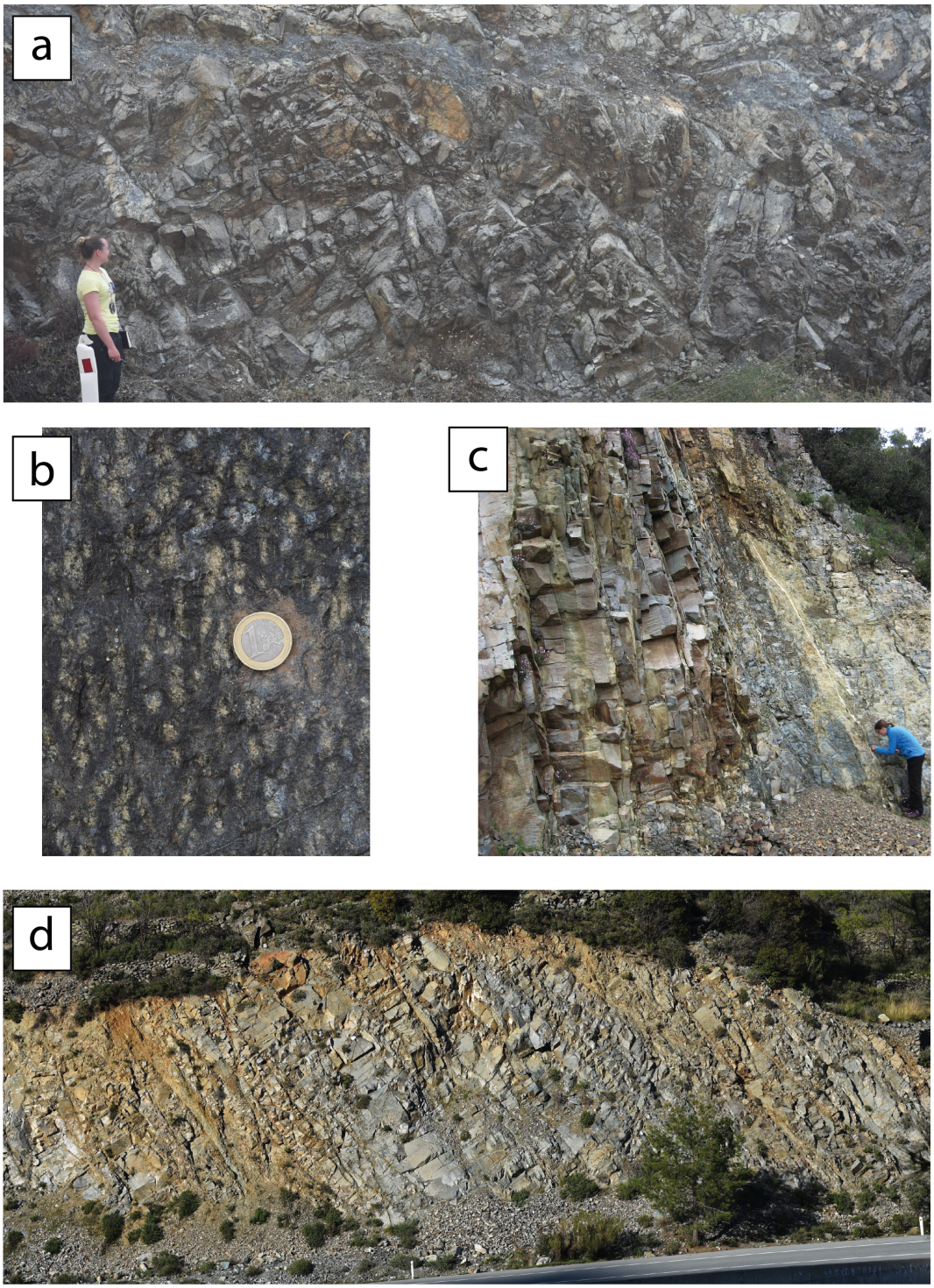


**Figure 2.6:** Field photographs of (a) serpentinised harzburgite from within the Southern Troodos Transform Fault Zone (not tectonised). (b) Serpentine after orthopyroxene (green bastites) defining an 'L-S-type' tectonite fabric. (c) Sheeted Dyke Complex taken from 34°58.44'N 32°58.01'E looking SE and (d) from 34°54.97'N 33°03.77'E looking NE. (a), (c) and (d) taken by Chris MacLeod.

### 2.2.2 Plutonic Sequence

The Plutonic Sequence sits directly on top of the lithospheric mantle and represents the petrological Moho between the mantle and crust (Fig. 2.5 Thy, 1987). This sequence is interpreted to represent the spreading centre's magma chamber cumulates (Malpas *et al.*, 1989). The sequence is complex because it contains several generations of intrusions (e.g. Allen, 1975; Benn and Laurent, 1987; Moores and Vine, 1971). Based on cross-cutting relationships and relative ages of deformation and magmatism, the Plutonic Sequence can be divided into two units: an Early Cumulate Suite and a Late Cumulate Suite (Benn and Laurent, 1987).

The Early Cumulate Suite comprises harzburgite tectonite, dunite with chromite, and layered and foliated gabbros and pyroxenites (Benn and Laurent, 1987; George, 1978). Many cumulates exhibit shape-preferred mineral alignments, which have been inferred as crystal segregation during fractional crystallisation (e.g. Gass, 1980). However, layering in these lithologies is typically very discontinuous, and they may exhibit small-scale isoclinal folds and well-developed L-S fabrics (Allen, 1975; Banks, 2004; George, 1978; Malpas *et al.*, 1989; Wilson, 1959), implying substantial deformation. The most recent reexamination of these fabrics suggests they are magmatic fabrics (melt-present transposition of mush 'slurry'; e.g. Banks, 2004). The Late Cumulate Suite comprises undeformed, massive poikilitic wehrlite, pyroxenites and gabbronorites with rare layering and little evidence for strong mineral fabrics (Banks, 2004).

The cumulate suites grade up into massive gabbros, which are comparable in thickness to the entire layered sequence beneath (estimated at ∼1km each). They are typically medium-coarse grained gabbronorites, gabbros and olivine gabbros containing plagioclase, ortho- and clinopyroxene (Banks, 2004; Malpas *et al.*, 1989; Thy, 1987).

High-level intrusives make up the top portion of the Plutonic Sequence and crop out irregularly between gabbros and the sheeted dykes above (Gass, 1980; Wilson, 1959). They occur as sills and dykes near the contact with the sheeted dyke complex-gabbro contact (Mukasa and Ludden, 1987). They are equigranular, fine- to medium-grained and made up of quartz, plagioclase, amphibole ± titanite, epidote, orthopyroxene, magnetite, zircon and apatite (Freund *et al.*, 2014). They also experienced hydrothermal alteration at upper

greenschist facies to amphibolite facies conditions (>350 °C) as highlighted by secondary quartz, epidote and amphibole mineralisation (Gillis and Roberts, 1999).

### 2.2.3 Sheeted Dyke Complex

The Sheeted Dyke Complex (SDC) forms a unit up to ∼1.5 km thick overlying the Plutonic Sequence (Fig. 2.5). This transition between the sheeted dykes and underlying Plutonic Sequence is not sharp. Instead, the transition is marked by gabbros assimilating the base of the sheeted dyke complex (Gillis and Roberts, 1999). The sequence is dominated by 0.3-3 m wide dykes (Fig. 2.6c-d), although locally the dykes reach up to ∼10 m in thickness.

Dykes are fine- to medium-grained, and were originally basaltic to andesitic in composition, with plagioclase and clinopyroxene as primary microphenocrysts and groundmass phases (Gass *et al.*, 1994). Hydrothermal alteration is pervasive (Chapter 4), consistent with greenschist facies conditions (∼300-450 °C), with most plagioclase altered to albite and calcite, and clinopyroxene to actinolite and chlorite with titanite after Fe-oxides. As well as these replacement phases, epidote, quartz and magnetite are common hydrothermal phases. Despite the pervasive alteration, the original igneous texture remains largely intact. Their grain size fines progressively, usually over a distance of <5 cm, towards their (now altered) glassy chilled margins. Cooling joints are observed in a variety of orientations including parallel to and normal to dyke margins. Dyke margins and joint surfaces can be weathered orange, highlighting oxidation.

### 2.2.4 Extrusive Sequence

The Extrusive Sequence dominantly crops out around the edge of the ophiolite (Fig. 2.4), most extensively and continuously along the northern and southern flanks of the ophiolite (Gass, 1960). At the base of this sequence, the Basal Group (BG) is a unit comprising mixed lavas and dykes, and marks the gradual transition between the extrusive lavas and SDC (Fig. 2.5). This transition is variable over a stratigraphic thickness of ∼100-200 m (e.g. Gass, 1960; Schouten and Kelemen, 2002). The boundary is marked by an increase in the proportion of dykes (down stratigraphy) to 80-90% and the transition

to greenschist facies metamorphic conditions (Gass and Smewing, 1973).

On top of the BG are extrusive pillow lavas (Fig. 2.5). These lavas are cogenetic with the SDC, with a decreasing proportion of sheeted dykes moving up the sequence (30-50% at the base). Towards the base of these lavas, lava domes, hyaloclasites and sheet flows, exhibiting columnar-jointing with large (usually >1 m wide) blue-green pillows are common. However, towards the top of the sequence, pillows are small (∼0.2-0.5 m diameter) and grey-black in colour with thick chilled margins. Sheet flows and dyke intrusions are rare towards the top of the sequence.

The thickness of the extrusive lavas is variable but typically ∼1 km thick. The succession of extrusive lavas is topped by patchy metalliferous sediments that pass upwards into radiolarian mudstones, shales and cherts (Perapedhi Formation), and finally widespread pelagic chalks that record the post-accretion history and ultimate uplift of the Troodos ophiolite (summarised in section 2.4.3).

## 2.3 Southern Troodos Transform Fault Zone

The southern margin of the Troodos ophiolite has suffered a distinct and more sustained tectonic and magmatic history than the remaining igneous massif to the north (Fig. 2.7). The Limassol Forest is separated from the main part of the Troodos mountains by a prominent 0.5-1.5 km wide E-W trending valley (Arakapas Fault Belt valley; Fig. 2.7), which can be traced for almost 40 km from Kato Dhrys in the east to Perapedhi in the west and passes through Arakapas village. The Arakapas Fault Belt's strike-slip character has long been recognized, as early as 1960 (Bear, 1960), with Moores and Vine (1971) suggesting that the fault zone may represent a fossil oceanic transform fault. Mapping of the Limassol Forest Complex during the 1980s showed that this adjoining area also represented part of the strike-slip dominated fault zone. This 400 $km^2$ region has been disrupted by ocean-floor (pre-sediment) strike-slip faulting in the Limassol Forest Complex and Arakapas Fault Belt (Fig. 2.7) and was interpreted as representing an oceanic transform fault zone (Gass *et al.*, 1994; MacLeod, 1990; Moores and Vine, 1971; Murton, 1986a; Simonian and Gass, 1978), termed the Southern Troodos Transform Fault Zone (STTFZ) (Gass *et al.*, 1994; MacLeod, 1990; MacLeod and Murton, 1995). However, its

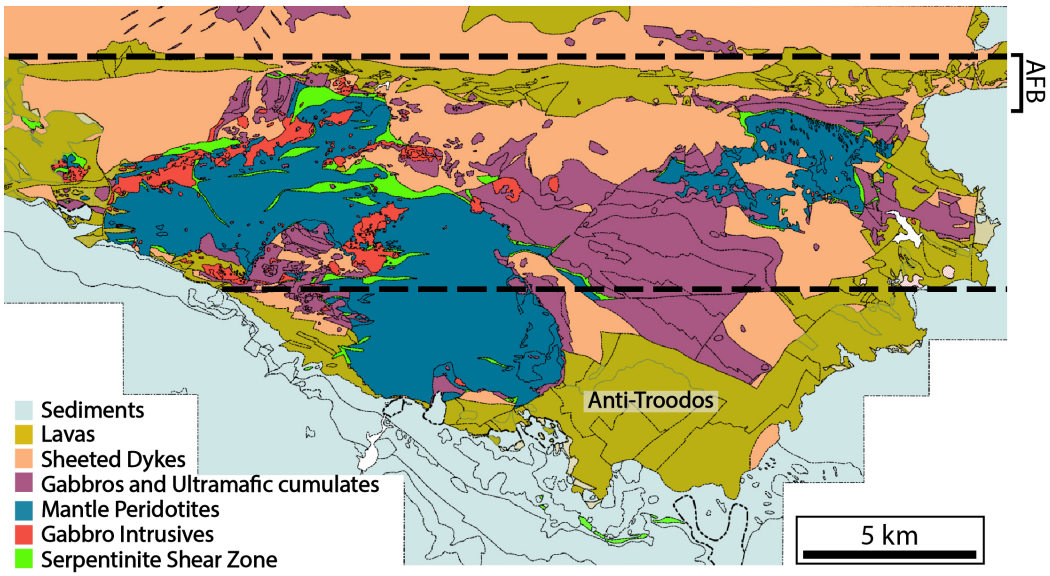


**Figure 2.7:** Geological map of the Southern Troodos Transform Fault Zone, originally mapped at a scale of 1:5000 by Murton (1986b); Simonian (1975) and MacLeod (1988) and published in Gass *et al.* (1994). The dashed black lines represent the approximate northern and southern margins of transform deformation. Deformation of the mafic crust is best recorded in the sheeted dyke layer within the Arakapas Fault Belt (AFB) at the northern limit of the transform-tectonised zone. 'Anti-Troodos' refers to a fragment of non-transform-tectonised crust identified as lying on the opposite side of the transform fault zone (MacLeod *et al.*, 1990).

sense of slip has been debated (section 2.3.1).

The STTFZ has an exposed across-strike width of >5 km and is traceable for >60 km (E-W) along strike (Gass *et al.*, 1994; MacLeod and Murton, 1993, 1995; Moores and Vine, 1971; Murton, 1986b; Simonian and Gass, 1978). 1:5000 scale field mapping of the entire Limassol Forest Complex and Arakapas Fault Belt by Murton (1986b); Simonian (1975) and MacLeod (1988) (reported in Gass *et al.*, 1994) has allowed ocean-floor deformation and kinematics to be identified and deconvolved from that relating to later deformation of the ophiolite (discussed in section 2.4). Transform-related deformation within the STTFZ is typically localised into steeply dipping, E-W striking features with subhorizontal lineations within the crust and lithospheric mantle of the ophiolite. Abundant deformation is documented in all lithological layers (e.g. Fagereng and MacLeod, 2019; MacLeod and Murton, 1993).

The ophiolite and STTFZ's unique preservation and exposure allows a detailed field study of deformation in all stratigraphic levels. The outcrops stud-

ied throughout this thesis have been chosen to avoid any later extensional and thrust overprint (section 2.4), that is distinct from transform-related structures in the Limassol Forest Complex and Arakapas Fault Belt (Gass *et al.*, 1994; MacLeod, 1990), and to represent structures kinematically consistent with transform faulting.

### 2.3.1 Sense of slip of the Southern Troodos Transform Fault Zone

There has been much debate over the sense of shear of the STTFZ in the past. Some studies of its internal structure have suggested sinistral slip (Murton, 1986a,b), while others have suggested dextral slip (MacLeod, 1988, 1990). It has even been suggested that it actually reversed its sense of slip by ridge jumping (e.g. Dilek *et al.*, 1992; Grand *et al.*, 1993; van Everdingen and Cawood, 1995) or by later, post-seafloor spreading reactivation during late Cretaceous microplate rotation (MacLeod, 1988; MacLeod *et al.*, 1990).

The first interpretations of the kinematics of the structures within the western Limassol Forest Complex concluded that slip was sinistral (Murton, 1986a,b). Little attempt of a kinematic analysis of the serpentinite shear zones in this area was made because of the complexity of the internal fabrics, and the limited microtectonic tools available at the time. Therefore, the interpretation of a sinistrally slipping transform fault was based on (a) small gabbro mylonite shear zones that were unequivocally sinistral, and (b) the general NE-SW orientation of Transform Sequence dykes within the western Limassol Forest Complex, which were interpreted as tension gashes within a sinistral slipping regime (Murton, 1986a,b). In contrast, MacLeod (1988); MacLeod *et al.* (1990) found dextral kinematic indicators in serpentinite shear zones within the eastern Limassol Forest Complex, but at that time, could not prove that they recorded seafloor slip.

The sheeted dykes within the Troodos massif, just north of the STTFZ show a rotation about a vertical axis over ∼5-10 km, from N-S striking to E-W striking as they approach the STTFZ as introduced in section 2.1.3 (Fig. 2.4; Simonian and Gass, 1978). This change in orientation was initially interpreted in two ways, one requiring the STTFZ to be dextral, the other consistent with sinistral shear: (1) the sheeted dykes were intruded N-S and because of the

drag along a dextrally slipping transform fault, they were subjected to bulk clockwise rotation (Simonian and Gass, 1978) and (2) the swing of the dykes is a primary feature reflecting dyke-opening directions that relate to a sigmoidal stress field induced by a sinistrally slipping transform fault (e.g. Cann *et al.*, 2001; Hurst *et al.*, 1994; Moores *et al.*, 1990; Murton, 1986a; Varga and Moores, 1985).

To resolve the issue of slip sense, the two models were tested using palaeomagnetic studies. Dykes that intruded N-S and rotated during dextral slip would have a different palaeomagnetic orientation to those that were emplaced in a sigmoidal stress field and did not subsequently rotate (i.e. in a sinistral slip interpretation). Palaeomagnetic studies (e.g. Allerton and Vine, 1990; Bonhommet *et al.*, 1988; MacLeod *et al.*, 1990; Morris *et al.*, 1990) show that the dyke swing records clockwise, vertical-axis rotations that may be explained by drag on a dextrally slipping transform. MacLeod *et al.* (1990) showed that these rotations were imparted entirely at the inside corner ridge-transform intersection (<5 km from the ridge axis; Fig. 2.4). This rotation was then frozen in place and translated passively once the strain was partitioned onto the main STTFZ. Therefore, the deformation north of the STTFZ, within this zone of rotation, does not reflect a 5-15 km wide damage zone associated with the STTFZ.

MacLeod and Murton (1995) revisited all the evidence for slip sense from the STTFZ and concluded that the internal fabrics (e.g. sigmoidal shear structures and offsets of disaggregated clasts) from serpentinite shear zones in the Limassol Forest Complex support dextral motion in all E-W striking shear zones, with only local sinistral indicators, and along Riedel shears (MacLeod and Murton, 1995). Therefore, despite some sinistral structures being preserved (Murton, 1986b), they are restricted to a few mylonitic shear zones relating to geometrical complexities associated with Transform Sequence gabbroic plutons within the Limassol Forest Complex, and are of limited extent. MacLeod and Murton (1995) concluded that the field and palaeomagnetic data are overwhelmingly in support of dextral slip. That these limited sinistral structures can be explained by local geometrical effects also supports the idea that there is no need to explain the varying sense of motion by ridge jumping and consequent slip reversal as previously invoked.

### 2.3.2 Slip rate of the Southern Troodos Transform Fault Zone

The slip rate and magnitude of offset on the STTFZ are both undetermined. This is because while attempts at radiometric dating of plutonic rocks from the Troodos ophiolite have been made, they have been hampered by a lack of cross-strike outcrop of datable plutonic rocks (e.g. Mukasa and Ludden, 1987). The presence of detachment faulting and widespread seafloor stretching (Varga and Moores, 1985) implies slow-spreading when comparing to the slow-spreading Mid-Atlantic Ridge. However, the low relief of fault scarps (typically <20 m), which is inconsistent with slow-spreading ridges, has been used to suggest that the Troodos ophiolite formed at an intermediate- to fast-spreading centre (>60 mm/yr; Allerton and Vine, 1987). More recent (provisional) results from MacLeod and Parrish (2004) indicate that, based on high-pressure U-Pb zircon dates obtained by thermal ionisation mass spectromety from sites spaced tens of kilometres apart across the mean Troodos dyke strike, suggest a slow to intermediate spreading rate for the Troodos ophiolite and consequently slip rate for the STTFZ.

### 2.3.3 'Leaky' Oceanic Transform Fault

The main ophiolite stratigraphy in the STTFZ was intruded by a series of small ultramafic and mafic-acidic plutons, most commonly cutting the mantle sequence, and predominantly found within the western Limassol Forest Complex (Fig. 2.7). This series of intrusions has been called the Transform Sequence and comprises a stage of intrusions dominated by wehrlite plutons and dykes, followed by a stage of gabbro pluton emplacement and abundant dolerite dyke swarms. Mutually cross-cutting relationships between E-W striking STTFZ deformation and Transform Sequence intrusions led MacLeod and Murton (1993, 1995); Murton (1986b) and Gass *et al.* (1994) to hypothesise that the STTFZ was, at least locally, transtensional and 'leaky' with as much as 22% extension accommodated by the magmatism.

## 2.4 Post oceanic transform fault deformation

### 2.4.1 Detachment faulting in the Southern Troodos Transform Fault Zone

Locally significant extensional deformation overprints and reactivates some of the transform-related strike-slip structures within the STTFZ, particularly in the Anti-Troodos crustal section of the eastern Limassol Forest Complex (Gass *et al.*, 1994; MacLeod, 1988, 1990). For example, within the eastern Limassol Forest Complex, tilted lavas and sheeted dykes sit directly, with horizontal faulted contact, on serpentinised mantle (MacLeod, 1988, 1990). This extensional deformation post-dated volcanism and strike-slip transform faulting but was contemporaneous with hydrothermal sediment (umber) deposition, documenting a period of significant extension oblique to the transform in the Turonian-Campanian immediately postdating active seafloor spreading/transform faulting (MacLeod, 1990). During this period the Troodos and Anti-Troodos terranes were pulled apart in response to NE-SW extension, as a result of which many originally E-W transform-related structures within the Limassol Forest Complex were reactivated and rotated as low-angle 'bookshelf' normal faults above a low-angle detachment fault, termed the 'Akapnou Forest Décollement' (MacLeod, 1990; MacLeod and Murton, 1993). This change in extension direction was attributed to emplacement-related deformation that culminated in the 90° anticlockwise rotation of the Troodos ophiolite (section 2.4.2) (MacLeod, 1990).

The structures associated with this extension are planar and localised structures that gently dip to the south. These structures cross-cut the steeply dipping structures, typically with E-W, subhorizontal lineations, that characterise the transform fault zone (Chapters 3 and 4). Because of their different kinematics, the later detachment-related structures can be easily identified from, and their effects stripped off, original transform fault geometry (Gass *et al.*, 1994; MacLeod, 1990).

### 2.4.2 Juxtaposition of Troodos with Mamonia and microplate rotation

The period of extension that affected the STTFZ and Anti-Troodos domains during the Turonian-Campanian ultimately led to the mixing and juxtaposition of Troodos with the Mamonia Complex in the southwest of Cyprus along a series of arcuate lineaments by a complex combination of thrust, extensional and strike-slip faulting during the latest Campanian and Maastrichtian (∼73-65 Ma) (Bailey *et al.*, 2000; Robertson and Woodcock, 1979; Swarbrick and Naylor, 1980). The Mamonia Complex is an Upper Triassic-Lower Cretaceous-age assemblage of sedimentary units, mafic igneous units and minor metamorphic rocks derived from exotic continental and oceanic remnants of Neotethys (e.g. Robertson *et al.*, 2012). Faults relating to the juxtaposing of Mamonia with Troodos occur predominately in the southwest and south of Cyprus and include slivers of serpentinite and other ophiolitic material with STTFZ affinity (e.g. Bailey *et al.*, 2000; Morris *et al.*, 1990; Robertson and Woodcock, 1979).

The juxtaposition of Troodos with the Mamonia Complex corresponded with 90° anticlockwise rotation of the Troodos microplate during the Late Cretaceous-Early Eocene as indicated by palaeomagnetic studies (Clube *et al.*, 1985; Clube and Robertson, 1986; Moores and Vine, 1971). The Troodos spreading centre was therefore orientated approximately E-W prior to this rotation and the E-W transform fault structures we see today originally trended N-S on the Cretaceous seafloor. The rotation of the Troodos microplate initiated at ∼80 Ma, initially rotating ∼60° during the Upper Campanian to Maastrichtian (Clube *et al.*, 1985; Clube and Robertson, 1986), with the final ∼30° rotation happening from the Maastrichtian to Early Eocene.

Several reasons have been put forward to explain the rotation of the Cyprus microplate including (1) the passive rotation of the Troodos microplate in response to essentially colliding with the African plate (Clube and Robertson, 1986; MacLeod, 1988, 1990; Robertson, 1990; Robertson and Mountrakis, 2006); (2) the collision of Troodos with a Mamonia Seamount (Moores *et al.*, 1984; Murton, 1990); and (3) oblique subduction beneath Cyprus (Clube *et al.*, 1985).

### 2.4.3 Post-Maastrichtian Exhumation of the Troodos Ophiolite

The Troodos ophiolite was progressively uplifted during the Cenozoic. This emergence has been well-preserved within the sedimentary record on the island that overlies the ophiolite. The Troodos ophiolite is topped conformably by Turonian-aged sediments. The oldest sediments on top of the Troodos ophiolite are patchily-distributed Fe-Mn-rich brown umbers (hydrothermal sediments) of Turonian age (Blome and Irwin, 1985), <35 m in thickness, which pass upwards into Turonian-Campanian radiolarian mudstones, shales and cherts (Robertson, 1975, 1977; Urquhart and Banner, 1994). These are collectively known as the Perapedhi Formation. The Perapedhi Formation is in turn overlain by radiolarian cherts, bentonites and volcanoclastic sandstones of the Campanian-Maastrichtian Kannaviou Formation (Clube and Robertson, 1986; Robertson, 1975). The absence of carbonate-rich sediments within these Late Cretaceous-aged Peraphedi and Kannaviou Formations indicates that during this time, the Troodos ophiolite remained in a deep water setting, below the carbonate compensation depth, which is thought to have been ∼3500 m deep (Robertson and Hudson, 1973; Van Andel, 1975). Because of large tectonic instability during the Maastrichtian, exotic clasts (+ serpentinite slivers) were included in the Mamonia Complex. The change in sedimentation between the Peraphedi and Kannaviou is thought to mark the juxtaposition of Troodos and Mamonia discussed in the previous section.

Pelagic carbonates of the Maastrichtian- to Oligocene-aged Lefkara Formation accumulated on top of the Perapedhi and Kannaviou Formations within the oceanic basin that was once the Troodos ophiolite (Blome and Irwin, 1985; Robertson *et al.*, 2012; Urquhart and Banner, 1994) documenting a change to shallow seas at the end of the Cretaceous (Robertson, 1977). They are typically interpreted as having been deposited in calm conditions and relatively deep water (shallower than the carbonate compensation depth, probably 2000-3000 m water depth; Kähler and Stow, 1998; Robertson, 1976). Disconformably on top of the Lefkara Formation, increasing amounts of bioturbation and sediment instability is documented (Lower to Mid- Miocene-aged Pakhna Formation), indicative of continued shallowing conditions (Kinnaird and Robertson, 2012; Kinnaird *et al.*, 2011; Lord, Panayides, Urquhart, Xenophontos, and Mal-

pas, Lord *et al.*; Robertson, 1977). This change in setting from calm, stable conditions (Lefkara Formation) to rapid uplift and resedimentation (Pakhna Formation) is associated with underthrusting beneath Cyprus at this time and major compression/uplift event (Robertson *et al.*, 2012). This is considered to be around the time the initial emergence of the Troodos ophiolite, centred on the Limassol Forest, occurred. Patch reefs and evaporites were deposited during the latest Miocene (Messinian-aged Kalavasos Formation) further supporting shallowing seas. The shallowing of seas was a result of tectonic uplift coupled with eustatic sea level fall associated with the Messian salinity crisis, however, tectonic exhumation of Troodos exceeded the rate of sea level change (Robertson *et al.*, 1991).

Subduction below Cyprus in the early-middle Miocene resulted in thrust faulting and folding in Cyprus. For example, at the southwestern edge of the STTFZ, serpentinised lithospheric mantle and parts of the crustal sequence have been thrust towards the southwest on top of younger sediments in the Yerasa Fold and Thrust Belt (Maastrichtian to Oligocene Lefkara formation chalks; Gass *et al.*, 1994; Murton, 1986b). Here, chalks are deformed into upright folds whose axial plane strikes NW-SE, orthogonal to the convergence direction. Within southern Cyprus, it was dominantly WNW-ESE faults that were reactivated as thrust faults associated with this convergence, rather than E-W striking STTFZ faults. The WNW-ESE faults are inferred to have formed in the latest Cretaceous during the extensional reactivation/microplate rotation phase and were the right orientation to be reactivated when extension turned to compression in the Lower to Middle Miocene (Gass *et al.*, 1994; MacLeod, 1990). Therefore, deformation along WNW-ESE striking faults with steeply plunging lineations associated with convergence can be distinguished from gently plunging lineations on E-W striking STTFZ structures (Chapters 3 and 4).

Cyprus experienced more rapid uplift during the Late Pliocene-Early Pleistocene (∼2.6 Ma) transitioning from a marine to subaerial environment (Kinnaird *et al.*, 2011; Robertson, 1990). This rapid uplift is thought to have occurred following the collision and underthrusting of the Eratosthenes seamount with a trench to the south of Cyprus, impeding subduction (Kinnaird and Robertson, 2012; Robertson, 1998; Robertson *et al.*, 2012). This regional uplift of the Troodos ophiolite was centred below Mt. Olympus, and was aided by

the mantle wedge serpentinisation beneath the island, resulting in the diapiric uplift (Evans *et al.*, 2021; Gass and Masson-Smith, 1963; Robertson, 1990). This resulted in the deepest stratigraphic levels cropping out in the central and highest part of the ophiolite (Mt. Olympus), with successively shallower levels exposed radially outwards (Fig. 2.4). Uplift of Cyprus continues today, at a rate of up to 4 mm/yr (Harrison *et al.*, 2013).

## 2.5 The Southern Troodos Transform Fault Zone as a case example of oceanic transform-related deformation

The Troodos ophiolite represents one of the few ophiolites that contains an oceanic transform fault accessible for direct geological study. Occurring at the southern margin of the Troodos ophiolite, the STTFZ cuts all stratigraphic levels of a regular layer-cake stratigraphy of oceanic lithosphere. Despite exhumation of the Troodos ophiolite and STTFZ, tectonic overprinting relating to post-transform deformation (section 2.4) can be readily identified and deconvolved from STTFZ strike-slip kinematics, with a dominant dextral shear sense, on typically E-W striking, subvertical structures. Temperature constraints on STTFZ deformation in the mafic crust (Chapter 4) and serpentinised lithospheric mantle (Chapter 3) suggest deformation occurred at $T$ <600 °C - within the thermally-defined seismogenic zone (section 1.7.1).

Active oceanic transforms slip largely aseismically within the thermally-defined seismogenic zone (section 1.7.2) and are considered mechanically weak structures. However, the geological processes allowing for aseismic slip and mechanical weakness are uncertain. Exposures of serpentinised lithospheric mantle (Chapter 3) and sheeted dykes (Chapter 4) within the STTFZ allows for the unique opportunity to gain insights into the geological controls on the rheology of oceanic transforms. The Troodos ophiolite is inferred to have formed at a slow to intermediate spreading ridge (section 2.3.2), suggesting the STTFZ may be an appropriate analogue for active oceanic transforms at slow to intermediate spreading ridges.

# Chapter 3

# Shear zone development in serpentinised mantle: Implications for the strength of oceanic transform faults

## 3.1 Abstract

Oceanic transform faults display fewer and smaller-magnitude earthquakes than expected for their length. Several mechanisms have been inferred to explain this seismic slip deficit, including increased fault zone damage resulting in elevated fluid flow, and the alteration of olivine to serpentine. However, to date, these possible mechanisms are not supported by direct observation. We use micro- to kilometre scale observations from an exhumed oceanic transform fault in the Troodos ophiolite, Cyprus, to determine mineral-scale deformation mechanisms and infer likely controls on seismic behaviour of serpentinised lithospheric mantle in active oceanic transform faults. We document a range of deformation fabrics including massive, scaly and phyllonitic serpentinite, attesting to mixed brittle-ductile deformation within serpentinite shear zones. The progressive development of a foliation, with cumulative strain, is an efficient weakening mechanism in scaly and phyllonitic serpentinite. Further weakening is promoted by a transition in the serpentine polytype from lizardite-dominated massive and scaly serpentinites to chrysotile-dominated phyllonitic serpentinite. The development of a foliation and polytype transi-

tion requires dissolution-precipitation processes. Discrete faults and fractures locally crosscut, but are also deformed by, foliated serpentinites. These brittle structures can be explained by local and transient elevated strain rates, and play a crucial role in strain localisation by providing positive feedback for dissolution-precipitation by increasing permeability. We propose that the evolution in structure and deformation style documented within the serpentinised lithospheric mantle of the Southern Troodos Transform Fault Zone is a viable explanation for the dominantly creeping behaviour and long-term weakness of oceanic transform faults.

### Author contributions

This chapter is based on a published manuscript: Cox, S., Fagereng, A., and MacLeod, C. J. (2021). Shear zone development in serpentinized mantle: Implications for the strength of oceanic transform faults. Journal of Geophysical Research: Solid Earth, 126, e2020JB020763. https://doi.org/10.1029/2020JB020763

Sophie Cox is the main author of this work and undertook fieldwork, microstructural and geochemical analysis, and wrote the manuscript. Ake Fagereng, Christopher MacLeod and Chris Tulley helped with fieldwork. Ake Fagereng and Christopher MacLeod provided supervision of the work and during the writing of the manuscript. Chris Tulley and Matthew Tarling (University of Otago) jointly performed the Raman spectra analysis. Three anonymous reviewers provided constructive reviews that helped improve it.

## 3.2 Introduction

Oceanic transform faults offset mid-ocean ridge segments for up to 100s of kilometres. Therefore, according to scaling relationships between fault length and earthquake magnitude (Wells and Coppersmith, 1994), they are expected to produce relatively frequent, large earthquakes. For example, assuming a 25 km thick seismogenic zone (e.g. Prigent *et al.*, 2020), rupture of a 200 km long, vertical transform fault would produce an Mw ∼8 earthquake. Yet, despite their length and the fact they cross-cut the brittle crust, geophysical observations show they host fewer and smaller earthquakes (rarely ≥Mw 7.0) than expected, and globally about 85% of their displacement occurs by aseismic creep (Boettcher and Jordan, 2004). Typically, oceanic transforms are difficult to study geologically, compared to continental transforms, with geological data often limited to seafloor sampling including dredges, dives and borehole observations.

The base of the seismogenic zone, defined as the depth range where earthquakes can nucleate, has been correlated with the 600°C isotherm based on the comparison of numerical thermal models and the depth-limit of earthquake focal depths (Abercrombie and Ekström, 2001; Roland *et al.*, 2010). This thermal control coincides with a change to ductile, velocity-strengthening behaviour in olivine as extrapolated from laboratory deformation data (Boettcher *et al.*, 2007). Recent studies, however, show that fluid-driven weakening and strain localisation may change the dominant rheology (Kohli and Warren, 2020; Prigent *et al.*, 2020). In addition, the ratio between the observed seismic moment and that expected from plate tectonic models (seismic coupling, $\chi$; Scholz (2002)) varies along-strike (e.g. Braunmiller and Nábělek, 2008) and between (e.g. Boettcher and Jordan, 2004) oceanic transforms without accompanying changes in inferred thermal structure. For example, along the East Pacific Rise most oceanic transforms accommodate displacement almost entirely aseismically, with a $\chi < 0.2$ (Boettcher and Jordan, 2004).

The spatial distribution of seismic and aseismic behaviour can vary along strike (e.g. Froment *et al.*, 2014) and down dip (e.g. Kuna *et al.*, 2019). The observation of aseismic slip within the thermally-defined seismogenic zone implies that thermal structure alone cannot explain the distribution of seismicity. Several processes have been suggested to promote creep along oceanic

transforms, including; (1) hydration of olivine to serpentine and other frictionally weak minerals, which can favour creep behaviour (Boettcher and Jordan, 2004; Moore *et al.*, 1997), (2) elevated fluid pressures reducing seismic coupling (Scholz, 1998), (3) deep fluid flow leading to progressive formation of weak mylonitic shear zones (Kohli and Warren, 2020; Prigent *et al.*, 2020) and (4) increased fault zone damage resulting in locally enhanced porosity, favouring swarms of microseismicity rather than large earthquakes (Froment *et al.*, 2014; McGuire *et al.*, 2012). However, it is unclear which, or what combination of these processes, if any, are responsible for the lack of seismicity observed along modern transforms at temperatures <600°C.

The existing models for the seismic behaviour of transform faults lack constraints by direct geological observation. Several recent papers have attempted to address this observational gap by examining the deformation history of samples dredged from modern oceanic transform faults (Kohli and Warren, 2020; Prigent *et al.*, 2020) and collected from an exhumed transform fault (Bogota Peninsular shear zone) in the Massif du Sud ophiolite in New Caledonia (Chatzaras *et al.*, 2020). However, these studies have focused on relatively high-temperature deformation (>600°C), and are therefore more relevant to deformation occurring beneath the inferred thermally-controlled seismogenic zone. The temperature and depth limitations of these studies can be addressed using observations from the Southern Troodos Transform Fault Zone (STTFZ), Cyprus, where we are able to make micro- to kilometre-scale observations of exhumed rocks deformed within the inferred thermally-controlled seismogenic zone. The STTFZ is a unique example of an intact oceanic transform fault zone preserved on-land, and hence presents a unique opportunity to characterise the deformation and inferred rheology of serpentinite shear zones (SSZs) within the kinematic context of strike-slip faulting (Fig. 3.1).

Rock deformation experiments indicate that the presence of serpentine can strongly influence rheology. Experimental studies, simulating conditions from the shallow crust to depths equivalent to ∼8 GPa and 800°C, indicate a low frictional strength for serpentine, with a friction coefficient as low as $\mu = 0.1$ at room temperature (Moore *et al.*, 1997; Reinen, 2000; Reinen *et al.*, 1991). Previous studies have used serpentine's low frictional strength and velocity-strengthening behaviour extrapolated to geological strain rates (Moore and Lockner, 2004; Moore *et al.*, 1997; Reinen *et al.*, 1991, 1994) to explain fault

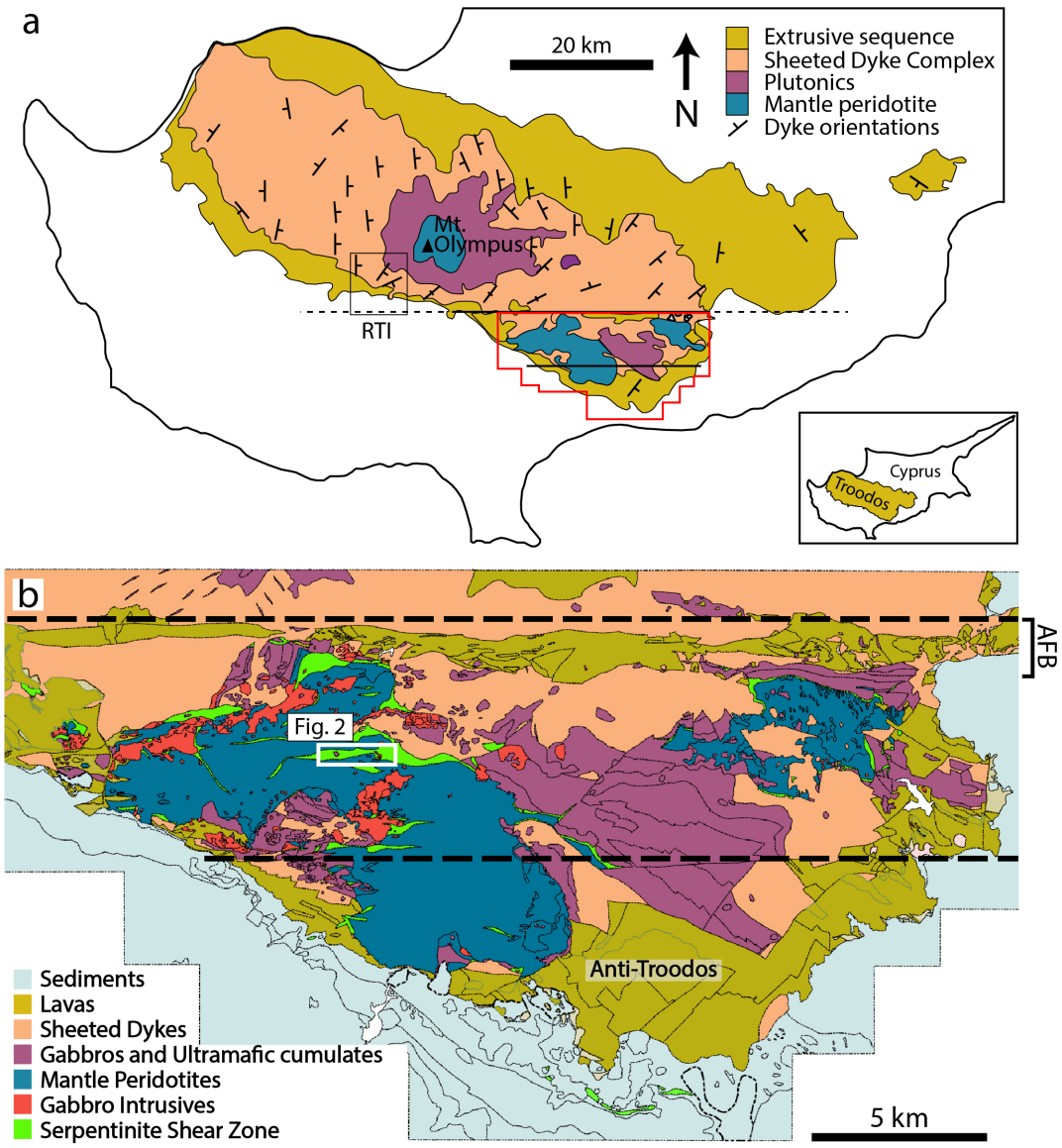


**Figure 3.1:** (a) Outline of the Troodos ophiolite geology, Cyprus (after Fagereng and MacLeod (2019)). The Southern Troodos Transform Fault Zone is located at the southern margin of the ophiolite, within the region known as the Limassol Forest Complex (outlined in red). Dyke orientations are shown north of the transform-tectonised zone reflecting clockwise rotation of the dykes. RTI - ridge-transform intersection from MacLeod *et al.* (1990). (b) Detailed geological map of the Limassol Forest Complex showing the 'Southern Troodos Transform Fault Zone' and the approximate limit (dashed lines) of oceanic transform fault deformation (after Gass *et al.*, 1994). The Southern Troodos Transform Fault Zone, which includes the E-W trending Arakapas Fault Belt (AFB; the northern limit of transform deformation) and much of the Limassol Forest Complex areas, was originally mapped at 1:5000 scale by Murton (1986b); Simonian (1975) and MacLeod (1988). 'Anti-Troodos' refers to a fragment of non-transform-tectonised crust identified as lying on the opposite side of the transform fault zone (MacLeod, 1990). The white box in (b) shows the location of Fig. 3.2.

zone weakness, strain localisation and aseismic creep along many major faults including the San Andreas Fault System (Andreani *et al.*, 2005; Irwin and Barnes, 1975; Moore *et al.*, 1996; Moore and Rymer, 2007), in subduction zones (Hilairet *et al.*, 2007; Hirauchi *et al.*, 2010; Tarling *et al.*, 2019), as well as along several oceanic transforms (e.g. Boettcher *et al.*, 2007; Boettcher and Jordan, 2004; Froment *et al.*, 2014; Hirth and Guillot, 2013; Kuna *et al.*, 2019; McGuire *et al.*, 2012).

Here we investigate the progressive development of serpentinite deformation fabrics within well-exposed SSZs in the pervasively serpentinised lithospheric mantle of the STTFZ. Based on our field and microstructural observations, we propose a model of strain-controlled evolution of fault-rock fabric from massive serpentinite through the formation of a scaly fabric, and, ultimately, phyllonitic serpentinite. We use the term 'phyllonitic' to represent a closely-spaced, penetrative foliation defined by the preferential orientation of fine-grained fibrous or platy minerals. This definition is consistent with recent studies and texts (e.g. Collettini *et al.*, 2011; Fossen, 2016; Mével, 2003; Smith *et al.*, 2011). Similar serpentinite fabrics have previously been referred to as schistosity (e.g. Andreani *et al.*, 2005; Hirauchi and Yamaguchi, 2007; Wicks and Whittaker, 1977); however, the term 'schist' is typically reserved for coarser grained rocks with centimetre-scale foliation spacing (e.g. Fossen, 2016) and we therefore adopt the term that better emphasises the fine grain size and small foliation spacing characteristic of the rocks we observe. Finally, using the progressive model we derive, we discuss the spatiotemporal distribution of deformation within the serpentinised lithospheric mantle and the potential controls on the geophysically observed seismic behaviour and rheology of active oceanic transform faults.

## 3.3 Geological setting of the Southern Troodos Transform Fault Zone

The Troodos ophiolite of Cyprus is a fragment of Late Cretaceous oceanic lithosphere, which formed in a supra-subduction zone setting (e.g. Mukasa and Ludden, 1987; Pearce, 1975; Robertson *et al.*, 2012) and was exhumed during the latest Cretaceous to Miocene (e.g. Robertson, 1977). The southern margin of the Troodos ophiolite has been disrupted by ocean-floor (pre-sediment)

strike-slip faulting in the Limassol Forest Complex and Arakapas Fault Belt (Fig. 3.1), perpendicular to the broadly N-S trend of sheeted dykes in the main Troodos ophiolite. Together, these areas are interpreted as representing a dextral oceanic transform fault zone, termed the Southern Troodos Transform Fault Zone (STTFZ) (Gass *et al.*, 1994; MacLeod and Murton, 1995). The STTFZ has an exposed thickness of $\geq$5 km and is traceable for >60 km along strike (Gass *et al.*, 1994; MacLeod and Murton, 1993, 1995; Moores and Vine, 1971; Murton, 1986a,b; Simonian and Gass, 1978). 1:5000 Scale field mapping of the entire Limassol Forest Complex and Arakapas Fault Belt by Simonian (1975), Murton (1986b) and MacLeod (1988) (reported in Gass *et al.*, 1994) has allowed ocean-floor deformation and kinematics to be identified and deconvolved from that relating to the emplacement and exhumation of the ophiolite. Later detachment and thrust faulting locally overprints, and is distinct from, transform-related structures in the Limassol Forest Complex and Arakapas Fault Belt (Gass *et al.*, 1994; MacLeod, 1990). The outcrops we study here have been chosen to avoid the later deformation overprint and to represent structures kinematically consistent with transform faulting. The main transform-related deformation is within the $\sim$5 km-wide STTFZ and is typically localised into steeply dipping, E-W striking features within the crust and lithospheric mantle of the ophiolite.

Whilst abundant deformation is also documented in the crustal section (e.g. Fagereng and MacLeod, 2019; MacLeod, 1990; MacLeod and Murton, 1993, Chapter 4), the focus of this paper is specifically on mechanisms of deformation within the mantle lithosphere. Deformation of lithospheric mantle rocks is hosted in anastomosing SSZs that are $\leq$500 m wide and traceable for $\leq$12 km along strike (lime green in Figs. 3.1 and 3.2), displaying brittle and ductile deformation of serpentinite to various intensities (Fagereng and MacLeod, 2019; MacLeod and Murton, 1993; Murton, 1986a). Serpentinisation of STTFZ mantle rocks initiated early and is nearly pervasive, probably >95% down to several kilometre depth. Mapping by MacLeod and Murton (1993) suggests that the degree of serpentinisation is higher in SSZs and decreases into less deformed wall-rock. Many SSZs contain isolated wehrlite and gabbro plutons with associated dykes, interpreted as a suite of (boninitic) intrusions that were coeval with the transform-related deformation (MacLeod and Murton, 1993, 1995; Murton, 1986a). Mutually cross-cutting relationships

between STTFZ deformation and Transform Sequence intrusions led MacLeod and Murton (1993); Murton (1986a) and MacLeod and Murton (1995) to hypothesise that the STTFZ was, at least locally, transtensional and 'leaky'.

The original pre-serpentinisation lithology that constitutes the mantle lithosphere within the STTFZ is predominantly harzburgite (>90%; Gass et al., 1994). Dunite is present in the form of m- to 10-m-scale pods, or as massive dunite (100s-m-scale) in the NE Limassol Forest Complex. Although all are now pervasively or near-pervasively serpentinised, the original lithology can normally be recognised if shearing is absent. Orthopyroxene in harzburgite is replaced by bastite, which may be elongated and sometimes outline an original, steeply-dipping, high-temperature tectonite fabric. In a high proportion of cases, however, serpentinisation obscures evidence for earlier fabrics. Dunite is completely serpentinised and can be distinguished from a harzburgite protolith by the lack of bastites and higher proportion (< a few percent) of lustrous Cr-spinel. These porphyroclastic fabrics were interpreted as remnants of high-temperature deformation that formed in the convecting asthenosphere (Gass *et al.*, 1994; Murton, 1986b), and are comparable to L-S tectonic fabrics found in most mantle peridotites (e.g. Ceuleneer *et al.*, 1988). These asthenospheric fabrics trend predominately NW/NNW on the kilometre-scale and document a clockwise rotation towards an E-W foliation in the western Limassol Forest Complex (Murton, 1986b). They are distinguished from the discrete, localised and more intensely foliated shear zones that are restricted to the STTFZ and are predominately E-W striking and steep. The asthenospheric fabrics are commonly cross-cut by E-W striking SSZs, ruling out their control on the localisation of SSZs within the STTFZ (Gass *et al.*, 1994).

## 3.4 Methods

In order to constrain the conditions and evolution of transform related deformation in the mantle lithosphere of the STTFZ, microstructural observations were made on standard 30 $\mu$m thick polished thin sections. We chose samples representative of the various deformation styles observed at the macroscale. Incohesive samples were set using Epofix cold-setting embedding resin, a low-fluorescence epoxy, and cut along a sub-horizontal plane containing the slip vector and maximum asymmetry. Thin sections were studied using a range

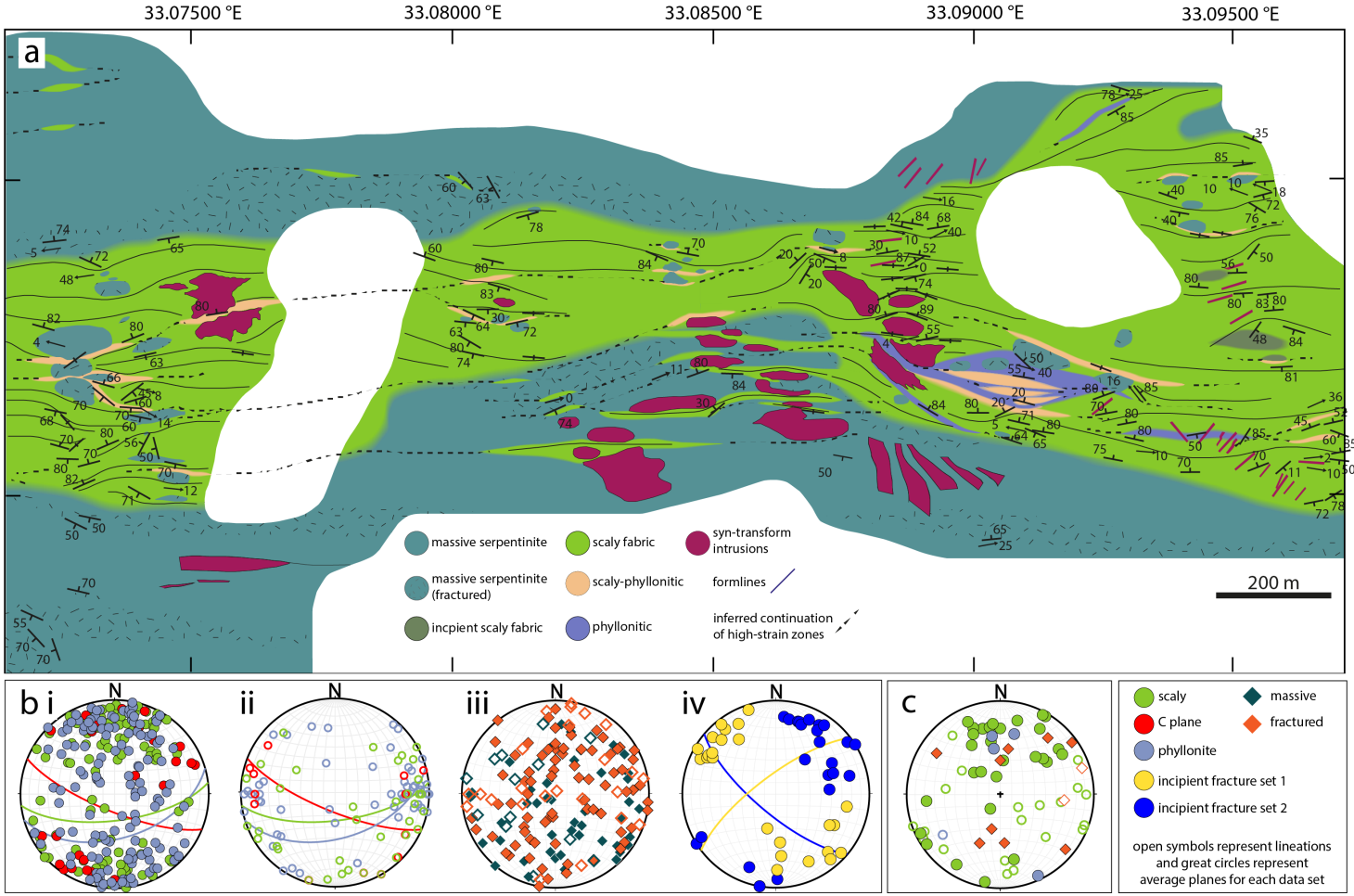


**Figure 3.2:** (a) Detailed geological map (WGS84) of the internal structure and variable distribution of deformation fabrics within a serpentinite shear zone in the Limassol Forest Complex (white box in Fig. 3.1b). The map highlights areas of scaly and phyllonitic fabric, pods of massive to fractured serpentinite and transform sequence intrusions (dykes - drawn as far as observed). (b) Orientations of the fabrics mapped in (a) are summarised in lower hemisphere, equal area stereonets of (i) poles to planes of S-C fabrics from scaly and phyllonitic serpentinite, (ii) lineations from the serpentinite shear zone with great circles showing average foliations from (i), (iii) lineations and fractures in massive and fractured serpentinite and (iv) fractures in the incipient scaly fabric. (c) shows detailed measurements of fractures and scaly foliation from a 10m wide localised shear zone dominated by a scaly to phyllonitic fabric. Descriptions of the various serpentinite fabrics are in section 3.5.1.

of optical microscope, scanning electron microscope (SEM) and Raman spectroscopy methods. Brief sample descriptions and locations can be found in Appendix A.

### 3.4.1 Raman spectroscopy

Raman spectroscopy was used to identify the serpentine polytypes (e.g. Rooney *et al.*, 2018) and Raman spectroscopy mapping was conducted using an Alpha 300R+ confocal Raman microscope (WITec GmbH, Ulm, Germany) in the Chemistry department of Otago University, New Zealand, following procedures of Rooney *et al.* (2018) and Tarling *et al.* (2019).

### 3.4.2 Scanning electron microscope

Energy-dispersive X-ray spectroscopy (EDS) maps were produced from polished thin sections coated in 10-15 nm of carbon. Data were acquired using a Zeiss Sigma HD Field Emission Gun Analytical scanning electron microscope (SEM) fitted with two Oxford Instruments 150 $mm^2$ energy dispersive X-ray spectrometers in the School of Earth and Environmental Sciences at Cardiff University. EDS mapping was carried out at an accelerating voltage of 20 kV with a nominal beam current of 4.3 nA under a high vacuum.

## 3.5 Results

### 3.5.1 Macroscopic field observations

Mapping of an $\sim$2 $km^2$ area of the exposed mantle section within the Limassol Forest Complex reveals that deformation is heterogeneously distributed, with intensity varying on a metre to kilometre scale (Fig. 3.2). The particular shear zone mapped here displays an anastomosing tectonic fabric with an average moderate to steeply dipping foliation striking $\sim$E-W (083/67° S) and gently plunging lineation ($<$30°), consistent with sub-seafloor deformation under conditions associated with an oceanic transform fault, and distinct from structures associated with later uplift and exhumation (Fig. 3.2b). From our field observations, we divide the serpentinite into five groups based on their macroscale fabrics (Fig. 3.3).

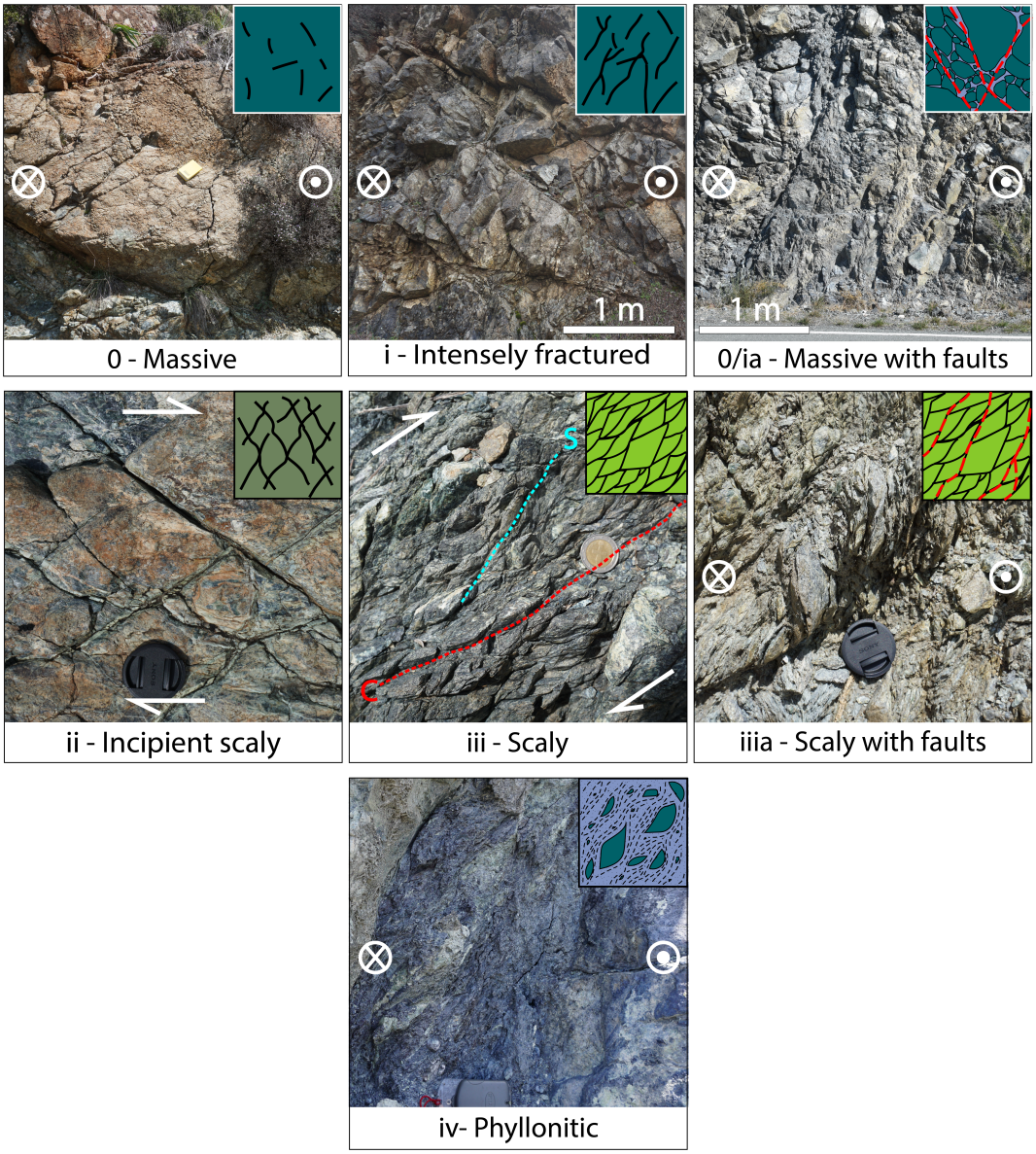


**Figure 3.3:** Descriptive categorisation of deformation styles observed in the Southern Troodos Transform Fault Zone serpentinised lithospheric mantle with schematic representations. 0 - massive serpentinite (near WGS84: 34.8128°N 33.0706°E) i - intensely fractured (near 34.8128°N 33.0706°E) 0/ia - (near 34.7755°N 33.0806°E) ii - (near 34.8193°N 33.0957°E) iii - (near 34.7932°N 33.0868°E) iiia - (near 34.8159°N 33.0726°E) iv - (near 34.8067°N 33.0042°E). Colour scheme as in Fig. 3.2.

(0) *Massive serpentinite* comprises a blocky texture with variably oriented fractures (Fig. 2.6a-b), centimetres to metres long and spaced at a similar scale. Primary olivine and orthopyroxene are rare (<1%), with serpentine after olivine and elongate bastite pseudomorphs (<1 cm in length) after orthopyroxene (Fig. 3.4a). Massive serpentinite dominates the mantle section away from SSZs and within SSZs it commonly occurs as pods surrounded by scaly and phyllonitic fabrics.

(i) *Intensely fractured serpentinite* is comparable to the massive serpentinite described above, but with an increased number of fractures without a preferred orientation. Fractured serpentinite is most common near the margins of well-developed SSZs (Fig. 3.2a-b)

(ii) *Incipient scaly serpentinite* is also similar to massive serpentinite, but contains two discrete, <2 cm thick, planar fracture sets that intersect at a high angle (typically ∼80°) to form rhomboidal blocks (Fig. 3.2b). The fractures are in places filled with fibrous serpentine, reflecting either extensional or transtensional opening.

(iii) *Scaly serpentinite* defines individual serpentinite phacoids by a network of anastomosing disjunctive cleavage (e.g. Shervais *et al.*, 2005; Vannucchi *et al.*, 2003). Phacoids are variably sized (centimetres to decimetres) with polished surfaces. They are commonly asymmetric with sub-horizontal, E-W trending long axes. Their short axes are predominantly sub-horizontal and trend N-S. The alignment of phacoids in this way defines an E-W striking sub-vertical foliation. Discrete shear planes cross-cut the foliation at an angle of ∼30° (Fig. 3.2b) giving an S-C-like geometry (Fig. 3.3iii), which is almost always consistent with dextral slip on steeply dipping planes. Serpentinite phacoid surfaces commonly contain a coating of fibrous serpentine recording shear deformation with a locally variable orientation (Fig. 3.4c). Fibrous serpentine may also form lineations on C planes. Fractured serpentinite phacoids are common (Fig. 3.4d), with some fractures containing crack-seal veins.

(iv) *Phyllonitic serpentinite* is defined by a narrowly (<2 mm) spaced cleavage that is more planar than in scaly serpentinite, with S and C planes effectively parallel. Serpentinite phacoids are present but isolated (Fig. 3.4e). Other, more angular blocks of serpentinite and Transform Sequence intrusions can also be found within the phyllonitic fabric, forming a block-in-matrix fabric. Phyllonitic zones form relatively narrow anastomosing strands up to 10

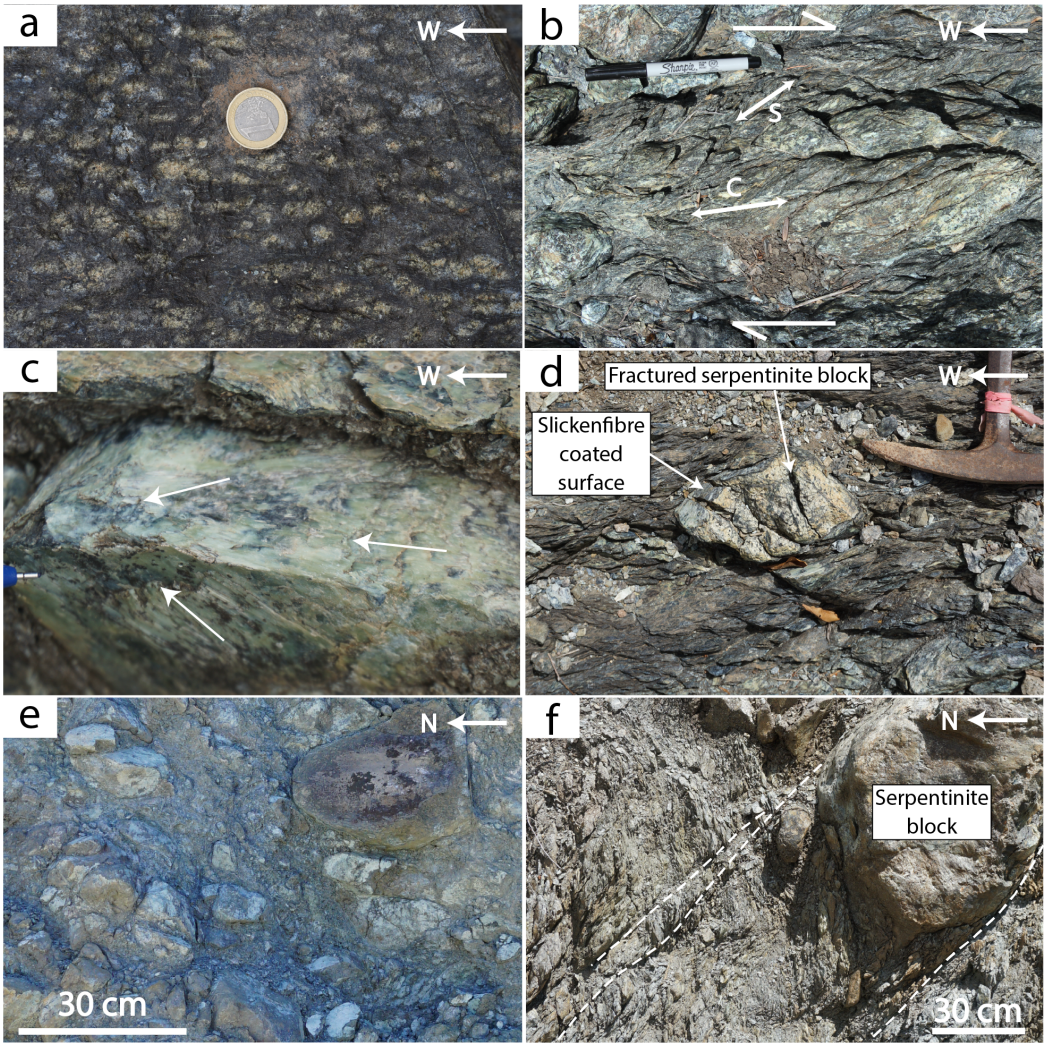


**Figure 3.4:** Structures recorded within serpentinite shear zones. (a) Steeply dipping porphyroclastic fabric (defined by bastite pseudomorphs after orthopyroxene) within massive serpentinite pseudomorphing the highest temperature ductile deformation in the Southern Troodos Transform Fault Zone (near WGS84: 34.7751°N 33.0808°E). (b) Typical scaly serpentinite with an S-C fabric (near 34.7921°N 33.0861°E). (c) Slickenfibre-coated phacoid making up the scaly fabric (near 34.8170°N 33.0811°E). (d) Fractured serpentinite block within a scaly serpentinite zone (near 34.8177°N 33.1099°E). (e) Phyllonitic serpentinite with a block-in-matrix type fabric (near 34.7740°N 33.0784°E). (f) Discrete plane parallel to the edge of a serpentinite block cutting scaly serpentinite (near 34.8159°N 33.0726°E). (a-d) look at horizontal surfaces; (e-f) are looking at approximately vertical cliffs.

m in total thickness and can be traced for ∼300 m along strike (Fig. 3.2). Phyllonites can also occur more locally as tabular, <1 m wide zones at the boundaries between scaly and massive serpentinite.

The various serpentinite groups highlight that mixed-mode deformation is common in the STTFZ lithospheric mantle. It is also apparent that variations along and across strike between dominantly brittle, mixed brittle-ductile and dominantly ductile deformation regions exist (Fig. 3.5). We use the term 'ductile' to describe spatially continuous deformation at the outcrop scale (Fig. 3.3iii-iv and 3.4b and e). This contrasts to 'brittle', which we use to define discontinuous deformation at the same scale of observation (Fig. 3.3i-ii, iia-iiia and 3.4d and f). Areas dominated by brittle deformation (Fig. 3.5a) contain steeply dipping, E-W striking discrete faults (Fig. 3.6), <5 cm thick, that are comparable to C planes and contain gently plunging slickenfibres. These discrete faults crosscut entire outcrops, and can be traced for up to ∼10 m along-strike length, limited by outcrop continuity. The total amount of slip along these discrete planes is unknown because of a lack of marker horizons. Angular blocks of serpentinite (from centimetres to >3 m) sit within a poorly interconnected scaly matrix in dominantly brittle zones. In contrast to these dominantly brittle zones, ductile portions are characterised by isolated, usually more rounded serpentinite blocks of various size, millimetres to >2 m long, sat in a well-interconnected scaly to phyllonitic serpentinite matrix and without any discrete through-going faults (Fig. 3.5c). Mixed brittle-ductile portions contain a relatively well-interconnected scaly matrix, and faults and fractures that, in places, occur parallel to block boundaries (Fig. 3.4f and 3.5b). The scaly fabric and fractures define a mutually cross-cutting relationship.

The SSZs are highly complex and heterogeneous in their internal structure. However, the overall style of SSZ deformation roughly coincides with various block:matrix proportions and distributions, with areas that are more block-supported showing a higher number of obvious faults at the outcrop scale than those that are matrix-supported. However, this does not preclude many foliation-subparallel faults or faults being overprinted by ductile deformation in the more matrix-rich outcrops. Locally, the style of deformation can also relate to contrasting competency, e.g. at the boundaries of some of the largest serpentinite clasts, tabular zones of phyllonite may be documented, although that is not always the case. The deformation styles more commonly grade

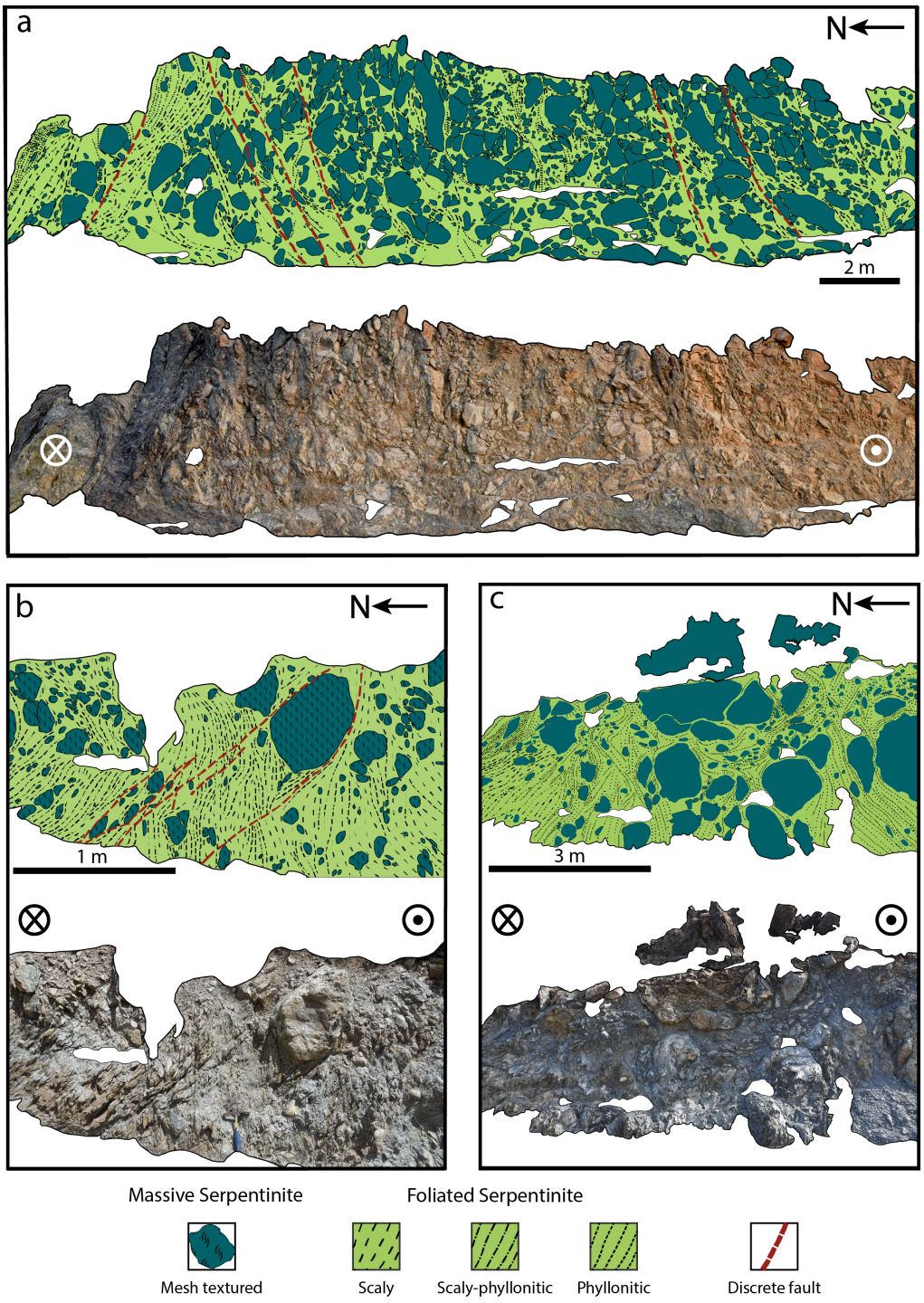


**Figure 3.5:** Roadside maps of vertical oucrop of a serpentinite shear zone, looking along the foliation. Vertical roadside outcrop maps of a serpentinite shear zone, looking along the foliation towards the East, showing their highly variable nature of deformation. (a) Dominantly brittle section with multiple, discrete through-going planes and fractured blocks (near WGS84: 34.7921°N 33.0861°E). (b) Brittle-ductile zone with mutually cross-cutting fractures and a scaly fabric (near 34.8159°N 33.0726°E). (c) Ductile portion of the same serpentinite shear zone as (a), with a well-developed block-in-matrix fabric and phyllonitic matrix (near 34.7934°N 33.0861°E). Equal area lower hemisphere stereonets are shown in Fig. 3.6.

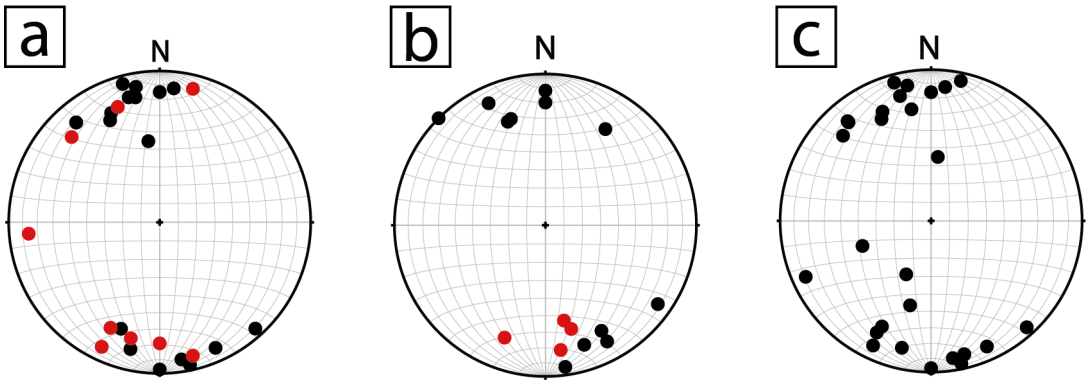


**Figure 3.6:** Accompanying lower hemisphere, equal area stereonets (black dots = all foliation; red dots = discrete faults) for Fig. 3.5. A; Dominantly brittle sections, B; Mixed brittle-ductile sections and C; Ductile section of a serpentinite shear zone.

between one another, sometimes at the metre scale and sometimes at much larger scales.

### 3.5.2 Microscopic observations of serpentinite shear zones

The observations we make at the microscale reveal distinct microstructural groups, which are related, but not equivalent, to the serpentinite groups we defined (section 3.5.1 above) at the outcrop scale where we divided the serpentinite into massive, fractured, scaly and phyllonitic serpentinite.

#### Mesh microstructure

Massive serpentinite shows pseudomorphic mesh and bastite microstructures (Fig. 3.7a), after olivine and pyroxene respectively, typical of hydrated oceanic peridotite (Viti and Mellini, 1998; Wicks and Whittaker, 1977). Accessory minerals include primary chrome spinel. Magnetite is present as a product of serpentinisation of olivine and most commonly concentrated at mesh rim boundaries, although also present within mesh rims and cores. Serpentinisation is pervasive and original olivine or pyroxene grains are rare.

Raman spectroscopy identifies an intensity peak at 3683 $cm^{-1}$ for mesh rims suggesting, in comparison to published Raman spectra for serpentinite polytypes (Rooney *et al.*, 2018), that they comprise lizardite (Fig. 3.8), while spectra from the ultra-fine grained cores reveal intensity peaks consistent with mixed chrysotile and lizardite (mesh core in Fig. 3.8). Lizardite grains in mesh rims are <5-10 $\mu$m in size (Fig. 3.9). Observations with a gypsum

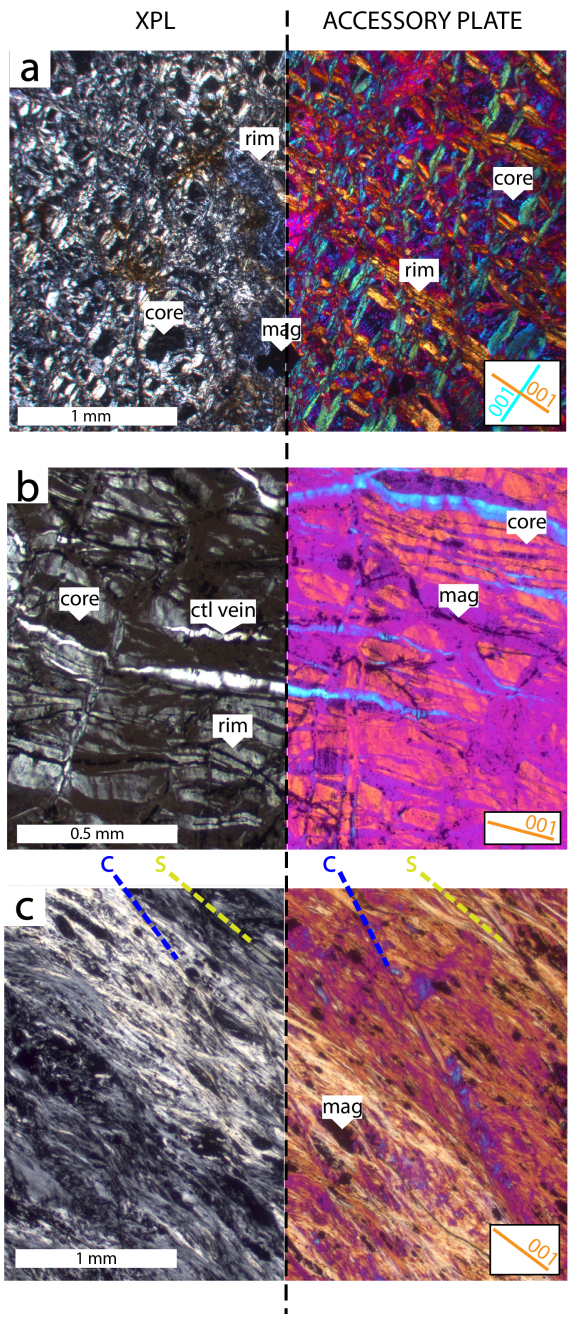


**Figure 3.7:** Serpentinite microstructures within variably deformed serpentinite. Each panel shows the left half of the image in cross-polarised light, and the right half with a gypsum tint plate. (a) Untectonised mesh microstructure (17CS17). The gypsum plate illuminates pink mesh cores (core) and yellow and blue lizardite rims (rim) with near-perpendicular (001) plane orientations. (b) Ribbon microstructure (deformed mesh microstructure in 17CS01) with one dominant rim orientation (yellow colour under the gypsum plate) and reduced core volume. This microstructure is commonly observed at the edges of serpentinite phacoids in scaly serpentinite. Seams of magnetite define the ribbon cells. (c) Phyllonite (17CS19) preserving no original mesh microstructure but a fibrous chrysotile schistosity with (S) and C planes (C). In (b) and (c), the (001) planes are parallel to the foliation, which also approximates the shear plane. The sample in (a) is not foliated. Magnetite forms as seams and concentrates into clusters within the foliation.

tint plate inserted in an optical microscope illuminate two, near-orthogonal crystallographic preferred orientations (CPO) of lizardite grains in mesh rims, surrounding poorly crystalline cores (Fig. 3.7a). Viti and Mellini (1998) and Viti *et al.* (2018) interpret similar observations to represent variation in orientation of the (001) lizardite axes. Antigorite (Raman shift at 3657 $cm^{-1}$) is only a trace constituent of massive serpentinites (<1 %) observed locally along rim boundaries (Fig. 3.9). Bastite comprises a fine-grained serpentine, much like mesh cores, and commonly retains a pseudomorphic pyroxene cleavage. Chrysotile veins cross-cut mesh microstructures and are dominantly extensional.

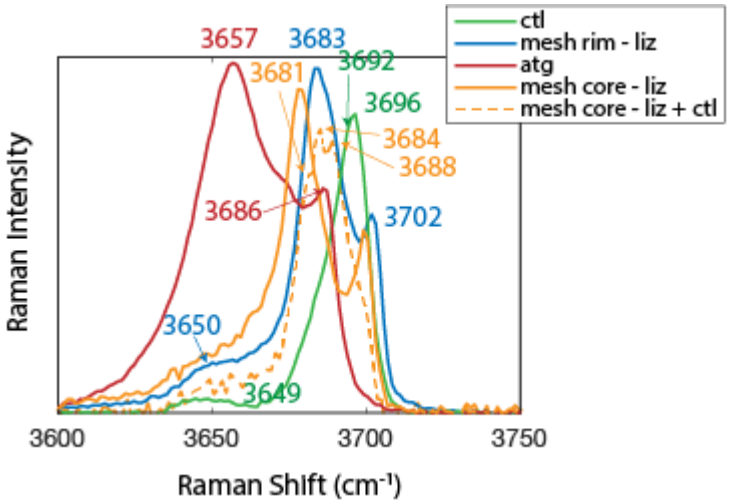


**Figure 3.8:** Raman point spectra for antigorite grains, lizardite dominant rims, mixed lizardite-chrysotile cores in the mesh microstructure, and chrysotile making up the phyllonitic serpentinite. ctl = chrysotile, liz = lizardite and atg = antigorite.

### Ribbon microstructure

Scaly phacoids contain a ribbon microstructure in which mesh cells (one cell consists of a single mesh core with surrounding rims) are sigmoidal. Much like mesh microstructure, ribbon microstructure comprises lizardite-dominant rims and mixed lizardite-chrysotile cores. Gypsum tint plate observations highlight one dominant rim CPO in sigmoidal ribbon cells that form a 3D interconnecting network of well-aligned lizardite, defining a foliation (Fig. 3.7b). Ribbon cells generally comprise smaller cores than mesh cells. Magnetite grains, <10 $\mu$m, are concentrated at ribbon boundaries and defines seams traceable up to

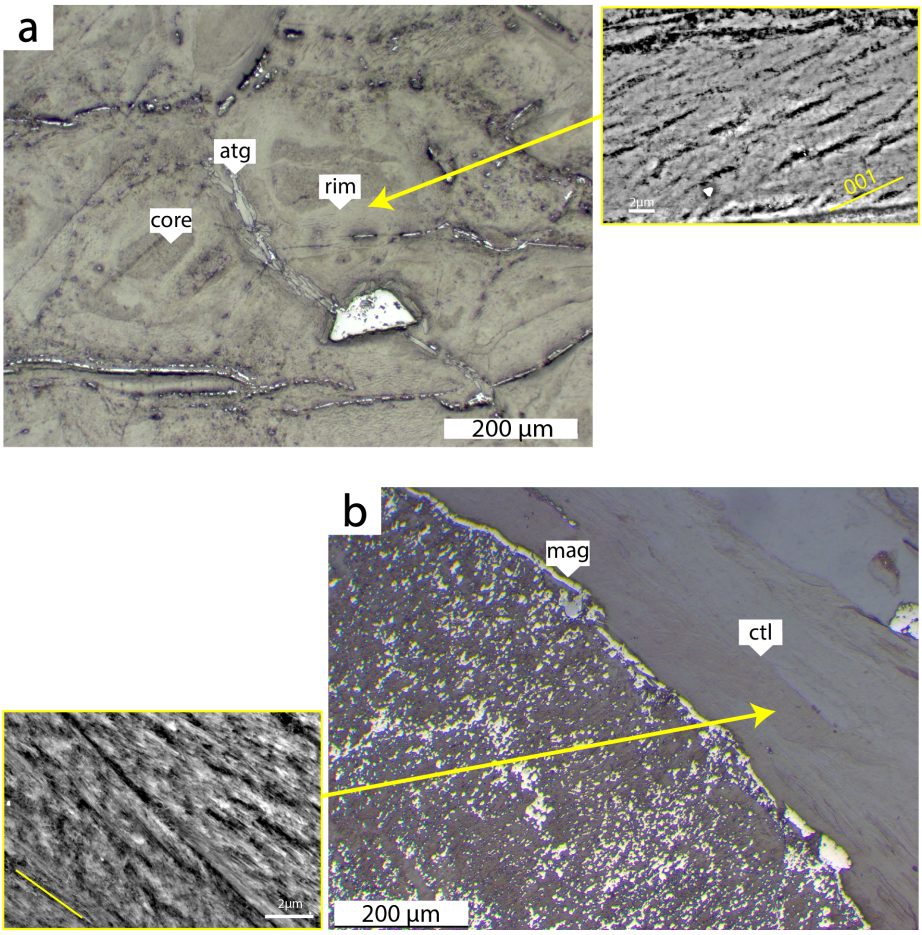


**Figure 3.9:** Microstructures of variably deformed serpentinite. (a) antigorite (atg) along mesh rims in massive serpentinite with high magnification BSE image of aligned lizardite making up rims (17CS01). (b) Magnetite (mag) concentration at the edge of a clast at the boundary with the phyllonitic serpentinite (19CS03) with a high magnification BSE image of aligned fibrous chrysotile making up the phyllonitic serpentinite.

a few millimetres (Fig. 3.7b). This ribbon fabric is particularly well-developed towards the edges of massive serpentinite phacoids with a mesh microstructure.

### Fibrous microstructure

The microstructure of phyllonitic serpentinite differs from massive and scaly serpentinite. It comprises a penetrative foliation of serpentine fibres, <1 $\mu$m wide, with few rigid serpentinite clasts (~1 mm) that contain a mesh or ribbon microstructure. Reflected light images show clasts are wrapped by the foliation, and have asymmetric pressure shadows indicating dextral shear sense. SEM and optical microscope observations show the phyllonitic cleavage is defined by well-aligned serpentine fibres (Fig. 3.7c). Fibre orientations vary in

space because they are locally deflected by sub-millimetre clasts, but overall they are subparallel to the bulk shear plane of the STTFZ. Magnetite is distributed throughout the foliation as individual grains, asymmetric clusters, and seams up to a few millimetres long parallel to the foliation (Fig. 3.7c). Phyllonitic serpentinite contains discrete C planes defined by fractures creating an S-C like geometry at the microscale, with an acute angle between S and C planes (Fig. 3.7c) and consistent with the inferred dextral shear sense of the STTFZ.

Raman spectroscopy identifies a spectrum with peaks at 3692 and 3696 $cm^{-1}$ for serpentine fibres, consistent with chrysotile being the predominant polytype in phyllonitic serpentinites (Fig. 3.8 and 3.10). Relict $\sim$10 $\mu$m sized grains of lizardite are locally present, but only in the form of scattered grains at low concentration (<5%) throughout the phyllonitic foliation (Fig. 3.10). Raman-point analysis shows mixed lizardite and chrysotile signals at the boundary between the lizardite clasts and the chrysotile foliation (Fig. 3.10).

### 3.5.3 Comparison of microstructure with mineral composition

SEM back-scatter electron (BSE) images of serpentinites showing mesh and ribbon microstructures reveal a density contrast between cores and rims (Fig. 3.11a-d). The distribution of major elements within and between serpentine polytypes and fabric types should reflect the conditions of formation. Using energy-dispersive spectroscopy (EDS) we analysed the major element composition of mesh rims, mesh cores, bastites, phyllonitic textures (chrysotile), and antigorite and lizardite clasts. Although a detailed analysis of serpentine chemistry is beyond the scope of this study, we highlight differences between serpentines of differing microstructures.

EDS analysis indicate that most, but not all, mesh rims are Mg-rich relative to their cores. Conversely, most rims have lower Fe concentrations than their cores. The exception to Mg-rich and Fe-poor rims come from a single sample. Bastites are generally lower in Mg than mesh rims, comparable to mesh cores but higher in Fe compared with most serpentine after olivine (Fig. 3.12). The chemical difference between bastite and the mesh microstructure likely relates

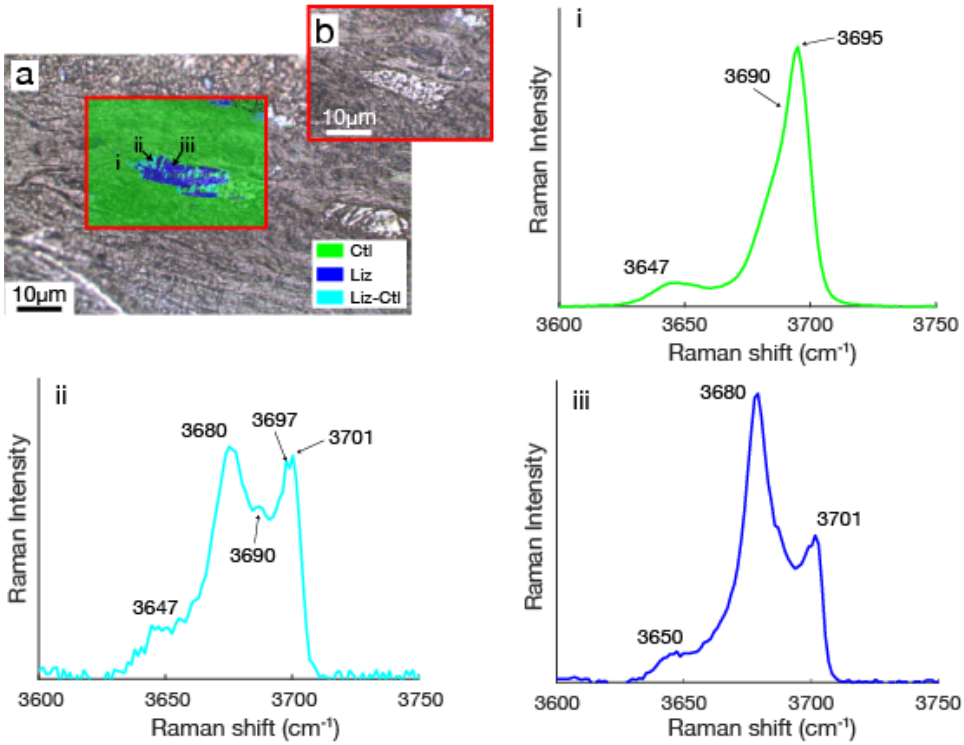


**Figure 3.10:** Raman spectroscopy point analysis and mapping of various serpentinite microstructures. (a) Raman map overlain on a reflected light image showing a lizardite grain that has partially broken down into chrysotile phyllonitic serpentinite (17CS19). (b) Reflected light image of the mapped area in (a). Point spectra for each of the three locations mapped in (a) show a transition from (i) a chrysotile signal, (ii) mixed chrysotile-lizardite signal to (iii) a lizardite signal.

to the initial Mg and Fe compositions of olivine and pyroxene from which they formed.

Although there are variations within our sample set, distinct chemical groups arise for each microstructure. In particular, the phyllonitic serpentine is distinct with lower and more homogeneous Fe-, and higher Al-concentrations (Fig. 3.12), but is similar to pressure shadow material adjacent to massive serpentine phacoids. Phyllonitic serpentinites occasionally reveal a density contrast in BSE images, mimicking the scaly fabric and consistent with variations in Mg content (Fig. 3.11e-f). Relict lizardite grains within phyllonitic serpentinite are similar in size and have compositions comparable to lizardite grains making up mesh rims (Fig. 3.12).

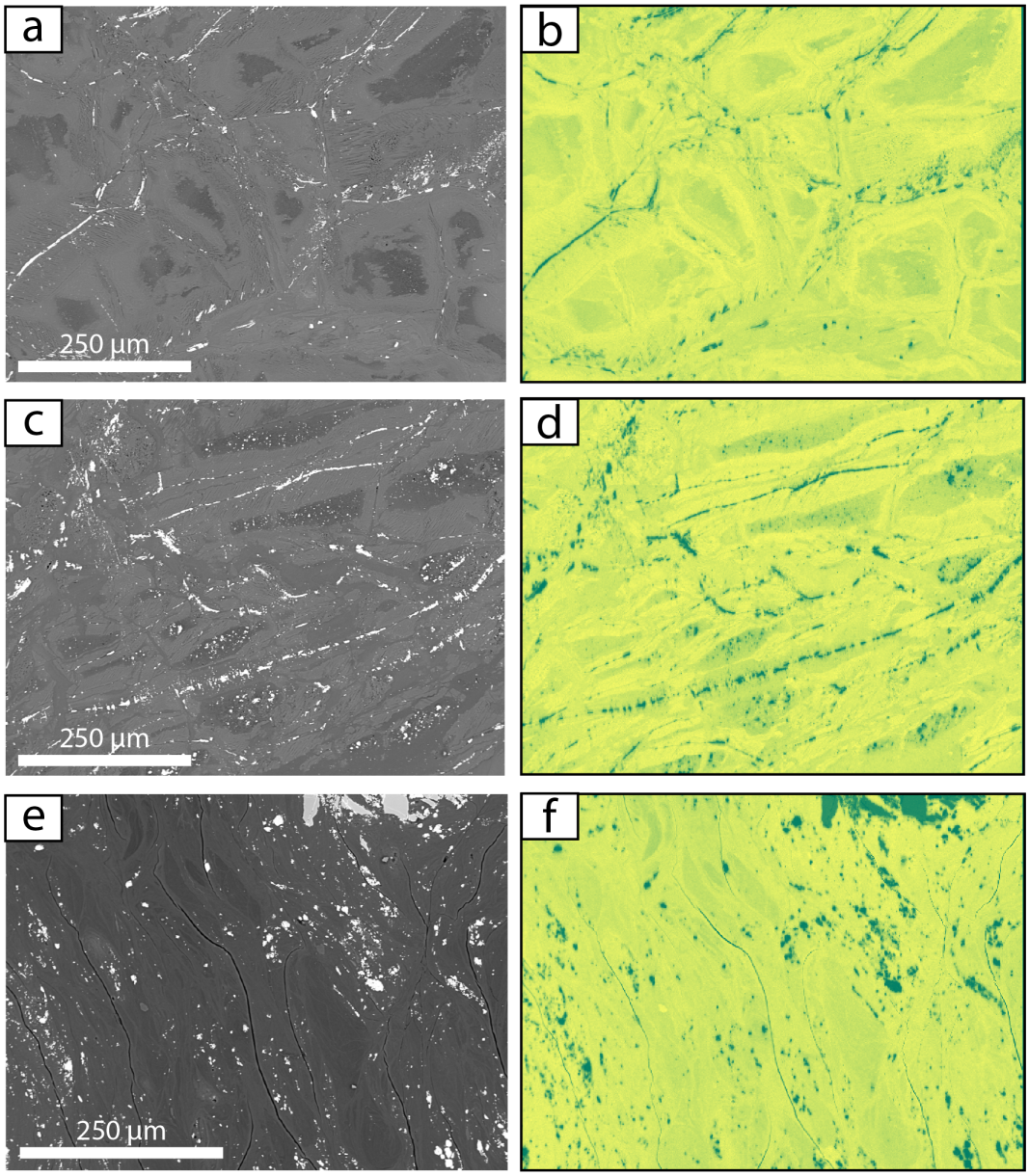


**Figure 3.11:** BSE and EDS maps of variably deformed serpentinite. (a)-(b); Mesh microstructure with Mg-rich rims and Mg-poor cores (17CS01). (c)-(d); Ribbon microstructure (17CS17) displaying a similar chemical variation between rims and cores as in (b). (e)-(f); Phyllonitic serpentinite (17CS19) with Mg variations illuminating a scaly fabric. Green = low MgO counts, yellow = high MgO counts.

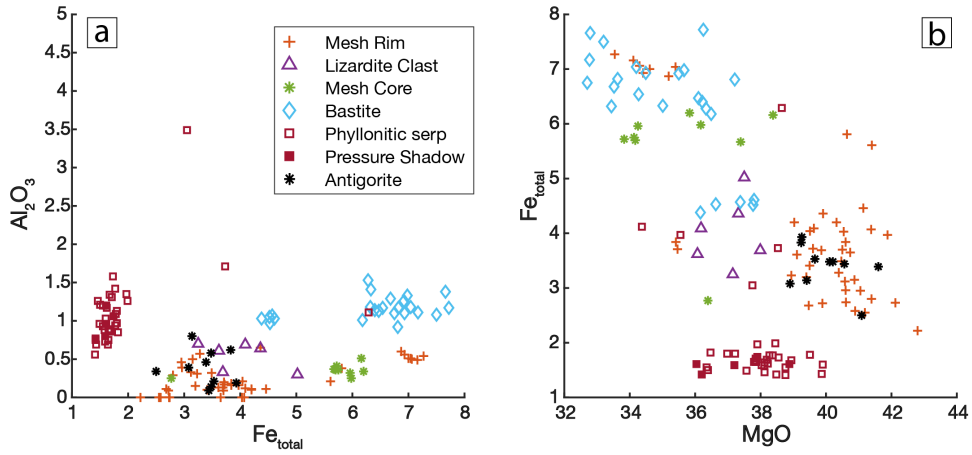


**Figure 3.12:** Plots from quantitative EDS point analyses of oxide weight percent from different serpentinite microstructures. (a) $Al_2O_3$ vs. total Fe (as in $Fe_2O_3$ and FeO) (b) total Fe vs. MgO plots showing each microstructure as chemically distinct and relatively internally homogeneous. A small cluster of relatively high-Fe, low-Mg mesh rims is an exception to these distinct and homogeneous groups. Chrysotile phyllonite contains lower Fe and higher Al than the serpentine making up mesh microstructures.

## 3.6 Discussion

### 3.6.1 Conditions of serpentinisation of the lithospheric mantle before and during faulting

#### Temperature of serpentinisation and deformation

The deformation described within SSZs in the STTFZ represents deformation in the shallow, serpentinised mantle lithosphere within the transform-tectonised zone. Almost all preserved transform-related deformation occurred when the lithospheric mantle had been or was being serpentinised. This is based on a variety of lines of evidence including transform-related lineations defined by serpentine minerals (see also Gass *et al.*, 1994; MacLeod and Murton, 1993). The Troodos ophiolite is generally believed to have formed at a relatively slow-spreading ridge (e.g. Varga and Moores, 1985), and hence the STTFZ was a slow-slipping, probably moderate-offset transform (e.g. MacLeod and Murton, 1993). The intact magmatic crustal thickness of the Troodos ophiolite is estimated to have been 4-5 km (Gass *et al.*, 1994), although this originally 'layer-cake' magmatic crust was subject to geometrically complex tectonic dismemberment within, and up to a few kilometres away from, the transform-tectonised zone. Crustal thickness estimates are not therefore in-

dicative of depths of deformation beneath the seafloor. Although the mantle lithosphere deformation we document is therefore representative of depths from as much as 4-6 km below the seafloor, some of it undoubtedly took place at much shallower depths. There is, however, little or no evidence for exposure of serpentinite on the seafloor within the STTFZ (Gass *et al.*, 1994).

The structural and mineralogical development of serpentinite within the STTFZ was progressive. Serpentinisation of the mantle harzburgite likely occurred as a two-stage process (e.g. Rouméjon *et al.*, 2018): (1) initial localised serpentinisation along microfractures that are defined by planes of magnetite (Fig. 3.7a) and also represented by lizardite-dominated mesh rims, then (2) more diffuse serpentinisation, resulting in fine-grained mesh cores. Minor amounts of antigorite occur along some mesh rims in STTFZ serpentinites (Fig. 3.6), consistent with serpentinisation temperatures of >300°C along these microfractures; (Evans, 2004). Mesh microstructures comprising lizardite and chrysotile are known to form directly from the serpentinisation of olivine, whereas antigorite typically forms a distinct interpenetrating texture (Wicks and Whittaker, 1977). As the untectonised serpentinised harzburgites of both the central Troodos (Mount Olympus) and Limassol Forest (STTFZ) outcrops (Fig. 3.1a) are dominated by lizardite and chrysotile mesh texture serpentine, we suspect that they record the initial serpentinisation of the peridotite (harzburgite and dunite). If the lizardite-chrysotile mixture overprinted an earlier antigorite serpentine, at least some evidence of interpenetrating textures should have been preserved. The occurrence of minor amounts of antigorite suggests that pressure and temperature conditions during the initial serpentinisation were within the range where antigorite, lizardite and chrysotile coexist. At the relatively low pressures expected for the shallow mantle setting, lizardite and chrysotile are stable at <400 °C, and antigorite at >300 °C (Evans, 2004). These constraints suggest the initial serpentinisation occurred at lower greenschist facies conditions, 300-400 °C. In scaly and phyllonitic serpentinite, lizardite and chrysotile are present without antigorite, suggesting that deformation occurred along SSZs at $T$ <300 °C (Evans, 2004). The formation of magnetite as a product of serpentinisation places a lower $T$ limit on serpentinisation since Fe is more favourably incorporated into magnetite than serpentine at $T$ >200 °C (Rouméjon *et al.*, 2018). Therefore, serpentinisation during STTFZ deformation can be roughly constrained to a $T$-window

of 200-300 °C.

### Fluid availability during serpentinisation and deformation

Serpentinisation in the STTFZ is pervasive and occurred in an ocean-floor setting (Gass *et al.*, 1994; MacLeod and Murton, 1993, 1995; Murton, 1986a) demonstrating that fluids, likely seawater, were readily available throughout the lithospheric mantle section that is now exposed in the Troodos ophiolite. Because lizardite is thought to form from near-stoichiometric water:rock ratios (e.g. Viti and Mellini, 1998), the lizardite mesh microstructures observed suggest water:rock ratios were therefore likely to have been relatively low during the first phase of serpentinisation. Chrysotile, which dominates slickenfibres, veins and some deformed serpentinites in the STTFZ (Fig. 3.4c-d, and Fig. 3.10), is most commonly formed by the recrystallisation of pre-existing serpentine minerals where water:rock ratios are high (e.g. Andreani *et al.*, 2005; Mumpton and Thompson, 1975; O'Hanley, 1991; O'Hanley *et al.*, 1989). Therefore, the transition from lizardite to chrysotile in phyllonitic serpentinites (Fig. 3.10) can be interpreted as a marker of locally elevated water:rock ratios (e.g. Evans, 2004; Rouméjon *et al.*, 2015). Such elevation of water:rock ratios is likely to reflect locally enhanced fluid flow, because chrysotile preferentially occurs along localised shear zones where porosity and permeability are also elevated. Similar processes have been suggested for serpentinites in the San Andreas Fault (Moore *et al.*, 1996).

### Serpentinite chemistry

The major element compositions of mesh rims, mesh cores, bastites, chrysotile in phyllonites, and antigorite and lizardite clasts within scaly and phyllonitic serpentinites are similar within each microstructually-defined group (Fig. 3.12). Mesh rims and mesh cores contrast with bastite compositions, which are taken as representing the initial compositions of olivine and orthopyroxene, respectively. We find that chrysotile slickenfibres and phyllonitic shear fabrics have distinct and more homogeneous chemistry compared to lizardite in mesh microstructures, an observation that is consistent with higher water:rock ratios in the most deformed serpentinites (e.g. Rouméjon *et al.*, 2015). This is a consequence of the higher mobility of major elements, which would homogenise the composition of individual grains. The co-precipitation of magnetite with

chrysotile is a possible explanation for the loss of Fe in the chrysotile compared with lizardite. Because mineralogical and chemical variability correlates well with distinct microstructures (Fig. 3.12) within the STTFZ, we deduce that serpentinisation was ongoing, and occurred in progressive stages under slightly different conditions as serpentinisation became more localised with increasing strain. The preservation of this chemical variability argues against these fabrics having experienced any substantial reserpentinisation subsequent to transform deformation, as a late-stage, post-ocean floor fluid influx and serpentinisation event (e.g. Neogene emplacement-related uplift and weathering; Gass *et al.* (1994); MacLeod and Murton (1993)) would be expected to overprint and homogenise their chemical and mineralogical differences (e.g. Nuriel *et al.*, 2009).

### Comparison between the Southern Troodos Transform Fault Zone and active oceanic transform faults

Serpentinite deformation was the predominant mode of deformation in the mantle lithosphere within the STTFZ and clearly exerted the primary control on the rheological behaviour of the active transform plate boundary. The deformation model we propose is likely to be widely applicable to many, if not most, oceanic transform faults.

Our observations from Troodos require that seafloor serpentinisation in the active domain of the transform was rapid and highly efficient, related to high fracture permeability and seawater influx deep into the mantle lithosphere. Such serpentinisation, resulting in well-interconnected serpentinite, occurs wherever mantle rocks are in contact with water at temperatures within the serpentine stability field. In many cases in the STTFZ, serpentinisation demonstrably predated syn-kinematic 'transform sequence' ultramafic and mafic magmatism (Gass *et al.*, 1994; MacLeod and Murton, 1993; Murton, 1986a). Hydrothermal cooling and alteration is also common along active oceanic transforms, including recent evidence from the Blanco (Kuna *et al.*, 2019) and Shaka and Prince Edward (Prigent *et al.*, 2020) transform faults. In addition, the mafic crust at oceanic transforms is believed to be reduced in thickness relative to a 'Penrose-type' layer-cake igneous crust (e.g. Auzende *et al.*, 1989), either from reduced melt supply (e.g. Cannat, 1993; Cannat *et al.*, 1995) or tectonic thinning (e.g. Fox and Gallo, 1984; Karson and Dick, 1983).

Even at some intermediate- and fast-spreading settings (e.g. the Garrett transform on the East Pacific Rise; Hekinian *et al.*, 1992) serpentinised mantle is exposed on the seafloor within the transform-tectonised domain, and therefore, it is reasonable to assume that our serpentinite deformation model could be applicable in these cases too.

Insight into seafloor serpentinisation may also be gained from extensional oceanic fault systems. Microseismicity suggests fluid flow from the sea floor to at least 12 km depth along the Mid Atlantic Ridge (Parnell-Turner *et al.*, 2017) and 17 km at the South West Indian Ridge (Grevemeyer *et al.*, 2019). This fluid flow is associated with greenschist facies phyllosilicate growth and deformation at the bases of detachment faults (Escartín *et al.*, 2003; MacLeod *et al.*, 2002). By analogy with these extensional faults at mid-ocean ridges, we predict serpentinisation and serpentinite deformation is likely to be typical of the shallow lithosphere of most transform faults. Note also that the strength of partially serpentinised peridotites drops to that of serpentine at only ∼10-15% alteration (Escartín *et al.*, 2001). Therefore, the principle of hydration state and fabric development governing deformation of the lithospheric mantle in an oceanic transform fault is likely to be applicable in any location where serpentinisation is an important process - i.e. where fluids are introduced to the transform fault in mantle rocks within the serpentine stability field.

In our observations, lizardite and chrysotile are the stable serpentine phases, and this is typically the case at relatively shallow depth and low temperature (T<400 °C; Evans, 2004), hence serpentinite rheology should be widely appropriate for any hydrated lithospheric mantle where T <400 °C. In the STTFZ, there is little evidence for antigorite, implying the rocks deformed at < 400 °C, and this may be common in the near-transform mantle because of hydrothermal cooling (e.g. Roland *et al.*, 2010). However, if temperatures of serpentinisation were higher than in the rocks we observe, antigorite may occur instead of lizardite. The specific rheological differences between these polytypes are unclear, but antigorite has also been inferred to be weak (Hilairet *et al.*, 2007) and velocity-strengthening (Chernak and Hirth, 2010) at T <600 °C from laboratory constraints. Therefore, antigorite could still account for SSZ weakness, albeit deforming by different mechanisms.

### 3.6.2 Fabric development of serpentinite shear zones with progressive shear strain

On the basis of our observations we find that macroscale fabrics in SSZs evolve from massive through scaly to phyllonitic with an inferred increase in bulk strain. This macroscale fabric evolution is accompanied by an evolution in microstructure from a mesh to a ribbon to a fibrous microstructure. Each microstructure is characterised by a distinct mineral composition, polytype and a dominant deformation mechanism (summarised in Fig. 3.13). We deduce that the deformation mechanisms represented by each successive macroscale fabric and microstructure constrain the rheology of the serpentinised lithospheric mantle during transform-related deformation.

#### Evolution from massive to incipient scaly serpentinite

From our macroscopic observations we deduce that progressive development from massive (or fractured) serpentinite to an incipient scaly fabric is controlled by the formation and intersection of two fracture sets that accommodate shear displacement. These fractures are filled with fibrous chrysotile and isolate low-strain angular, rhomboidal serpentinite blocks (Fig. 3.3iii). The rhomboidal blocks (phacoids) retain the same low-strain mesh microstructure as in massive serpentinite, however, locally some blocks contain a ribbon texture, reflecting incipient ductile strain. In places, fractures with orientations and kinematics distinct from the phacoid-bounding shears and the STTFZ margins are observed, and can be explained as Riedel shears or as accommodating local rotation of more rigid blocks within the broad STTFZ (MacLeod and Murton, 1993, 1995).

#### Evolution from incipient scaly serpentinite to a scaly fabric

With progressive transform displacement rhomboidal blocks defining the incipient scaly fabric develop into smaller sigmoidal phacoids with higher aspect ratios (Fig. 3.3iii). Scaly serpentinite phacoids have asymmetry indicating bulk dextral slip sub-parallel to the STTFZ margin (Fig. 3.4b). Compared to their cores, phacoid margins may have greater concentrations of magnetite or fibrous chrysotile (Fig. 3.9b and 3.13b). These mineralogical variations are inferred to reflect, respectively, local dissolution of serpentine, enhancing

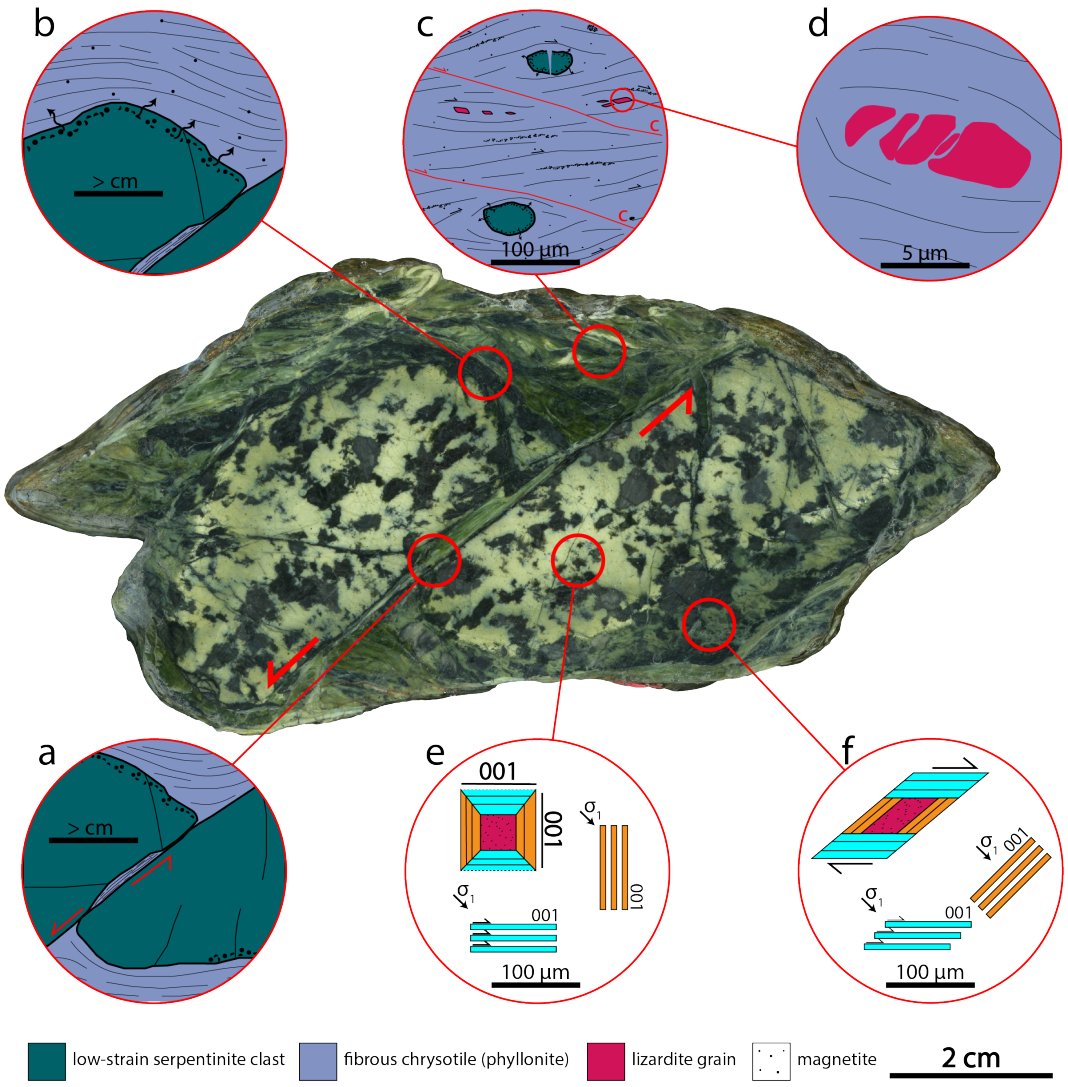


**Figure 3.13:** Microstructure summary of deformation within Southern Troodos Transform Fault Zone serpentinites (19CS03). (a) Brittle fracture of massive serpentinite blocks increasing permeability and fluid flow, and precipitation of chrysotile fibres. (b) Dissolution at the edges of serpentinite blocks, concentrating magnetite. (c) Scaly to phyllonitic fabric defining an S-C geometry and accommodating deformation by fibre-on-fibre slip between well aligned fibres of chrysotile. (d) Breakdown of relict lizardite grains by fracturing and dissolution to precipitate chrysotile. (e) Low strain mesh microstructure towards the core of blocks that deforms at the edges to a ribbon microstructure (f) following shearing. This transition is accommodated by a combination of rotation of mesh rims, pressure solution and (001) glide.

the concentration of relatively insoluble magnetite, and local dilation providing space for the precipitation of fibrous chrysotile as shear vein coatings. Dissolution-precipitation processes are therefore important in the progressive development of scaly serpentinite fabrics, as also suggested by Vannucchi *et al.* (2003) and Schleicher *et al.* (2012).

The low-strain mesh microstructure common in massive serpentinite is replaced by a pervasive ribbon microstructure in scaly serpentinite. During this transition mesh cores become smaller but progressively more elongated with increasing bulk strain, with their long axes parallel to the long axis of the strain ellipsoid. The transition from mesh to ribbon microstructure is controlled by mesh rims deforming differently depending on their orientation relative to the maximum principal compressive stress ($\sigma_1$). When sheared, they can respond in two ways: either they maintain a favourable angle between their (001) plane and the kinematic XY plane, or else they rotate, becoming unfavourably oriented to the shear direction (Viti *et al.*, 2018). Favourably oriented rims, subparallel to the XY plane, (45° to $\sigma_1$) experience maximum shear stress and form anastomosing 3D networks of aligned lizardite that define a foliated, anisotropic ribbon microstructure. Once formed, a ribbon microstructure comprises a strong shape preferred orientation (SPO) in aligned lizardite grains, defining a foliation, and where deformation can be controlled by easy basal (001) glide (Fig. 3.13e-f) (e.g. Viti *et al.*, 2018) because of lizardite's simple structure and slip systems (e.g. Amiguet *et al.*, 2014; Hilairet *et al.*, 2007; Hirauchi *et al.*, 2010; Viti *et al.*, 2018). In contrast, unfavourably oriented rims experience higher normal stresses, and favour deformation by pressure solution (Viti *et al.*, 2018), rather than undergoing deformation by dislocation creep or kinking. This microstructural transition, largely controlled by dissolution, allows the concentration of insoluble magnetite around ribbon cells, forming seams traceable up to a few millimetres (Fig. 3.7b). These magnetite-rich seams have the potential to influence local rheology since magnetite is strong and brittle compared to serpentine. This may promote unstable slip, as suggested by Tarling *et al.* (2018).

### Evolution from scaly to phyllonitic serpentinite

Phyllonitic fabrics characterise the most highly-strained serpentinites exposed in the STTFZ. The progression from scaly fabric to phyllonitic fabric involves

low-strain phacoids in scaly serpentinite becoming progressively smaller and volumetrically less significant. In addition, the chrysotile component of serpentinite becomes increasingly dominant over lizardite. As a consequence of the reduction in phacoid size, cleavage becomes more planar (Fig. 3.4b,e). Chrysotile fibres form an interconnecting network with a strong SPO reflecting bulk shear zone kinematics (Fig. 3.7c) and surround isolated low-strain phacoids that internally preserve a mesh to ribbon microstructure. This observation is comparable to other examples of SSZs (e.g. Andreani *et al.*, 2005; Collettini *et al.*, 2011, 2009; Hirauchi and Yamaguchi, 2007; Smith *et al.*, 2011; Wicks and Whittaker, 1977).

In the phyllonitic serpentinite, chrysotile fills fractures in relict lizardite grains (Fig. 3.10a), suggesting lizardite deformed brittlely, at least locally, and was actively replaced by chrysotile during transform-related shearing. This is supported by the observation that lizardite grains are aligned to the foliation but not present in strain shadows. The formation of chrysotile by dissolution of lizardite should be particularly efficient in areas characterised by low strain rates and fine grain size (e.g. Rutter, 1976).

A strong SPO in chrysotile in phyllonitic serpentinite has been previously explained by two processes (Andreani *et al.*, 2005; Reinen, 2000): (1) mechanical, rigid-body rotation of pre-existing chrysotile fibres controlled by the finite extension direction, and/or (2) the synkinematic growth of newly precipitated chrysotile controlled by the local opening direction. The aligned fibrous chrysotile grains in phyllonitic serpentinite contrasts in shape to the shorter, more equant lizardite grains and ultra-fine chrysotile that make up mesh rims and cores (Fig. 3.6). This supports the deduction that the chrysotile in phyllonitic serpentinite grew synkinematically, subparallel to the shear direction, rather than by the reorientation of pre-existing chrysotile. Dissolution-precipitation has been proposed as a mechanism for synkinematic growth, at low strain rates and temperatures up to $\sim$450 °C, for forming phyllonitic serpentinite within several other serpentinite-bearing fault zones (e.g. Padrón-Navarta *et al.*, 2012; Wassmann *et al.*, 2011) including the Santa Ynez Fault along the San Andreas fault system (e.g. Andreani *et al.*, 2005). Dissolution-precipitation processes are inferred to be the low-$T$ equivalent of dynamic recrystallisation for serpentine (e.g. Amiguet *et al.*, 2014) and is the operative process in the STTFZ because the temperatures were too cold for efficient

dislocation creep in lizardite.

Where the phyllonitic serpentinite fabric is well-developed, most of the original mesh and ribbon microstructure has been replaced by chrysotile fibres. The strong SPO and 3D interconnectivity of chrysotile domains promotes fibre-on-fibre slip as a deformation mechanism (Viti *et al.*, 2018) (Fig. 3.13c) because of chrysotile's low frictional strength ($\mu \sim 0.15$; Tesei *et al.*, 2018). Chrysotile fibres are commonly bent or curved, as resolved from undulose extinction, suggesting some deformation is taken up by the ease of bending rather than dislocation creep as a bulk deformation mechanism.

### Brittle deformation in serpentinite shear zones

While we infer that most of the preserved fabrics formed by dissolution-precipitation following the formation of a relatively small-displacement fracture fabric, brittle deformation features have mutually cross-cutting relationships with all the dominant macroscale ductile fabrics (Figs. 3.2, 3.3 and 3.5). Macroscopically, discrete fault planes are observed adjacent and parallel to block margins (Fig. 3.5a-b). This observation is significant because it implies that steep gradients in strain and strain rates expected at the boundaries between foliated matrix and low-strain blocks promote brittle fracturing (e.g. Fagereng and Sibson, 2010; Kenkmann and Dresen, 1998), in a similar way to that modelled by Beall *et al.* (2019). Macro- and microscale S-C geometries (Fig. 3.4b, 3.5 and 3.7c) within SSZs highlight the coeval brittle-ductile deformation across all scales, with dissolution common along curved foliation planes, and localised displacement on more planar C-planes (Fig. 3.13c). These competing frictional-viscous deformation processes and S-C geometries are directly comparable to observations from other scaly fault zones (e.g. Vannucchi *et al.*, 2003). Fracturing as a mechanical means of breaking down serpentinite blocks and phacoids in scaly and phyllonitic serpentinites is also common (Fig. 3.4b and 3.13a), as a result of block interaction accommodating bulk rotation during shearing. Brittle deformation is an important mechanism allowing localised and elevated water:rock ratios in shear zones to promote the dissolution-precipitation mechanisms, the precipitation of chrysotile and foliation development.

**Summary of the progressive deformation and evolution of serpentinite shear zones**

In summary, we document a progressive development from (1) isotropic lizardite-rich mesh microstructure through (2) lizardite-rich ribbon microstructure in low-strain, scaly serpentinite with local chrysotile precipitated around phacoids, to (3) a fibrous chrysotile phyllonite with a well developed foliation. These transitions can be inferred to represent a bulk strain progression, and may also reflect a temporal evolution within an individual SSZ within the broader active transform fault zone. However, bulk strain within the STTFZ is not homogeneously distributed; rather, deformation is partitioned into anastomosing SSZs which are themselves composed of multiple zones of the different fabric types discussed above. These zones of different fabric types have composite thicknesses ranging from centimetres to several hundreds of metres, each reflecting different amounts of accumulated strain. It is important to emphasise that total strains accumulated on individual SSZs are accommodated by all fabric types combined and most likely simultaneously.

### 3.6.3 Are serpentinite shear zones weak?

Previous studies have considered how the deformation of serpentinite affects the rheology and seismic behaviour of oceanic transform faults from dredged samples (e.g. Kohli and Warren, 2020; Prigent *et al.*, 2020; Warren and Hirth, 2006) and exhumed mantle on the Bogota Peninsula, New Caledonia (e.g. Chatzaras *et al.*, 2020). Chatzaras *et al.* (2020) discuss the contribution of stress changes imposed following a downward propagation of a seismic rupture from the crust into the mantle. They discuss the change in deformation mechanism from brittle fracture during the coseismic period to dynamic crystallisation at the postseismic stage of the earthquake cycle at temperatures >820 °C. Kohli and Warren (2020) and Prigent *et al.* (2020) considered deformation at ∼500-875 °C and depths of 20-25 km recorded in samples dredged from the Shaka and Prince Edward oceanic transforms, documenting brittle and ductile deformation of mylonites. These studies conclude that fluid-rock interaction promotes the crystallisation of weak mineral phases and grain-size reduction, which in turn provide mechanisms that can account for fault weakening and strain localisation, including dissolution-precipitation, as we suggest

is also important at lower $T$ (<300 °C).

The studies of dredged and exhumed mylonites document higher-temperature brittle deformation than expected for the base of the thermally-controlled seismogenic zone (>600 °C isotherm) but do explain geophysical observations (e.g. Kuna *et al.*, 2019; McGuire *et al.*, 2012; Roland *et al.*, 2010; Wolfson-Schwehr *et al.*, 2014) of seismicity locally extending much deeper (e.g. down to 25 km; Prigent *et al.*, 2020) and therefore to temperatures approaching 1000 °C (e.g. Froment *et al.*, 2014; McGuire *et al.*, 2012; Wolfson-Schwehr *et al.*, 2014). A consequence of this observation is that fractures may allow fluids to flow into the dominantly viscous mantle below the seismogenic layer, inducing fluid-related weakening mechanisms and strain localisation (Kohli and Warren, 2020). Therefore, whilst in the STTFZ we are not able to characterise deformation corresponding to such depths or temperatures, relict high-$T$ mylonites (e.g. 3.4a) previously documented in the lithospheric mantle of the STTFZ almost certainly correspond to an earlier higher-temperature, pre-serpentinisation deformation episode for which limited evidence has been documented by Murton (1986a), MacLeod and Murton (1993), Gass *et al.* (1994) and Fagereng and MacLeod (2019) within the STTFZ mantle section.

It is very clear that serpentine, not olivine, controlled the lithospheric mantle rheology in the STTFZ during the active strike-slip plate boundary phase of deformation. It is evident that the overall structure and composition of SSZs within the STTFZ represents deformation within well-hydrated, pervasively serpentinised lithospheric mantle along oceanic transform faults active at $T$ <300 °C. Because serpentinites in the STTFZ contain a range of microstructures and different serpentine polymorphs, the strength of the serpentinites may vary in space and time as a function of deformation mechanism and serpentine polytype. On the basis of deformation experiments extrapolated to geological strain rates, elevated pressures (>200-300 MPa) and temperatures (>300 °C) we can deduce that lizardite and chrysotile are weak phases. Both lizardite and chrysotile have frictional strengths, $\mu$, of ∼0.2 from room temperature up to ∼200 °C and effective normal stresses of 5-120 MPa, i.e. conditions consistent with those in the brittle upper lithosphere (Tesei *et al.*, 2018). Chrysotile can have a $\mu$ as low as 0.1 at shallow burial depths, <3 km (Moore *et al.*, 1997). In contrast to individual serpentine polytypes, mesh microstructures have stronger frictional strengths, $\mu \approx 0.3$ under the same con-

ditions (Tesei *et al.*, 2018), and remain weak at elevated temperatures (Viti *et al.*, 2018) and pressures up to 400 MPa (Escartín *et al.*, 1997b). Therefore, the frictional weakness of serpentine polytypes and microstructure is likely to play a role in SSZ weakness.

From our observations we document not only a strain-progressive change in serpentine polytype, from lizardite to chrysotile, that would explain minor weakening ($\Delta\mu \leq 0.1$), but also a change in the microstructure from mesh to ribbon and phyllonitic serpentinite. The ease of (001) plane sliding in lizardite is expected to be similar to that of micas, where glide is easiest when the basal plane is oriented at $\leq 45°$ to the axis of greatest compression (Kronenberg *et al.*, 1990) such that, when (001) crystallographic planes rotate towards the shear plane with increasing strain (Fig. 3.13e/section 3.6.2), the lizardite basal planes form a mechanically weak foliation.

We deduce that weakening of the SSZs is likely to have occurred by ongoing dissolution-precipitation processes coupled to frictional sliding (e.g. Bos and Spiers, 2002; Tesei *et al.*, 2018). Macroscopically, fractures and cleavage planes in scaly serpentinites are highly anastomosing, which would limit the ease of frictional sliding of phacoids. However, with increased shearing, phacoid sizes and proportions are reduced and at least partially replaced with fibrous chrysotile, a process aided by dissolution-precipitation. It is well accepted that the interconnectivity of the weak phase is important in controlling bulk shear zone rheology (Handy, 1990). Therefore, as the volume proportion of fibrous chrysotile increases, the volume and interconnectivity of the weak phase increases bulk weakening of the SSZs.

Our evidence from the STTFZ suggests that the frictional strength of individual SSZs decreases with cumulative shear strain when high porosity, permeability and pervasive fluid flow promotes the formation of foliated serpentinite (ribbon or phyllonitic microstructure). Foliation development acts as an efficient weakening mechanism in low- and high-strain serpentinites, providing a mechanism of strain localisation that may be active along many oceanic transform faults in the shallow (serpentinised) lithospheric mantle at temperatures $\sim$300 °C. This is similar to the long-term weakening of continental transforms that is suggested to occur following the development of chlorite or muscovite phyllonites by a broadly comparable process (Holdsworth *et al.*, 2001; Imber *et al.*, 1997). As well, our model suggests that the development of a well-

interconnected, well-foliated serpentinite implies high fluid pressures are not required to generate the low fault strength that is often inferred for oceanic transforms (e.g. Angelier *et al.*, 2000; Homberg *et al.*, 2010).

The relative internal proportion and distribution of serpentinite fabrics within shear zones is important. Strain accumulation is heterogeneous (Fig. 3.5/section 3.6.2) and therefore strength will also be spatially (and temporally) heterogeneous. Areas that did not experience serpentinisation early during deformation, or retain a low-strain mesh microstructure, have the potential to act as strong asperities within weak, foliated SSZs (e.g. Fig. 3.5).

### 3.6.4 Seismic style of serpentinite shear zones

At the macroscale, bulk deformation occurred in a distributed, ductile manner within scaly and phyllonitic serpentinites. This style of distributed deformation is similar to that thought to accommodate steady creep at low shear stresses in serpentinite along the San Andreas Fault (e.g. Andreani *et al.*, 2005; Irwin and Barnes, 1975; Moore and Rymer, 2007).

At slow slip rates ($\sim 10^{-9}$ m/s) serpentinites deformed in laboratory experiments are generally weak and display velocity-strengthening behaviour (Andreani *et al.*, 2005; Kohli *et al.*, 2011; Moore *et al.*, 1997, 1996; Reinen *et al.*, 1994). However, it is suggested that velocity-weakening, seismogenic behaviour can occur in lizardite-rich serpentinites in response to elevated slip rates ($\sim$0.1 m/s; Kohli *et al.* (2011)), potentially induced by processes such as: (1) earthquake nucleation elsewhere; (2) local or temporal stress concentrations; (3) shear strength decrease due to increased fluid pressure; (4) changes to the thickness of the deforming zone (Reinen *et al.*, 1991, 1994); and/or (5) increased temperature by shear heating (Hirth and Guillot, 2013; Moore and Lockner, 2004; Moore *et al.*, 1997). In contrast to lizardite, however, chrysotile exhibits a velocity-independent behaviour, remaining velocity-strengthening at all laboratory strain rates under hydrothermal conditions (Moore *et al.*, 1997, 1996; Reinen, 2000). This is significant, as it suggests chrysotile-rich phyllonitic serpentinites, such as those we document in the exhumed STTFZ, are likely to favour stable creep under all conditions.

Scaly fabrics similar to those documented here from the STTFZ can be found in various tectonic settings and mineral assemblages, and are often associated with the whole spectrum of slip speeds, from creep (Vannucchi *et al.*,

2003) to earthquake rupture propagation (e.g. during the 2011 M9 Tohoku-Oki earthquake; Chester *et al.* (2013)). This contrasts with the occurrence of discrete C planes throughout scaly serpentinite outcrops that partly retain lizardite-rich mesh and ribbon microstructures. We suspect, therefore, that discrete deformation structures, such as throughgoing fault planes (e.g. Fig. 3.4b and f), in the STTFZ developed where slip velocities were most easily elevated spatially (locally) or temporally. Principal slip zones are likely necessary for seismic slip (Ikari, 2015), but have not been observed within the serpentine phyllonites we describe here. The phyllonites can therefore be interpreted as favouring aseismic shear, although we cannot exclude the possibility of transient seismic slip, nucleating elsewhere but propagating along discrete surfaces that were not preserved (see also section 3.6.5 below).

Most of the brittle fractures preserved are those defining low-strain serpentinite phacoids, with traced lengths on the order of tens of centimetres. The size of a fracture plays a role in the moment magnitude, Mw, of an earthquake generated by slip along that fracture (Hanks and Kanamori, 1979). Mw is proportional to log of the moment, $M_0$, which is defined as a scalar by the rupture area (A) * average slip (d) * shear modulus of surrounding rock (G) (Aki, 1966). Following scaling relations by Kanamori and Anderson (1975), circular ruptures with diameter $\sim$10 cm (i.e. on the same order of magnitude as the fractures in scaly serpentinite) will produce Mw of $\sim$-1, if displacement is caused by a single event (G of serpentinite = 20 GPa; Reynard *et al.* (2007)). Seismicity of Mw >0 (reflecting faults with $\sim$30 cm radius, still within the range of fractures within scaly serpentinite), has been documented along several active oceanic transform faults such as the Gofar (e.g. Froment *et al.*, 2014; McGuire *et al.*, 2012), Blanco (e.g. Kuna *et al.*, 2019) and Discovery faults (e.g. Wolfson-Schwehr *et al.*, 2014) in the course of highly detailed ocean bottom seismometer surveys. However, whilst individual fractures in scaly serpentinite are small, it is likely that deformation is accomplished by localised slip along C-planes, or on numerous fractures that interact and link up to accommodate greater overall displacements and magnitudes than calculated above.

SSZs in the STTFZ are internally variable in their deformation style, with zones of dominantly brittle deformation, mixed brittle-ductile deformation and ductile deformation (Fig. 3.5). They contrast with many other mélanges from other geological environments in that most of the blocks and matrix are de-

rived from the same protolith, so ultimately the strength contrast within SSZs has to come from a strain weakening mechanism. In the case of the STTFZ we have shown here that this occurred through the development of a foliation from an initial isotropic mesh microstructure, accompanied by reactions replacing lizardite with chrysotile, and grain size reduction (section 3.6.3). Areas that are dominated by massive serpentinite and display discrete faults could therefore act as asperities (Fig. 3.14), whilst areas that are dominated by well-interconnected scaly or phyllonitic fabric are more likely representative of weak serpentinite. Where phacoid proportions are high, and scaly or phyllonitic matrix is poorly interconnected (Fig. 3.5a), discrete through-going fractures are widespread, potentially reflecting locally elevated strain rates (Fagereng and Sibson, 2010). Those portions of SSZs dominated by well-interconnected scaly to phyllonitic serpentinite, on the other hand, predominately record distributed deformation, and most likely acted as a creeping matrix at the macroscale (Fig. 3.5c).

The structure and rheology of the lithospheric mantle must evolve as a function of time, strain and serpentinisation (therefore, as a function of permeability and fluid flux), much like inferred for the Shaka and Prince Edward oceanic transforms (Prigent *et al.*, 2020). On the basis of our observations mixed, low-temperature brittle-ductile deformation occurs pervasively throughout SSZs, with coeval structures. Some of these structures may record seismicity, but others are likely to have been aseismic (Fig. 3.14), under temperatures far less than the inferred thermally-controlled base of the seismogenic zone at ∼600°C (e.g. Abercrombie and Ekström, 2001; Braunmiller and Nábělek, 2008). These different deformation styles can occur simultaneously where fracturing and dissolution-precipitation processes compete, or may alternate between one another where increased slip rate allows brittle fracture of an otherwise creeping serpentinite. This is analogous to, and provides a rheological framework for, a 'multimode' conceptual model for the behaviour of the serpentinised lithospheric mantle within oceanic transform faults (e.g. Boettcher and Jordan, 2004), which proposes individual fault segments can undergo both seismic and aseismic slip at different times. This is also similar to the model presented by Kuna *et al.* (2019), who suggested that the lithospheric mantle part of the Blanco transform fault undergoes seismic and aseismic slip at different times.

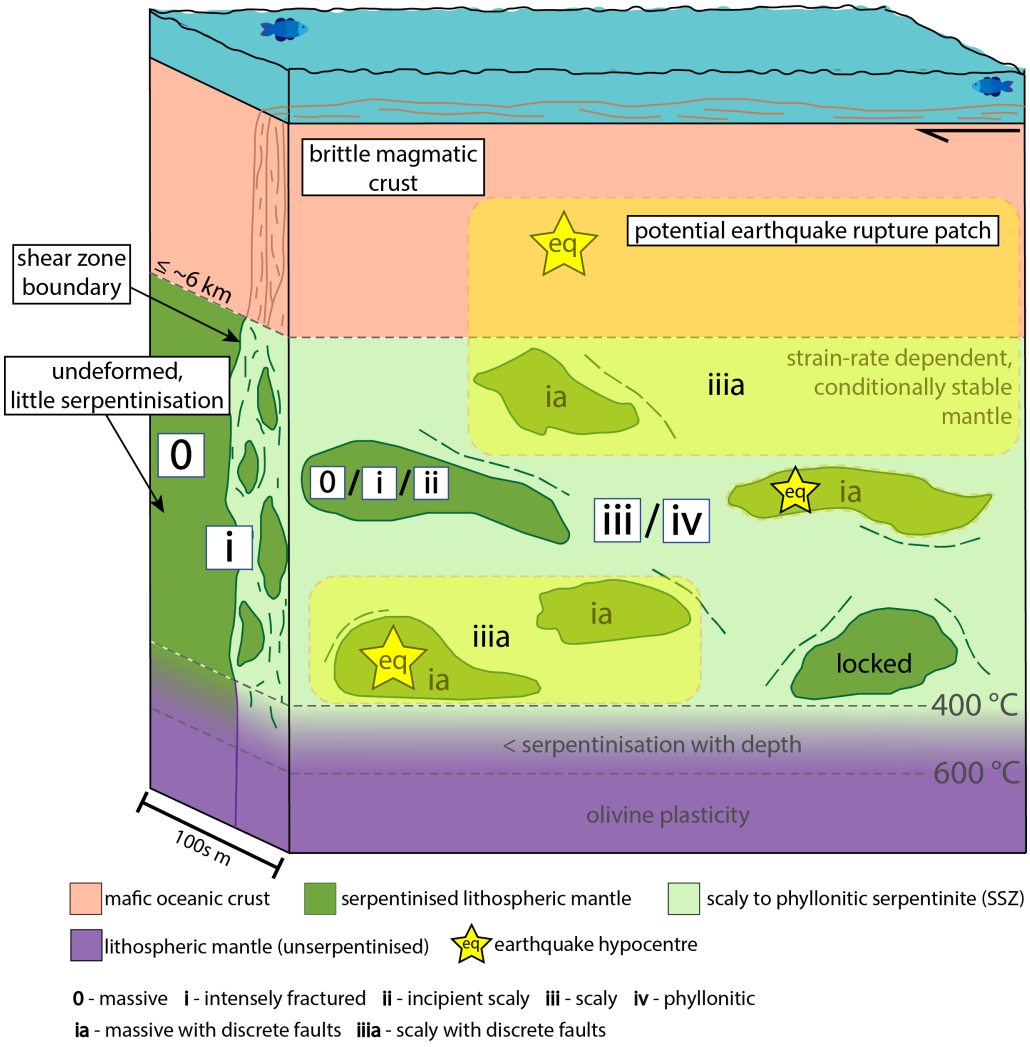


**Figure 3.14:** Schematic summary of the deformation and mode of slip along an oceanic transform fault based on observations from the mantle lithosphere of the Southern Troodos Transform Fault Zone. Crustal thickness of ≤6 km shown is a simplified, approximate maximum depth to the base of a magmatic crustal layer, while the depths to the 400 and 600 °C isotherms would depend on a range of factors including the geothermal gradient, spreading rate, magmatic crustal thickness and fluid infiltration. Pervasively serpentinised lithospheric mantle transitions progressively through scaly to phyllonitic serpentinite (0-iv; as in Fig. 3.4) with continued deformation, and is accompanied by a transition from microseismicity to aseismic creep at $T$ <600°C. Preserved mesh-textured serpentinite areas (darker green) may represent parts of the lithospheric mantle that were not well serpentinised during deformation, and hence acted as locked patches that acted as the sites of earthquake nucleation and allowing the propagation of an earthquake (yellow patch), as a result of loading from the otherwise creeping lithospheric mantle. Similarly, an earthquake nucleating in the brittle mafic crust may be capable of propagating downward into the serpentinised lithospheric mantle, as a consequence of the conditionally stable nature of serpentine.

### 3.6.5 The interaction between mantle shear zones and crustal faults

Many of the structures we document are intrinsic, having formed from local processes within individual SSZs. However, this does not rule out some features, particularly the larger through-going discrete faults, having been imposed from elsewhere, formed from the propagation of a co-seismic rupture that nucleated in a potentially distant asperity, for example in the mafic oceanic crust (Fig. 3.14). This raises the important question of how the crust and mantle are coupled along oceanic transform faults. Brittle faults could nucleate in the mafic crust, perhaps as a result of being loaded by the creeping serpentinised lithospheric mantle below, and propagate downwards into the lithospheric mantle, as suggested for the Romanche Abercrombie and Ekström (2001) and Blanco transform faults Kuna *et al.* (2019), introducing fluids and promoting serpentinisation. Alternatively, creeping SSZs within the serpentinised lithospheric mantle could load adjacent undeformed serpentinite, comprising a mesh microstructure that creeps at a slower rate, explaining how seismic slip can occur within the serpentinised lithospheric mantle (Fig. 3.14). Earthquakes that nucleate in massive serpentinite, loaded by surrounding creeping SSZs, may also propagate back up into the mafic crust. Because the fluids responsible for hydration to serpentinite are seawater and percolate down into the lithospheric mantle, it is consistent with the idea that SSZs are generally the down-dip continuation of crustal faults.

It is important to recognise that the well-documented, multi-scale geological complexity of the Southern Troodos Transform Fault Zone is almost certainly mirrored by modern oceanic transform fault zones, although their details can only be hinted at. Along many slow- and ultra-slow spreading ridges a regular, continuous magmatic oceanic crust is now known to be absent or incompletely developed, especially near ridge axial discontinuities, and the interplay between magmatism and tectonic extension is complex (e.g. Cann *et al.*, 1997; Cannat, 1993; Cannat *et al.*, 1995; Karson *et al.*, 2006). Even within the STTFZ in the Troodos ophiolite where, at the ridge axis, a continuous Penrose-type mafic ocean crust was generated, detailed field mapping of the transform-tectonised domain has documented substantial vertical, oblique and rotational displacements on many transform related fault zones, consequently juxtaposing crust

and mantle lithologies on a range of scales adjacent to and within the active transform tectonised zone Gass *et al.* (1994); MacLeod (1990); MacLeod *et al.* (1990); MacLeod and Murton (1993, 1995); Murton (1986a). Furthermore, magmatic intrusions, documented in the STTFZ (into already serpentinised mantle: Gass *et al.*, 1994; MacLeod and Murton, 1993; Murton, 1986a,b) and also some modern transforms (e.g. Constantin, 1999), can influence the local *P*-*T* conditions and induce metasomatic reactions that affect local rheology (e.g. Tarling *et al.*, 2019). Variation in fluid flow and associated serpentinisation will also influence the seismic behaviour due to the heterogeneous distribution of frictionally weak, hydrous minerals (e.g. Boettcher and Jordan, 2004; Moore *et al.*, 1997) and heterogeneous fluid pressures (e.g. Scholz, 1998). Therefore, there are circumstances where different and additional mechanisms are likely to operate at a variety of spatial and temporal scales.

## 3.7 Conclusions

The Southern Troodos Transform Fault Zone (STTFZ) records sub-seafloor faulting and deformation within a Tethyan oceanic transform fault. Subsequent exhumation has allowed us a unique insight into its 3D internal structure and geological evolution, and an examination of deformation mechanisms within the shallow lithospheric mantle that corresponds to the deeper part of the seismogenic zone in modern oceanic transform fault zones. We show that transform plate motion in the lithospheric mantle was accommodated almost exclusively by deformation of serpentinite. Steeply dipping, E-W striking (transform-parallel), serpentinite shear zones (SSZs) with strike-slip lineations document original seafloor deformation within a once dextrally-slipping oceanic transform fault zone. Exhumation-related overprinting is absent or minor, and readily accounted for in selected exposures. Present-day outcrop of serpentinised mantle peridotite preserves a record of variable deformation at the macro- and microscale. The dominant structures that accommodated deformation within the lithospheric mantle are shear zones comprising a serpentinite mélange within which the volumetric proportion of foliated serpentinite matrix increases with inferred cumulative strain. Individual SSZs are of the order of 10s-100 m wide, with anastomosing geometries, and can be traced for up to several kilometres along strike, within an overall transform-tectonised

zone ∼5 km wide.

Massive serpentinite has a mesh texture at the microscale, resulting from passive influx of water into the olivine lattice. This microstructure is pervasive within the overall STTFZ and implies extensive seawater penetration from above along both transform- and ridge-parallel faults. From a detailed examination of the internal structure of SSZs within the transform-tectonised zone as a whole, we find a progressive transition from massive serpentinite to scaly and phyllonitic serpentinite at the macroscale. This is matched by a textural change from mesh to ribbon and fibrous microstructures, along with a change in dominant serpentine type from lizardite to chrysotile. This scaly fabric experienced basal (001) glide and pressure solution to form a foliated ribbon microstructure. In concert with this, dissolution-precipitation along fractures was responsible for the formation of a chrysotile-rich phyllonitic serpentinite at the expense of the lizardite-rich mesh and ribbon microstructures. Once a foliated chrysotile developed, fibre-on-fibre slip acted as an efficient weakening mechanism promoting stable creep. Brittle fracture of serpentinite occurred locally and is important, because the fractures promoted fluid flow, enhancing many of these deformation mechanisms without the need for elevated fluid pressures.

We have shown here that SSZs are mechanically weak because of the intrinsic nature of foliated lizardite and chrysotile, and that they deform largely by aseismic creep at geological strain rates and low temperatures (from 400 °C down to seafloor temperature). SSZ strength decreases with the development of a foliation caused by progressive shearing. SSZs can, however, be capable of hosting coseismic slip if external factors allow an increase in slip rate, because this promotes velocity-weakening behaviour in lizardite Kohli *et al.* (2011). We argue that these observations and inferences can explain spatial and temporal variations in the rheology and seismic behaviour of modern oceanic transforms. Seismically coupled segments may occur in regions where serpentinisation is less pervasive, or where zones retain an original mesh microstructure, and are therefore relatively strong. The rheological evolution of the oceanic lithosphere is therefore heterogeneous where it is controlled by the spatiotemporal variation in serpentinite fabric development, which in turn is controlled by heterogeneous fracturing, permeability and fluid flow. On the basis of evidence from the Southern Troodos Transform Fault Zone of Cyprus we deduce that

the ‘seismic deficit’ and requirement for abundant aseismic creep in the shallow lithospheric mantle in oceanic transform faults is explained by the weak mechanical behaviour of compound serpentinite shear zones, whose complex internal structures are capable of hosting spatially and temporally variable seismic behaviour.

# Chapter 4

# The structural and rheological evolution of brittle fault zones in the mafic crust: Implications for the strength of the oceanic transform faults

## 4.1 Abstract

Oceanic transform faults slip at high angles to the maximum principal stress, and are considered to be anomalously weak compared to the surrounding oceanic crust. Additionally, oceanic transform faults typically display far fewer and smaller magnitude earthquakes than expected for their size, and may slip aseismically within the thermally defined seismogenic zone ($T$ <600 °C). While several processes have been proposed to explain the weakness and tendency for aseismic slip, as yet, none have been founded on direct geological observations from an oceanic transform fault, modern or ancient.

We constrain the effects of fault zone damage and fluid flow (alteration) on deformation of sheeted dolerite dykes within hydrothermally altered mafic upper oceanic crust of the Southern Troodos Transform Fault Zone, an exhumed Cretaceous-aged oceanic transform fault preserved in the Troodos ophiolite of Cyprus. We document low to medium temperature (<450 °C; greenschist facies) brittle and macroscopically ductile deformation, localised in steeply

dipping, E-W striking, anastomosing fault strands up to hundreds of metres thick. Geological mapping reveals several distinct types of fault rock derived from dolerite dykes, including crackle breccias, cemented breccias and foliated fault gouges that are interpreted to reflect progressive increase in strain.

Differing fractal dimensions of particle size distributions in the different categories of fault rock suggest that deformation mechanisms varied spatially and temporally within individual fault strands. Low fractal dimension, $Ds$, values associated with crackle breccias (<1.3) suggest brittle fracture and fragmentation were common in small-displacement faults, which gave way to cataclasis and constrained comminution in breccias ($Ds$ = 1.32-1.68), and then to abrasion and foliation development in large-displacement faults characterised by phyllosilicate-rich fault gouges ($Ds$ >1.7).

We suggest an evolution from relatively intact dolerite to well-interconnected and frictionally weak chlorite-rich fault gouges. This evolution results from a combination of progressive brittle deformation, in conjunction with locally elevated fluid pressures, but in the absence of fault healing. The effect of this progressive deformation is to weaken individual fault strands along the oceanic transform plate boundary.

### Author contributions

Sophie Cox is the main author of this work and undertook field work and data analysis. Ake Fagereng, Christopher MacLeod helped with field work and supervision of data analysis and the writing of the manuscript. Chris Tulley helped with fieldwork.

## 4.2 Introduction

Oceanic transform faults form parallel to the spreading direction, and approximately perpendicular to the spreading ridges they connect. Because normal faults predominate along spreading ridges (Lay and Wallace, 1995; Wilson, 1965), according to Anderson's theory of faulting, the maximum principal stress, $\sigma_1$, is vertical, while the greatest horizontal stress is parallel to the spreading ridge and perpendicular to the strike of the oceanic transform fault. Consequently, the smallest horizontal compressive stress is perpendicular to the spreading ridge and parallel to the oceanic transform. However, oceanic transform faults are dominated by strike-slip faulting and according to Anderson, $\sigma_1$ should instead be horizontal and trend at an angle of $\sim$30° to the fault. Following this reasoning the strike-slip nature of oceanic transform faults does not obey Anderson's theory of faulting (assuming Byerlee friction of $\mu = 0.6$, faults contain $\sigma_2$ and form $\sim$30° to $\sigma_1$) and they maintain an unfavourable orientation to the principal stresses (very high angle, $\theta$, to $\sigma_1$). For example, principal stress orientations determined from earthquake focal-plane mechanisms and borehole measurements indicate that the strike of some transform faults (e.g. the Tjörnes Fracture Zone and San Andreas Fault) is nearly perpendicular to $\sigma_1$ (Angelier *et al.*, 2000; Homberg *et al.*, 2010; Townend and Zoback, 2004; Zoback, 1991; Zoback *et al.*, 1987).

In the absence of documented stress rotations, in order to preserve the near-orthogonal relationship with mid-ocean ridges, oceanic transforms must be rheologically very weak compared to the surrounding crust (e.g. Behn *et al.*, 2002; Oldenburg and Brune, 1972). For comparison, the continental San Andreas Fault is inferred to deform at shear stresses of $\sim$20 MPa (Zoback, 1991) and 2-D numerical models show that its frictional strength ($\mu$) must be low, $\sim$0.2 (e.g. Townend and Zoback, 2004; Zoback, 1991). In the case of the Tjörnes Fracture Zone, an oceanic transform fault in northern Iceland, the required effective friction (accounting for the effect of pore fluid pressure) is required to be extremely low, $\sim$0.01, if it is to explain both fault-parallel and fault-perpendicular compressions (e.g. Homberg *et al.*, 2010).

Many mechanisms have been proposed to explain the inherent weakness of oceanic transform faults, including: (1) Elevated fluid pressure ($Pf$) lowering the effective normal stress ($\sigma_n^{'} = \sigma_n - Pf$) and promoting velocity-

strengthening creep (Scholz, 1998); (2) hydration of mafic and ultramafic minerals to frictionally-weak phyllosilicates and serpentine (Boettcher and Jordan, 2004; Cox *et al.*, 2021; Froment *et al.*, 2014; McGuire *et al.*, 2012; Moore *et al.*, 1997; Roland *et al.*, 2010, 2012) which can favour creep behaviour; and (3) deep fluid flow leading to the progressive formation of weak mylonite shear zones by low-stress deformation mechanisms within the lithospheric mantle (Kohli and Warren, 2020; Prigent *et al.*, 2020). However, to date, it remains unclear which of the above processes, or combination of processes, plays a role in the weakness of oceanic transform faults within the oceanic crust and lithosphere. Cox *et al.* (2021)/Chapter 3 suggested that, in the lithospheric mantle section of the Southern Troodos Transform Fault Zone in Cyprus, weakening occurred by a transition from olivine-controlled rheology in peridotite to a phyllosilicate-controlled rheology in serpentinite. However, in the overlying mafic crust, other mechanism(s) is(are) needed to explain weakening.

Most oceanic transform faults accommodate a large proportion of slip (∼85% globally) by aseismic creep accompanied by microseismicity (e.g. Behn *et al.*, 2002; Boettcher and Jordan, 2004; Okal and Langenhorst, 2000) despite cross-cutting the potentially seismogenic brittle crust. Furthermore, from 3D boundary element modelling it has been shown that seismic coupling, $\chi$ (defined as the ratio between the observed seismic moment and the expected seismic moment for a given fault; see section 1.7.2 for details) as low as 0.05 (Behn *et al.*, 2002) best explains the observed patterns of strike-slip (transform fault) and normal (ridge) faulting. Despite their dominant aseismic behaviour, some oceanic transforms contain segments that rupture quasi-periodically in earthquakes of Mw >6.0 separated by aseismic/microseismically active regions (Braunmiller and Nábělek, 2008; Froment *et al.*, 2014; McGuire *et al.*, 2005; Sykes and Ekström, 2012), while others experience both seismic slip and aseismic creep along the same fault segments, but at different times (Abercrombie and Ekström, 2001; Hilley *et al.*, 2020; McGuire *et al.*, 1996). Therefore, oceanic transform faults' weakness may be connected to their lack of seismicity. A link between fault strength and seismic behaviour has been suggested experimentally for several materials (e.g. Ikari *et al.*, 2011, and Chapter 5).

Most existing studies on the weakness of upper crustal transform faults focus on continental faults and lack constraints based on direct geological observations from oceanic transform faults, which are submarine and therefore

largely inaccessible. Using the example of a well-preserved ancient oceanic transform fault preserved in the Troodos Ophiolite, Cyprus, we document field observations from the micro- to kilometre-scale to describe the initiation and evolution of faults within the mafic oceanic crust. We infer that fault zone damage, and the formation of foliated chlorite-rich fault gouges, results in the long-term weakness of oceanic transform faults within the shallow crust.

## 4.3 Geological Setting of the Southern Troodos Transform Fault Zone

As introduced in Chapter 2, the Troodos Ophiolite in Cyprus is a Cretaceous-aged fragment of oceanic lithosphere with an oceanic transform fault, the Southern Troodos Transform Fault, preserved at its southern margin (Fig. 4.1; Gass *et al.*, 1994). The ophiolite and STTFZ's unique preservation and exposure allows a detailed and focused field study of oceanic transform fault deformation from the perspective of its palaeoseismicity to address the questions posed above. The outcrops studied here were chosen to avoid any later structural overprinting relating to the exhumation and contain structures that are kinematically consistent with seafloor transform deformation.

Deformation in the STTFZ is typically localised onto steeply dipping, E-W striking structures throughout all stratigraphic levels (Fig. 4.1b). Mantle depth deformation occurred predominantly by viscous flow within serpentinite shear zones, described in detail by Cox *et al.* (2021)/Chapter 3. In the mafic crust, deformation is most clearly displayed by faulted sheeted dykes throughout the Arakapas Fault Belt and northern Limassol Forest Complex areas (Fig. 4.1b). These faults are clustered in broad, anastomosing belts of deformation that can be traced (intermittently) for up to 7 km along strike, enclose slivers of less deformed sheeted dykes (Gass *et al.*, 1994; MacLeod and Murton, 1993), and are generally parallel to pre-existing fractures such as dyke margins and cooling joints that occur in a range of orientations. Within the STTFZ, individual faults can usually only be traced continually for tens of metres at most due to a lack of outcrop continuity.

North of the Arakapas Fault Belt, outside of the main transform tectonised zone, dykes generally strike ∼NE-SW to E-W and dip steeply. NE-SW striking dykes are extensively deformed by clockwise, vertical-axis rotation (from an

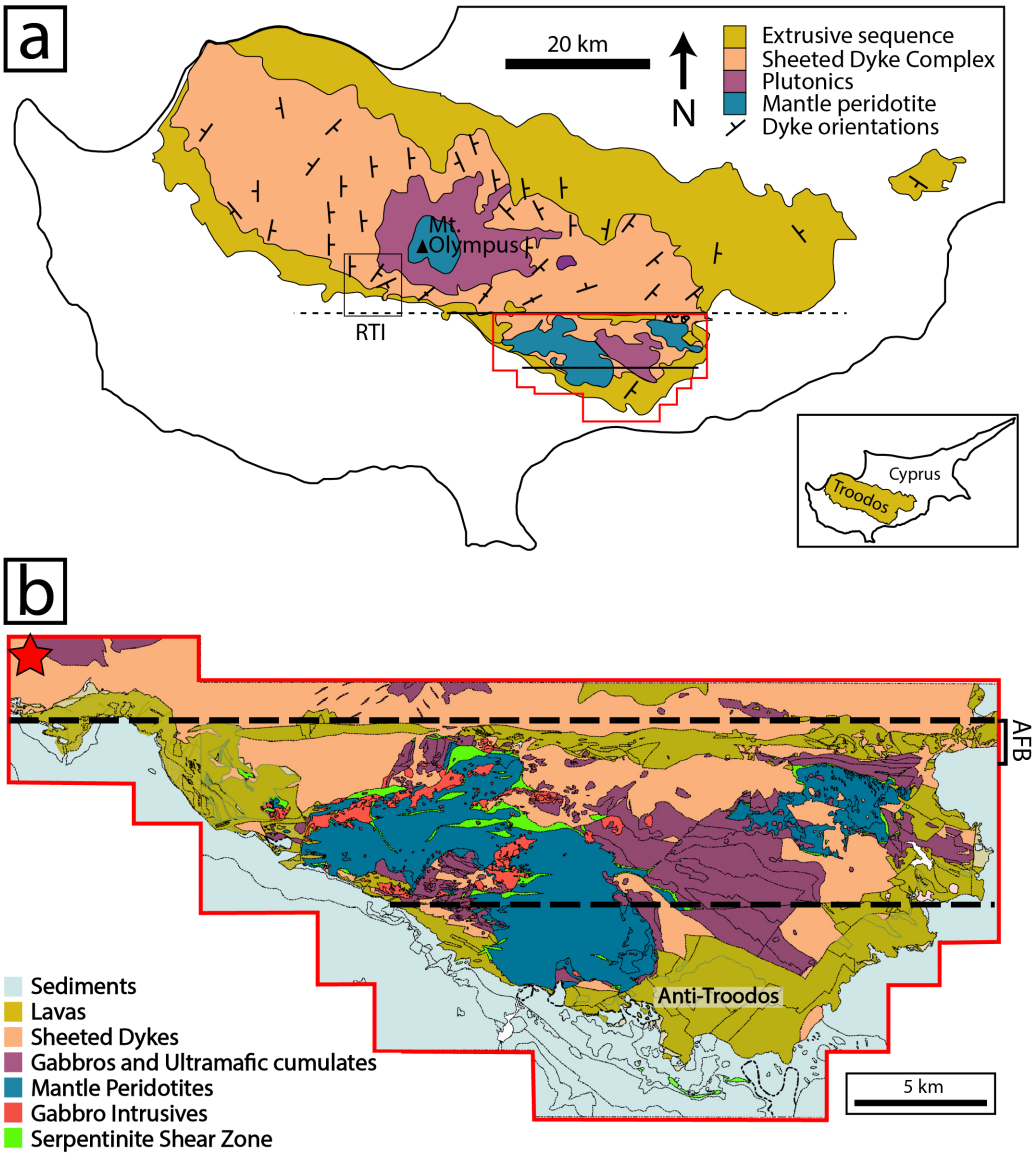


**Figure 4.1:** (a) Simplified geological map of the Troodos Ophiolite, Cyprus, including regional dyke orientations (after Fagereng and MacLeod, 2019). The location of the Southern Troodos Transform Fault Zone is shown by the red box. RTI - ridge-transform intersection from MacLeod *et al.* (1990). (b) Simplified geological map of the Southern Troodos Transform Fault Zone. 'Anti-Troodos' refers to a fragment of non-transform-tectonised crust identified as lying to the south of the transform fault zone (MacLeod *et al.*, 1990). AFB = Arakapas Fault Belt. Location of Fig. 2 is shown by the red star.

initial N-S or NW-SE) at the inside corner of the ridge-transform intersection associated with drag along the transform fault (MacLeod *et al.*, 1990; MacLeod and Murton, 1995). Palaeomagnetic evidence from sites in the Limassol Forest Complex argue for substantial clockwise rotations (up to ∼150°) about steeply plunging axes (Gass *et al.*, 1994; MacLeod, 1988). The faults in this region are dominantly dyke margin-parallel with some faults along joints (Fagereng and MacLeod, 2019). Dyke margin-parallel faults typically contain sub-horizontal lineations that indicate strike-slip kinematics (Fig. 4.2). A small number of normal faults are also documented in the area. Despite being slightly north of the main transform tectonised zone (red star in Fig. 4.1b), the area near Moniatis offers an insight into the relationship between the types of faulting, that deformed under comparable $P$-$T$ conditions and the same deformation style as the STTFZ, at the hundreds of metres to kilometre-scale that is missing within the main STTFZ because of a lack of outcrop continuity. The fault rocks in the village of Moniatis are thought to record comparable deformation processes, albeit at lower bulk strains, to those operating widely within the STTFZ itself.

## 4.4 Results

### 4.4.1 Deformation of sheeted dyke complex

The sheeted dyke stratigraphic layer is the most extensively exposed layer of the Troodos ophiolite's mafic crust in the STTFZ, and displays substantial deformation. Outcrop studies across the STTFZ conducted here, coupled with 1:2000 scale mapping of an ∼2 km$^2$ area in the village of Moniatis (Fig. 4.2a), reveal the heterogeneous nature of deformation within the sheeted dykes. Deformation of the sheeted dolerite dykes can be classified into four deformation facies (Fig. 4.3) at the mesoscale including relatively intact sheeted dykes (pervasively cut by rectilinear cooling joints), crackle breccias, cemented breccias and fault gouges. Below we define each fault rock type by describing microstructures and mesoscale observations, before describing the distribution of these fault rocks. Microscopic observations were made using an optical microscope on samples that were set in epoxy resin before being cut perpendicular to the foliation and parallel to the shear direction. Sample descriptions and

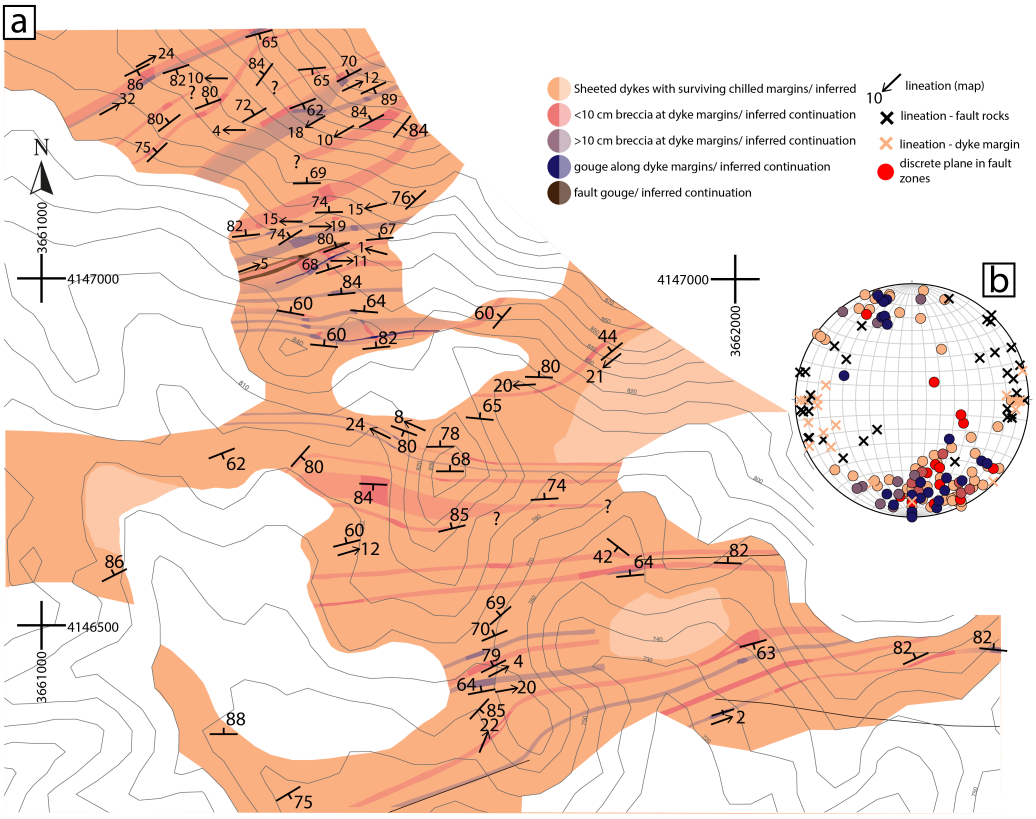


**Figure 4.2:** (a) Detailed geological map (WGS84) of the area near the village of Moniatis highlighting the anastomosing nature and variable distribution of fault rocks. Lightly shaded areas are inferred continuations based on limited outcrops. (b) Lower hemisphere, equal area stereonet showing orientations of dyke margin faults and striations. Filled circles are poles to planes following the same colour scheme as the map in (a).

locations can be found in Appendix A.

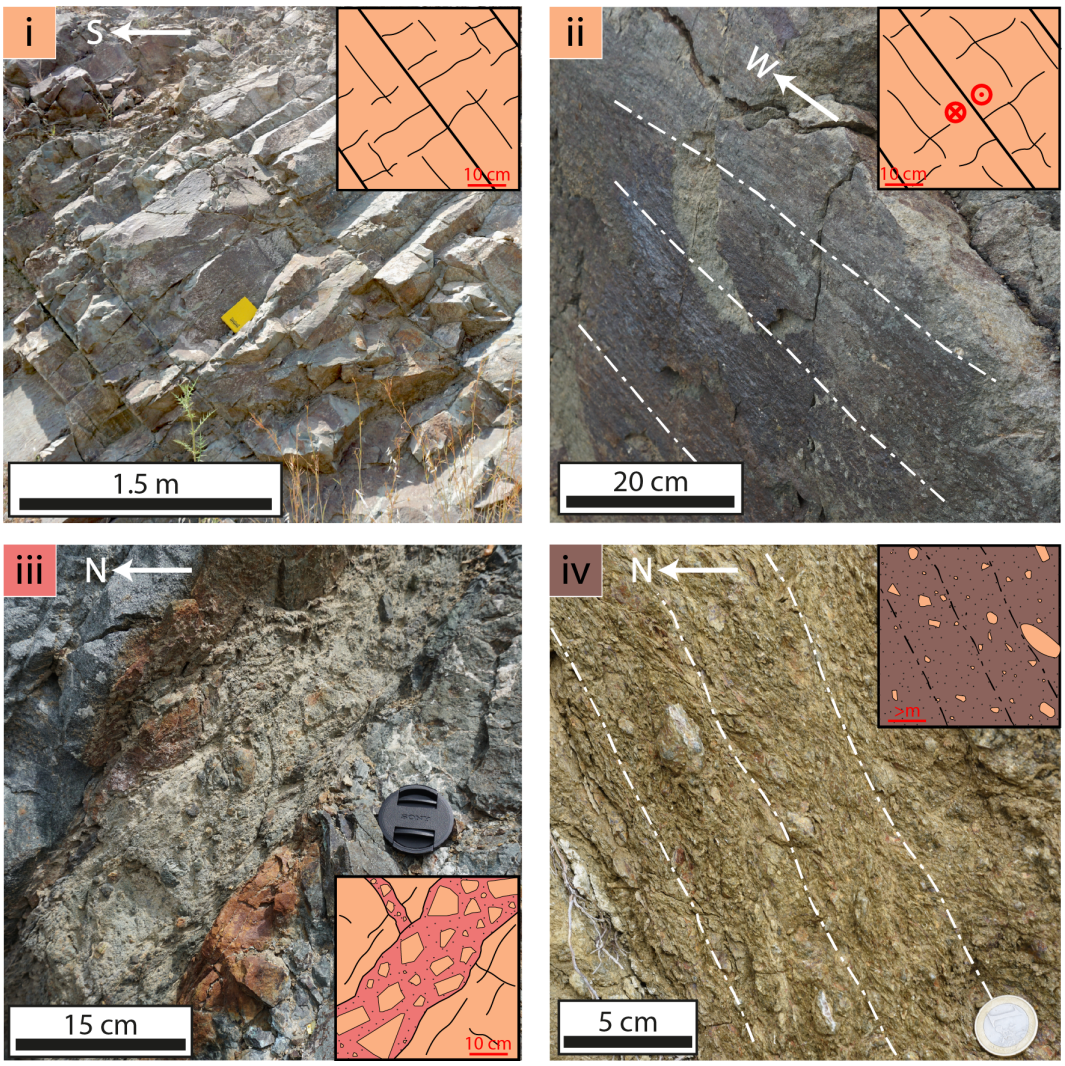


**Figure 4.3:** Descriptive classification of deformation facies observed within the sheeted dykes within the Southern Troodos Transform Fault Zone and Moniatis, with schematic representation of (i) intact sheeted dykes (34.8751°N 32.8906°E), (ii) reactivated dyke margin with striations in crackle breccia (34.8769°N 32.8889°E), (iii) cemented breccia (34.8765°N 32.8899°E) and (iv) foliated fault gouge (34.8503°N 33.0651°E). Colours as in Fig. 4.2.

### Description and classification of fault rocks

The fault rocks are defined at the mesoscale (tens of centimetres to metres), and over larger distances multiple fault rock types occur together within larger scale fault zones. A defining factor of the classification of fault rocks is the proportion of clasts within the fault rock, where a clast is defined as material with the same microstructural fabric as undeformed dolerite dykes. The clas-

sification of the four fault rock types in the sheeted dolerite dykes follows that of Woodcock and Mort (2008).

(i) Intact sheeted dykes (Fig. 2.6c-d and 4.3i) consist of tabular dykes that are usually <2 m wide. The dykes contain cooling joints parallel and perpendicular to their chilled margins. They are mostly aphyric dolerites, originally comprising plagioclase and clinopyroxene. However, they experienced pervasive hydrothermal alteration at greenschist facies conditions to form an assemblage dominated by albite, chlorite, epidote and actinolite. Locally, minor malachite, epidote, quartz and pyrite are also present. The intact dykes usually lack any internal transform-related deformation, however, dyke margins may locally record gently plunging slickenlines to the E or W that are consistent with STTFZ kinematics. These margins record dyke margin-parallel discrete slip without the formation of any fault rock.

(ii) Crackle breccias (Fig. 4.3ii) are defined by nearly 100% clasts separated by fractures and form fault zones at the scale of individual dykes. They are recognised by fractures, in addition to primary cooling fractures, parallel and perpendicular to the dyke margins, that result in the formation of large, angular clasts that have experienced little rotation with respect to one another. This gives the appearance of a densely fractured dolerite dyke that retains its tabular nature. The primary cooling fractures and dyke margins commonly show evidence of fault slip in the form of gently plunging slickenlines.

(iii) Cemented breccias (Fig. 4.3iii) are indurated, clast-supported (>50%) breccias. The dolerite clasts are unsorted (millimetre to metre-sized), angular to sub-rounded and set within a fine-grained matrix (Fig. 4.4a-b and 4.5a). The matrix of these breccias is mineralogically similar to clasts (±quartz), albeit more finely grained, having appeared to have experienced the same greenschist facies alteration as the dolerite clasts (Fig. 4.4b).

(iv) Fault gouge (Fig. 4.3iv) refers to faults that have <<50% rounded, isolated dolerite clasts that are typically centimetre-sized or smaller set within a chlorite-rich matrix. Locally clasts >10 cm are present. Optical microscope observations show minor quartz (<5 mm) and calcite ($\leq$100 $\mu$m) throughout the chlorite-rich gouges (Fig. 4.4c-d). The fault gouge commonly contains a foliation in the form of a macroscopic scaly fabric defined by an intense shape preferred orientation (SPO) of aligned chlorite minerals (Fig. 4.4c-d and Fig. 4.5d). Fault gouges can form as anastomosing seams (less than centimetre

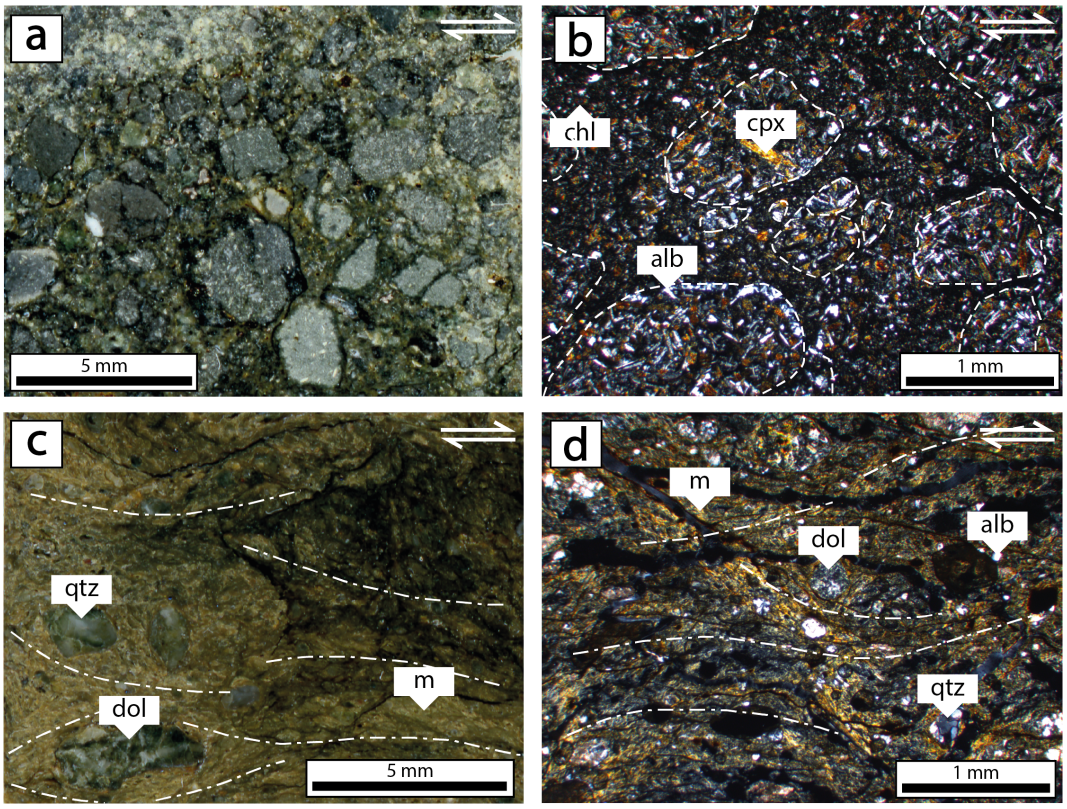


**Figure 4.4:** Photomicrographs of cemented breccias and fault gouges. (a) Reflected light image of cemented dolerite breccia (18CS25), (b) cemented dolerite breccia in cross polarised light with clasts highlighted by a dashed line (18CS25). The matrix and clasts comprise the same mineral assemblage and differ in grain size. (c) Foliated fault gouge (19CS11) in reflected light and (d) in cross polarised light. Traces of the foliation, that is locally quite variable around clasts, are highlighted by dashed white lines in (c) and (d). alb - albite, chl - chlorite, cpx - clinopyroxene, qtz - quartz, dol - dolerite clast, m - chlorite-rich matrix.

thick; Fig. 4.5b-c) or in broad fault zones (up to ∼10 m thick; Fig. 4.5d). Locally polished, slickensided surfaces are steeply dipping with gently plunging lineations, consistent with STTFZ-related kinematics.

### "End-member" fault zone types

Three main "end-member" fault zone types within the STTFZ are recognised: (1) distributed fault zones where dykes remain relatively intact; (2) breccia-dominated fault zones and (3) gouge-dominated fault zones.

In the wide, distributed fault zones, cemented breccias are very common (Fig. 4.2a) and typically found making up ∼10-20 cm thick fault zones adjacent to dyke margins and cooling joints (Fig. 4.3iii). At the outcrop scale many adjacent dyke margins can be sheared and, locally, cemented breccias


**Figure 4.5:** Field photos of (a)-(c); large breccia-dominated fault zone near Vavla (34.8408°N, 33.2639°E) with discrete chlorite-rich planes (b and c) and (d); Gouge-dominated fault zone near Arakapas village (34.8503°N, 33.0651°E) with a well-foliated chlorite-rich gouge (inset). (c) and (d) are looking at a vertical plane, along direction of shearing.

also cross-cut dykes. The result of this is tens of metres wide, distributed fault zones containing anastomosing breccias that separate internally coherent dyke fragments. In places, chlorite-rich fault gouges fill the narrow, tens of centimetres-wide fault zones parallel to dyke margins.

Breccia-dominated fault zones are present throughout the STTFZ (e.g. Fig. 4.5a), and are up to ∼10 m thick. The full extent of individual fault zones is unknown as they are constrained by the continuity of outcrop. These breccia-dominated fault zones rarely preserve identifiable dyke margins within

the breccia zones and are commonly parallel to dyke margins, especially in the area near Moniatis (Fig. 4.2). While the sheeted dykes are, in bulk, weaker parallel to their margins, we recognise that dyke margins are not always rotated to parallelism with the transform, in these cases faults may initiate along surfaces other than dyke margins such as variably oriented cooling joints. The broad breccia-dominated fault zones contain localised, centimetre-scale, chlorite-rich seams (Fig. 4.5a-c), which form anastomosing bands that mimic the larger scale fault geometry. These localised chlorite-rich seams typically display low-angle slickenlines consistent with STTFZ kinematics. Surrounding these chlorite-rich seams, matrix-rich fault rocks progressively transition over $\sim$<50 cm into more clast-rich breccias (Fig. 4.5c).

In contrast to breccia-dominated fault zones, in which fault gouges form narrow anastomosing bands only, gouge-dominated fault zones contain fault gouge ($\pm$foliation) spanning $\sim$1-10 m thick (e.g. Fig. 4.5d). No dyke margins are preserved within these gouge-rich zones. Individual gouge-dominated faults can be traced along strike up to $\sim$20-30 m in the field, a minimum length constrained by outcrop continuity. Gouge-dominated fault zones contain anastomosing strands of intense grain-size reduction (Fig. 4.5d). Breccias are usually located along the edges of these faults, defining a damage zone up to $\sim \pm$5m metres away from the fault zone.

### 4.4.2 Clast size analysis of Southern Troodos Transform Fault Zone fault rocks

#### Methods

Clast size analysis and fractal distributions have long been used as a way of reflecting the variety of geological conditions, deformation styles and material behaviour in many geological materials (e.g. Blenkinsop, 1991; Turcotte, 1986a; Zhong Yan *et al.*, 1990). Clast size analysis was performed on the various fault rock types identified within the STTFZ at outcrop and thin section scale, based on high-resolution photos and photomicrographs of the different fault rocks. The sizes of >100 clasts (defined in 4.4.1) for individual samples were measured where possible (Table 4.1) using 2D image analysis in ImageJ (FIJI) version 2.0.0. In two samples (m and o), identified as crackle breccias, fewer clasts were measured because of their larger clast sizes. Sample photos were digitised in

Adobe Illustrator by manually outlining clasts. Clast long (p) and short (q) axes were automatically measured in ImageJ assuming a best-fit ellipse for each clast. To avoid a sample bias, all whole clasts inside the defined areas (1 $m^2$, 100 $cm^2$ and 10 $cm^2$) used to calculate the particle size distribution were analysed. Photos were usually taken of a plane perpendicular to the foliation, looking along the shear direction (i.e. looking at the YZ kinematic plane) because of the limitation of outcrop orientation. However, where possible, photos as well as measurements made on thin sections were taken in map view (i.e. looking at the XZ kinematic plane in the Y direction).

| Sample | Fault rock type | Size of area considered | Number of clasts | Area % of clasts | Range in $r$ (mm) | Fractal range (mm) | $Ds$ | Standard error in $Ds$ | $R^2$ |
|---|---|---|---|---|---|---|---|---|---|
| **A** | breccia | Centimetre | 724 | 47.9 | 5.26 | 0.85 | 1.32 | 0.017 | 0.994 |
| **B** | gouge | Decimetre | 236 | 34.5 | 86.39 | 24.91 | 1.71 | 0.047 | 0.995 |
| **C** | gouge | Decimetre | 257 | 39.7 | 28.87 | 3.28 | 1.75 | 0.039 | 0.993 |
| **D** | breccia | Decimetre | 439 | 56.8 | 33.02 | 6.30 | 1.60 | 0.031 | 0.992 |
| **E** | breccia | Decimetre | 330 | 27.5 | 13.75 | 2.09 | 1.49 | 0.030 | 0.992 |
| **F** | breccia | Decimetre | 414 | 49.6 | 21.54 | 7.04 | 1.35 | 0.011 | 0.999 |
| **G** | breccia | Decimetre | 433 | 49.0 | 20.62 | 2.09 | 1.68 | 0.034 | 0.992 |
| **H** | breccia | Decimetre | 439 | 65.2 | 90.50 | 11.00 | 1.62 | 0.027 | 0.997 |
| **I** | breccia | Decimetre | 261 | 24.2 | 106.00 | 31.50 | 1.45 | 0.036 | 0.994 |
| **J** | gouge | Decimetre | 312 | 10.8 | 77.00 | 23.00 | 1.81 | 0.150 | 0.980 |
| **K** | breccia | Decimetre | 809 | 47.0 | 107.50 | 43.50 | 1.52 | 0.026 | 0.993 |
| **L** | gouge | Decimetre | 455 | 15.0 | 22.48 | 7.09 | 1.97 | 0.019 | 0.999 |
| **M** | crackle breccia | Decimetre | 51 | 76.8 | 24.00 | 6.00 | 1.16 | 0.077 | 0.991 |
| **N** | breccia | Metre | 351 | 48.8 | 683.10 | 80.45 | 1.41 | 0.016 | 0.998 |
| **O** | crackle breccia | Metre | 25 | 97.2 | 827.00 | 31.00 | 1.09 | 0.112 | 0.987 |

**Table 4.1:** Tabulated particle size distribution data for fault rocks from the Southern Troodos Transform Fault Zone

Cataclasis (section 1.3.3) is a fundamental process in brittle faults and constrained comminution is the most widely accepted mechanism by which cataclasis occurs. Constrained comminution is a process whereby clasts fracture when they are surrounded by clasts of a similar size through stress bridges (Sammis *et al.*, 1987, 1986). Because of this mechanism, it has been argued that the distribution of clast sizes within a fault deformed by cataclasis should fit a power law distribution (Sammis *et al.*, 1987). Analysing power law distributions has become a widely accepted way to compare fault rocks (e.g. An and Sammis, 1994; Blenkinsop, 1991; Heilbronner and Keulen, 2006; Keulen *et al.*, 2007; Marone and Scholz, 1989; Monzawa and Otsuki, 2003; Sammis and Biegel, 1989; Steacy and Sammis, 1991). However, a recent review by Phillips and Williams (2021) concluded that in 91% of naturally and experimentally deformed fault rocks, the clast size distribution is not best described with the power-law distribution (constrained comminution) and that a log-normal distribution was a better fit. To compare our samples with past studies on fault rocks, the cumulative frequency of clast sizes was fitted using the power-law relationship: $N(r) \propto r^{-Ds}$, where, $r$ and $N(r)$ are the clast size (mm) and number of clasts larger than $r$, respectively, and $Ds$ is the fractal dimension (Mandelbrot, 1982; Turcotte, 1986b, 1989). For this study, $r$ is described as the arithmetic mean of the long and short axis of each clast, and log-log plots of $N(r)$ vs. $r$ are presented. Reported errors in $Ds$ are standard errors of regression to 95% confidence intervals. To determine whether a power-law distribution is the best fit to the clast size distributions, all samples in this study were also fitted to a log-normal distribution (see Appendix B).

The $Ds$ values in this study are recorded as the 2D fractal dimensions. 2D $Ds$ values can be converted to their 3D values by adding 1 (assuming that the orientation of the 2D section does not influence this), likewise, any values taken from studies where $Ds$ is reported in 3D can be converted to 2D by subtracting 1 (Sammis *et al.*, 1987). The reason 2D values diverge from their 3D counterpart is because there is likely to be a bias towards smaller clasts when working in 2D. This is because a 2D section through non-spherical particles will tend to underestimate clast dimensions (Blenkinsop, 1991; Exner, 1972).

### Clast size analysis of variable deformed fault rocks

A drop-off relative to a power-law distribution occurs towards the largest clast sizes, which can be explained by the presence of only a few large clasts whose size approach the scale of the sample (e.g. Blenkinsop, 1991; Hisada, 2004). Likewise, a 'roll-off' effect is seen at small values of $r$, a phenomenon explained by the smallest clasts being overlooked, counted as matrix or below the resolution of the image (e.g. Blenkinsop, 1991). Therefore, the largest and smallest values of $r$ are omitted in the analysis, and the data between the roll-off at small and large values are used. This is known as the fractal range. A straight line is fitted to the fractal range in log-log space, aiming for at least half of the clast size range, and used to calculate $Ds$. In all samples, from thin section to outcrop scale, the data fall on a straight line in a $log_{10}N(r)$ vs. $log_{10}r$ plot (e.g. Fig. 4.6) meaning the clast-size distribution is well described by a power law over the considered range in $r$ for each sample. For most samples analysed in this study we find a power law distribution provides a better fit to the data (greater $R^2$ value) compared with a log-normal distribution (see Appendix B), which also fits well. The linear correlation between $log_{10}N(r)$ and $log_{10}r$ is good in all samples from thin section to outcrop scale (Fig. 4.6b-c), with $R^2$ values greater than 0.980 and standard errors of regression calculated to 95% confidence <0.15, usually <0.08 (Table 1).

$Ds$ varies between the fault rock types ($1.09 \leq Ds \leq 1.97$) (Fig. 4.6). Crackle breccias have the lowest values ($Ds < 1.3$), cemented breccias have $Ds$ in the range 1.3-1.7 with an average of 1.52, while fault gouges have the highest recorded $Ds$ values up to 1.97, (average $Ds > 1.7$). Fault gouges also have the lowest proportion of dolerite clasts (Fig. 4.6a) with proportions as low as 11%. In contrast, low $Ds$ values are associated with the highest proportion of, and largest, clasts (>75%; Fig. 4.6a).

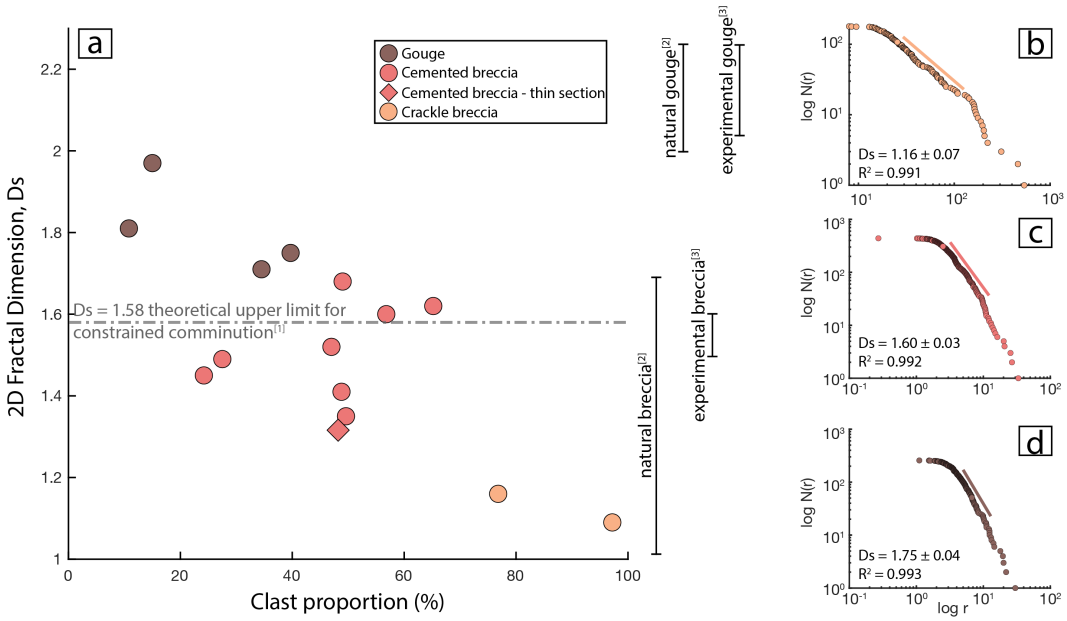


**Figure 4.6:** (a) Plot showing $Ds$ values of the various different fault rocks within the sheeted dykes. [1]Sammis *et al.* (1987), [2]Heilbronner and Keulen (2006), [3]Keulen *et al.* (2007). Example $\log_{10}N(r)$ vs. $\log_{10}r$ plots for (b) crackle breccia (c) cemented breccia and (d) a fault gouge.

### Inter-outcrop variation in the clast size distribution

Sketches based on a photomosaic of a gouge-dominated fault zone and on photos of a breccia-dominated fault zone show a range of clast proportions and sizes between localities (Fig. 4.7 and 4.8). Calculating $Ds$ from 1 m$^2$ boxes along a transect through a gouge-dominated fault zone shows that $Ds$ values vary across the fault zone (Fig. 4.7). Towards the margins $Ds$ is lower and comparable to values associated with crackle breccias (1.09-1.24). However, $Ds$ generally increases towards values in the range of 1.31-1.54 and up to 1.88 within the main fault zone (Fig. 4.7). These values reflect those associated with STTFZ cemented breccias and fault gouges, respectively (Fig. 4.6). Localised, anastomosing bands of more fine-grained material are present throughout fault exposures. These bands, which are no more than ∼10 cm thick, are below the scale used to determine the particle size distribution of the fault zone. The particle size distribution of these bands was calculated using a separate high-resolution photo and indicates $Ds$ values up to 1.97 (Fig. 4.7c).

Breccia-dominated fault zones have average $Ds$ values of 1.52 at the outcrop

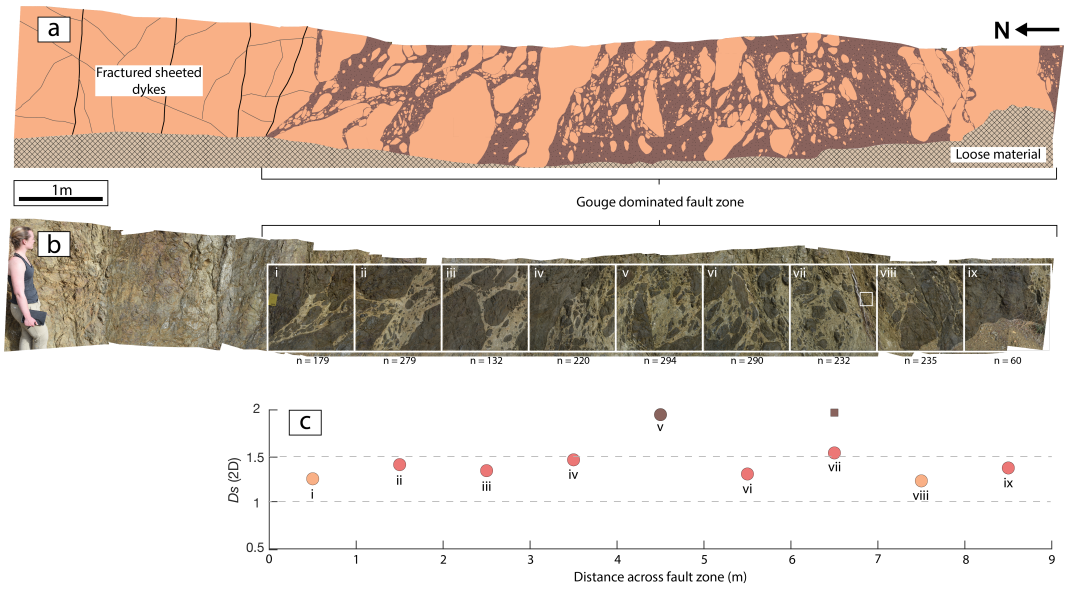


**Figure 4.7:** (a) Sketch and (b) photomosaic of a gouge-dominated fault zone (34.8503°N, 33.0651°E). Small white box in vii shows the location of the area used to calculate $Ds$ for a localised zone within the fault zone (shown by the brown box in c). (c) 2D fractal values across the fault zone calculated from 1m$^2$ areas starting adjacent to the wall rock/intact sheeted dykes (0 m). Colour scheme as in Fig. 4.6.

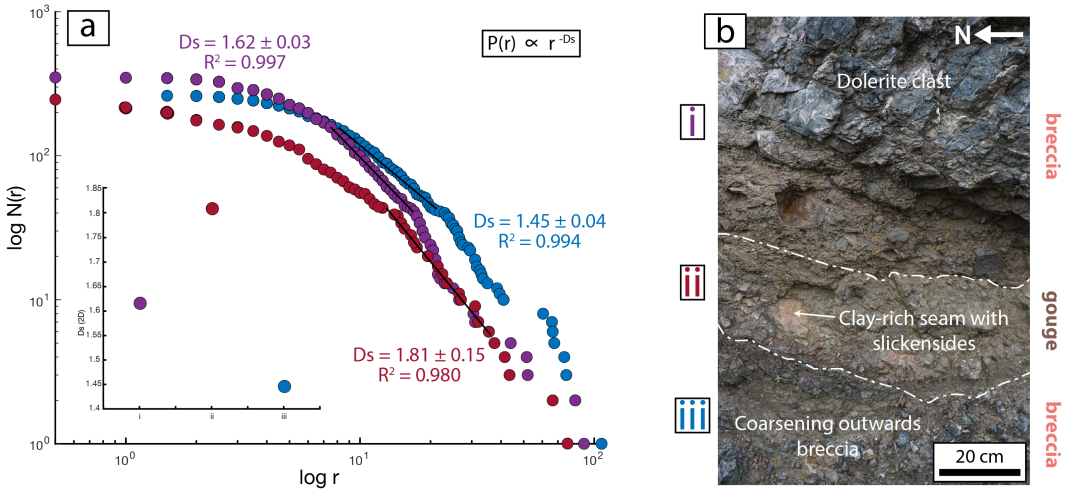


**Figure 4.8:** (a) Log $N(r)$ vs. log $r$ plot for the distance across a discrete plane within a breccia-dominated fault zone (34.8411°N 33.2622°E). $Ds$ increases towards the chlorite-rich seam, reflecting the relative increase in number of small clasts within the chlorite-rich zone compared to the surrounding breccia shown in (b).

scale. However, these fault zones contain discrete chlorite-rich seams (Fig. 4.5a; zone marked in Fig. 4.8b) the $Ds$ values of which deviates from this average. Towards the core of these chlorite-rich seams, the clast size and

proportion of dolerite in these breccias reduces. This is coincident with an increase in $Ds$ over a ∼20 cm wide zone from 1.45-1.62 in the breccias to 1.81 in the chlorite-rich seams (Fig. 4.8).

## 4.5 Discussion

### 4.5.1 Initiation of faults and their structural evolution

Geological mapping (Fig. 4.2) shows that deformation within the sheeted dykes was heterogeneous across all scales within the upper crust of the transform domain. At the kilometre-scale, deformation is concentrated into anastomosing fault strands (e.g. Faulkner *et al.*, 2003), which themselves contain variably deformed dolerite (e.g. Fig. 4.7 and 4.8).

From the various fault rocks documented within the STTFZ (crackle breccia, cemented breccias and fault gouges), the mafic crust is proposed to deform progressively. Slickensided surfaces with gently-plunging lineations indicate small-displacement strike-slip faulting along pre-existing dyke margins and cooling joints. Crackle breccias have low $Ds$ values (<1.3; Fig. 4.6), characteristic of rocks that have experienced small-displacements and low degrees of fragmentation and sliding (e.g. Storti *et al.*, 2003).

In contrast, the lower clast:matrix ratios (Table 1) and higher $Ds$ values (1.32-1.68; Fig. 4.6) of clast-supported breccias are consistent with faults that have experienced additional displacement and deformation. $Ds$ values for clast-supported breccias are similar to those theoretically derived value for deformation by constrained comminution ($Ds$ = 1.58; Sammis *et al.*, 1987) and to clast size distributions in natural fault breccias (e.g. An and Sammis, 1994; Blenkinsop, 1991; Heilbronner and Keulen, 2006; Keulen *et al.*, 2007; Marone and Scholz, 1989; Monzawa and Otsuki, 2003; Sammis and Biegel, 1989; Steacy and Sammis, 1991). This suggests that a transition from crackle to clast-supported breccias is controlled by continued cataclasis and constrained comminution.

Fault gouges have the largest $Ds$ values >1.7 (Fig. 4.6) and matrix proportions suggesting they are the most mature fault rocks and likely form in high-displacement faults. Continued cataclasis and grain-size reduction during progressive deformation can explain increasing matrix proportion in fault

rocks, eventually resulting in the formation of fault gouges. This is consistent with past field, theoretical and experimental studies (e.g. Engelder, 1974; Marone and Scholz, 1989; Sammis *et al.*, 1987). $Ds > 1.58$, i.e. larger than what is expected from grain-size reduction by comminution alone (Marone and Scholz, 1989; Sammis *et al.*, 1987), suggests that additional deformation mechanisms played a role in the deformation of the most mature faults. Abrasion (grain rolling and chipping) of larger clasts floating within a matrix can explain an increase in the smallest clasts to give values of $Ds$ >1.58 (e.g. Blenkinsop, 1991; Marone and Scholz, 1989). In clast-supported fault rocks abrasion is usually a negligible process because clasts are unable to move past one another. It is only thought to become an important process when clasts collide during shear within a well-interconnected matrix (Billi and Storti, 2004).

The volume proportion of chlorite in fault gouges is far higher (up to ∼70%) than that in the hydrothermally altered dolerite (5-10% chlorite) (Fig. 4.4c-d). Therefore, deformation may have involved the syn-kinematic alteration of hydrothermally-altered dolerite to form chlorite (e.g. Holdsworth *et al.*, 2001; Imber *et al.*, 2008). Conversely, the high proportion of chlorite in fault gouges may be linked to a compositional difference in the starting material. Either way, deformation of fault gouges is therefore controlled by a phyllosilicate-dominated rheology. Fault gouges are usually foliated (Fig. 4.3iv and 4.4c-d). Foliations could have formed in one of two ways depending on when the chlorite formed: (1) growth in a preferred orientation during deformation or (2) rotation of pre-existing chlorite. Fault gouges with similar foliations formed in laboratory experiments at slow slip speeds (<1 $\mu$m/s; Niemeijer, 2018; Niemeijer and Spiers, 2006). Foliated fault gouges deform by sliding along the foliation and chlorite basal planes (e.g. Collettini *et al.*, 2011, 2009; Smith *et al.*, 2011) since the ease of slip along chlorite grains is efficient enough to minimise fracturing of dolerite clasts (± pressure solution of hard clasts). Slickenlines on chlorite foliation surfaces are gently-plunging and sub-parallel to the main E-W transform trend, and therefore support that these surfaces accommodated transform displacement.

Within the STTFZ, $Ds$ varies across the strike of individual fault zones (Fig. 4.7 and 4.8). Variation in $Ds$ across a fault zone has been documented several times before. For example, Muto *et al.* (2015) and Storti *et al.* (2003) identify an increase from the wall-rock and damage zone adjacent to the fault,

to the fault core, suggesting strain localises into phyllosilicate-rich fault cores and produces the most evolved fault rock (high $Ds$). However, within the STTFZ, the variation in $Ds$ is much more variable across individual faults at the outcrop scale, which is consistent with faults accommodating a broad distribution of strain and subsequently comprising different fault rocks that are at different stages of deformation.

A relationship between fracture energy, $E$, and clast size distribution can be derived from the energy-size relationship: $E \propto R^{Dr-3}$ (Muto *et al.*, 2015). This indicates that $E$ increases with the fractal dimension of the fracture surface, $Dr$, which in turn can be related to $Ds$ by the following equation: $2Dr = Ds+3$ (Muto *et al.*, 2015; Nagahama and Yoshii, 1993). Therefore, $E$ increases with $Ds$. Following this logic, the increase in $Ds$ from crackle breccia to fault gouge requires an increase in cumulative fracture energy with displacement. However, this records the cumulative energy from the total displacement, so it remains unknown how many earthquake cycles at what magnitude earthquakes are required to create each fault rock.

### 4.5.2 Fault zone permeability

STTFZ faults go through a progressive deformation sequence from fractured dolerite (crackle breccias) through breccias that can be cemented and eventually chlorite-rich fault gouges. Fault zones commonly comprise multiple fault rocks, each at different stages of their progressive evolution and therefore the permeability of these faults is likely to change through space and time.

Evidence of fluid flow within the sheeted dykes is ubiquitous, with dolerite dykes being pervasively hydrothermally altered at greenschist facies conditions to albite, actinolite and chlorite. Hydrothermal mineralisation forming quartz, malachite, epidote and pyrite along dyke margins and cooling joints is common. These observations indicate that pre-existing dyke margins and cooling joints acted as conduits for fluid flow within the mafic crust. This pre-existing fracture density is increased during brittle deformation and cataclasis, creating more permeable pathways in crackle and clast-supported breccias (pre-cementation). Cementation of breccias, in contrast, reduces permeability. Fine-grained chlorite within fault gouges is well interconnected. Well-interconnected phyllosilicates are known to have low permeability, and foliated phyllosilicates smear out during continued deformation (e.g. Caine *et al.*,

1996). Therefore, brittle fracture, cementation and the formation of impermeable foliations are competing processes that generate and destroy permeability, respectively (Tenthorey *et al.*, 2003).

Low $Ds$ values imply that the packing properties of large clasts control the fault rock microstructure, favouring high porosity and permeability (e.g. Storti *et al.*, 2003). Conversely, the increased $Ds$ values that are characteristic of more mature fault rocks imply smaller grain sizes with better packing properties, which also leads to reduction of porosity and destruction of permeability. This in turn suggests that permeability is reduced in more mature fault rocks by grain-size reduction. The reduction in permeability in more mature fault rocks is also related to the fracture density in phyllosilicate-rich gouges being low compared to that of the fractured dolerite (e.g. Chester *et al.*, 1993). As a result, phyllosilicate-rich fault gouge permeability appears to be controlled by grain-scale permeability of phyllosilicates rather than the fracture permeability of dolerite (Caine *et al.*, 1996).

It may be concluded that the permeability, and likely pore fluid pressure, of crustal oceanic transform faults must vary both spatially and temporally. Such variations may be controlled by fault zone damage and the formation of foliations, with different fault rocks having different permeability structures, comparable to continental structures such as the Median Tectonic Line (Jefferies *et al.*, 2006).

### 4.5.3 Formation of broad fault zones

Deformation is inferred to have initiated along dyke margins and cooling joints and continued deformation of these resulted in the development of faults containing breccias or gouges. There are two end-member fault types observed within the STTFZ that form broad fault zones documented within the STTFZ mafic crust (Fig. 4.5): (1) gouge-dominated faults and (2) breccia-dominated faults.

Laboratory experiments commonly suggest chlorite-rich gouges are strain-hardening and have velocity-strengthening behaviour as deformation progresses (Morrow *et al.*, 1992, 1982; Rutter, 1986). Therefore, a localised, but strain-hardening, chlorite-rich fault zone may grow outwards into its damage zone, if the damage zone (i.e. fractured dolerite) is sufficiently permeable to allow sufficient fluid flow for the alteration of mafic minerals to chlorite, allowing

widening of the gouge-dominated fault zone.

Early- to intermediate-stage faults are inferred to form as discrete slip or breccias parallel to individual dyke margins, but macroscopically, many adjacent dyke margins could be sheared in this way, distributing the deformation over zones at least tens of metres wide (Fig. 4.2a). Therefore, individual localised fault zones adjacent to dyke margins could grow through the amalgamation of several less-mature anastomosing faults, as they each grow into their respective damage zones and merge, similar to above involving one strand, and to the broad anastomosing fault model of Faulkner *et al.* (2003).

Gouge-dominated fault zones (Fig. 4.5d) develop if the growth and amalgamation of the initially localised faults is efficient. However, if the gouge remains localised (e.g. Fig. 4.5a-c), a breccia-dominated fault could form. In such cases breccia-dominated faults may represent an earlier stage of deformation, in which interconnected gouge has not yet formed. Alternatively, breccia-dominated faults may form by the amalgamation of several damaged dykes, with little associated gouge formation but with cementation that is later cut by localised chlorite-rich faults. This contrasts with the model above, in which chlorite-rich seams are earlier features that form parallel to dyke margins or cooling joints rather than as later features through a cemented breccia.

### 4.5.4 Mechanical analysis of crustal faults

Based on tectonic reconstructions, the sheeted dolerite dykes within the STTFZ deformed at depths $\sim\leq$2 km within the active strike-slip domain of an oceanic transform fault zone (Gass *et al.*, 1994). Hydrothermal alteration and mineralisation (chlorite, epidote, actinolite, quartz etc.) suggest this deformation took place at temperatures within the range of greenschist facies conditions. Since temperatures associated with greenschist facies conditions fall within the thermally defined seismogenic zone (nominally inferred to be constrained to 600 °C for the oceanic lithosphere; section 1.7.1), coupled with the depth reconstructions, we can expect that the sheeted dolerite dykes within the STTFZ were within the shallow brittle lithosphere. Laboratory measurements of the frictional strength of greenschist facies altered oceanic dolerites at low $T$ indicate that these rocks are strong: direct-shear friction experiments in Chapter 5 show that the friction coefficient, $\mu = 0.69$.

Observed faults within low- to medium-strain within the sheeted dolerite

dyke complex are normally parallel or sub-parallel to dyke margins and/or joints, which can be sub-parallel to the main STTFZ. This poses the problem that the orientation of these pre-existing planes and the STTFZ are unfavourably oriented to the theoretical maximum principal stress ($\sigma_1$) if considering Anderson's theory of faulting. Typically, the minimum principal stress ($\sigma_3$) is considered perpendicular to mid-ocean ridges to allow spreading (E-W in present day coordinates for Troodos; section 2.1.3), making it approximately parallel to the strike of the oceanic transforms. Consequently, $\sigma_1$ is approximately perpendicular to it the transform, as $\sigma_2$ is vertical in Andersonian strike-slip faulting. Therefore, the principal stress orientations of oceanic transform faults are not favourable and these faults must be weak, or stress is not Andersonian, or slip occurs on planes with a different orientation from the main fault zone. However, from focal mechanisms, we know that earthquakes (Mw >6 ) often slip along faults that are parallel to sub-parallel with the main oceanic transform (e.g. Abercrombie and Ekström, 2001; Froment *et al.*, 2014; McGuire *et al.*, 2005). Slip along many plate boundary transform faults such as the San Andreas Fault (Townend and Zoback, 2004; Zoback, 1991) and Tjörnes Fracture Zone, Iceland (Angelier *et al.*, 2000; Homberg *et al.*, 2010), that are poorly oriented, has been explained by frictional weakness in previous studies ($\mu$ <<0.6).

Progressive deformation of dykes forms chlorite-rich foliated fault rocks. Previous laboratory friction experiments show $\mu$ ~0.3 for chlorite under a wide range of $P$-$T$ conditions (Fagereng and Ikari, 2020; Okamoto *et al.*, 2019), and experiments conducted here (reported in Chapter 5) on chlorite-dominated fault-gouge material from the STTFZ show a residual steady-state frictional strength of 0.25 (Chapter 5). Therefore, the occurrence of foliated chlorite acts as an effective weakening process of individual fault strands within the STTFZ on the condition that chlorite minerals become well-interconnected (e.g. Handy, 1990; Holdsworth *et al.*, 2001; Imber *et al.*, 2008; Wintsch *et al.*, 1995).

$\theta$ describes the angle between $\sigma_1$ and a fault, measured in the plane normal to $\sigma_2$. Well-oriented faults with Byerlee friction have $\theta$ ~30° (Sibson, 1985). Therefore, faults with a high $\theta$, such as oceanic transform faults, are considered poorly oriented to $\sigma_1$ and require $\mu$ <0.25 (Sibson, 1985). Geophysical studies of active oceanic transform faults suggest they require an effective friction

coefficient as low as 0.01 to slip under such stress states (e.g. Homberg *et al.*, 2010). Therefore chlorite-rich fault gouges ($\mu$ ~0.25 and cohesion, $C$ = 0.6 MPa; cohesion used from Ikari and Kopf (2011)) are not sufficiently frictionally weak if deformation is solely by frictional sliding.

Small differential stresses ($\sigma_1 - \sigma_3 \approx 8.5$ MPa at 2km depth) are required for sliding along poorly oriented incipient faults within dolerite ($\mu$ ~0.69, $C$ = 0 MPa) instead of creating new better oriented faults, if $\theta$ is 75° (Fig. 4.9). Under these conditions, chlorite-rich fault gouges ($\mu$ ~0.25, $C$ = 0.6 MPa) can also be reactivated, including on even more poorly oriented faults ($\theta$ >75°) due to the lower frictional strength of chlorite compared to dolerite (Fig. 4.9). Since the strengths of dolerite margins and joints, and chlorite-rich fault gouges, are variable at low normal stresses (Fig. 4.9), whichever is more favourably oriented would fail first. If either a fault with chlorite-dominated gouge, or a cohesion-less dyke margin or joint, is more favourably oriented than $\theta$ = 75°, as expected in places within an anastomosing fault system and dykes that have experienced variable degrees of rotation, then they would also fail at these conditions.

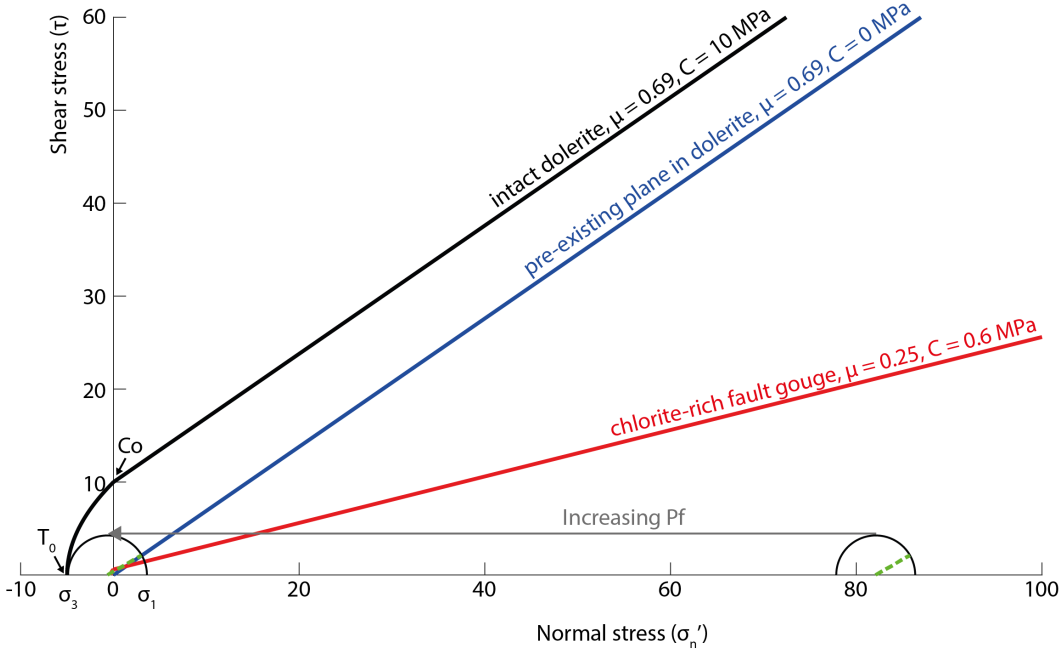


**Figure 4.9:** Mohr diagram (plot of shear stress, $\tau$, versus effective normal stress, $\sigma'_n$) illustrating the required conditions for shear failure of cohesionless pre-existing plane in dolerite (e.g. a dyke margin or cooling joint) ($\mu$ = 0.69) and chlorite-rich fault gouges ($\mu$ = 0.25) along pre-existing faults at a high angle ($\theta$ = 75°) to $\sigma_1$. Friction values were determined from experiments in Chapter 5.

Pressure solution can act to better orientate faults locally by removing fault irregularities and assist local slip by dissolving the material at high angles to $\sigma_1$ (e.g. Bos and Spiers, 2002; Durney *et al.*, 1976; Niemeijer and Spiers, 2005) within anastomosing strands. Pressure solution can significantly weaken fault gouges under some conditions and allow phyllosilicate-bearing faults to slide at shear stresses well below those expected from Byerlee's law (e.g. Bos and Spiers, 2002; den Hartog and Spiers, 2014). Pressure solution is a strain rate and grain size dependent process, much more efficient in fine-grained, thick shear zones deforming at low slip rates.

Alternatively, pore fluid pressure ($Pf$) is inferred to play a role in the strength of some major continental strike-slip faults like the Carboneras fault zone (Faulkner and Rutter, 2001), Median Tectonic Line (Jefferies *et al.*, 2006), and the San Andreas Fault (Fulton and Saffer, 2009; Wang, 2011), and could explain slip along poorly oriented oceanic transform faults. Despite the abundant evidence for early and widespread fluid-flow within the STTFZ recorded by alteration and mineralisation, there is no overwhelming evidence of fluid overpressure such as veins recording tensile fracturing (e.g. Scholz, 1998). At mid-ocean ridges $\sigma_1 = \sigma_{vertical}$, which changes to $\sigma_2 = \sigma_{vertical}$ for oceanic transform faults. Considering a 2 km thick crust (as suggested for the depth of the crust along the STTFZ in section 2.2; density ~2.9 g/cm$^3$) below 3 km of water (approximate depth of the Troodos lithosphere during transform deformation in section 2.4.3; density = 1.0 g/cm$^3$), $\sigma_{vertical}$ = ~85 MPa (Fig. 4.9). Because normal faults dominate at the ridge and strike-slip faults dominate along oceanic transform faults, this requires a stress rotation, which is easiest when differential stresses are small. If differential stresses are small then $\sigma_1$ at the transform can be comparable to $\sigma_1 = \sigma_{vertical}$ at the ridge (~85 MPa) and the maximum $Pf$ required for shearing along a pre-existing dyke margin or joint, or chlorite-rich fault gouge oriented at $\theta = 75°$ is ~80 MPa (Fig. 4.9). This maximum $Pf$ is greater than hydrostatic but not quite lithostatic (~95% of lithostatic), i.e. there is enough $Pf$ to weaken the poorly oriented faults so that they fail in shear failure but not enough to create tensile veining in intact dolerite (not enough to achieve the hydrofracture criterion, $Pf = \sigma_3 + \tau_0$), which we do not document in the field.

### 4.5.5 Implications for the long-term weakness and seismic style of oceanic transform faults

Oceanic transform faults display fewer, and smaller earthquakes than expected for their length and displacement (Bird *et al.*, 2002; Boettcher and Jordan, 2004; Brune, 1968). Geophysical observations indicate seismic moment only accounts for 10-15% of total fault slip globally (Boettcher and Jordan, 2004; Okal and Langenhorst, 2000). This means large amounts of shear strain is accommodated by aseismic slip processes (±microseismicity) within the thermally-defined seismogenic zone ($T$ <600 °C; Boettcher and Jordan, 2004). Despite the dominantly aseismic behaviour of oceanic transform faults, large earthquakes can occur quasi-periodically along the same fault patch (Braunmiller and Nábělek, 2008; Froment *et al.*, 2014; McGuire *et al.*, 2005; Sykes and Ekström, 2012). Seismic behaviour is commonly inferred to be controlled by fault zone damage; aseismic regions are characterised by reduced seismic velocities, and inferred as having increased permeability/fluid flow, and experience alteration to weak phyllosilicates. On the other hand, seismically locked patches are inferred to be more intact volumes of crust (Froment *et al.*, 2014; Roland *et al.*, 2010, 2012).

Laboratory measurements on quartzo-feldspathic and phyllosilicate-rich rocks indicate that some major continental faults, which have undergone prolonged deformation, fluid-rock interaction and alteration to phyllosilicate-rich fault zones (e.g. the Moine Thrust Belt, San Andreas Fault, Zuccale Fault and the Median Tectonic Line) are considerably weaker ($\mu$ ∼0.3) than their surrounding crust ($\mu$ ∼0.6-0.8) (e.g. Carpenter *et al.*, 2012; Collettini *et al.*, 2009; Ikari and Saffer, 2011; Jefferies *et al.*, 2006; Lockner *et al.*, 2011; Moore and Rymer, 2007; Schleicher *et al.*, 2012; Smith and Faulkner, 2010; Tesei *et al.*, 2012; Wibberley, 2005). Some studies suggest similar fluid-rock reactions are responsible for the weakness of oceanic core complexes (deMartin *et al.*, 2007; Escartín *et al.*, 2003; Grevemeyer *et al.*, 2013). Therefore, the progressive evolution from dolerite to chlorite-rich fault gouge suggests individual fault strands within oceanic transform faults become progressively weaker with increased deformation (Fig. 4.9 and 4.10).

The low permeability and compaction potential of foliated phyllosilicates limits the effects of fault healing or fluid-assisted strengthening by processes

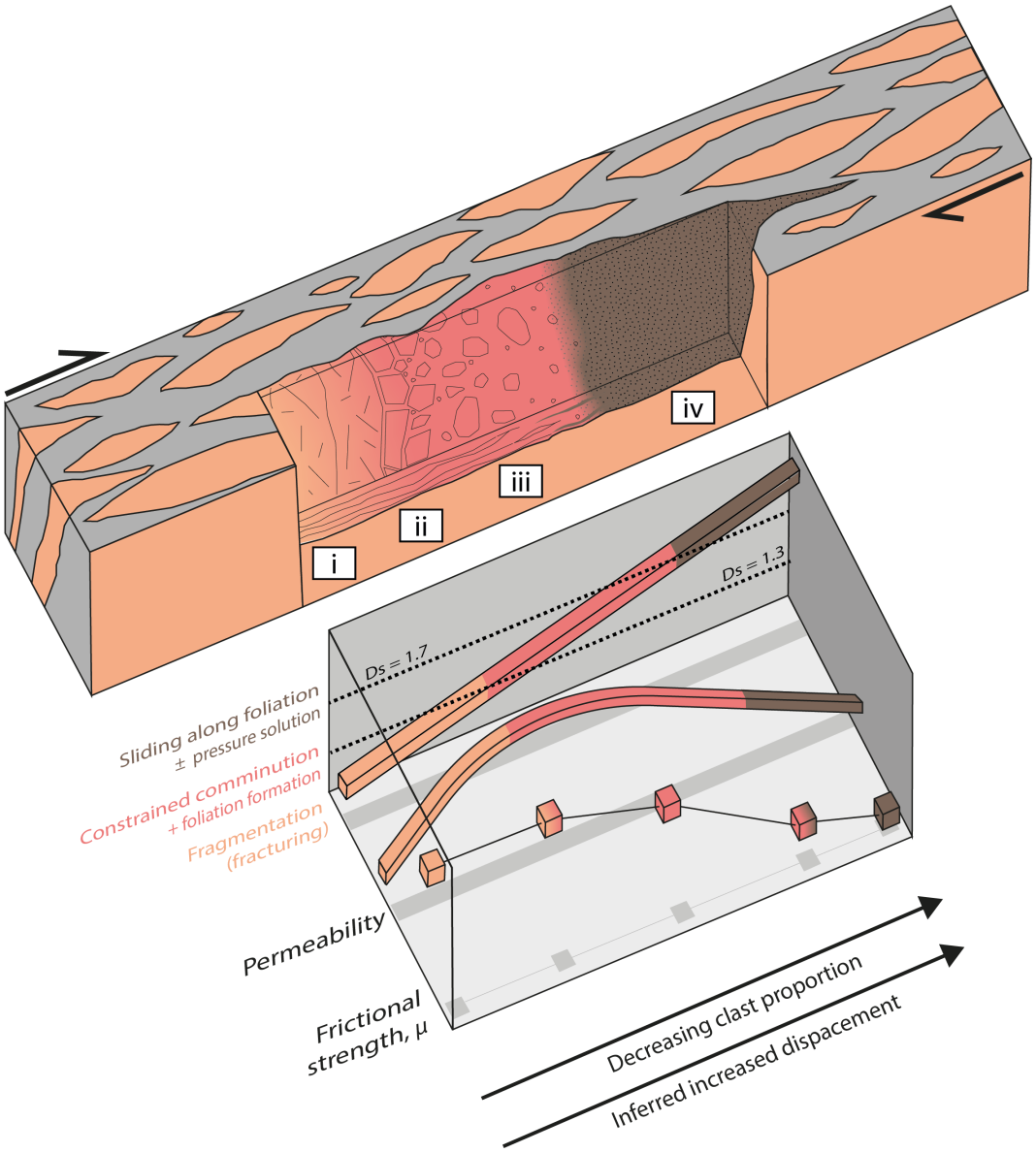


**Figure 4.10:** Schematic summary of the progressive deformation of sheeted dolerite dykes with displacement highlighting the transition from (i) dolerite dykes to (ii) crackle breccias, (iii) cemented breccias and (iv) chlorite-rich fault gouge. The 3D plot shows schematically how $Ds$, permeability and frictional strength changes with increased deformation.

such as compaction and solution-transfer (Niemeijer and Spiers, 2006; Tesei *et al.*, 2012; van den Ende and Niemeijer, 2019), applicable within the most mature chlorite-rich fault gouges of the STTFZ. Frictional healing, controlled by the growth of asperity contacts during solution transfer processes (Niemeijer and Spiers, 2006) is limited in STTFZ fault gouges due to the lack of compaction potential. This means these processes are unlikely to have acted to heal the most mature faults and recover strength after their formation.

Therefore, we suggest that because of the eventual decrease in permeability and formation of foliated chlorite within the most mature STTFZ faults, individual fault strands within an oceanic transform fault can be very weak over long timescales (when coupled with fluid pressures ∼95% lithostatic) under hydrated upper crustal conditions (summarised in Fig. 4.10).

Foliated, chlorite-rich fault gouges are typically velocity-strengthening (Imber *et al.*, 1997; Schleicher *et al.*, 2012; Smith and Faulkner, 2010, Chapter 5). The tendency for frictional weakness to be associated with velocity-strengthening behaviour is consistent with previous work on a wide range of natural and analogue fault gouges (e.g. Beeler, 2007; Carpenter *et al.*, 2011; Ikari *et al.*, 2016, 2011; Morrow *et al.*, 1992; Shimamoto and Logan, 1981; Tesei *et al.*, 2012, and Chapter 5). Therefore, STTFZ weak gouge-dominated faults are likely analogous to "rupture barrier" regions along active oceanic transform faults, that are inferred from their characteristic low seismic velocities as being regions of increased damage and hydrothermal alteration (e.g. Boettcher and Jordan, 2004; Cox *et al.*, 2021; Froment *et al.*, 2014; McGuire *et al.*, 2012; Moore *et al.*, 1997; Roland *et al.*, 2010, 2012).

In contrast to weak gouge-dominated fault zones, areas of intact dolerite and cemented breccias (e.g. Fig. 4.3i-ii and 4.5a) are likely representative of stronger crust that can act as locked regions of an oceanic transform fault. This is supported by cemented breccia-dominated fault zones recording brittle deformation, with strain localisation along chlorite-rich seams (e.g. Fig. 4.5c) that could explain discrete slip and potentially seismic behaviour.

The spatial distribution of deformed zones within the crust of the STTFZ suggests repeated stress cycles may not localise all strain onto the same faults. Instead, strain may be dispersed across the entire deforming width of the transform fault as previously proposed by MacLeod and Murton (1995), and a process also inferred from field studies of more deeply exhumed transform faults (Chatzaras *et al.*, 2020; Cox *et al.*, 2021, and Chapter 3).

## 4.6 Conclusions

The Southern Troodos Transform Fault Zone records Cretaceous-aged oceanic transform fault deformation from at and below the ocean floor. Within the sheeted dykes, hydrothermal alteration to albite, actinolite and chlorite sug-

gest deformation of the shallow crust occurred at temperatures associated with greenschist facies alteration (<450 °C) and within the expected oceanic seismogenic zone (<600 °C).

Deformation of the sheeted dolerite dykes was progressive, first controlled by fracturing (slight increase in $Ds$) during small displacement events and the formation of crackle breccias ($Ds$ <1.3). Continued deformation increases $Ds$ in clast-supported breccias, to near 1.58, implying a change from early fracturing to later cataclasis and constrained comminution as displacement is inferred to increase. $Ds$ values for fault gouges >1.7 suggest deformation in inferred large-displacement faults was aided by abrasion. Syn-kinematic alteration to chlorite requiring the addition of fluid may have aided the formation of chlorite-rich gouges. Slip within chlorite-rich fault gouges was accommodated by sliding along grain boundaries and foliation planes ±pressure solution.

Thick (<10 m), chlorite-rich gouge zones likely develop from the growth and amalgamation of thin gouge-rich faults that grow into their damage zones. The formation of foliated chlorite-rich fault gouges generates fault zones with a phyllosilicate rheology that is much weaker than the intact dolerite dykes. Therefore, we deduce that with increased displacement and subsequent damage and gouge formation, individual fault strands became progressively weaker and strain could localise into these zones.

Fault zones within the STTFZ are poorly oriented for failure in an Andersonian stress field, but can also form barriers to fluid flow (cemented breccias and fault gouges), such that high fluid pressures may build up locally. This would aid slip along poorly oriented faults. The lack of tensile veins implies that the STTFZ would have slipped at fluid pressures that were insufficient for hydrofracturing, but sufficient to reactivate poorly oriented faults, which we calculate to be ∼95% of lithostatic pressure (section 4.5.4).

In general, our model suggests that weakening of an oceanic transform fault can happen as a function of damage, much like what has been inferred from geophysical observations for "rupture barrier" regions of some active transforms (e.g. McGuire *et al.*, 2005). Our field and fault rock observations support a relationship between increased fault zone damage and long-term weakness of oceanic transform faults through the formation of foliated chlorite-rich gouges within the upper oceanic crust. The combination of fracture, cataclastic flow and gouge formation could also be used to explain a transition from seismic to

aseismic behaviour at the same $T$ ($\sim$300 °C).

# Chapter 5

# Frictional characteristics of oceanic transform faults: Progressive deformation and alteration controls seismic style

## 5.1 Abstract

Oceanic transform faults are dominantly aseismic and are inferred to be very weak relative to the surrounding oceanic crust. Neither their weakness nor their tendency to creep are well explained. To test the effects of fault rock evolution on transform fault frictional strength and stability we conducted direct-shear friction experiments on dolerite from the East Pacific Rise and natural fault rocks from the exhumed Southern Troodos Transform Fault Zone, Cyprus. These samples represent different stages of a progressive deformation sequence in oceanic crust, and were tested at room temperature, 10 MPa normal stress and fluid-saturated conditions. Dolerites and cemented breccias are frictionally strong ($\mu$ = 0.52-0.85) but velocity-weakening (i.e. strength decreases with increasing slip velocity, characteristic of earthquakes). In contrast, matrix-rich breccias and fault gouges, rich in chlorite, are frictionally weak ($\mu$ = 0.25-0.48) and velocity-strengthening (characteristic of stable creep). A transition from velocity-weakening to velocity-strengthening is coupled to frictional weakening, consistent with the hypothesis that along-strike variations in seismic behaviour are controlled by decreased dolerite clast proportion and in-

creased chlorite content. In this model, earthquake nucleation can occur within more intact doleritic crust, whereas areas of increased damage, alteration, and chlorite-content tend to slip aseismically.

### Author contributions

Sophie Cox is the main author of this work, conducted experiments and microstructural observations. Sophie Cox wrote the manuscript. Matt Ikari helped with the experimental procedure. Matt Ikari, Ake Fagereng and Christopher MacLeod provided constructive comments on the manuscript prepared for submission.

## 5.2 Introduction

Oceanic transform faults display far fewer and much smaller earthquakes than expected from fault length-magnitude scaling relations, based on the Harvard centroid moment tensor catalogue (e.g. Bird *et al.*, 2002). Instead, up to 95% of displacement occurs aseismically, despite the faults cross-cutting the brittle mafic crust (Boettcher and Jordan, 2004). This earthquake deficit has been explained in two ways: (1) oceanic transforms experience both earthquakes and aseismic creep along the same fault segments, but at different times (e.g. Abercrombie and Ekström, 2001; Hilley *et al.*, 2020; McGuire *et al.*, 1996); and/or (2) oceanic transforms are segmented into "locked patches" hosting quasi-periodic earthquakes of $Mw$ >6.0, and microseismically active "rupture barriers" dominated by creep, as suggested for the Blanco (Braunmiller and Nábělek, 2008; McGuire *et al.*, 2005), Heezen (Sykes and Ekström, 2012), Gofar and Discovery transforms (Boettcher and McGuire, 2009; Froment *et al.*, 2014; McGuire, 2008; Roland *et al.*, 2012; Wolfson-Schwehr *et al.*, 2014). Variable fault zone damage inferred from geophysically-constrained mechanical properties (e.g. Froment *et al.*, 2014; Roland *et al.*, 2012) coupled to enhanced fluid circulation (reflected in variable P- and S-wave velocities) and the growth of frictionally weak, hydrous phyllosilicates (Roland *et al.*, 2010), provides one hypothesis to explain persistent along-strike segmentation in seismic behaviour.

On geological time scales, the stress state of oceanic transform faults requires them to be mechanically weak relative to the surrounding crust (Zoback, 1991). Many mechanisms have been proposed to explain the inherent weakness of oceanic transform faults in the shallow, brittle regime, including hydration of mafic and ultramafic minerals to frictionally weak (friction coefficient, $\mu$, <0.6) phyllosilicates and serpentine (Behn *et al.*, 2007; Moore *et al.*, 1997), and elevated fluid pressure lowering the effective normal stress (Bergerat *et al.*, 2000; Sykes and Ekström, 2012). Interconnected phyllosilicates have also been inferred to promote aseismic (velocity-strengthening) behaviour of weak, mature continental faults (e.g. Imber *et al.*, 1997; Schleicher *et al.*, 2012). Within the oceanic lithosphere, the specific phyllosilicate chlorite has been found to contribute to strain localisation along weak oceanic detachment faults (Escartín *et al.*, 2003; MacLeod *et al.*, 2002). However, there is a lack of geological or laboratory deformation evidence for comparable processes occurring along oceanic

transform faults; instead, experimental data on basalt and gabbro deformation have shown velocity-weakening behaviour and $\mu$, $\geq$0.6 (Cox, 1990; He *et al.*, 2007; Phillips *et al.*, 2020; Zhang *et al.*, 2017). If, however, creeping segments host increased damage and alteration, frictional properties must differ from those of intact oceanic crust, so these experiments may not be relevant.

To date, most studies on the weakness of transform faults focus on continental faults, or are limited to seafloor sampling including dredges, dives and 1D borehole observations on of largely inaccessible oceanic transform faults. We present the results of the first laboratory direct-shear friction experiments targeting a natural sample set including intact dolerite from the East Pacific Rise (EPR) in Hess Deep, and samples of variably altered fault rocks from the doleritic crustal section of the exhumed Southern Troodos Transform Fault Zone (STTFZ) in the Troodos ophiolite, Cyprus (for details on geological setting of the STTFZ see Chapter 2 and for the deformation of the mafic crust, see Chapter 4). The data provide a test of the hypothesis that fault rock damage controls transform fault strength and slip style.

## 5.3 Experimental methods and samples

We obtained frictional properties of two dredged dolerite samples representing intact dolerite, and natural fault rocks collected from the STTFZ (Fig. 5.1), that represent minor (cemented breccia), moderate (matrix-rich breccia) and intense (fault gouge) deformation and alteration (Fig. 5.2). The sampled dolerites were generated at the fast-spreading East Pacific Rise (EPR) and collected from the Hess Deep rift in the equatorial east Pacific during RRS *JamesCook* cruise JC21 (MacLeod *et al.*, 2008). The STTFZ samples include an indurated indurated (cemented) dolerite breccia, a matrix-rich breccia and a fault gouge (following the fault rock classification of Sibson (1977)). The proportion of relatively intact dolerite clasts within the fault rocks was used as a proxy for fault zone damage, with decreasing clast proportion representing increased alteration and deformation. Clast proportions for the various fault rocks were obtained from backscatter scanning electron images of the sample prior to experiments. To do this, sample photos of pre-experiment samples (at the thin section scale) were digitised in Adobe Illustrator by manually outlining clasts. Clast proportions were then determined using ImageJ software (FIJI)

version 2.0.0.

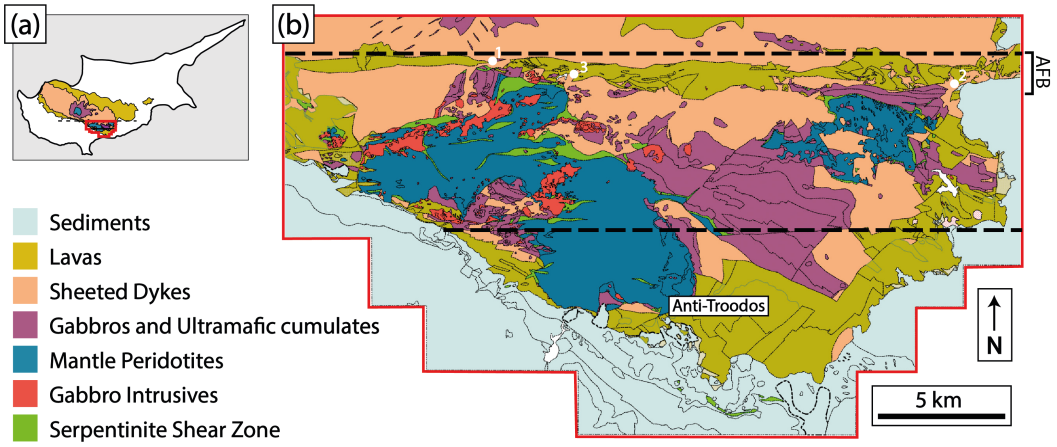


**Figure 5.1:** (a) Simplified geological map of the Troodos ophiolite, Cyprus and location of the Southern Troodos Transform Fault Zone (STTFZ) (red box). (b) Geological map of the STTFZ showing sample locations for the cemented breccia (1), matrix-rich breccia (2) and fault gouge (3) are shown by the white circles. AFB = Arakapas Fault Belt at the northern limit of the STTFZ.

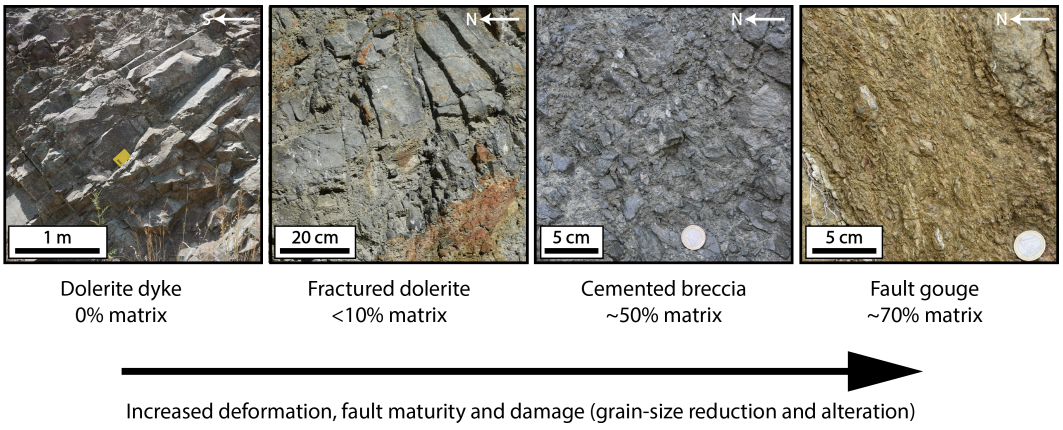


**Figure 5.2:** Field photographs illustrating the progressive deformation inferred in the Southern Troodos Transform Fault Zone, Cyprus. Dolerite dykes progressively deform by fracturing and cataclasis to fractured dolerite and cemented breccias. With continued deformation, abrasion and syn-kinematic alteration (leading to the growth of chlorite) playing a role in the development of matrix-rich breccias and fault gouges.

Optical microscopy shows that the relatively intact EPR dolerites experienced typical hydrothermal alteration at greenschist facies conditions, and contains predominately ~60% plagioclase, ~30% pyroxene/actinolite and ~5-10% chlorite present within the crystalline texture. One of the dolerite samples (fractured dolerite) also contains variably oriented fractures. Among the

rocks sampled from the STTFZ, cemented dolerite breccia comprises ∼75% dolerite clasts (∼0.2-9.0 mm) hydrothermally altered to albite, actinolite and <10% chlorite, within a fine-grained non-foliated matrix that contains the same minerals, in approximately the same proportions as the dolerite clasts. The matrix-rich breccia sample contains ∼45% dolerite clasts (∼0.1-9.0 mm) that are surrounded by a chlorite-rich matrix. The fault gouge sample comprises a foliated chlorite-rich matrix with only ∼25% dolerite clasts (∼0.05-4.5 mm) and minor amounts of quartz and calcite, minerals that are absent from the other samples.

Laboratory single direct-shear friction experiments were carried out using a GIESA RS5 direct-shear apparatus (Fig. 5.3) (Ikari et al., 2013 G3) at the Marum Research Faculty at the University of Bremen, Germany, at room temperature ∼20°C (in a climate-controlled room), 10 MPa normal stress and under fluid-saturated conditions (3.5% NaCl brine), appropriate for samples deforming within the upper crust of a vertical oceanic transform fault, where brittle deformation is expected. For one sample (intact dolerite; see Appendix C.1) the peak strength at 10 MPa $\sigma_n$ exceeded the apparatus limit and was therefore initially broken under 1 MPa $\sigma_n$, before increasing the load to 10 MPa for the velocity step test.

All five samples were tested both as intact minicores and powders. Minicores were cut with their *in-situ* fabric parallel to the shearing plane of the experiment apparatus. Powdered samples were crushed by hand using a pestle and mortar and sieved to <125 $\mu$m grain size. The sieved powder was then mixed with simulated seawater (3.5% NaCl brine) into a stiff paste and pressed into the sample cell.

The sample cell is set up as two stacked plates housing cylindrical samples ∼20 mm in height and 25 mm diameter. Once the samples were loaded, they were left to consolidate overnight (∼12+ h) under a normal stress of 10 MPa, which was applied to the sample by a vertical steel ram. The samples were allowed to equilibrate until the sample thickness had reached a steady state. This was measured as a change in sample height over time (compaction rate reduced to zero). During compaction, the samples were allowed to drain at the top and bottoms via porous metal frits allowing for any excess pore pressure that may have developed during loading to dissipate (pore pressure = 0) therefore making the applied stress equal the effective normal stress, $\sigma'_n$

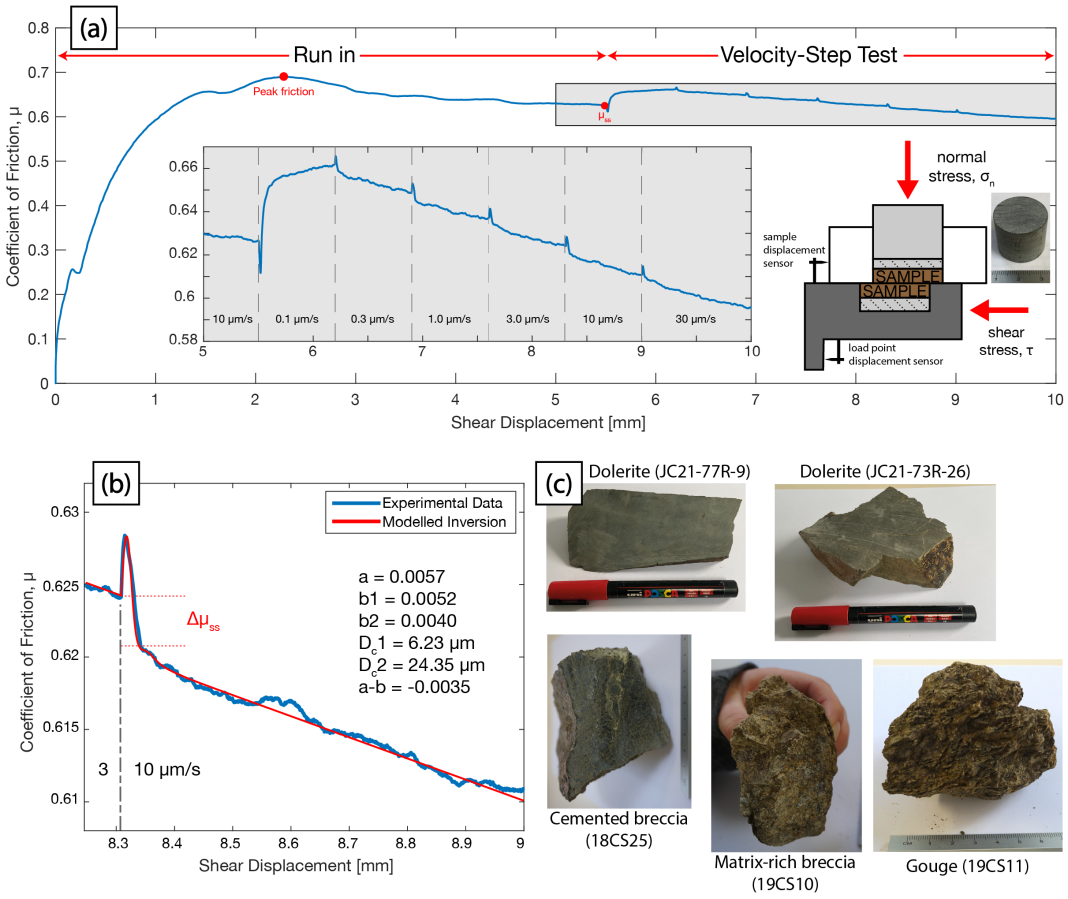


**Figure 5.3:** (a) Example of a friction-displacement curve, in this case for a sample exhibiting velocity weakening behaviour ($a$-$b$ <0), i.e. the conditions required for earthquake propagation. Right inset shows a schematic representation of the laboratory set up. Larger inset shows a close-up of the velocity-step test. (b) An individual velocity step (3 to 10 $\mu$m/s velocity step), overlain with an inverse model from which rate-and-state friction parameters are obtained (modelled using $RSFit3000$). For explanations of the rate-and-state friction parameters see Skarbek and Savage (2019). (c) Starting materials for this study. Brief sample descriptions and locations can be found in Appendix A.

(for further details see Ikari *et al.* (2015) online).

The direct-shear apparatus has two horizontal displacement sensors (Fig. 3.8), one which monitors the machine driving or load point velocity ($V_{lp}$) and one measuring the offset of the cell plates and the sample velocity ($V$). During rapid changes, for example sample fracture or stick slip events, these two velocities can deviate ($V > V_{lp}$).

To deform the sample, the lower plate is displaced relative to the top plate by an electric motor and where the two plates meet, the relative displacement induces a "localised" shear plane within the sample (Fig. 5.3; Ikari *et al.* (2015);

Ikari and Kopf (2011) for details). At the start of the experiment, we applied an initial constant displacement rate of 10 $\mu$m/s until a steady-state shear strength, $\tau$, was reached, typically after $\sim$5-6 mm displacement (Fig. 5.3). In some cases, steady-state was not reached within 6 mm and in these cases, we measured $\tau$ at 6 mm to allow for comparison between experiments. We continually measured $\tau$ throughout the experiments and use this to calculate residual sliding friction coefficient, $\mu$, as $\mu = \tau/\sigma'_n$. We have assumed our samples to be cohesionless when calculating $\mu$, noting that this is not always the case and so $\mu$ reported in this study are apparent values.

Once steady-state shear strength (or 6 mm displacement) was reached, we began the velocity step test (VST) experiment. We conducted the experiment using a three-fold increase in the sliding velocity ($V$) in the range of 0.1-30 $\mu$m/s. We measured the velocity dependence of friction as the rate-and-state friction parameter *a-b*. *a-b* is defined by $a\text{-}b = \Delta\mu_{ss}/\Delta lnV$, where $\Delta\mu_{ss}$ is the change in steady-state friction after the change in slip velocity, $V$ (e.g. Dietrich, 1979, 1981 and Marone, 1998). The frictional response to a velocity up-step can be described by the rate-and-state friction relations:

$$\mu = \mu_0 + aln\left(\frac{V}{V_0}\right) + b_1 ln\left(\frac{V_0\theta_1}{Dc_1}\right) + b_2 ln\left(\frac{V_0\theta_2}{Dc_2}\right) \tag{5.1}$$

and

$$\frac{\delta\theta_i}{\delta_t} = 1 - \frac{V\theta_i}{Dc_i}, i = 1, 2 \tag{5.2}$$

where $a$, $b_1$ and $b_2$ are dimensionless constants, $\theta_1$ and $\theta_2$ are state variables which describe ageing, and $Dc_1$ and $Dc_2$ are critical slip distances over which the friction evolves to a new steady-state (Blanpied *et al.*, 1998; Dieterich, 1981; Marone, 1998). In cases where the friction response to the velocity change are well described by a single-state variable, $b_2$ and $Dc_2$ are 0. The second equation describes the evolution of friction to a steady-state at the new velocity, $V$, and is known as the Dieterich law. This law explicitly considers that friction can evolve as a function of time and not necessarily slip (Dieterich and Kilgore, 1994). We use the ageing law because it better describes natural phenomena (Kanu and Johnson, 2011; Rubin, 2008), but note that the slip law (section 1.3.2; Ruina, 1983) also fits our data relatively well (see full results in Appendix

C). For each velocity step we determined the individual parameters $a$, $b_1$, $b_2$, $Dc_1$ and $Dc_2$ using inverse modelling techniques in $RSFit3000$ (Skarbek and Savage, 2019), which also includes an expression for the finite system stiffness, $k$.

The parameter $a$-$b$ is important in predicting fault slip behaviour. Values of $a$-$b$ >0 indicate velocity-strengthening behaviour and are associated with stable fault creep, whilst $a$-$b$ <0 indicates velocity-weakening behaviour, i.e. the strength of the rock decreases with increasing slip velocity, characteristic of unstable fault slip and required for earthquake nucleation (Dieterich, 1979, 1981; Marone, 1998; Scholz, 1998).

Following the experiments, samples were dried, set in epoxy resin and cut parallel to the shear direction and perpendicular to the slip surface to analyse the slip surface in cross-section view. Backscatter scanning electron images were acquired using a Zeiss Sigma HD Field Emission Gun analytical scanning electron microscope (ASEM), operated in a high vacuum mode with an accelerating voltage of 20 kV and 60 $\mu$m aperture in the School of Earth and Environmental Sciences at Cardiff University.

Compositions of each sample tested was determined using a combination of optical microscopy and X-ray diffraction (XRD) analysis (summarised in Fig. 5.4). Bulk analysis was carried out on powdered samples using a Philips PW1710 Automated Powder Diffractometer using Cu K$\alpha$ radiation at 35kV and 40mA. Analysis was carried out at a scan rate of 0.02 °2$\theta$/s between 2 and 70 °2$\theta$.

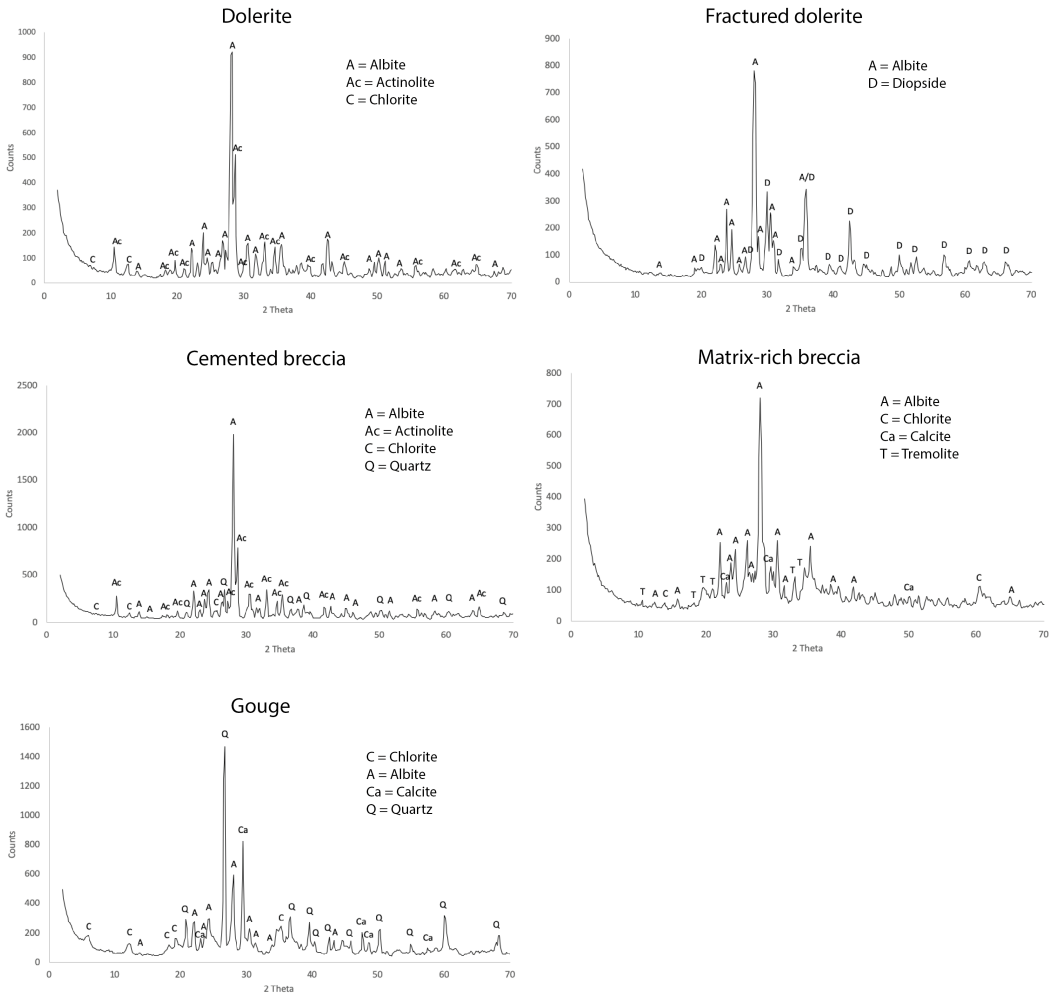


**Figure 5.4:** Compositions of each sample determined by XRD analysis.

## 5.4 Results

### 5.4.1 Frictional strength of fault rocks

Steady-state friction for minicores decreases from $\mu = 0.85$ in EPR dolerite to $\mu = 0.28$ in the chlorite-rich fault gouge (Fig. 5.5a). For powdered samples, the residual steady-state friction is $\mu = 0.69$ in EPR dolerite, decreasing to 0.25 in the chlorite-rich gouge. Powdered samples are systematically weaker than their intact minicore equivalents (Fig. 5.5a). We document a linear correlation between decreasing $\mu$ and clast proportion ($R = 0.94$ for minicores and $R = 0.87$ for powders).

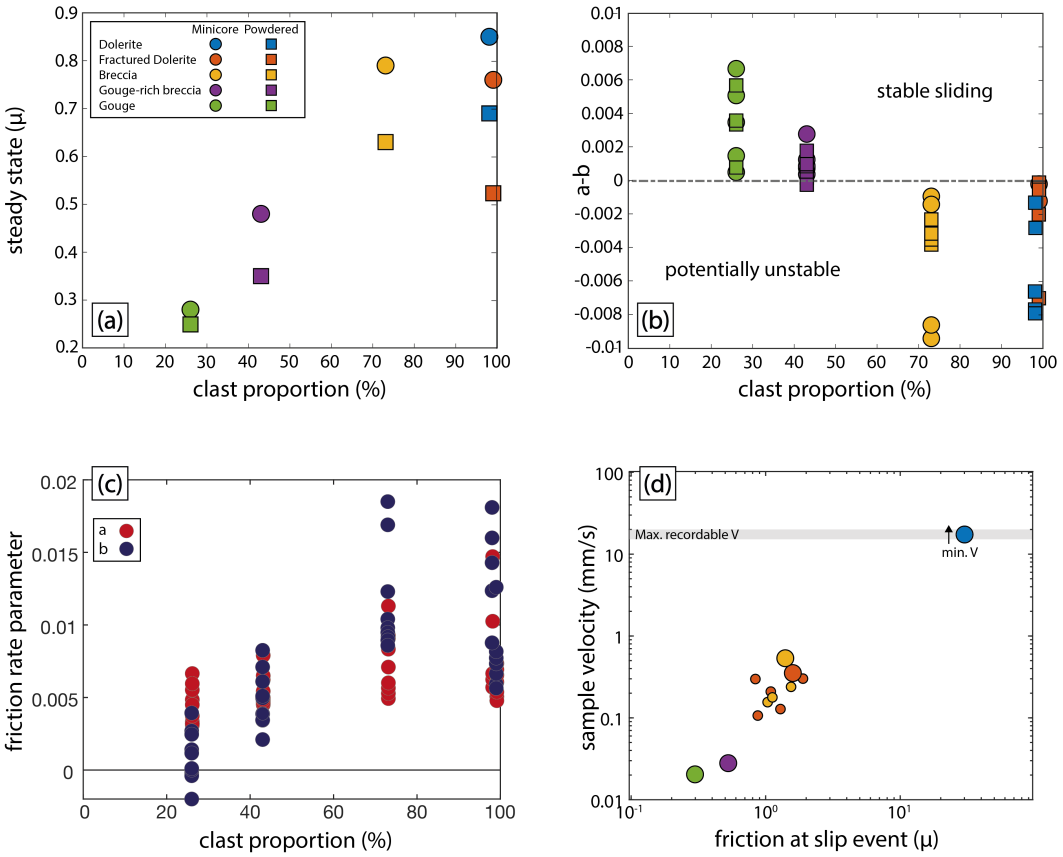


**Figure 5.5:** (a) Measured coefficient of sliding friction for each of the samples in this study as a function of clast proportion. (b) $a$-$b$ values as a function of clast proportion. (c) Friction rate parameters $a$ and $b$ as a function of clast proportion showing that the increase in $a$-$b$ correlates with a decrease in $b$. (d) Sample velocity vs. coefficient of sliding friction. The initial fracture for each experiment is shown by the larger symbols, smaller symbols represent subsequent breaks. The maximum recordable velocity in the system is ~15-20 mm/s (grey shaded area). The intact dolerite (in blue) was broken under 1 MPa $\sigma_n$, all other samples under 10 MPa.

### 5.4.2 Velocity-dependence of friction

For the EPR dolerites, and cemented breccia from the STTFZ, strictly velocity-weakening frictional behaviour is observed in both intact and powdered samples (Fig. 5.5b). Only two $a$-$b$ values were determined for the fractured dolerite minicore, and none for the dolerite minicore because of irregular fluctuations in the measured data, likely due to the roughness of the fractured surfaces. Strictly velocity-strengthening frictional behaviour is observed in both intact and powdered STTFZ fault gouge. Dominantly velocity-strengthening behaviour is observed for the matrix-rich breccia with positive $a$-$b$ values for the

minicore, and $a$-$b$ from -0.0002 to 0.0018 for the powdered sample (Fig. 5.5b). We observe no dependence of $a$-$b$ on sliding velocity (Fig. 5.6). The transition from velocity-weakening to velocity-strengthening behaviour is largely correlates with a decrease in $b$ while a varies less (Fig. 5.5c).

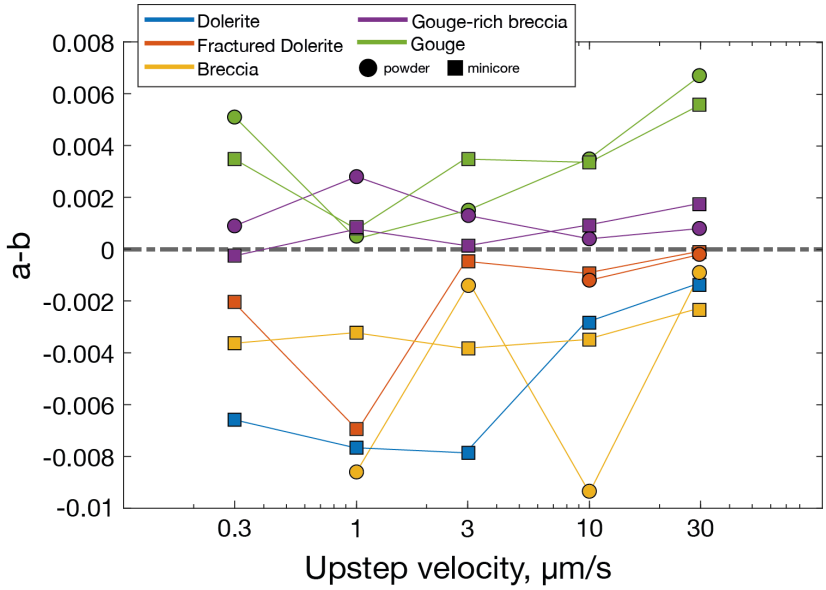


**Figure 5.6:** Plot of the friction rate parameter $a$-$b$ vs. upstep load point velocity.

Overall, $a$-$b$ increases with decreasing clast proportion, with the dolerite having the lowest $a$-$b$ and fault gouge has the highest. $a$-$b$ also correlates with $\mu$, with a crossover in behaviour from velocity-strengthening to velocity-weakening at $\mu \approx 0.5$ (Fig. 5.7), consistent with previous experimental work (Ikari *et al.*, 2011).

### 5.4.3 Initial rock failure

A range of peak sliding velocities occurred during the initial failure of the minicore samples. $V$ of the fault gouge and matrix-rich breccia largely reflected the applied slip rate, reaching maximum slip speeds of ~0.02-0.03 mm/s. However, the cemented breccia and both dolerite samples showed several distinct frictional slip events where $V$ exceeded the applied rate (Fig. 5.5d). The cemented breccia and fractured dolerite exhibited peak sliding velocities reaching 0.55 mm/s and 0.36 mm/s, respectively (Fig. 5.5d). The dolerite minicore slipped audibly at a velocity of 18.65 mm/s immediately following peak friction (Fig. 5.5d). The maximum measurable $V$ in the direct-shear device is ~15-20 mm/s,

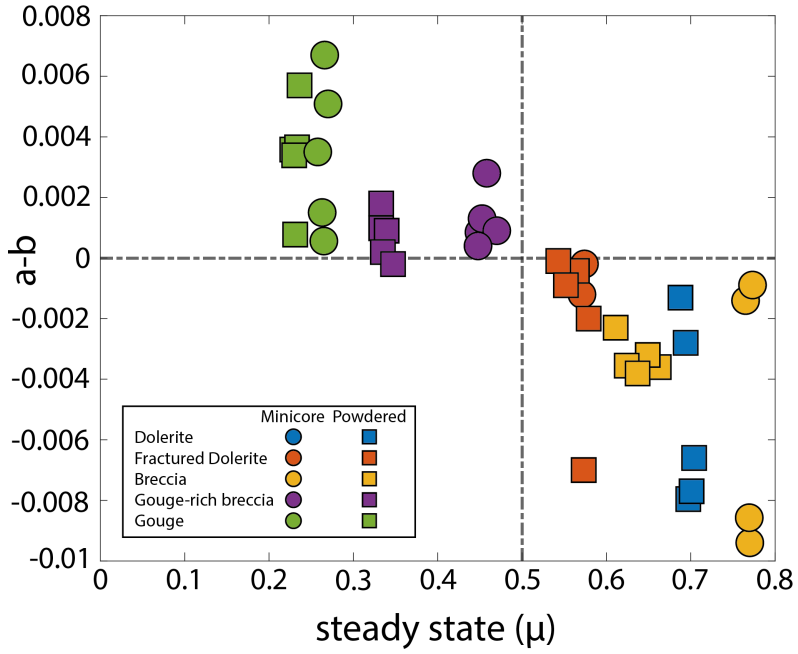


**Figure 5.7:** Plot of $a$-$b$ vs. $\mu$ showing a general decrease in $a$-$b$ with increasing steady-state friction.

suggesting that our recorded value of 18.65 mm/s is a minimum value, and the real $V$ could be much higher. Slip velocities on the order of mm/s are rare in direct-shear friction experiments, and the dolerite minicore's maximum $V$ falls within the range of seismic slip speeds of $>\sim$1 mm/s (e.g. Daub *et al.*, 2011; Rowe and Griffith, 2015; Rubin, 2008).

### 5.4.4 Microstructural observations

Cross-sectional backscatter electron images of the sheared samples show that brittle fracture and grain-size reduction are common processes over an irregular zone of deformation up to $\sim$4 mm thick within the dolerite and breccia minicores (Fig. 5.8a,c), and up to $\sim$0.5 mm on either side of the shear zone within the dolerite and breccia powders (Fig. 5.8b,d). In the dolerite minicore, fragments up to several millimetres in length are surrounded by much finer clasts down to $\sim$1 $\mu$m (Fig. 5.9a). The cemented breccia minicore also shows fine clasts sizes down to $\sim$1 $\mu$m that surround fragments up to $\sim$2 mm in the shear zone (Fig. 5.8c and 5.9c). The fragment size in the experimentally-deformed cemented breccia minicore is, in part, controlled by the size of the pre-existing dolerite clasts. Riedel shears formed during experimental deforma-

tion of the EPR dolerites and the STTFZ cemented breccia (Fig. 5.8a-d). The matrix-rich breccia shows a weakly-developed foliation accompanied by grain-size reduction over zone ∼3 mm in the minicore and <1 mm in the powdered sample (Fig. 5.8e,f and 5.9e). The fault gouge end-member sample shows a well-developed foliation, bending towards parallelism with a narrower, ∼1-3 mm wide, shear zone, defined by aligned chlorite grains in both the minicore and powdered samples (Fig. 5.8g-i and 5.9f,g).

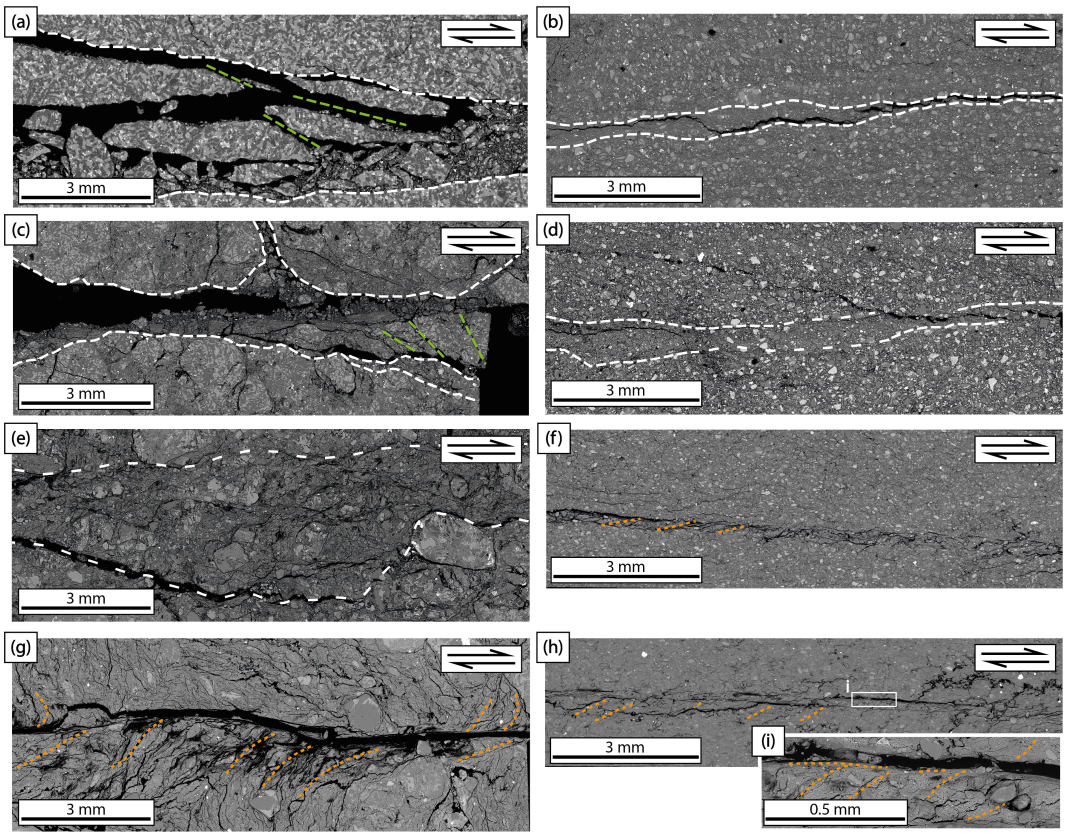


**Figure 5.8:** Backscatter scanning electron images of sheared (a) dolerite minicore, (b) powdered dolerite, (c) cemented breccia minicore (∼70% clasts), (d) powdered cemented breccia, (e) matrix-rich breccia minicore, (f) matrix-rich breccia powder, (g) gouge minicore (∼25% clasts) and (h-i) powdered gouge. Dashed white lines show approximate boundaries of shear deformation. Fractures with orientations representing Riedel R shears are showing in green. Dashed orange lines highlight foliation in (g-i).

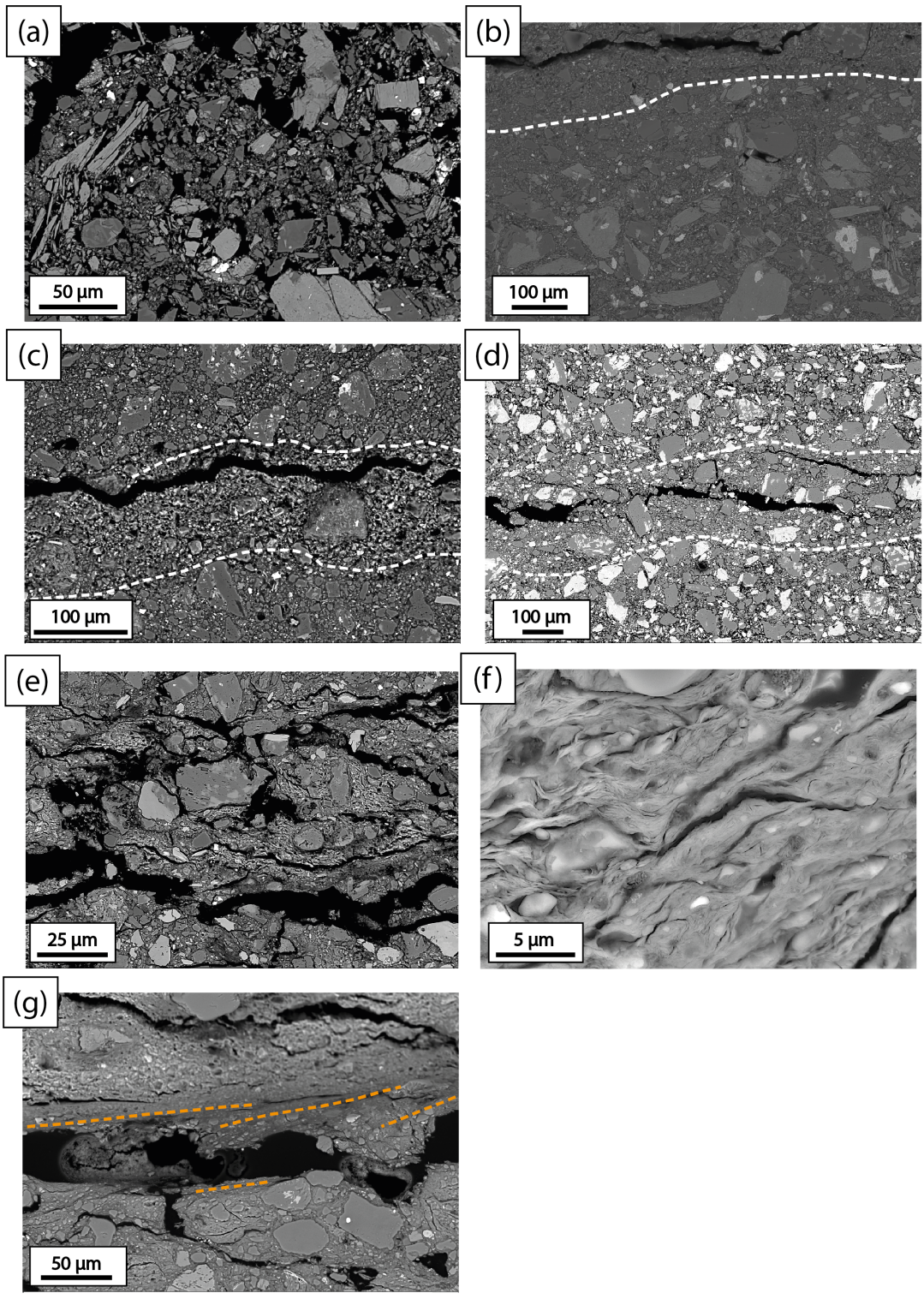


**Figure 5.9:** Backscatter scanning electron images of sheared experimental samples. (a) Dolerite minicore. (b) Powdered dolerite, with grain size reduction towards the shear plane over a distance of ∼100 $\mu$m (top of image). Cemented breccia (c) minicore and (d) powdered sample with grain size reduction towards the shear plane. (e) Matrix-rich breccia with foliation development and grain size reduction. (f) Gouge minicore with anastomosing and well-aligned chlorite (surrounding quartz and albite grains) from within the shear plane. (g) Powdered gouge showing aligned chlorite defining a foliation, that is well-developed.

## 5.5 Discussion

### 5.5.1 Frictional strength of intact and faulted mafic crust

The results show a clear correlation between frictional strength and clast proportion (Fig. 5.5a). The high frictional strength obtained for the EPR dolerites is related to a load-bearing framework of minerals (albite, actinolite, relict pyroxene) that have replaced the original igneous assemblage at greenschist facies hydrothermal conditions. These minerals are relatively strong in laboratory experiments performed at greenschist facies pressures and temperatures (He *et al.*, 2013). The STTFZ cemented breccia is from an exhumed fault zone but also experienced greenschist facies hydrothermal conditions and is cemented with a similar albite-actinolite mineral assemblage (±quartz). Because of this cementation, the breccia is relatively strong despite being more faulted and having a lower clast proportion than the EPR dolerites. In contrast, the matrix-rich breccia and fault gouge samples show steady-state frictional strengths that are much lower. These fault rocks are more chlorite-rich, and chlorite is known to be weak ($\mu$ ~0.3) under almost all laboratory conditions from room temperature and 10 MPa pressure (Fagereng and Ikari, 2020), up to 400 MPa and 600 °C (Okamoto *et al.*, 2019). The interconnectivity of the weak phase is important to control fault strength and frictional stability (Collettini *et al.*, 2009; Handy, 1990). In the dolerites, the chlorite proportion is small (~5-10%) and poorly interconnected, relative to a higher proportion (~35-70%) and better interconnectivity in the matrix-rich breccia and fault gouge (Fig. 5.8). Therefore, the weakness of the matrix-rich breccia and fault gouge can be attributed to an increase in chlorite content and interconnectivity.

A foliation was present prior to laboratory deformation of the fault gouge minicore and developed during the experiments on the powdered fault gouge sample (Fig. 5.8h-i). This agrees with field observations that a foliation develops in the most mature, highest strain faults, and suggests gouge deformation occurs by sliding along basal planes of the chlorite that defines the foliation. Fabric development defined by phyllosilicate alignment can result in fault weakening (Collettini *et al.*, 2009; Holdsworth *et al.*, 2011; Ikari *et al.*, 2011; Schleicher *et al.*, 2010) and allows shear to localise onto foliation planes (Haines *et al.*, 2013). The less well-developed foliation and brittle deformation in the matrix-rich breccia may therefore explain why it remains stronger than

the foliated fault gouge.

Minicores sheared with pre-existing *in situ* fabrics aligned to the experimental shear direction where possible, are consistently stronger than powdered samples (Fig. 5.5a). The strength difference between the minicore and powdered samples of the matrix-rich breccia and fault gouge is smaller than for the EPR dolerites and the cemented breccia. The difference in strength between powders and minicores is attributed to cohesion (cohesion being the shear strength at zero $\sigma_n$), with the cohesion being greater for the cemented rocks compared to more damaged ones. Also, the powdered matrix-rich breccia and fault gouge samples develop a foliation during the experiments (Fig. 5.8f,h), explaining the similarity in strength to their minicore versions which have their original foliation preserved (Fig. 5.8e,g).

### 5.5.2 Frictional stability of dolerite and dolerite-derived fault rocks

EPR dolerite and STTFZ cemented breccia display velocity-weakening behaviour (Fig. 5.5b), consistent with the brittle fractures that developed (Fig. 5.8a-d). In contrast, the foliated, chlorite-rich STTFZ matrix-rich breccia and fault gouge are velocity-strengthening (Fig. 5.5b). This velocity-strengthening behaviour is consistent with other studies of foliated, chlorite-rich fault gouges (e.g. Imber *et al.*, 1997; Schleicher *et al.*, 2012; Smith and Faulkner, 2010). The tendency for frictional weakness to be associated with velocity-strengthening behaviour (Fig. 5.5a-b and 5.7) is consistent with previous work on a wide range of natural and analogue fault gouges (e.g. An *et al.*, 2021; Beeler, 2007; Carpenter *et al.*, 2011; Ikari *et al.*, 2016, 2011; Morrow *et al.*, 1992; Shimamoto and Logan, 1981; Tesei *et al.*, 2012).

The change in frictional stability, $a$-$b$, with decreasing clast proportion is largely controlled by a decrease in the friction rate parameter $b$ whereas the effect of $a$ is smaller (Fig. 5.5c). $b$ describes the velocity-dependent loss in strength caused by changes in contact area (evolution effect; Dieterich and Kilgore (1994)). Since our matrix-rich breccia and foliated fault gouge comprises platy chlorite grains that are well aligned (Fig. 5.8g-i), the contact area between grains may be at a maximum, explaining low values of $b$ (Ikari *et al.*, 2016; Saffer and Marone, 2003), and high $a$-$b$ for the chlorite-rich samples.

Chlorite can form from hydration of greenschist facies mafic rocks on a cooling path, or during greenschist facies hydrothermal activity (An *et al.*, 2021; Diener *et al.*, 2016). Chlorite could therefore have formed during hydrothermal activity prior to transform faulting. In the sampled STTFZ, however, the change in slip behaviour from velocity-weakening to velocity-strengthening is consistent with an increase in fault zone damage (decreased clast proportion) and associated alteration (increase in chlorite) (Fig. 5.10), which may be a general feature of oceanic transform faults. Brittle fractures, as observed in the dolerites and cemented breccia (Fig. 5.8a-d), provide a mechanism for increasing the permeability of the faults. This increased permeability can enhance fluid flow and alteration to chlorite, as suggested for rupture barrier regions along active oceanic transform faults that have been imaged geophysically (Fig. 5.10; e.g. Froment *et al.* (2014); Roland *et al.* (2010, 2012)).

### 5.5.3 Slip behaviour of oceanic transform faults

Experimental observations are consistent with geophysical observations that (1) along-strike seismic behaviour is controlled by the along-strike variation in fault zone damage and alteration (summarised in Fig. 5.10; Froment *et al.* (2014); Roland *et al.* (2010, 2012)), and (2) faults within the transform domain are frictionally weaker than the surrounding crust (Behn *et al.*, 2002; Beutel and Okal, 2003; Homberg *et al.*, 2010). Crustal transform faults that contain matrix- or gouge-rich material with interconnected phyllosilicates are likely to be weak and aseismic, as has been inferred based on seismic velocities for some segments of active oceanic transform faults (e.g. Froment *et al.*, 2014; Roland *et al.*, 2010, 2012), while regions of the crust that have not experienced much damage or alteration (or are cemented) remain strong and are capable of hosting earthquake slip. This is supported by seismic slip rates recorded during initial fracturing (Fig. 5.5d; >1 mm/s) of dolerite and cemented breccia samples, whereas such fast rates were not recorded when shearing samples with a small dolerite clast proportion.

Based on field observations in Chapter 4, deformation in the STTFZ's mafic crust occurred along pre-existing fractures such as dyke margins and cooling joints, which occur in a range of orientations. Assuming that the same control on inital fault location is applicable to active oceanic transform faults, there are abundant new surfaces for fault strands to form along and continue to supply

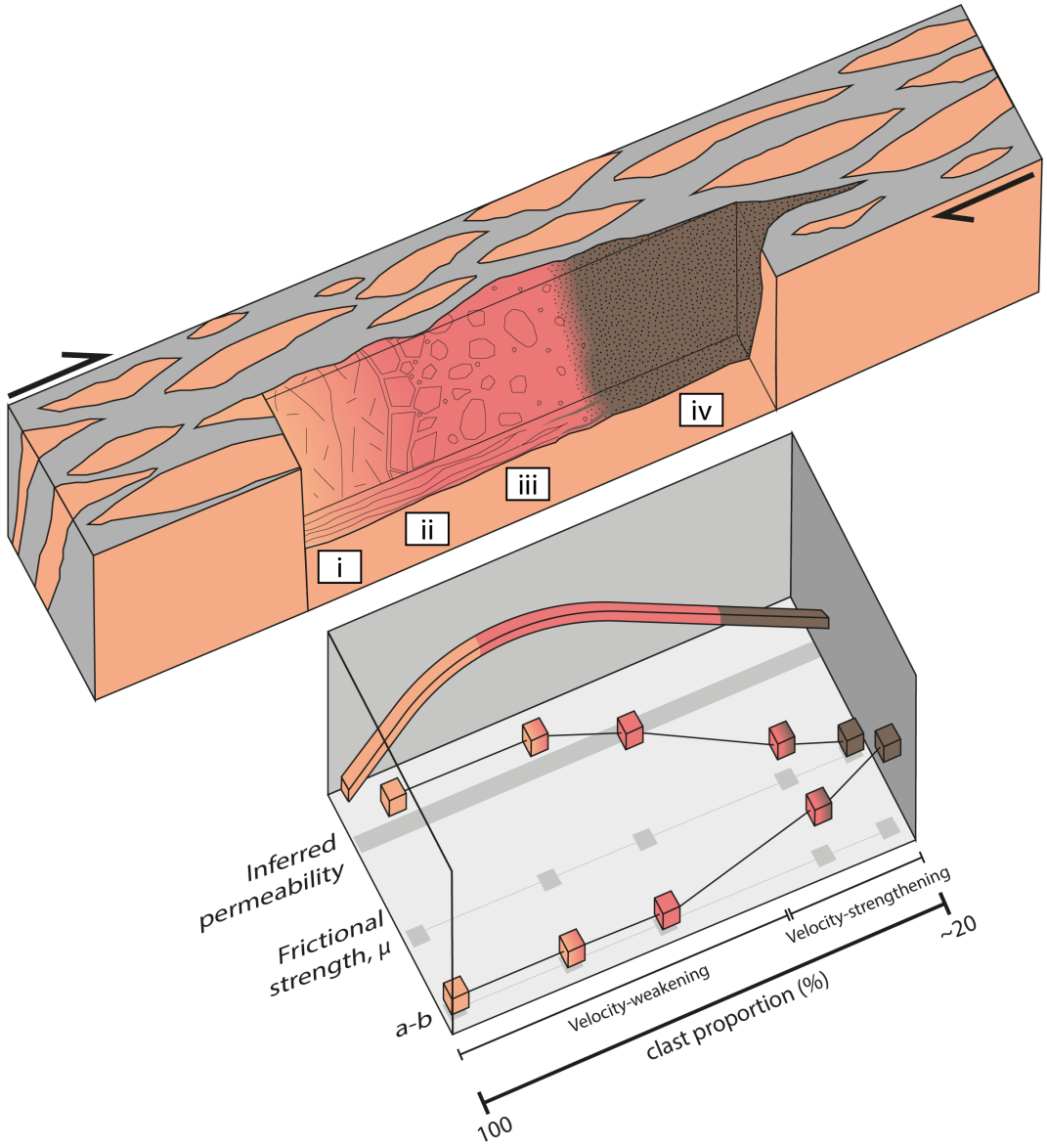


**Figure 5.10:** Schematic representation of the progressive deformation of the mafic crust within a single strand in an oceanic transform fault within a wider oceanic transform fault setting. Deformation progresses from (i) intact dolerite dykes to (ii) fractured dolerite, (ii) dolerite breccias and finally, to a (iv) chlorite-rich fault gouge. Changes in the permeability, frictional strength and velocity dependence of friction ($a$-$b$) with clast proportion (i.e. fault zone damage) are shown.

new intact material (e.g. Bergerat *et al.*, 2000; Homberg *et al.*, 2010; MacLeod and Murton, 1993). Geometrical complexities (e.g. Embley and Wilson, 1992; Fox and Gallo, 1984; MacDonald *et al.*, 1986; Pockalny *et al.*, 1988; Searle, 1981) and spatial variation in damage and alteration can result in a heterogeneous seismic behaviour of oceanic transform faults. New intact dolerite, here found to be strong and velocity-weakening, can be continually faulted leading to the local nucleation of seismicity as intact dolerite rocks fracture (Fig. 5.5d) even if mature fault zones have developed elsewhere.

## 5.6 Conclusions

We conducted direct-shear friction experiments on intact and powdered samples of dolerite from the East Pacific Rise (Hess Deep) and a series of mafic fault rocks from the exhumed Southern Troodos Transform Fault Zone of Cyprus. With decreasing dolerite clast proportion (hence increasing volume fraction of phyllosilicate-rich matrix), frictional strength decreases from $\mu = 0.85$ to 0.28 in minicore and from $\mu = 0.69$ to 0.25 in powdered samples, and frictional stability changes from velocity-weakening to velocity-strengthening. We deduce that, in modern transform fault zones, continuing deformation along faults leads to progressive changes in composition, from frictionally strong minerals in dolerite (and in fractured dolerite and cemented breccia) to well-interconnected and frictionally weak phyllosilicates (chlorite) in matrix- and gouge-rich fault rocks. This change occurs over multiple earthquakes cycles and is assisted by fluid flow to facilitate phyllosilicate growth. Our observation that frictional stability changes with fault rock type/clast proportion agrees with geophysical observations from active oceanic transform faults that suggest aseismic fault segments are characterised by increased damage and alteration.

# Chapter 6

# General discussion

This thesis is based on fieldwork conducted in the exhumed Southern Troodos Transform Fault Zone (STTFZ) in Cyprus (Chapter 2). Deformation preserved within the STTFZ is consistent with Late Cretaceous-aged, seafloor, strike-slip deformation. Within the STTFZ, later detachment and thrust faulting, associated with the emplacement and exhumation of the ophiolite, locally overprints the strike-slip transform deformation. The outcrops studied in this thesis were chosen to avoid this later deformation overprint and represent structures kinematically consistent with transform faulting. Steeply-dipping, E-W striking faults and shear zones with subhorizontal lineations are documented within the mafic crust (notably the sheeted dyke stratigraphic layer) and the serpentinised lithospheric mantle, respectively. Both the faults and the shear zones are wide (up to hundreds of metres) zones in map view, within which the degree of deformation varies. Together, the crustal faults and mantle shear zones give insight into the deformation processes that occur in an oceanic transform fault setting at $T$ <600 °C. A combination of field and microstructural observations, geochemical methods and direct-shear friction experiments allowed me to analyse the rheological evolution of the exhumed STTFZ and infer geological controls on the seismic behaviour and strength of active oceanic transform faults.

## 6.1 Summary of research questions

The overall aim of this research was to understand the geological controls on the variable seismic behaviour and weakness of oceanic transform faults

(outlined in sections 1.5-1.7), with a specific focus on deformation within the thermally-defined seismogenic zone ($T$ <600 °C), and address the following questions:

Q1: How does deformation evolve within the thermally-defined seismogenic zone of oceanic transform faults and what are the deformation mechanisms responsible?

Q2: What is the role of fluids within oceanic transform faults?

Q3: What is the geological nature of the locked and creeping patches along oceanic transform faults?

Q4: How weak are oceanic transform faults?

Below, the findings in Chapters 3, 4 and 5 are discussed to address these questions, and highlight the implications for active oceanic transform faults. This is followed by conclusions summarising the main findings and suggestions for potential future work.

### Q1: How does deformation evolve within the thermally-defined seismogenic zone of oceanic transform faults and what are the deformation mechanisms responsible?

Within the STTFZ, faults within the sheeted dykes of the crust, and shear zones in the lithospheric mantle, are particularly well exposed. Where this deformation facilitated fluid flow, deformation structures are commonly associated with hydrothermal alteration. Alteration within fault zones in the mafic crust is associated with elevated chlorite content within hydrothermally altered dolerite, while in serpentinised mantle shear zones, lizardite-dominant serpentinites are replaced by chrysotile-dominant serpentinites.

Shear zones in the lithospheric mantle section of the STTFZ are characterised by scaly and phyllonitic serpentinite, in contrast to the massive serpentinite that is predominant outside the shear zones (section 3.5). Microscopically, massive serpentinite has an isotropic lizardite-rich mesh microstructure, which differs to scaly serpentinite that has a foliated lizardite-rich ribbon texture, and phyllonitic serpentinite that has a well-foliated, fibrous chrysotile microstructure. Within serpentinite shear zones mesh textures are locally replaced with foliated scaly and phyllonitic serpentinites, inferred to reflect local

gradients in strain. Assuming that strain gradients in space represent a temporal progression of deformation, these three serpentinite types are inferred to represent a progressive deformation sequence.

Foliated lizardite-rich ribbon texture in scaly serpentinite is inferred to form from mesh textured serpentinite (massive serpentinite) by the rotation of lizardite crystals/laths into a preferred orientation (Fig. 3.13) and the dissolution of poorly-oriented lizardite crystals/laths. This microstructural transition was aided by dissolution-precipitation creep of poorly-oriented laths coupled to grain-boundary sliding, leading to the alignment of lizardite grains (Fig. 3.13) as also inferred by Viti *et al.* (2018) in their review of retrograde serpentinites in the oceanic lithosphere. The aligned lizardite grains in ribbon-textured scaly serpentinite define a foliation that allows sliding along basal planes if the foliation is well oriented relative to the principal stresses. Progressive deformation of scaly serpentinite is associated with the alteration of lizardite to chrysotile in phyllonitic serpentinite by dissolution-precipitation, as also suggested by Andreani *et al.* (2005) for serpentinites along the San Andreas System. The phyllonitic chrysotile serpentinites are foliated and deformed dominantly by fibre-on-fibre sliding.

In the STTFZ mafic crust, fault zones are characterised by dolerite breccias and chlorite-rich fault gouges, in contrast to the relatively intact sheeted dykes outside of the fault zones (section 4.4). The replacement of dolerite with breccias and chlorite-rich fault gouges in fault zones is inferred to reflect local gradients in strain, and therefore represent a temporal progression of deformation, comparable to what has been suggested for the lithospheric mantle serpentinite shear zones. This progressive deformation sequence involves intact and/or hydrothermally altered dolerite transitioning into foliated gouge-dominated fault zones that are rich in chlorite. Chlorite is present as a hydrothermal alteration mineral in dolerite ($\sim$5-10%) and as the dominant mineral in fault gouges ($<$70%). It is unknown if the higher concentration of chlorite in fault gouges is the result of mineralogical differences that predate transform faulting, or if the chlorite grew syn-kinematically during deformation.

Grain size analysis of various fault rocks (section 4.4.2/Fig. 4.6) shows that the fractal dimension, $Ds$, increases from $<$1.3 for fractured dolerites to $\sim$1.6 for breccias and to $>$1.7 for fault gouges. Together with field observations of

brittle fracture and grain size reduction in fault zones, these values suggest deformation occurred by brittle fracture ($Ds$ <1.3 for small-displacement faults), cataclasis involving constrained comminution ($Ds$ values ∼1.6 for intermediate breccias and mid-displacement faults; Sammis *et al.*, 1987), and abrasion ($Ds$ >1.7 for fault gouges and large-displacement faults; e.g. Blenkinsop, 1991; Marone and Scholz, 1989). Brittle deformation created permeability and consequent localised fluid flow that allowed the formation of a gouge, and helps to explain values of $Ds$ >1.7. Deformation of chlorite-rich gouge-dominated faults was dominated by sliding along the chlorite foliation ± pressure solution. Fracturing of the crust also allows for the local increase in permeability and fluid flow that is required to form serpentinite shear zones in the lithospheric mantle below.

The strength of a fault or shear zone is controlled by its mineralogy and the dominant deformation mechanism (Knipe, 1989). The foliation development in both the crust and lithospheric mantle is dominantly controlled by a combination of dissolution-precipitation creep coupled to grain-boundary sliding/sliding along phyllosilicate foliations. The rate of foliation development is therefore limited by the rate of dissolution-precipitation, which is dependent on temperature and grain size (section 1.4.1). Furthermore, deformation by sliding along grain boundaries or phyllosilicate foliations is controlled by the frictional properties of the grain surface and the effective normal stress acting on the foliation (section 1.3). Therefore, because the dominant mechanisms change with progressive strain, in the lithospheric mantle and mafic crust, there should be a change in the rheology of oceanic transforms with increasing strain.

**Q2: What is the role of fluids within oceanic transform faults?**

Throughout the lithospheric mantle and mafic crust of the STTFZ, evidence of fluids is ubiquitous. This presence of fluids is important for deformation as they allow for a range of processes, such as: (1) the alteration of oceanic lithosphere to mechanically weak hydrous minerals including serpentine and chlorite; (2) the operation of dissolution-precipitation; and (3) sufficient reduction in the effective normal stress by fluid pressurisation, to explain slip along poorly oriented faults.

Dolerite dykes are pervasively hydrothermally altered at greenschist facies

conditions to albite, actinolite and chlorite from their original clinopyroxene and plagioclase composition. The alteration mineralogy is more hydrous than the original igneous composition, requiring addition of fluids. As well, the abundant mineralisation including pyrite, epidote and quartz that is documented within transform-related faults and along joints within the dolerite dykes attests to localised fluid flow within the crust. Fracturing of the mafic crust during brittle deformation and cataclasis created permeable pathways in crackle and clast-supported breccias, to promote hydration and the growth of chlorite in more mature, gouge-dominated fault zones (section 4.5.2). These observations of mineralisation and chlorite growth indicate that pre-existing dyke margins and cooling joints acted as conduits for localised fluid flow within the mafic crust prior to and during STTFZ deformation. This localised fluid flow is in addition to the fluid circulation that is responsible for the pervasive hydrothermal alteration of the dolerite crust outside of fault zones. In contrast to the growth of chlorite facilitating weakening, the cementation of dolerite-rich breccias (e.g. Fig. 4.4) attests to abundant fluid flow within the sheeted dolerite dykes that act to strengthen faults (see Q4). Therefore, fluid-rock reactions leading to cementation and chlorite growth are competing processes that strengthening or weaken faults, respectively.

Additionally, the lithospheric mantle is pervasively serpentinised from its original olivine and pyroxene composition. This hydration results in the rheological weakening of the lithospheric mantle (e.g. Escartín *et al.*, 2001; Tesei *et al.*, 2018). Strike-slip kinematics, consistent with STTFZ deformation, are recorded in the serpentinite fabrics (section 3.5) suggesting serpentinisation occurred pre- or syn-transform deformation. Deformation of the serpentinised lithospheric mantle involves the replacement of lizardite with chrysotile. This concentration of chrysotile in serpentinite shear zones suggests that fluid flow was localised during deformation, because higher water:rock ratios favour chrysotile rather than lizardite (Evans, 2004). An important deformation mechanism in the lithospheric mantle is dissolution-precipitation creep (section 3.6.2); a mechanism that requires the presence of fluids (section 1.4) and aids the transition from lizardite to chrysotile in serpentinite shear zones.

Since freshly formed oceanic lithosphere is dry, the presence of fluid is required to form rheologically-weak serpentine (lithospheric mantle) and chlorite (mafic crust) during deformation like we see in faults and shear zones within

the STTFZ. This hydration is aided by the brittle fracturing of the mafic crust and lithospheric mantle locally increasing permeability, allowing for localised fluid flow within fault and shear zones. These hydration reactions promote lower frictional strengths during oceanic transform deformation (see Q4).

Finally, while fluids are required for the replacement of strong framework minerals with hydrous, weak phyllosilicates, fluids also play a role in the weakness of oceanic transforms in the form of fluid pressure. High fluid pressures are required to explain the weakness and failure of poorly-oriented oceanic transform faults by lowering the effective normal stress sufficiently (by ∼95%; Fig. 4.9) to allow deformation by frictional sliding (section 4.5.4 and Q4). To develop high fluid pressures within a transform fault requires hydrothermal flow driving fluids into the fault at a rate quicker than the fluids can escape (e.g. Faulkner and Rutter, 2001). This requires reduced permeability such as the growth of well-interconnected phyllosilicates or (e.g. Caine *et al.*, 1996) or the cementation of breccias.

**Q3: What is the geological nature of the locked and creeping patches along oceanic transform faults?**

According to geophysical observations, the seismogenic zone of oceanic transform faults can be described by two models (section 1.7): (1) A "multimode" model, where both earthquakes and aseismic creep occur along the same fault segments, but at different times (e.g. Abercrombie and Ekström, 2001; Hilley *et al.*, 2020; McGuire *et al.*, 1996); or, (2) a "single-mode, wide seismogenic patches" model, where oceanic transforms are segmented along strike into "locked patches" that can host quasi-periodic earthquakes of Mw >6.0, and creeping or microseismically active "rupture barriers", as suggested for East Pacific Rise transform faults (e.g. McGuire *et al.*, 2005). The geological nature of these locked and creeping regions has been unclear, but geological mapping of areas within the STTFZ shows that the nature and intensity of deformation varies spatially both within the lithospheric mantle (Chapter 3) and the mafic crust (Chapter 4).

Within the lithospheric mantle, foliations in scaly and phyllonitic serpentinite are inferred to develop by dissolution-precipitation creep (section 3.6.2). Additionally, serpentine is known to be velocity-strengthening at slow slip rates (∼$10^{-9}$ m/s; section 1.6; Andreani *et al.*, 2005; Kohli *et al.*, 2011; Moore

*et al.*, 1997, 1996; Reinen *et al.*, 1994). Together these observations suggest that serpentinite shear zones (scaly and phyllonitic) are likely representative of creeping portions of the lithospheric mantle. In contrast, massive and fractured serpentinites, that maintain a mesh microstructure, potentially reflect locked or relatively undeformed patches because they record little finite strain.

Direct-shear deformation experiments at room temperature and 10 MPa normal stress showed that STTFZ chlorite-rich fault gouges are velocity-strengthening (i.e. strength increases with increasing slip velocity) (Fig. 5.5b). This behaviour is consistent with these fault rocks having hosted steady creep. Additionally, gouge-rich faults within the mafic crust are typically foliated and, according to laboratory experiments, foliated fault gouges develop during slow steady creep at slip speeds $<1$ $\mu$m/s (Niemeijer, 2018; Niemeijer and Spiers, 2006). However, large portions of the crust within the STTFZ contain relatively intact dolerite and cemented breccias, which record brittle deformation (section 4.4). In the direct-shear experiments performed for this project (Chapter 5), intact dolerite and cemented breccias are velocity-weakening (i.e. strength decreases with increasing slip velocity, characteristic of earthquakes), and initially break at high slip velocities (section 5.4.3). The slip velocities for the initial breaks in dolerite observed in my experiments range from 0.36 to $>18.65$ mm/s (Fig. 5.5d), characteristic of seismic slip ($>1$ mm/s; Daub *et al.*, 2011; Rowe and Griffith, 2015; Rubin, 2008).

Scaly and phyllonitic serpentinite shear zones in the lithospheric mantle, and chlorite-rich fault gouges in the mafic crust, are interpreted to have contrasting seismic behaviour to massive serpentinite and relatively intact dolerite. This distinction may be consistent with the *"single-mode, wide seismogenic patches"* model (e.g. Gofar, Discovery and Quebreda faults on the East Pacific Rise; McGuire *et al.*, 2005). In this model, increased damage and alteration of the mafic crust and lithospheric mantle promotes creep behaviour at low $T$ (within the thermally-defined seismogenic zone) without the onset of plasticity. Intact dolerite, cemented breccias and mesh textured serpentinite represent strongly seismically coupled regions while the most deformed and altered chlorite-rich fault zones and foliated serpentinite shear zones represent poorly seismically coupled regions. This implies that with time, the slip style of a fault can transition from being locked and seismic to creeping as a function of damage and alteration.

From the micro- to macro-scale, discrete fractures and ductile fabrics are mutually cross-cutting in serpentinite shear zones (Fig. 3.5), suggesting that these macroscopically ductile shear zones may not strictly creep. An explanation for this observation is the conditionally stable nature of serpentine – serpentine creeps at low slip rates, while at higher slip velocities ($\sim$0.1 mm/s; Kohli *et al.*, 2011), it can become velocity-weakening and allow the propagation of earthquakes. According to laboratory experiments, like serpentine, phyllosilicates can creep at low strain rates providing the rate of pressure solution can keep up with the slip rate ($<$1 $\mu$m/s; Niemeijer, 2018; Niemeijer and Spiers, 2006). However, at higher sliding velocities foliated fault gouges may allow velocity-weakening behaviour and the propagation of earthquakes ($>$1 $\mu$m/s; Niemeijer, 2018; Niemeijer and Spiers, 2006). Increased slip rates promoting a velocity-weakening response in serpentinite shear zones (and possibly chlorite-rich fault gouges) may be caused by failure within the mafic crust propagating down, or failure of locked lithospheric mantle adjacent to these creeping segments (Fig. 6.1). This highlights that the seismic behaviour of oceanic transforms depends on the conditions of deformation where transient behaviour can occur depending on the slip rates (summarised in Fig. 6.1). Therefore, oceanic transforms follow the *"multimode fault"* model (e.g. Charlie-Gibbs transform on the Mid Atlantic Ridge; Aderhold and Abercrombie, 2016).

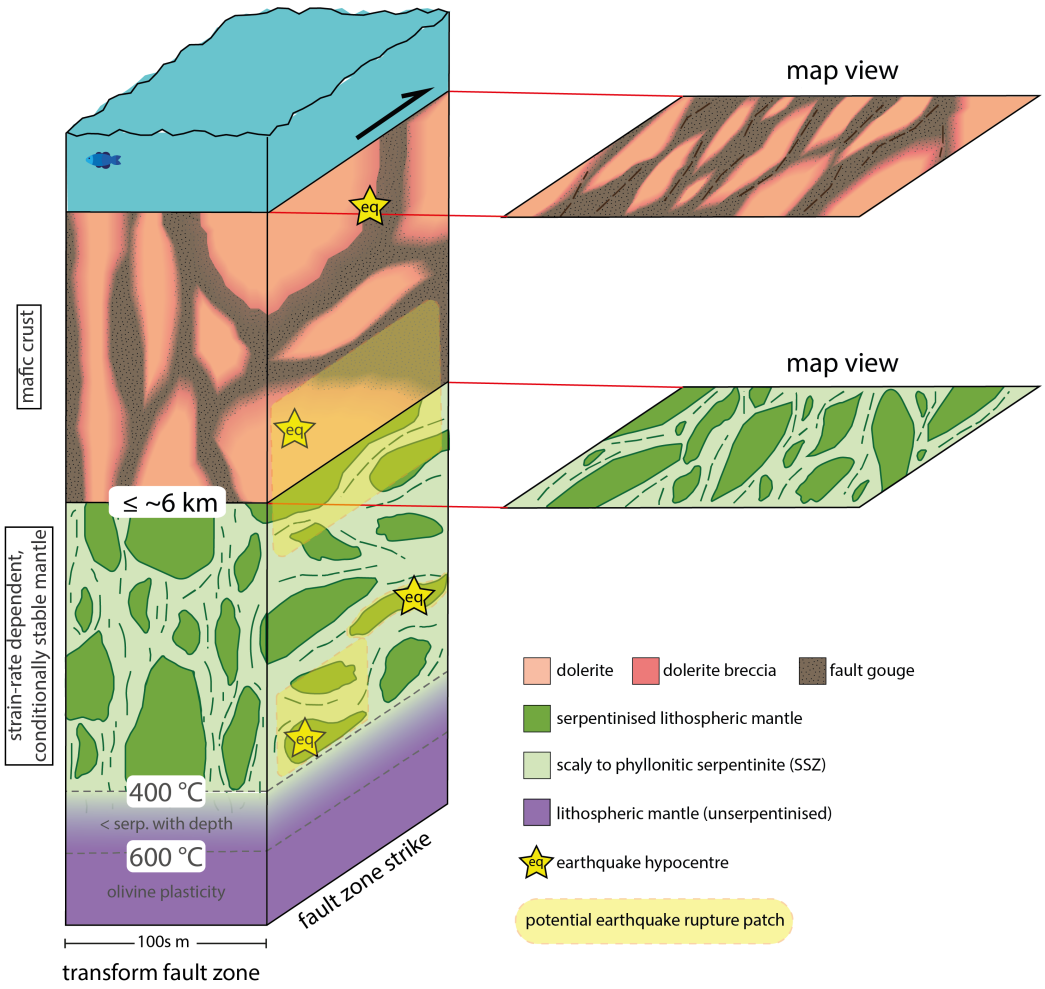


**Figure 6.1:** Schematic summary diagram showing the deformation and mode of slip (locked, creeping and conditionally stable patches) along an oceanic transform fault based on observations from the Southern Troodos Transform Fault Zone. Regions comprising intact dolerite, dolerite breccia (cemented) and massive serpentinised lithospheric mantle (dark green) represent potential locked sites where earthquakes can nucleate (e.g. yellow stars). Fault gouge in the crust and scaly to phyllonitic serpentinite in the lithospheric mantle can creep (at low strain rates) or allow the propagation of earthquakes (at elevated strain rates; shaded yellow areas). The inferred progressive deformation observed in the Southern Troodos Transform Fault Zone suggests a brittle to ductile transition that is induced by the growth of serpentine and chlorite, at temperatures well below the base of thermally-defined seismogenic zone (<600 °C). For more details on the deformation of the lithospheric mantle and mafic crust see Figs. 3.14 and 4.10.

**Q4: How weak are oceanic transform faults?**

Oceanic transforms are typically active at high angles to the maximum principal stress, $\sigma_1$, sometimes nearly perpendicular to it (e.g. Angelier *et al.*, 2000; Homberg *et al.*, 2010; Townend and Zoback, 2004; Zoback, 1991; Zoback *et al.*, 1987) (section 4.5.4). In order to slip at such unfavourable orientations, oceanic transforms must be rheologically extremely weak compared to the surrounding crust (Behn *et al.*, 2002; Bergerat *et al.*, 2000; Beutel and Okal, 2003; Homberg *et al.*, 2010; Zoback, 1991). For example, an effective friction as low as $\sim$0.01 is suggested for the Tjörnes Fracture Zone (Homberg *et al.*, 2010). One hypothesis used to explain the inherent weakness of oceanic transform faults is the hydration of mafic and ultramafic minerals to frictionally-weak phyllosilicates and serpentine (Behn *et al.*, 2007; Boettcher and Jordan, 2004; Froment *et al.*, 2014; McGuire *et al.*, 2012; Moore *et al.*, 1997; Roland *et al.*, 2010, 2012; Van Avendonk *et al.*, 2001). This hypothesis is supported by STTFZ observations where alteration of mafic and ultramafic minerals to chlorite (Chapter 4) and serpentine (Chapter 3), respectively, is ubiquitous within faults and shear zones.

Fresh ultramafic rocks, dominated by olivine and pyroxene, are considered strong (e.g. Boettcher *et al.*, 2007). Likewise, hydrothermally altered dolerite is strong (section 5.4.1), with a $\mu$ >0.6 (Fig. 6.2). Cemented breccias are also strong (0.6< $\mu$ <0.8) according to the same experiments despite having a lower dolerite clast proportion. This is because cemented breccias are cemented with the same greenschist facies mineral assemblage as the dolerite clasts (+quartz). In contrast to this, serpentine is known to be weak with mesh textured serpentinite having a $\mu$ $\sim$0.3 under shallow crustal conditions (Moore *et al.*, 1997), and chrysotile serpentine having a frictional strength as low as $\sim$0.1 under the same conditions (Tesei *et al.*, 2018). Similarly, experiments conducted in this thesis, at room $T$ and 10 MPa normal stress (Chapter 5), show that the frictional strength of mature, chlorite-rich, crustal fault gouge from the STTFZ is <0.3 (Fig. 6.2). Therefore, the presence of serpentine and chlorite, particularly where well foliated and interconnected (Handy, 1990), is an effective weakening mechanism for oceanic transforms (as suggested for mature continental faults; e.g. Carpenter *et al.*, 2012; Collettini *et al.*, 2009; Imber *et al.*, 1997; Lockner *et al.*, 2011; Schleicher *et al.*, 2012; Wallis *et al.*, 2013; Wibberley, 2005).

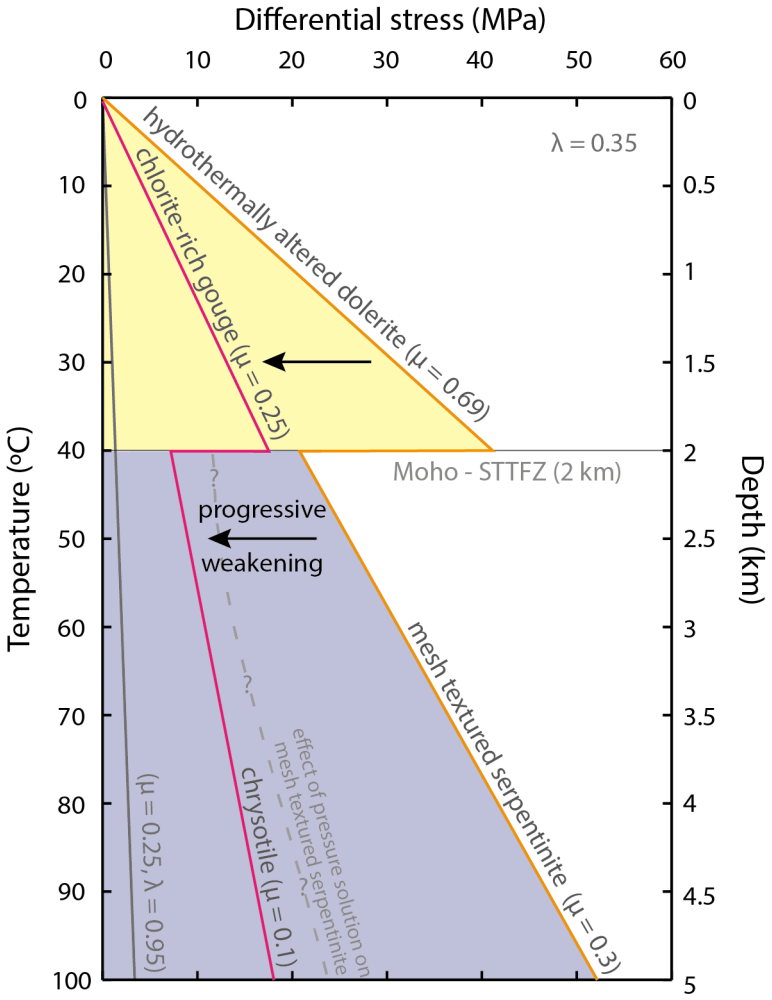


**Figure 6.2:** Strength profile for the oceanic lithosphere summarising the results in this thesis. Within the Southern Troodos Transform Fault Zone (STTFZ) deformation is inferred to progress from hydrothermally altered dolerite ($\mu$ = 0.69; Chapter 5) to chlorite-rich fault gouges ($\mu$ = 0.25; Chapter 5) in the crust and from mesh textured serpentinite ($\mu$ = 0.3; Moore *et al.*, 1997) to chrysotile-dominant phyllonitic serpentinite ($\mu$ = 0.1; Tesei *et al.*, 2018) in the serpentinised lithospheric mantle. This transition promotes progressive weakening - solid orange line to solid pink line. High pore fluid pressures ($\lambda$ = 0.95; Chapter 4) are required for slip along poorly oriented oceanic transform faults, which act to weaken faults (solid grey line). Pressure solution (dashed line) is considered an important process for deformation in the STTFZ, especially within the serpentinised lithospheric mantle. Although there are no constraints on the rate of pressure solution in serpentine, it would be expected to reduce the differential stress of faults below that of their frictional strengths (e.g. Rutter, 1976). The depth to the Moho in Cyprus is thought to sit at ~2 km (Gass *et al.*, 1994). Yellow shaded area represents the mafic crust and the purple shaded area represent the lithospheric mantle.

The frictional strength of foliated serpentine and chlorite (Fig. 6.2) is, however, not sufficiently low to explain the angle between some active transform faults and the principal stresses. Elevated fluid pressures act to lower the effective normal stress (section 1.3) and have been suggested to play a role in reducing the strength of some major continental strike-slip faults (Faulkner and Rutter, 2001; Fulton and Saffer, 2009; Jefferies *et al.*, 2006; Wang, 2011). Therefore, elevated fluid pressures could also explain slip along poorly oriented oceanic transforms (section 4.5.4). However, within the STTFZ, there is little evidence for fluid overpressure such as veining recording tensile fracturing. This implies that the STTFZ was reactivated at fluid pressures insufficient for hydrofracturing, but sufficient to reactivate poorly oriented faults (Fig. 6.2). Mohr circle calculations (Fig. 4.9; section 4.5.4) assumed $\sigma_1 = \sigma_{vertical}$ at the ridge and 2 km thick crust (density = 2.9 g/cm$^3$) below 3 km of water (density = 1.0 g/cm$^3$) to estimate $\sigma_{vertical} = \sim$85 MPa. For failure to occur on a poorly oriented fault ($\theta = 75°$) at this vertical stress, such as what is inferred for the STTFZ, fluid pressures are needed to be $\sim$95% lithostatic values.

The weakness of oceanic transforms within the thermally-defined seismogenic zone ($T$ <600 °C) is likely a result of the hydration of ultramafic and mafic minerals to frictionally weak serpentine and phyllosilicates following fault zone damage and increased fluid flow, and aided by high fluid pressures (Fig. 6.2). In addition to the effect of fluids stabilising weak minerals, fluid present conditions allow the operation of pressure solution creep in serpentinites (section 1.4) and maybe also in crustal faults where conditions allow (i.e. slow slip rates).

# Chapter 7

# Conclusions and Future Work

## 7.1 Conclusions

The ultimate aim of this thesis was to investigate the geological controls on the variable seismic behaviour observed along active oceanic transform faults, and the reasons for their inferred mechanical weakness. To address these aims, observations made in the field were combined with microstructural observations, some geochemical analysis, grain-size analysis and the results of direct-shear friction experiments of samples from the Southern Troodos Transform Fault Zone, Cyprus, and the East Pacific Rise. The main conclusions are as follows:

- Deformation within the Southern Troodos Transform Fault Zone was accommodated heterogeneously. More specifically, deformation of the sheeted dyke stratigraphic layer and lithospheric mantle was localised into anastomosing faults and serpentinite shear zones, respectively.

- Serpentinite deformed progressively from massive serpentinite with a lizardite-dominant mesh texture to chrysotile-dominated phyllonitic serpentinite. The progressive development of foliated serpentinite fabrics (ribbon-textured scaly and phyllonitic serpentinites) is an effective mechanical weakening mechanism within serpentinite shear zones. This work shows that pressure solution and frictional sliding are important mechanisms contributing to the progressive deformation of serpentinite.

- Ductile deformation of the serpentinised lithospheric mantle took place at $T$ ∼200-300 °C, well within the thermally-defined seismogenic zone in olivine-dominated oceanic lithosphere ($T$ <600 °C). Ductile deformation

of serpentinite can therefore explain fault weakness and aseismic creep at temperatures far cooler than the inferred base of the thermally-controlled seismogenic zone at slow slip speeds. Abundant brittle fractures mutually cross-cut with fabrics in serpentinite shear zones, attesting to mixed brittle-ductile deformation and possibly a multimode behaviour for serpentinite shear zones. Events such as earthquake propagation down from the crust could rupture the serpentinised lithospheric mantle due to the conditionally stable nature of serpentinite, whose frictional stability is dependent on velocity. Similarly, regions of the lithospheric mantle that are poorly serpentinised could act as sites of earthquake nucleation that could propagate into the surrounding serpentinite shear zones, if loaded by surrounding creeping zones.

- Deformation of the mafic crust took place within conditions associated with greenschist facies alteration ($T$ ~300 °C), therefore at $T$ well within the expected thermally-defined seismogenic zone ($T$ <600 °C). Progressive deformation is documented within the sheeted dyke stratigraphic layer. Brittle deformation of the sheeted dykes initially occurred along faults parallel to pre-existing features such as dyke margins and cooling joints. With an inferred increase in deformation, cataclasis and gouge formation (±pressure solution) were active deformation mechanisms and resulted in the transition from intact dolerite to dolerite-breccias and ultimately a chlorite-rich fault gouge.

- The transition from relatively intact dolerite to chlorite-rich fault gouge in crustal faults is accompanied by a weakening from $\mu$ ~0.7 in intact dolerite to $\mu$ <0.3 for fault gouges. A change in frictional stability from velocity-weakening (capable of seismic slip) in dolerites and cemented breccias to velocity-strengthening behaviour (creeps aseismically) in (uncemented) matrix-rich breccias and fault gouges also occurs. These results suggested frictional weakness is associated with velocity-strengthening behaviour/more stable sliding along oceanic transform faults.

- The frictional strength of Southern Troodos Transform Fault Zone chlorite-rich fault gouge ($\mu$ = 0.3) is higher than the effective friction of ~0.01 that is suggested for transform faults (e.g. Homberg *et al.*, 2010). Therefore, high pore fluid pressures (near lithostatic) are required to facilitate

slip along faults and explain oceanic transform fault weakness if faults are severely misoriented relative to the greatest principal compressive stress.

- Overall, within the thermally-defined seismogenic zone, aseismic behaviour and oceanic transform fault weakness can be explained by the progressive formation of chrysotile-rich foliated serpentinite shear zones in the mantle and chlorite-rich foliated fault gouges in the crust. In both the crust and mantle, hydration reactions replace stronger phases with weak phases that are more frictionally stable. Therefore, brittle deformation and fluid-rock reactions are key factors in the distribution of seismicity and fault strength; with weak hydrated regions dominated by creep (with the potential to host local seismic slip at elevated slip rates) and unaltered, relatively intact regions dominated by seismic slip. The role of fluid pressure is also important since high fluid pressures can act to lower the normal stress on a fault and make it more frictionally stable. Therefore, along-strike variation in material properties and fluid pressures play key roles in controlling the seismic behaviour and strength of oceanic transform faults.

## 7.2 Future work

The results of this work have led to several new questions related to the deformation and seismic style of oceanic transform faults that have not been addressed in this thesis. These are discussed briefly below:

A progressive weakening model is proposed for individual faults within the mafic crust and lithospheric mantle of the Southern Troodos Transform Fault Zone. This model suggests that these faults weaken and become more aseismic with cumulative strain (continued damage and alteration). However, how many earthquake cycles or how much displacement is required to sufficiently alter the mafic crust to form substantially weak faults remains unclear. Some studies suggest that some faults can experience rapid mineralogical and structural alteration (e.g. Lacroix *et al.*, 2015). However, the rate of fault rock formation and alteration along oceanic transform faults is poorly constrained. Fieldwork and sampling

of fault rocks along a transect along fault, away from the ridge, could allow an assessment of the displacement-fault rock/alteration relationship. An opportunity to constrain this may be found in the Tjönes Fracture Zone, Iceland. However, this would only apply to near-surface conditions in the Tjörnes Fracture Zone because of limited exhumation.

Some oceanic transforms display quasi-repeating earthquakes that rupture the same fault patch (e.g. the EPR transform faults; McGuire *et al.*, 2005). So why do some earthquakes that are generated at oceanic transform faults recur on the same fault patch at somewhat predictable intervals (e.g. Gofar and Discovery faults on the EPR; McGuire, 2008)? An explanation for this may be low rates of alteration of the dolerite or high rates of cementation to maintain strong portions of the fault. A possible way to test this would be to carry out fieldwork along these fault zones to collect dredged samples from locked and creeping portions of the fault to see if they comprise fault rocks with variable amounts of phyllosilicates/cement. However, collecting representative samples from the right depth range would be difficult to target. Sampling would have to take place where there was some level of exhumation of a fault on the seafloor.

The global average seismic coupling for oceanic transform faults is ∼0.15 (Boettcher and Jordan, 2004), however some faults have a much higher seismic coupling. For example, the Clipperton fault has a seismic coupling of 0.53 (Boettcher and Jordan, 2004) and the Charlie Gibbs transform fault may have a seismic coupling as high as 0.88 (Aderhold and Abercrombie, 2016). This raises the question as to why the seismic coupling of some oceanic transform faults is so high, particularly given that only relatively small amounts of alteration is required to form some very weak faults (e.g. Escartín *et al.*, 2001, suggest ∼10-15% serpentinisation is required to weaken a fault to that of pure serpentine). Variation in the degree of alteration and/or cementation may also explain variable coupling between different oceanic transforms and so could be tested by sampling along transects of these active faults to determine if there are different degrees of alteration between different active faults. However, like the question above, it is unknown if these samples would be representative of appropriate deformation.

Serpentine is considered a critical mineral in controlling the strength and seismic behaviour of oceanic transforms and largely deforms by dissolution-precipitation creep. However, the rates of dissolution-precipitation /pressure solution in serpentine are poorly constrained. A way of investigating the rates of pressure solution in serpentine could be done by laboratory indentation experiments such as those carried out on quartz by Gratier *et al.* (2009), on calcite by Zubtsov *et al.* (2005) and on antigorite by Hansen *et al.* (2020).

In Chapter 3 a progressive evolution from mesh textured serpentinite through ribbon textured scaly serpentinite to a chrysotile phyllonite was proposed. This transition was inferred to represent a progressive weakening due to the formation of a foliation. However, a quantitive assessment of how this fabric evolution (and polytype change) contributed to the weakening of the lithospheric mantle was not made in this thesis. A way to constrain this quantitively is to conduct high temperature and pressure experiments (e.g. Chernak and Hirth, 2010) on these natural fault rocks, whose microstructure and serpentine types are well constrained, at conditions where pressure solution creep is efficient at laboratory strain rates (i.e. small grain sizes and high temperatures).

Progressive deformation in the mafic dolerite crust in the STTFZ resulted in cemented breccia-dominated fault zones and gouge-dominated fault zones (Chapter 4). Chlorite is present as a hydrothermal alteration mineral in dolerite ($\sim$5-10%) and as the dominant mineral in fault gouges ($<$70%). It is unknown if the chlorite in fault gouges grows syn-kinematically or is the result of a pre-existing compositional difference. Consequently, there are two ways to form a foliation in the gouge-dominated fault zones: (1) growth of chlorite in a preferred orientation during deformation or (2) the rotation and alignment of pre-existing chlorite. If chlorite was grown syn-kinematically, chlorite would be observed in stress shadows or as slickenfibres within the fault. Conversely, for the rotation model, chlorite would not be found in these areas. Further field work in the STTFZ and microstructural work on collected samples to look for such evidence may help to determine, which of these models are correct. Additionally, the formation of cemented breccias may require different conditions to the formation of chlorite-rich fault gouges,

such as a change in temperature. Chlorite and amphibole spot SEM or probe analysis could be used for geothermometry to determine the temperatures of formation for each of the fault rocks.

In fault zones, where brittle fracture and cataclasis are common, it is unclear how high pore fluid pressures can be maintained in a subvertical fault system. However, calculations in Chapter 4 suggests that oceanic transform faults require high pore fluid pressures owing to their unfavourable stress orientations (Chapter 4). This requires the fluid influx into the faults to be greater than the leakage from the fault system (e.g. Faulkner and Rutter, 2001). A test of the permeability of the variable fault rocks in the Southern Troodos Transform Fault Zone may explain if the permeability is plausibly low, and in which fault rocks, to cause fluid pressurisation and allow slip.

# References


Abercrombie, R. E. and Ekström, G. (2001). Earthquake slip on oceanic transform faults. *Nature*, *410*, 74–77.

Aderhold, K. and Abercrombie, R. E. (2016). The 2015 Mw 7.1 earthquake on the Charlie-Gibbs transform fault: Repeating earthquakes and multimodal slip on a slow oceanic transform. *Geophysical Research Letters*, *43*(12), 6119–6128.

Aki, K. (1966). Generation and propagation of G waves from the Niigata Earthquake of June 16, 1964. Part 2. Estimation of earthquake movement, released energy, and stress-strain drop from the G wave spectrum. *Bulletin of the Earthquake Research Institute, University of Tokyo*, *44*, 73–88.

Allen, C. G. (1975). *The petrology of a portion of the Troodos plutonic complex, Cyprus*. Unpublished Ph.D. Thesis, Cambridge.

Allerton, S. and Vine, F. J. (1987). Spreading structure of the Troodos ophiolite, Cyprus: some paleomagnetic constraints. *Geology*, *15*, 593–597.

Allerton, S. and Vine, F. J. (1990). Palaeomagnetic and structural studies of the southeastern part of the Troodos complex. *Proceedings of the Symposium, Troodos 1987*, *Geological Survey Department*, 99–110.

Allerton, S. and Vine, F. J. (1991). Spreading evolution of the Troodos ophiolite, Cyprus. *Geology*, *19*, 637–640.

Alt, J. C., Honnorez, J., Laverne, C., and Emmermann, R. (1986). Hydrothermal alteration of a 1 km section through the upper oceanic crust, Deep Sea Drilling Project Hole 504B: Mineralogy, chemistry and evolution of seawater-basalt interactions. *Journal of Geophysical Research: Solid Earth*, *91*(B10), 10309–10335.

Amiguet, E., Reynard, B., Caracas, R., Van De Moortéle, B., Hilairet, N., and Wang, Y. (2012). Creep of phyllosilicates at the onset of plate tectonics. *Earth and Planetary Science Letters*, *345-348*, 142–150.

Amiguet, E., Van De Moortéle, B., Cordier, P., Hilairet, N., and Reynard, B. (2014). Deformation mechanisms and rheology of serpentines in experiments and in nature. *Journal of Geophysical Research*, *119*, 4640–4655.

An, L.-J. and Sammis, C. G. (1994). Particle size distribution of cataclastic fault materials from Southern California: A 3D study. *Pure and Applied Geophysics*, *143*(1), 203–227.

An, M., Zhang, F., Min, K.-B., Elsworth, D., Marone, C., and He, C. (2021). The Potential for Low-Grade Metamorphism to Facilitate Fault Instability in a Geothermal Reservoir. *Geophysical Research Letters*, *48*(11), e2021GL093552.

Anderson, E. M. (1951). *The dynamics of faulting and dyke formation with applications to Britain*. Edinburgh: Oliver and Boyd.

Andreani, M., Boullier, A. M., and Gratier, J. P. (2005). Development of schistosity by dissolution-crystallization in a Californian serpentinite gouge. *Journal of Structural Geology*, *27*(12), 2256–226.

Andreani, M., Mével, C., Boullier, A. M., and Escartín, J. (2007). Dynamic control on serpentine crystallization in veins: Constraints on hydration processes in oceanic peridotites. *Geochemistry, Geophysics, Geosystems*, *8*(2).

Angelier, J., Bergerat, F., and Homberg, C. (2000). Variable coupling across the weak oceanic transform fault: Flateyjarskagi, Iceland. *Terra Nova*, *12*, 97–101.

Auzende, A.-L., Escartín, J., Walte, N. P., Guillot, S., Hirth, G., and Frost, D. J. (2015). Deformation mechanisms of antigorite serpentinite at subduction zone conditions determined from experimentally and naturally deformed rocks. *Earth and Planetary Science Letters*, *411*, 229–240.

Auzende, J. M., Bideau, D., Bonatti, E., Cannat, M., Honnorez, J., Lagabrielle, Y., Malavieille, J., Mamaloukas-Frangoulis, V., and Mével, C.

(1989). Direct observation of a section through slow-spreading oceanic crust. *Nature*, *337*(6209), 726–729.

Bach, W., Paulick, H., Garrido, C. J., Ildefonse, B., Meurer, W. P., and Humphris, S. E. (2006). Unraveling the sequence of serpentinization reactions: petrography, mineral chemistry, and petrophysics of serpentinites from MAR 15°N (ODP Leg 209, Site 1274). *Geophysical Research Letters*, *33*(13).

Bailey, W. R., Holdsworth, R. E., and Swarbrick, R. E. (2000). Kinematic history of a reactivated oceanic suture: the Mamonia Complex Suture Zone, SW Cyprus. *Journal of the Geological Society*, *157*(6), 1107–1126.

Banks, G. J. (2004). *Accretion of the lower oceanic crust in the Troodos ophiolite: textural and geochemical constraints from drill core CY-4, Cyprus*. Unpublished Ph.D. Thesis, Cardiff.

Beall, A., Fagereng, A., and Ellis, S. (2019). Strength of Strained Two-Phase Mixtures: Application to Rapid Creep and Stress Amplification in Subduction Zone Mélange. *Geophysical Research Letters*, *46*(1), 169–178.

Bear, L. M. (1960). The geology and mineral resources of the Akaki-Lythrodonda area. *Cyprus Geological Survey Department Memoir No. 3*, 122.

Beeler, N. M. (2007). *The Seismogenic Zone of Subduction Thrust Faults*, 370–449. Columbia University Press.

Behn, M. D., Boettcher, M. S., and Hirth, G. (2007). Thermal structure of oceanic transform faults. *Geology*, *35*(4), 307–310.

Behn, M. D., Lin, J., and Zuber, M. T. (2002). Evidence for weak oceanic transform faults. *Geophysical Research Letters*, *29*(24), 60–64.

Benn, K. and Laurent, R. (1987). Intrusive suite documented in the Troodos ophiolite plutonic complex, Cyprus. *Geology*, *15*, 821–824.

Bergerat, F., Angelier, J., and Homberg, C. (2000). Tectonic analysis of the Husavik-Flatey Fault (northern Iceland) and mechanisms of an oceanic transform zone, the Tjörnes Fracture Zone. *Tectonics*, *19*(6), 1161–1177.

Beutel, E. K. and Okal, E. A. (2003). Strength asperities along oceanic transform faults: A model for the origin of extensional earthquakes on the Eltanin transform system. *Earth and Planetary Science Letters*, *216*(1-2), 27–41.

Bickert, M., Lavier, L., and Cannat, M. (2020). How do detachment faults form at ultraslow mid-ocean ridges in a thick axial lithosphere? *Earth and Planetary Science Letters*, *533*.

Billi, A. and Storti, F. (2004). Fractal distribution of particle size in carbonate cataclastic rocks from the core of a regional strike-slip fault zone. *Tectonophysics*, *384*(1-4), 115–128.

Bird, P., Kagan, Y. Y., and Jackson, D. D. (2002). Plate Tectonics and Earthquake Potential of Spreading Ridges and Oceanic Transform Faults. *Geodynamics Series 30*, 203–218.

Blanpied, M. L., Marone, C. J., Lockner, D. A., Byerlee, J. D., and King, D. P. (1998). Quantitative measure of the variation in fault rheology due to fluid-rock interactions. *Journal of Geophysical Research: Solid Earth*, *103*(B5), 9691–9712.

Blenkinsop, T. G. (1991). Cataclasis and Processes of Particle Size Reduction. *Pageoph*, *136*(1), 59–86.

Blome, C. D. and Irwin, W. P. (1985). Equivalent radiolarian ages from ophiolitic terranes of Cyprus and Oman. *Geology*, *13*, 401–404.

Boettcher, M. S., Hirth, G., and Evans, B. (2007). Olivine friction at the base of oceanic seismogenic zones. *Journal of Geophysical Research: Solid Earth*, *112*, B01205.

Boettcher, M. S. and Jordan, T. H. (2004). Earthquake scaling relations for mid-ocean ridge transform faults. *Journal of Geophysical Research: Solid Earth*, *109*(B12), B12302.

Boettcher, M. S. and McGuire, J. J. (2009). Scaling relations for seismic cycles on mid-ocean ridge transform faults. *Geophysical Research Letters*, *36*(21), 1–5.

Bonhommet, N., Roperch, P., and Calza, F. (1988). Paleomagnetic arguments for block rotations along the Arakapas fault (Cyprus). *Geology*, *16*, 422–425.

Bos, B. and Spiers, C. J. (2002). Frictional-viscous flow of phyllosilicate-bearing fault rock: Microphysical model and implications for crustal strength profiles. *Journal of Geophysical Research: Solid Earth*, *107*(B22028), 1–13.

Boudier, F., Baronnet, A., and Mainprice, D. (2010). Serpentine Mineral Replacements of Natural Olivine and their Seismic Implications: Oceanic Lizardite versus Subduction-Related Antigorite. *Journal of Petrology*, *51*(1-2), 495–512.

Brace, W. F. and Kohlstedt, D. L. (1980). Limits of lithospheric stress imposed by laboratory experiments. *Journal of Geophysical Research*, *85*(B11), 6248–6252.

Brantut, N., Passelegue, F. X., Deldicque, D., Rouzaud, J.-N., and Schubnel, A. (2016). Dynamic weakening and amorphization in serpentinite during laboratory earthquakes. *Geology*, *44*(8), 607–610.

Braunmiller, J. and Nábělek, J. (2008). Segmentation of the Blanco Transform Fault Zone from earthquake analysis: Complex tectonics of an oceanic transform fault. *Journal of Geophysical Research*, *113*(B7), B07108.

Brune, J. N. (1968). Seismic moment, seismicity, and rate of slip along major fault zones. *Journal of Geophysical Research*, *73*(2), 777–784.

Bürgmann, R. and Dresen, G. (2008). Rheology of the Lower Crust and Upper Mantle: Evidence from Rock Mechanics, Geodesy, and Field Observations. *Annual Review of Earth and Planetary Sciences*, *36*(1), 531–567.

Byerlee, J. D. (1978). Friction of Rocks. *Pageoph*, *116*, 615–626.

Caine, Jonathan, S., Evans, James, P., and Forster, C. B. (1996). Fault zone architecture and permeability structure. *Geology*, *24*(11), 1025–1028.

Cann, J., Prichard, H., Malpas, J., and Xenophontos, C. (2001). Oceanic inside corner detachments of the Limassol Forest area, Troodos ophiolite, Cyprus. *Journal of the Geological Society*, *158*(Nicosia,), 757–767.

Cann, J. R., Blackman, D. K., Smith, D. K., McAllister, E., Janssen, B., Mello, S., Avgerinos, E., Pascoe, A. R., and Escartín, J. (1997). Corrugated slip

surfaces formed at ridge-transform intersections on the Mid-Atlantic Ridge. *Nature*, *385*(6614), 329–332.

Cannat, M. (1993). Emplacement of mantle rocks in the seafloor at mid-ocean ridges. *Journal of Geophysical Research: Solid Earth*, *98*(B3), 4163–4172.

Cannat, M., Mével, C., Maia, M., Deplus, C., Durand, C., Gente, P., Agrinier, P., Belarouchi, A., Dubuisson, G., Humler, E., and Reynolds, J. (1995). Thin crust, ultramafic exposures, and rugged faulting patterns at the Mid-Atlantic Ridge (22°-24°N). *Geology*, *23*(1), 49–52.

Carpenter, B. M., Marone, C., and Saffer, D. M. (2011). Weakness of the San Andreas Fault revealed by samples from the active fault zone. *Nature Geoscience*, *4*(4), 251–254.

Carpenter, B. M., Saffer, D. M., and Marone, C. (2012). Frictional properties and sliding stability of the San Andreas fault from deep drill core. *Geology*, *40*(8), 759–762.

Ceuleneer, G., Nicolas, A., and Boudier, F. (1988). Mantle flow patterns at an oceanic spreading centre: The Oman peridotites record. *Tectonophysics*, *151*, 1–26.

Chatzaras, V., Tikoff, B., Kruckenberg, S. C., Titus, S. J., Teyssier, C., and Drury, M. R. (2020). Stress variations in space and time within the mantle section of an oceanic transform zone: Evidence for the seismic cycle. *Geology*, *48*, 569–573.

Chen, G. and Robertson, A. (2020). Formation of a Late Cretaceous continental margin arc and an Early Cenozoic back-arc basin in the Kyrenia Range, northern Cyprus related to S-Neotethyan subduction. *22nd EGU General Assembly*.

Chen, G. and Robertson, A. H. F. (2019). Provenance and magmatic-tectonic setting of Campanian-aged volcaniclastic sandstones of the Kannaviou Formation in western Cyprus: Evidence for a South-Neotethyan continental margin volcanic arc. *Sedimentary Geology*, *388*, 114–138.

Chernak, L. J. and Hirth, G. (2010). Deformation of antigorite serpentinite at high temperature and pressure. *Earth and Planetary Science Letters*, *296*(1-2), 23–33.

Chester, F. M., Evans, J. P., and Biegel, R. L. (1993). Internal structure and weakening mechanisms of the San Andreas Fault. *Journal of Geophysical Research: Solid Earth*, *98*(B1), 771–786.

Chester, F. M., Rowe, C. D., Ujiie, K., Kirkpatrick, J., Regalla, C., Remitti, F., Casey Moore, J., Toy, V. G., Wolfson-Schwehr, M., Bose, S., Kameda, J., Mori, J. J., Brodsky, E. E., Eguchi, N., Toczko, S., 343, E., and Scientists, T. (2013). Structure and Composition of the Plate-Boundary Slip Zone for the 2011 Tohoku-Oki Earthquake. *Science*, *342*(6163), 1208–1211.

Chopra, P. N. and Paterson, M. S. (1984). The role of water in the deformation of dunite. *Journal of Geophysical Research*, *89*, 7861–7876.

Clube, T. M. M., Creer, K. M., and Robertson, A. H. F. (1985). Palaeorotation of the Troodos microplate, Cyprus. *Nature*, *317*, 522–525.

Clube, T. M. M. and Robertson, A. H. F. (1986). The palaeorotation of the troodos microplate, cyprus, in the late mesozoic-early cenozoic plate tectonic framework of the Eastern Mediterranean. *Surveys in Geophysics*, *8*(4), 375–437.

Collettini, C., Niemeijer, A., Viti, C., and Marone, C. (2009). Fault zone fabric and fault weakness. *Nature*, *462*(7275), 907–910.

Collettini, C., Niemeijer, A., Viti, C., Smith, S. A. F., and Marone, C. (2011). Fault structure, frictional properties and mixed-mode fault slip behavior. *Earth and Planetary Science Letters*, *311*(3-4), 316–327.

Collettini, C., Tesei, T., Scuderi, M. M., Carpenter, B. M., and Viti, C. (2019). Beyond Byerlee friction, weak faults and implications for slip behavior. *Earth and Planetary Science Letters*, *519*, 245–263.

Collettini, C., Viti, C., Smith, S. A. F., and Holdsworth, R. E. (2009). Development of interconnected talc networks and weakening of continental low-angle normal faults. *Geology*, *37*(6), 567–570.

Constantin, M. (1999). Gabbroic intrusions and magmatic metasomatism in harzburgites from the Garrett transform fault: Implications for the nature of the mantle-crust transition at fast-spreading ridges. *Contributions to Mineralogy and Petrology*, *136*(1), 111–130.

Cox, S., Fagereng, A., and MacLeod, C. J. (2021). Shear Zone Development in Serpentinized Mantle: Implications for the Strength of Oceanic Transform Faults. *Journal of Geophysical Research: Solid Earth*, *126*(5), e2020JB020763.

Cox, S. J. D. (1990). Velocity-dependent friction in a large direct shear experiment on gabbro. *Geological Society, London, Special Publications*, *54*(1), 63–70.

Custódio, S. and Archuleta, R. J. (2007). Parkfield earthquakes: Characteristic or complementary? *Journal of Geophysical Research: Solid Earth*, *112*(B5).

Daub, E. G., Shelly, D. R., Guyer, R. A., and Johnson, P. A. (2011). Brittle and ductile friction and the physics of tectonic tremor. *Geophysical Research Letters*, *38*(10).

deMartin, B. J., Sohn, R. A., Pablo Canales, J., and Humphris, S. E. (2007). Kinematics and geometry of active detachment faulting beneath the Trans-Atlantic Geotraverse (TAG) hydrothermal field on the Mid-Atlantic Ridge. *Geology*, *35*(8), 711–714.

den Hartog, S. A. M. and Spiers, C. J. (2014). A microphysical model for fault gouge friction applied to subduction megathrusts. *Journal of Geophysical Research: Solid Earth*, *119*(2), 1510–1529.

Department, C. G. S. (2017). Seismicity in Cyprus. *http://www.gsd-seismology.org.cy/en*, accessed on 22 July 2021.

Department, C. G. S. (2020). Seismic Maps. Available online:. *http://www.moa.gov.cy/moa/gsd/gsd.nsf/All/22DFDADB34114C14C22583C4003B526C?OpenDocument*, accessed on 26 July 2020.

Dick, H. J. B. (1989). Abyssal peridotites, very slow spreading ridges and ocean ridge magmatism. *Geological Society, London, Special Publications*, *42*(1), 71.

Diener, J. F. A., Fagereng, A., and Thomas, S. A. J. (2016). Mid-crustal shear zone development under retrograde conditions: pressure-temperature-fluid constraints from the Kuckaus Mylonite Zone, Namibia. *Solid Earth*, *7*(5), 1331–1347.

Dieterich, J. H. (1979). Modelling of rock friction: 1. Experimental results and constitutive equations. *Journal of Geophysical Research: Solid Earth*, *84*(B5), 2161–2168.

Dieterich, J. H. (1981). Constitutive Properties of Faults With Simulated Gouge. *in Mechanical Behavior of Crustal Rocks*, *24*, 103–120.

Dieterich, J. H. (1992). Earthquake nucleation on faults with rate-and state-dependent strength. *Tectonophysics*, *211*(1), 115–134.

Dieterich, J. H. and Kilgore, B. D. (1994). Direct observation of frictional contacts: New insights for state-dependent properties. *Pure and Applied Geophysics*, *143*(1), 283–302.

Dilek, Y., Thy, P., Moores, E. M., and Ramsden, T. W. (1992). Tectonic evolution of the Troodos Ophiolite within the Tethyan Framework. *Tectonics*, *11*, 916–923.

Durney, D. W. (1972). Solution-transfer, an Important Geological Deformation Mechanism. *Nature*, *235*(5337), 315–317.

Durney, D. W., Ramsay, J. G., and Wood, D. S. (1976). Pressure-solution and crystallization deformation. *Philosophical Transactions of the Royal Society of London*, *A283*(1312), 229–240.

Embley, R. W. and Wilson, D. S. (1992). Morphology of the Blanco Transform Fault Zone-NE Pacific: Implications for its tectonic evolution. *Marine Geophysical Researches*, *14*(1), 25–45.

Engelder, J. T. (1974). Cataclasis and the Generation of Fault Gouge. *GSA Bulletin*, *85*(10), 1515–1522.

Escartín, J., Hirth, G., and Evans, B. (1997a). Effects of serpentinization on the lithospheric strength and the style of normal faulting at slow spreading ridges. *Earth and Planetary Science Letters*, *151*, 181–189.

Escartín, J., Hirth, G., and Evans, B. (1997b). Nondilatant brittle deformation of serpentinites: Implications for Mohr-Coulomb theory and the strength of faults. *Journal of Geophysical Research: Solid Earth*, *102*(B2), 2897–2913.

Escartín, J., Hirth, G., and Evans, B. (2001). Strength of slightly serpentinized peridotites: Implications for the tectonics of oceanic lithosphere. *Geology*, *29*(11), 1023–1026.

Escartín, J., Mével, C., MacLeod, C. J., and McCaig, A. M. (2003). Constraints on deformation conditions and the origin of oceanic detachments: The Mid-Atlantic Ridge core complex at 15°45'N. *Geochemistry, Geophysics, Geosystems*, *4*(8), 1–37.

Evans, A. D., Teagle, D. A. H., Craw, D., Henstock, T. J., and Falcon-Suarez, I. H. (2021). Uplift and Exposure of Serpentinized Massifs: Modeling Differential Serpentinite Diapirism and Exhumation of the Troodos Mantle Sequence, Cyprus. *Journal of Geophysical Research: Solid Earth*, *126*(6), e2020JB021079.

Evans, B. W. (2004). The Serpentinite Multisystem Revisited: Chrysotile is Metastable. *International Geology Review*, *46*(6), 479–506.

Exner, H. E. (1972). Analysis of Grain- and Particle-Size Distributions in Metallic Materials. *International Metallurgical Reviews*, *17*(1), 25–42.

Fagereng, A. and Ikari, M. J. (2020). Low-Temperature Frictional Characteristics of Chlorite-Epidote-Amphibole Assemblages: Implications for Strength and Seismic Style of Retrograde Fault Zones. *Journal of Geophysical Research: Solid Earth*, *125*(4), 1–16.

Fagereng, A. and MacLeod, C. J. (2019). On Seismicity and Structural Style of Oceanic Transform Faults: A Field Geological Perspective from the Troodos Ophiolite, Cyprus. *Transform Plate Boundaries and Fracture Zones, Elsevier*, 437–459.

Fagereng, A. and Sibson, R. H. (2010). Mélange rheology and seismic style. *Geology*, *38*(8), 751–754.

Faulkner, D. R., Lewis, A. C., and Rutter, E. H. (2003). On the internal structure and mechanics of large strike-slip fault zones: Field observations

of the Carboneras fault in southeastern Spain. *Tectonophysics*, *367*(3), 235–251.

Faulkner, D. R. and Rutter, E. H. (2001). Can the maintenance of overpressured fluids in large strike-slip fault zones explain their apparent weakness? *Geology*, *29*(6).

Feld, C., Mechie, J., Hübscher, C., Hall, J., Nicolaides, S., Gurbuz, C., Bauer, K., Louden, K., and Weber, M. (2017). Crustal structure of the Eratosthenes Seamount, Cyprus and S. Turkey from an amphibian wide-angle seismic profile. *Tectonophysics*, *700-701*, 32–59.

Fonseca, R. O. C., Kirchenbaur, M., Ballhaus, C., Münker, C., Zirner, A., Gerdes, A., Heuser, A., Botcharnikov, R., and Lenting, C. (2017). Fingerprinting fluid sources in Troodos ophiolite complex orbicular glasses using high spatial resolution isotope and trace element geochemistry. *Geochimica et Cosmochimica Acta*, *200*, 145–166.

Fossen, H. (2016). *Structural Geology*. Cambridge: Cambridge University Press.

Fox, P. J. and Gallo, D. G. (1984). A tectonic model for ridge-transform-ridge plate boundaries: Implications for the structure of oceanic lithosphere. *Tectonophysics*, *104*(3-4), 205–242.

Freund, S., Haase, K. M., Keith, M., Beier, C., and Garbe-Schönberg, D. (2014). Constraints on the formation of geochemically variable plagiogranite intrusions in the Troodos Ophiolite, Cyprus. *Contributions to Mineralogy and Petrology*, *167*(2), 978.

Froment, B., McGuire, J. J., van der Hilst, R. D., Gouédard, P., Roland, E. C., Zhang, H., and Collins, J. A. (2014). Imaging along-strike variations in mechanical properties of the Gofar transform fault, East Pacific Rise. *Journal of Geophysical Research: Solid Earth*, *119*(9), 7175–7194.

Fulton, P. M. and Saffer, D. M. (2009). Potential role of mantle-derived fluids in weakening the San Andreas Fault. *Journal of Geophysical Research: Solid Earth*, *114*(B7).

Gass, I. G. (1960). IThe geology and mineral resources of the Dhali area. *Cyprus Geological Survey Department*, *4*, 116.

Gass, I. G. (1968). Is the Troodos Massif of Cyprus a Fragment of Mesozoic Ocean Floor? *Nature*, *220*, 39.

Gass, I. G. (1980). The Troodos massif: Its role in the unravelling of the ophiolite problem and its significance in the understanding of constructive plate margin processes. *in: Ophiolites, Proceedings: International Ophiolite Symposium, Cyprus 1979. The Geological Survey Department, Ministry of Agriculture and Natural Resources, Nicosia, Cyprus*, 23–25.

Gass, I. G., MacLeod, C. J., Murton, B. J., Panayiotou, A., Simonian, K. O., and Xenophontos, C. (1994). *The Geological Evolution of the Southern Troodos Transform Fault Zone, Cyprus*, Volume 9 of *Geological Survey Memoir*. Nicosia: Geological Survey Department.

Gass, I. G. and Masson-Smith, D. (1963). The geology and gravity anomalies of the Troodos Massif, Cyprus. *The Royal Society*, *255*(1060), 417–467.

Gass, I. G., Neary, C. R., Plant, J., Robertson, A. H. F., Simonian, K. O., Smewing, J. D., Spooner, E. T. C., and Wilson, R. A. M. (1975). Comments on 'The troodos ophiolitic complex was probably formed in an island arc', by A. Miyashiro and subsequent correspondence by A. Hynes and A. Miyashiro. *Earth and Planetary Science Letters*, *25*(2), 236–238.

Gass, I. G. and Smewing, J. D. (1973). Intrusion, Extrusion and Metamorphism at Constructive Margins: Evidence from the Troodos Massif, Cyprus. *Nature*, *242*(5392), 26–29.

George, R. P. J. (1978). Structural petrology of the Olympus ultramafic complex in the Troodos ophiolite, Cyprus. *GSA Bulletin*, *89*(6), 845–865.

Gillis, K. M. and Roberts, M. D. (1999). Cracking at the magma-hydrothermal transition: evidence from the Troodos Ophiolite, Cyprus. *Earth and Planetary Science Letters*, *169*(3), 227–244.

Grand, T., Lapierre, H., Mascle, G. H., Ohnenstetter, M., and Angelier, J. (1993). Superimposed tectonics of the Cyprus ophiolitic massifs. *Tectonics*, *12*(1), 93–101.

Gratier, J.-P., Dysthe, D. K., and Renard, F. (2013). The Role of Pressure Solution Creep in the Ductility of the Earth's Upper Crust. *Advances in Geophysics*, *54*, 47–179.

Gratier, J.-P., Guiguet, R., Renard, F., Jenatton, L., and Bernard, D. (2009). A pressure solution creep law for quartz from indentation experiments. *Journal of Geophysical Research: Solid Earth*, *114*(B3).

Greenbaum, D. (1977). The chromitiferous rocks of the Troodos ophiolite complex, Cyprus. *Economic Geology*, *72*, 1175–1194.

Grevemeyer, I., Hayman, N. W., Lange, D., Peirce, C., Papenberg, C., Van Avendonk, H. J. A., Schmid, F., de La Peña, L. G., and Dannowski, A. (2019). Constraining the maximum depth of brittle deformation at slow- and ultraslow-spreading ridges using microseismicity. *Geology*, *47*(11), 1069–1073.

Grevemeyer, I., Ranero, C. R., and Ivandic, M. (2018). Structure of oceanic crust and serpentinization at subduction trenches. *Geosphere*, *14*(2), 395–418.

Grevemeyer, I., Reston, T. J., and Moeller, S. (2013). Microseismicity of the Mid-Atlantic Ridge at 7°S-8°15'S and at the Logatchev Massif oceanic core complex at 14°40-N-14°50'N. *Geochemistry, Geophysics, Geosystems*, *14*(9), 3532–3554.

Guillot, S., Schwartz, S., Reynard, B., Agard, P., and Prigent, C. (2015). Tectonic significance of serpentinites. *Tectonophysics*, *646*, 1–19.

Haines, S. H., Kaproth, B., Marone, C., Saffer, D., and van der Pluijm, B. (2013). Shear zones in clay-rich fault gouge: A laboratory study of fabric development and evolution. *Journal of Structural Geology*, *51*, 206–225.

Handy, M. R. (1990). The solid-state flow of polymineralic rocks. *Journal of Geophysical Research: Solid Earth*, *95*(B6), 8647–8661.

Hanks, T. C. and Kanamori, H. (1979). A moment magnitude scale. *Journal of Geophysical Research: Solid Earth*, *84*(B5), 2348–2350.

Hansen, L. N., David, E. C., Brantut, N., and Wallis, D. (2020). Insight into the microphysics of antigorite deformation from spherical nanoindentation. *Philosophical Transactions of the Royal Society*, *378*(2165), 20190197.

Harrison, R. W., Tsiolakis, E., Stone, B. D., Lord, A., McGeehin, J. P., Mahan, S. A., and Chirico, P. (2013). Late Pleistocene and Holocene uplift history of Cyprus: implications for active tectonics along the southern margin of the Anatolian microplate. *Geological Society, London, Special Publications*, *372*(1), 561–584.

He, C., Luo, L., Hao, Q.-M., and Zhou, Y. (2013). Velocity-weakening behavior of plagioclase and pyroxene gouges and stabilizing effect of small amounts of quartz under hydrothermal conditions. *Journal of Geophysical Research: Solid Earth*, *118*(7), 3408–3430.

He, C., Wang, Z., and Yao, W. (2007). Frictional sliding of gabbro gouge under hydrothermal conditions. *Tectonophysics*, *445*(3-4), 353–362.

Heilbronner, R. and Keulen, N. (2006). Grain size and grain shape analysis of fault rocks. *Tectonophysics*, *427*(1-4), 199–216.

Hekinian, R., Bideau, D., Cannat, M., Francheteau, J., and Hebert, R. (1992). Volcanic activity and crust-mantle exposure in the ultramafic Garrett transform fault near 13°28'S in the Pacific. *Earth and Planetary Science Letters*, *108*, 259–275.

Hekinian, R., Bideau, D., Hebert, R., and Niu, Y. (1995). Magmatism in the Garrett transform fault (East Pacific Rise near 13°27'S). *Journal Of Geophysical Research-solid Earth*, *100*(B6), 10163–10185.

Hensen, C., Duarte, J. C., Vannucchi, P., Mazzini, A., Lever, M. A., Terrinha, P., Géli, L., Henry, P., Villinger, H., Morgan, J., Schmidt, M., Gutscher, M.-A., Bartolome, R., Tomonaga, Y., Polonia, A., Gràcia, E., Tinivella, U., Lupi, M., Çağatay, M. N., Elvert, M., Sakellariou, D., Matias, L., Kipfer, R., Karageorgis, A. P., Ruffine, L., Liebetrau, V., Pierre, C., Schmidt, C., Batista, L., Gasperini, L., Burwicz, E., Neres, M., and Nuzzo, M. (2019). Marine Transform Faults and Fracture Zones: A Joint Perspective Integrating Seismicity, Fluid Flow and Life. *Frontiers in Earth Science*, *7*(39).

Hilairet, N., Reynard, B., Wang, Y., Daniel, I., Merkel, S., Nishiyama, N., and Petitgirard, S. (2007). High-pressure creep of serpentine, interseismic deformation and initiation of subduction. *Science*, *318*(318), 1910–1913.

Hilley, G. E., Sare, R. M., Aron, F., Baden, C. W., Caress, D. W., Castillo, C. M., Dobbs, S. C., Gooley, J. T., Johnstone, S. A., Liu, F., McHargue, T., Nevitt, J. M., Paull, C. K., Shumaker, L., Traer, M. M., and Young, H. H. (2020). Coexisting seismic behavior of transform faults revealed by high-resolution bathymetry. *Geology*, *48*(4), 379–384.

Hirauchi, K.-i., Katayama, I., Uehara, S., Miyahara, M., and Takai, Y. (2010). Inhibition of subduction thrust earthquakes by low-temperature plastic flow in serpentine. *Earth and Planetary Science Letters*, *295*(3-4), 349–357.

Hirauchi, K.-i. and Yamaguchi, H. (2007). Unique deformation processes involving the recrystallization of chrysotile within serpentinite: Implications for aseismic slip events within subduction zones. *Terra Nova*, *19*(6), 454–461.

Hirth, G. and Guillot, S. (2013). Rheology and Tectonic Significance of Serpentinite. *Elements*, *9*(2), 107–113.

Hisada, E. (2004). Clast-size analysis of impact-generated pseudotachylite from Vredefort Dome, South Africa. *Journal of Structural Geology*, *26*(8), 1419–1424.

Holdsworth, R. E., Stewart, M., Imber, J., and Strachan, R. A. (2001). The structure and rheological evolution of reactivated continental fault zones: a review and case study. *Geological Society, London, Special Publications*, *184*, 115–137.

Holdsworth, R. E., van Diggelen, E. W. E., Spiers, C. J., de Bresser, J. H. P., Walker, R. J., and Bowen, L. (2011). Fault rocks from the SAFOD core samples: Implications for weakening at shallow depths along the San Andreas Fault, California. *Journal of Structural Geology*, *33*(2), 132–144.

Homberg, C., Bergerat, F., Angelier, J., and Garcia, S. (2010). Fault interaction and stresses along broad oceanic transform zone: Tjörnes Fracture Zone, north Iceland. *Tectonics*, *29*(1), 1–12.

Hurst, S. D., Moores, E. M., and Varga, R. J. (1994). Structural and geophysical expression of the Solea graben, Troodos Ophiolite, Cyprus. *Tectonics*, *13*(1), 139–156.

Hyndman, R. D. and Peacock, S. M. (2003). Serpentinization of the forearc mantle. *Earth and Planetary Science Letters*, *212*(3), 417–432.

Ide, S., Baltay, A., and Beroza, G. C. (2011). Shallow Dynamic Overshoot and Energetic Deep Rupture in the 2011 Mw 9.0 Tohoku-Oki Earthquake. *Science*, *33*(6036), 1426–1429.

Ikari, M. J. (2015). Principal slip zones: Precursors but not recorders of earthquake slip. *Geology*, *43*(11), 955–958.

Ikari, M. J., Carpenter, B. M., and Marone, C. (2016). A microphysical interpretation of rate- and state-dependent friction for fault gouge. *Geochemistry, Geophysics, Geosystems*, *17*(5), 1660–1677.

Ikari, M. J., Ito, Y., Ujiie, K., and Kopf, A. J. (2015). Spectrum of slip behaviour in Tohoku fault zone samples at plate tectonic slip rates. *Nature Geoscience*, *8*(11), 870–874.

Ikari, M. J., Kameda, J., Saffer, D. M., and Kopf, A. J. (2015). Strength characteristics of Japan Trench borehole samples in the high-slip region of the 2011 Tohoku-Oki earthquake. *Earth and Planetary Science Letters*, *412*, 35–41.

Ikari, M. J. and Kopf, A. J. (2011). Cohesive strength of clay-rich sediment. *Geophysical Research Letters*, *38*(16).

Ikari, M. J., Marone, C., and Saffer, D. M. (2011). On the relation between fault strength and frictional stability. *Geology*, *39*(1), 83–86.

Ikari, M. J., Niemeijer, A. R., and Marone, C. (2011). The role of fault zone fabric and lithification state on frictional strength, constitutive behavior, and deformation microstructure. *Journal of Geophysical Research*, *116*(B8).

Ikari, M. J. and Saffer, D. M. (2011). Comparison of frictional strength and velocity dependence between fault zones in the Nankai accretionary complex. *Geochemistry, Geophysics, Geosystems*, *12*(4).

Imber, J., Holdsworth, R. E., Butler, C. A., and Lloyd, G. E. (1997). Fault-zone weakening processes along the reactivated Outer Hebrides Fault Zone, Scotland. *Journal of the Geological Society, London*, *154*, 105–109.

Imber, J., Holdsworth, R. E., Smith, S. A. F., Jefferies, S. P., and Collettini, C. (2008). Frictional-viscous flow, seismicity and the geology of weak faults: a review and future directions. *Geological Society, London, Special Publications*, *299*(1), 151–173.

Irwin, W. P. and Barnes, I. (1975). Effect of geological structure and metamorphic fluids on seismic behaviour of the San Andreas Fault System in central and northern California. *Geology*, *3*(12), 713–716.

Jackson, J. and McKenzie, D. (1984). Active tectonics of the Alpine-Himalayan Belt between western Turkey and Pakistan. *Geophysical Journal International*, *77*(1), 185–264.

Jaeger, J. C., Cook, N. G. W., and Zimmerman, R. (2007). *Fundamentals of Rock Mechanics* (4 ed.). Blackwell.

Jamtveit, B., Malthe-Sørenssen, A., and Kostenko, O. (2008). Reaction enhanced permeability during retrogressive metamorphism. *Earth and Planetary Science Letters*, *267*(3), 620–627.

Jefferies, S. P., Holdsworth, R. E., Shimamoto, T., Takagi, H., Lloyd, G. E., and Spiers, C. J. (2006). Origin and mechanical significance of foliated cataclastic rocks in the cores of crustal-scale faults: Examples from the Median Tectonic Line, Japan. *Journal of Geophysical Research: Solid Earth*, *111*(B12).

Kähler, G. and Stow, D. A. V. (1998). Turbidites and contourites of the Palaeogene Lefkara Formation, southern Cyprus. *Sedimentary Geology*, *115*(1), 215–231.

Kanamori, H. and Anderson, D. L. (1975). Theoretical basis of some empirical relations in seismology. *Bulletin of the Seismological Society of America*, *65*(5), 1073–1095.

Kanu, C. and Johnson, K. (2011). Arrest and recovery of frictional creep on the southern Hayward fault triggered by the 1989 Loma Prieta, California,

earthquake and implications for future earthquakes. *Journal of Geophysical Research: Solid Earth*, *116*(B4).

Kaproth, B. and Marone, C. (2013). Slow earthquakes, preseismic velocity changes, and the origin of slow frictional stick-slip. *Science*, *341*(6151), 1229–1232.

Karson, J. A. and Dick, H. J. B. (1983). Tectonics of ridge-transform intersections at the Kane fracture zone. *Marine Geophysical Researches*, *6*(1), 51–98.

Karson, J. A., Früh-Green, G. L., Kelley, D. S., Williams, E. A., Yoerger, D. R., and Jakuba, M. (2006). Detachment shear zone of the Atlantis Massif core complex, Mid-Atlantic Ridge, 30°N. *Geochemistry, Geophysics, Geosystems*, *7*(6), Q06016.

Kelemen, P. B. and Hirth, G. (2012). Reaction-driven cracking during retrograde metamorphism: Olivine hydration and carbonation. *Earth and Planetary Science Letters*, *345-348*, 81–89.

Kenkmann, T. and Dresen, G. (1998). Stress gradients around porphyroclasts: palaeopiezometric estimates and numerical modelling. *Journal of Structural Geology*, *20*(2/3), 163–173.

Keulen, N., Heilbronner, R., Stünitz, H., Boullier, A.-M., and Ito, H. (2007). Grain size distributions of fault rocks: A comparison between experimentally and naturally deformed granitoids. *Journal of Structural Geology*, *29*(8), 1282–1300.

Kinnaird, T. and Robertson, A. (2012). Tectonic and sedimentary response to subduction and incipient continental collision in southern cyprus, easternmost mediterranean region. *Geological Society Special Publication*, *372*(1), 585–614.

Kinnaird, T. C., Robertson, A. H. F., and Morris, A. (2011). Timing of uplift of the Troodos Massif (Cyprus) constrained by sedimentary and magnetic polarity evidence. *Journal of the Geological Society*, *168*(2), 457–470.

Klein, F., Bach, W., and McCollom, T. M. (2013). Compositional controls on hydrogen generation during serpentinization of ultramafic rocks. *Lithos*, *178*, 55–69.

Klein, F. and Le Roux, V. (2020). Quantifying the volume increase and chemical exchange during serpentinization. *Geology*, *48*, 552–556.

Knipe, R. J. (1989). Deformation mechanisms- recognition from natural tectonites. *Journal of Structural Geology*, *11*(1/2), 127–146.

Kohli, A. H., Goldsby, D. L., Hirth, G., and Tullis, T. (2011). Flash weakening of serpentinite at near-seismic slip rates. *Journal of Geophysical Research: Solid Earth*, *116*(B3), B03202.

Kohli, A. H. and Warren, J. M. (2020). Evidence for a Deep Hydrologic Cycle on Oceanic Transform Faults. *Journal of Geophysical Research: Solid Earth*, *125*(2), e2019JB017751.

Kronenberg, A. K., Kirby, S. H., and Pinkston, J. (1990). Basal slip and mechanical anisotropy of biotite. *Journal of Geophysical Research: Solid Earth*, *95*(B12), 257–278.

Kuna, V. M., Nábělek, J. L., and Braunmiller, J. (2019). Mode of slip and crust-mantle interaction at oceanic transform faults. *Nature Geoscience*, *12*, 138–142.

Lacroix, B., Tesei, T., Oliot, E., Lahfid, A., and Collettini, C. (2015). Early weakening processes inside thrust fault. *Tectonics*, *34*(7), 1396–1411.

Lay, T. and Kanamori, H. (1981). An asperity model of large earthquake sequences. *Earthquake prediction : an international review*, 579–592.

Lay, T. and Wallace, T. C. (1995). Modern Global Seismology. , *San Diego, CA: Academic Press*, 521.

Leeman, J. R., Saffer, D. M., Scuderi, M. M., and Marone, C. (2016). Laboratory observations of slow earthquakes and the spectrum of tectonic fault slip modes. *Nature Communications*, *7*(1), 11104.

Liu, Y., McGuire, J. J., and Behn, M. D. (2012). Frictional behavior of oceanic transform faults and its influence on earthquake characteristics. *Journal of Geophysical Research: Solid Earth*, *117*(B4).

Liu, Y., McGuire, J. J., and Behn, M. D. (2020). Aseismic transient slip on the Gofar transform fault, East Pacific Rise. *Proceedings of the National Academy of Sciences*, *117*, 10188–10194.

Lockner, D. A., Morrow, C., Moore, D., and Hickman, S. (2011). Low strength of deep San Andreas fault gouge from SAFOD core. *Nature*, *472*(7341), 82–85.

Lord, A. R., Panayides, I., Urquhart, E., Xenophontos, C., and Malpas, J. A biochronostratigraphical framework for the Late Cretaceous-Recent circum-Troodos sedimentary sequence, Cyprus. In *Proceedings of the Third International Conference on the Geology of the Eastern Mediterranean. Geological Survey Department, Nicosia*, Volume 289, 297–.

MacDonald, A. H. and Fyfe, W. S. (1985). Rate of serpentinization in seafloor environments. *Tectonophysics*, *116*, 123–135.

MacDonald, K. C., Castillo, D. A., Miller, S. P., Fox, P. J., Kastens, K. A., and Bonatti, E. (1986). Deep-tow studies of the Vema Fracture Zone: 1. Tectonics of a major slow slipping transform fault and its intersection with the Mid-Atlantic Ridge. *Journal of Geophysical Research: Solid Earth*, *91*(B3), 3334–3354.

Mackwell, S.J. Zimmerman, M. and Kohlstedt, D. (1998). High-temperature deformation of dry diabase with application to tectonics on Venus. *Journal of Geophysical Research: Solid Earth*, *103*(B1), 975–984.

MacLeod, C. and Parrish, R. (2004). Quantifying the spreading rate of the Troodos ophiolite. *32nd International Geological Congress*, Abstract 76–23.

MacLeod, C. J. (1988). *The Tectonic Evolution of the Eastern Limassol Forest Complex, Cyprus*. Unpublished Ph.D. Thesis, Milton Keynes.

MacLeod, C. J. (1990). Role of the Southern Troodos Transform Fault in the rotation of the Cyprus microplate: evidence from the Eastern Limassol

Forest Complex. *Proceedings of the Symposium, Troodos 1987*, *Geological Survey Department*, 75–85.

MacLeod, C. J., Allerton, S., Gass, I. G., and Xenophontos, C. (1990). Structure of a fossil ridge-transform intersection in the Troodos Ophiolite. *Nature*, *348*, 717–720.

MacLeod, C. J., Escartín, J., Banerji, D., Banks, G. J., Irving, D. H. B., Lilly, R. M., McCaig, A. M., Niu, Y., Allerton, S., and Smith, D. K. (2002). Direct geological evidence for oceanic detachment faulting: The Mid Atlantic Ridge, 14°45'N. *Geology*, *30*(10), 879–882.

MacLeod, C. J. and Murton, B. J. (1993). Structure and tectonic evolution of the Southern Troodos Transform Fault Zone, Cyprus. *Geological Society Special Publications*, *76*, 141–176.

MacLeod, C. J. and Murton, B. J. (1995). On the sense of slip of the Southern Troodos Transform Fault Zone, Cyprus. *Geology*, *23*(3), 257–260.

MacLeod, C. J., Teagle, D. A. H., Gillis, K. M., Cazenave, P. W., Hansen, H. E., Howard, K. A., Hurst, S. D., Ildefonse, B. M., Lissenberg, C. J., Morris, A., Shillington, D. J., and Tominaga, M. (2008). Accretion of the lower oceanic crust at fast-spreading ridges: a rock drill and near-bottom seafloor survey in support of IODP drilling in Hess Deep. Technical report, Cardiff University.

Maffione, M., van Hinsbergen, D. J. J., de Gelder, G. I. N. O., van der Goes, F. C., and Morris, A. (2017). Kinematics of Late Cretaceous subduction initiation in the Neo-Tethys Ocean reconstructed from ophiolites of Turkey, Cyprus, and Syria. *Journal of Geophysical Research: Solid Earth*, *122*(5), 3953–3976.

Magaritz, M. and Taylor Jr, H. P. (1974). Oxygen and hydrogen isotope studies of serpentinization in the Troodos ophiolite complex, Cyprus. *Earth and Planetary Science Letters*, *23*, 8–14.

Malpas, J., Robinson, P. T., and Salisbury, M. (1989). *Geology and geophysics of borehole CY-4 of the Cyprus Crustal Study Project: Summary*, Volume Paper 88-89, 381. Geological Survey of Canada.

Malvoisin, B. (2015). Mass transfer in the oceanic lithosphere: Serpentinization is not isochemical. *Earth and Planetary Science Letters*, *430*, 75–85.

Malvoisin, B., Brantut, N., and Kaczmarek, M.-A. (2017). Control of serpentinisation rate by reaction-induced cracking. *Earth and Planetary Science Letters*, *476*, 143–152.

Malvoisin, B., Brunet, F., Carlut, J., Rouméjon, S., and Cannat, M. (2012). Serpentinization of oceanic peridotites: 2. Kinetics and processes of San Carlos olivine hydrothermal alteration. *Journal of Geophysical Research: Solid Earth*, *117*(B4).

Mandelbrot, B. B. (1982). *The fractal geometry of nature*. New York: WH Freeman.

Mariani, E., Brodie, K. H., and Rutter, E. H. (2006). Experimental deformation of muscovite shear zones at high temperatures under hydrothermal conditions and the strength of phyllosilicate-bearing faults in nature. *Journal of Structural Geology*, *28*(9), 1569–1587.

Marone, C. (1995). Fault zone strength and failure criteria. *Geophysical Research Letters*, *22*(6), 723–726.

Marone, C. (1998). Laboratory-derived frictional laws and their application to seismic faulting. *Annual Review of Earth and Planetary Sciences*, *26*, 642–696.

Marone, C. and Scholz, C. H. (1989). Particle-size distribution and microstructures within simulated fault gouge. *Journal of Structural Geology*, *11*(7), 799–814.

McGuire, J. J. (2008). Seismic Cycles and Earthquake Predictability on East Pacific Rise Transform Faults. *Bulletin of the Seismological Society of America*, *98*(3), 1067–1084.

McGuire, J. J., Boettcher, M. S., and Jordan, T. H. (2005). Foreshock sequences and short-term earthquake predictability on East Pacific Rise transform faults. *Nature*, *434*(7032), 457–461.

McGuire, J. J., Collins, J. A., Gouédard, P., Roland, E., Lizarralde, D., Boettcher, M. S., Behn, M. D., and van der Hilst, R. D. (2012). Variations in earthquake rupture properties along the Gofar transform fault, East Pacific Rise. *Nature Geoscience*, *5*(5), 336–341.

McGuire, J. J., Ihmle, P. F., and Jordan, T. H. (1996). Time-domain observations of a slow precursor to the 1994 Romanche transform earthquake. *Science*, *274*, 82–85.

Mével, C. (2003). Serpentinization of abyssal peridotites at mid-ocean ridges. *Comptes Rendus Geoscience*, *335*(10-11), 825–852.

Miyashiro, A. (1973). The Troodos ophiolitic complex was probably formed in an island arc. *Earth and Planetary Science Letters*, *19*(2), 218–224.

Molnar, P. (1979). Earthquake recurrence intervals and plate tectonics. *Bulletin of the Seismological Society of America*, *69*(1), 115–133.

Molnar, P., Atwater, T., Mammerickx, J., and Smith, S. M. (1975). Magnetic Anomalies, Bathymetry and the Tectonic Evolution of the South Pacific since the Late Cretaceous. *Geophysical Journal International*, *40*(3), 383–420.

Monzawa, N. and Otsuki, K. (2003). Comminution and fluidization of granular fault materials: implications for fault slip behavior. *Tectonophysics*, *367*(1), 127–143.

Moore, D. E. and Lockner, D. A. (2004). The coefficient of friction of chrysotile gouge at seismogenic depths. *International Geology Review*, *46*, 1–14.

Moore, D. E. and Lockner, D. A. (2011). Frictional strengths of talc-serpentine and talc-quartz mixtures. *Journal of Geophysical Research: Solid Earth*, *116*(B1).

Moore, D. E., Lockner, D. A., Shengli, M., Summers, R., and Byerlee, J. D. (1997). Strengths of serpentinite gouges at elevated temperatures. *Journal of Geophysical Research: Solid Earth*, *102*(B7), 14787–14801.

Moore, D. E., Lockner, D. A., Summers, R., Shengli, M., and Byerlee, J. D. (1996). Strength of chrysotile-serpentinite gouge under hydrothermal con-

ditions: Can it explain a weak San Andreas Fault? *Geology*, *24*(11), 1041–1044.

Moore, D. E. and Rymer, M. J. (2007). Talc-bearing serpentinite and the creeping section of the San Andreas Fault. *Nature*, *448*(7155), 795–797.

Moores, E., Varga, R. J., Verosub, K., and Ramsden, T. (1990). Regional structure of the Troodos dyke complex. *In: Malpas, J., Moores, E.M., Panayiotou, A., Xenophontos, C. (Eds.), Troodos 1987: Ophiolites, Oceanic Crustal Analogues*, *Geol. Surv. Dept. Cyprus,*(Nicosia,), 27–35.

Moores, E. F., Robinson, P. T., Malpas, J., and Xenophonotos, C. (1984). Model for the origin of the Troodos massif, Cyprus, and other mideast ophiolites. *Geology*, *12*(8), 500–503.

Moores, E. M. and Vine, F. J. (1971). The Troodos Massif, Cyprus and other ophiolites as oceanic crust: Evaluation and implications. *Philosophical Transactions of the Royal Society of London*, *268*, 443–466.

Morris, A., Creer, K. M., and Robertson, A. H. F. (1990). Palaeomagnetic evidence for clockwise rotations related to dextral shear along the Southern Troodos Transform Fault, Cyprus. *Earth and Planetary Science Letters*, *99*, 250–262.

Morrow, C., Radney, B., and Byerlee, J. (1992). Frictional Strength and the Effective Pressure Law of Montmorillonite and lllite Clays. *in Fault Mechanics and Transport Properties in Rocks*, *Chapter 3*, 69–88.

Morrow, C. A., Shi, L. Q., and Byerlee, J. D. (1982). Strain hardening and strength of clay-rich fault gouges. *Journal of Geophysical Research: Solid Earth*, *87*(B8), 6771–6780.

Mukasa, S. B. and Ludden, J. N. (1987). Uranium-lead isotopic ages of plagiogranites from the Troodos Ophiolite, Cyprus, and their tectonic significance. *Geology*, *15*, 825–828.

Mumpton, F. A. and Thompson, C. S. (1975). Mineralogy and origin of the Coalinga asbestos deposit. *Clays and Clay Minerals*, *23*, 131–143.

Murton, B. J. (1986a). Anomalous oceanic lithosphere formed in a leaky transform fault: Evidence from the western Limassol Forest Complex, Cyprus. *Journal of the Geological Society, London*, *143*, 845–854.

Murton, B. J. (1986b). *The Tectonic Evolution of the Western Limassol Forest Complex, Cyprus*. Unpublished Ph.D. Thesis, Milton Keynes.

Murton, B. J. (1990). Was the Southern Troodos Transform Fault a victim of microplate rotation. Ophiolites. *Oceanic Crustal Analogues*, 87–89.

Muto, J., Nakatani, T., Nishikawa, O., and Nagahama, H. (2015). Fractal particle size distribution of pulverized fault rocks as a function of distance from the fault core. *Geophysical Research Letters*, *42*(10), 3811–3819.

Nagahama, H. and Yoshii, K. (1993). Fractal dimension and fracture of brittle rocks. *International Journal of Rock Mechanics and Mining Sciences*, *30*(2), 173–175.

Nicolas, A. and Violette, J. F. (1982). Mantle flow beneath oceanic ridges: models derived from ophiolites. *Tectonophysics*, *81*, 319–339.

Niemeijer, A. R. (2018). Velocity-dependent slip weakening by the combined operation of pressure solution and foliation development. *Scientific Reports*, *8*(1), 4724.

Niemeijer, A. R. and Spiers, C. J. (2005). Influence of phyllosilicates on fault strength in the brittle-ductile transition: insights from rock analogue experiments. *Geological Society, London, Special Publications*, *245*, 303.

Niemeijer, A. R. and Spiers, C. J. (2006). Velocity dependence of strength and healing behaviour in simulated phyllosilicate-bearing fault gouge. *Tectonophysics*, *427*(1-4), 231–253.

Noda, H. and Lapusta, N. (2013). Stable creeping fault segments can become destructive as a result of dynamic weakening. *Nature*, *493*(7433), 518–521.

Nuriel, P., Katzir, Y., Abelson, M., Valley, J. W., Matthews, A., Spicuzza, M. J., and Ayalon, A. (2009). Fault-related oceanic serpentinization in the Troodos ophiolite, Cyprus: Implications for a fossil oceanic core complex. *Earth and Planetary Science Letters*, *282*(1-4), 34–46.

O'Hanley, D. S. (1991). Fault-related phenomena associated with hydration and serpentine recrystallization during serpentinization. *Canadian Mineralogist*, *29*, 21–35.

O'Hanley, D. S. (1992). Solution to the volume problem in serpentinization. *Geology*, *20*(8), 705–708.

Okal, E. A. and Langenhorst, A. R. (2000). Seismic properties of the Eltanin Transform System, South Pacific. *Physics of the Earth and Planetary Interiors*, *119*, 185–208.

Okamoto, A. S., Verberne, B. A., Niemeijer, A. R., Takahashi, M., Shimizu, I., Ueda, T., and Spiers, C. J. (2019). Frictional Properties of Simulated Chlorite Gouge at Hydrothermal Conditions: Implications for Subduction Megathrusts. *Journal of Geophysical Research: Solid Earth*, *124*(5), 4545–4565.

Okazaki, K. and Katayama, I. (2015). Slow stick slip of antigorite serpentinite under hydrothermal conditions as a possible mechanism for slow earthquakes. *Geophysical Research Letters*, *42*(4), 1099–1104.

Oldenburg, D. W. and Brune, J. N. (1972). Ridge transform fault spreading pattern in freezing wax. *Science*, *178*, 301–304.

O'Hanley, D. S., Chernosky, J. V., and Wicks, F. J. (1989). The stability of lizardite and chrysotile. *Canadian Mineralogist*, *27*, 483–493.

Padrón-Navarta, J. A., Tommasi, A., Garrido, C. J., and Sánchez-Vizcaíno, V. L. (2012). Plastic deformation and development of antigorite crystal preferred orientation in high-pressure serpentinites. *Earth and Planetary Science Letters*, *349-350*, 75–86.

Parnell-Turner, R., Sohn, R. A., Peirce, C., Reston, T. J., MacLeod, C. J., Searle, R. C., and Simao, N. M. (2017). Oceanic detachment faults generate compression in extension. *Geology*, *45*(10), 923–926.

Paterson, M. S. (1973). Nonhydrostatic thermodynamics and its geologic applications. *Reviews of Geophysics*, *11*(2), 355–389.

Peacock, S. M. and Hyndman, R. D. (1999). Hydrous minerals in the mantle wedge and the maximum depth of subduction thrust earthquakes. *Geophysical Research Letters*, *26*(16), 2517–2520.

Pearce, J. and Robinson, P. (2010). The Troodos ophiolitic complex probably formed in a subduction initiation, slab edge setting. *Gondwana Research*, *18*, 60–81.

Pearce, J. A. (1975). Basalt geochemistry used to investigate past tectonic environments on Cyprus. *Tectonophysics*, *25*, 41–67.

Pearce, J. A. (2003). Supra-subduction zone ophiolites : The search for modern analogues. *Ophiolite concept and the evolution of geological thought*, *Geological Society of America Special paper 373*, 269–293.

Pearce, J. A. and Cann, J. R. (1973). Tectonic setting of basic volcanic rocks determined using trance element analysis. *Earth and Planetary Science Letters*, *19*, 290–300.

Pearce, J. A., Lippard, S. J., and Roberts, S. (1984). Characteristics and tectonic significance of supra-subduction zone ophiolites. *Geological Society Special Publications*, *16*, 77–94.

Phillips, N. J., Belzer, B., French, M. E., Rowe, C. D., and Ujiie, K. (2020). Frictional Strengths of Subduction Thrust Rocks in the Region of Shallow Slow Earthquakes. *Journal of Geophysical Research: Solid Earth*, *125*(3), 1–21.

Phillips, N. J. and Williams, R. T. (2021). To D or not to D? Re-evaluating particle-size distributions in natural and experimental fault rocks. *Earth and Planetary Science Letters*, *553*, 116635.

Plümper, O., Jamtveit, B., and Røyne, A. (2013). Can serpentinization induce fracturing? Fluid pathway development and the volume increase enigma. *EGU General Assembly Conference Abstracts*, EGU2013–10173.

Pockalny, R. A., Detrick, R. S., and Fox, P. J. (1988). Morphology and tectonics of the Kane Transform from Sea Beam bathymetry data. *Journal of Geophysical Research: Solid Earth*, *93*(B4), 3179–3193.

Prigent, C., Warren, J. M., Kohli, A. H., and Teyssier, C. (2020). Fracture-mediated deep seawater flow and mantle hydration on oceanic transform faults. *Earth and Planetary Science Letters*, *532*(532), 1–13.

Raleigh, C. B. and Paterson, M. S. (1965). Experimental deformation of serpentinite and its tectonic implications. *Journal of Geophysical Research*, *70*(6), 3965–3985.

Ramsay, J. G. (1967). *Folding and Fracturing of Rocks*. New York: McGraw-Hill.

Reid, H. F. (1910). The mechanics of the earthquake. The California Earthquake of April 18, 1906. *Report of the State Earthquake Investigation Commission*.

Reinen, L. A. (2000). Seismic and aseismic slip indicators in serpentinite gouge. *Geology*, *28*(2), 135–138.

Reinen, L. A., Weeks, J. D., and Tullis, T. E. (1991). The frictional behaviour of serpentinite: Implications for aseismic creep on shallow crustal faults. *Geophysical Research Letters*, *18*(10), 1921–1924.

Reinen, L. A., Weeks, J. D., and Tullis, T. E. (1994). The Frictional Behaviour of Lizardite and Antigorite Serpentinites: Experiments, Constitutive Models, and Implications for Natural Faults. *Pageoph*, *143*, 317–358.

Reynard, B., Hilairet, N., Balan, E., and Lazzeri, M. (2007). Elasticity of serpentines and extensive serpentinization in subduction zones. *Geophysical Research Letters*, *34*(13), 1–5.

Robertson, A. H. F. (1975). Cyprus umbers: basalt-sediment relationships on a Mesozoic ocean ridge. *Journal of the Geological Society*, *131*(5), 511–531.

Robertson, A. H. F. (1976). Pelagic chalks and calciturbidites from the lower Tertiary of the Troodos Massif, Cyprus. *Journal of Sedimentary Research*, *46*(4), 1007–1016.

Robertson, A. H. F. (1977). Tertiary uplift history of the Troodos massif, Cyprus. *Geological Society of America Bulletin*, *88*, 1763–1772.

Robertson, A. H. F. (1990). Tectonic evolution of Cyprus. *Proceedings of the Symposium, Troodos 1987*, *Geological Survey Department*.

Robertson, A. H. F. (1993). Spreading-induced faulting and fracturing of oceanic crust: examples from the Sheeted Dyke Complex of the Troodos ophiolite, Cyprus. *Geological Society, London, Special Publications*, *No. 76*, 121–139.

Robertson, A. H. F. (1998). Tectonic significance of the Eratosthenes Seamount: A continental fragment in the process of collision with a subduction zone in the eastern Mediterranean (Ocean Drilling Program Leg 160). *Tectonophysics*, *298*, 63–82.

Robertson, A. H. F. (2002). Overview of the genesis and emplacement of Mesozoic ophiolites in the Eastern Mediterranean Tethyan region. *Lithos*, *65*, 1–67.

Robertson, A. H. F., Eaton, S., Follows, E. J., and McCallum, J. E. (1991). The role of local tectonics versus global sea-level change in the Neogene evolution of the Cyprus active margin. *In Sedimentation, tectonics and Eustasy: Sea-level Changes at Active Margins*, 331–369.

Robertson, A. H. F. and Hudson, J. D. (1973). Cyprus umbers: Chemical precipitates on a Tethyan ocean ridge. *Earth and Planetary Science Letters*, *18*(1), 93–101.

Robertson, A. H. F. and Mountrakis, D. (2006). Tectonic development of the Eastern Mediterranean region: an introduction. *Geological Society, London, Special Publications*, *260*(1), 1.

Robertson, A. H. F., Parlak, O., and Ustaōmer, T. (2012). Overview of the Palaeozoic-Neogene evolution of Neotethys in the Eastern Mediterranean region (Southern Turkey, Cyprus, Syria). *Petroleum Geoscience*, *18*(4), 381–404.

Robertson, A. H. F. and Woodcock, N. H. (1979). Mamonia Complex, southwest Cyprus: Evolution and emplacement of a Mesozoic continental margin. *Geological Society of America Bulletin*, *90*(7), 651–665.

Robinson, P. T., Melson, W. G., O'Hearn, T., and Schmincke, H.-U. (1983). Volcanic glass compositions of the Troodos ophiolite, Cyprus. *Geology*, *11*(7), 400–404.

Roland, E., Behn, M. D., and Hirth, G. (2010). Thermal-mechanical behavior of oceanic transform faults: Implications for the spatial distribution of seismicity. *Geochemistry, Geophysics, Geosystems*, *11*(7), 1–15.

Roland, E., Lizarralde, D., McGuire, J. J., and Collins, J. A. (2012). Seismic velocity constraints on the material properties that control earthquake behavior at the Quebrada-Discovery-Gofar transform faults, East Pacific Rise. *Journal of Geophysical Research: Solid Earth*, *117*(B11).

Rooney, J. S., Tarling, M. S., Smith, S. A. F., and Gordon, K. C. (2018). Submicron Raman spectroscopy mapping of serpentinite fault rocks. *Journal of Raman Spectroscopy*, *49*(2), 279–286.

Rouméjon, S., Andreani, M., and Früh-Green, G. L. (2019). Antigorite crystallization during oceanic retrograde serpentinization of abyssal peridotites. *Contributions to Mineralogy and Petrology*, *174*(7).

Rouméjon, S., Cannat, M., Agrinier, P., Godard, M., and Andreani, M. (2015). Serpentinization and Fluid Pathways in Tectonically Exhumed Peridotites from the Southwest Indian Ridge (62-65° E). *Journal of Petrology*, *56*(4), 703–734.

Rouméjon, S., Williams, M. J., and Früh-Green, G. L. (2018). In-situ oxygen isotope analyses in serpentine minerals: Constraints on serpentinization during tectonic exhumation at slow- and ultraslow-spreading ridges. *Lithos*, *323*, 156–173.

Rowe, C. D. and Griffith, W. A. (2015). Do faults preserve a record of seismic slip: A second opinion. *Journal of Structural Geology*, *78*, 1–26.

Rubin, A. M. (2008). Episodic slow slip events and rate-and-state friction. *Journal of Geophysical Research*, *113*(B11), 1–18.

Ruina, A. (1983). Slip instability and state variable friction laws. *Journal of Geophysical Research: Solid Earth*, *88*(B12), 10359–10370.

Rüpke, L. H. and Hasenclever, J. (2017). Global rates of mantle serpentinization and H2 production at oceanic transform faults in 3-D geodynamic models. *Geophysical Research Letters*, *44*(13), 6726–6734.

Rutter, E. H. (1974). The influence of temperature, strain-rate and interstitial water in the experimental deformation of calcite rocks. *Tectonophysics*, *22*, 311–334.

Rutter, E. H. (1976). The kinetics of rock deformation by pressure solution. *Philosophical Transactions of the Royal Society of London*, *283*, 203–219.

Rutter, E. H. (1986). On the nomenclature of mode of failure transitions in rocks. *Tectonophysics*, *122*(3), 381–387.

Saffer, D. M. and Marone, C. (2003). Comparison of smectite- and illite-rich gouge frictional properties: application to the up-dip limit of the seismogenic zone along subduction megathrusts. *Earth and Planetary Science Letters*, *215*(1-2), 219–235.

Sammis, C. G. and Biegel, R. L. (1989). Fractals, fault-gouge, and friction. *Pageoph*, *131*(1/2), 255–271.

Sammis, C. G., King, G., and Biegel, R. (1987). The kinematics of gouge deformation. *Pageoph*, *125*(5), 777–812.

Sammis, C. G., Osborne, R. H., Anderson, J. L., Banerdt, M., and White, P. (1986). Self-similar cataclasis in the formation of fault gouge. *Pure and Applied Geophysics*, *124*(1), 53–78.

Savage, J. C., Byerlee, J. D., and Lockner, D. A. (1996). Is internal friction friction? *Geophysical Research Letters*, *23*(5), 487–490.

Schleicher, A. M., van der Pluijm, B. A., and Warr, L. N. (2010). Nanocoatings of clay and creep of the San Andreas fault at Parkfield, California. *Geology*, *38*(7), 667–670.

Schleicher, A. M., van der Pluijm, B. A., and Warr, L. N. (2012). Chlorite-smectite clay minerals and fault behavior: New evidence from the San Andreas Fault Observatory at Depth (SAFOD) core. *Lithosphere*, *4*(3), 209–220.

Scholz, C. H. (1998). Earthquake and friction laws. *Nature*, *391*, 37–42.

Scholz, C. H. (2002). The mechanics of earthquake faulting. *Cambridge University Press*, *2nd ed.*, 1–467.

Schouten, H. and Kelemen, P. B. (2002). Melt viscosity, temperature and transport processes, Troodos ophiolite, Cyprus. *Earth and Planetary Science Letters*, *201*(2), 337–352.

Searle, R. C. (1981). The active part of Charlie-Gibbs Fracture Zone: A study using sonar and other geophysical techniques. *Journal of Geophysical Research: Solid Earth*, *86*(B1), 243–262.

Searle, R. C. (1983). Multiple, closely spaced transform faults in fast-slipping fracture zones. *Geology*, *11*(10), 607–610.

Segall, P. and Rice, J. R. (1995). Dilatancy, compaction, and slip instability of a fluid-infiltrated fault. *Journal of Geophysical Research: Solid Earth*, *100*(B11), 22155–22171.

Segall, P., Rubin, A. M., Bradley, A. M., and Rice, J. R. (2010). Dilatant strengthening as a mechanism for slow slip events. *Journal of Geophysical Research: Solid Earth*, *115*(B12).

Shervais, J. W., Kolesar, P., and Andreasen, K. (2005). A Field and Chemical Study of Serpentinization-Stonyford, California: Chemical Flux and Mass Balance. *International Geology Review*, *47*(1), 1–23.

Shimamoto, T. and Logan, J. M. (1981). Effects of simulated clay gouges on the sliding behaviour of Tennessee Sandstone. *Tectonophysics*, *75*, 243–255.

Sibson, R. H. (1977). Fault rocks and fault mechanisms. *Journal of the Geological Society, London*, *133*, 191–213.

Sibson, R. H. (1984). Roughness at the base of the seismogenic zone: Contributing factors. *Journal of Geophysical Research: Solid Earth*, *89*(B7), 5791–5799.

Sibson, R. H. (1985). A note on fault reactivation. *Journal of Structural Geology*, *7*(6), 751–754.

Simonian, K. O. (1975). *The geology of the Arakapas Fault Belt area, Troodos Massif, Cyprus*. Unpublished Ph.D. Thesis, Milton Keynes.

Simonian, K. O. and Gass, I. G. (1978). Arakapas Fault Belt, Cyprus: A fossil transform fault. *Geological Society of America Bulletin*, *89*, 1220–1230.

Skarbek, R. M. and Savage, H. M. (2019). RSFit3000: A MATLAB GUI-based program for determining rate and state frictional parameters from experimental data. *Geosphere*, *15*(5), 1665–1676.

Smith, S. A. F. and Faulkner, D. R. (2010). Laboratory measurements of the frictional properties of the Zuccale low-angle normal fault, Elba Island, Italy. *Journal of Geophysical Research: Solid Earth*, *115*(B2), 1–17.

Smith, S. A. F., Holdsworth, R. E., Collettini, C., and Pearce, M. A. (2011). The microstructural character and mechanical significance of fault rocks associated with a continental low-angle normal fault: The Zuccale Fault, Elba Island, Italy. *Geological Society, London, Special Publications*, *359*(1), 97–113.

Steacy, S. J. and Sammis, C. G. (1991). An automaton for fractal patterns of fragmentation. *Nature*, *353*(6341), 250–252.

Stewart, L. M. and Okal, E. A. (1983). Seismicity and aseismic slip along the Eltanin Fracture Zone. *Journal of Geophysical Research: Solid Earth*, *88*(B12), 10495–10507.

Storti, F., Billi, A., and Salvini, F. (2003). Particle size distribution in natural carbonate fault rocks: insights for non-self-similar cataclasis. *Earth and Planetary Science Letters*, *206*, 173–186.

Suppe, J. (2014). Fluid overpressures and strength of the sedimentary upper crust. *Journal of Structural Geology*, *69*, 481–492.

Swarbrick, R. E. and Naylor, M. A. (1980). The Kathikas mélange, SW Cyprus: late Cretaceous submarine debris flows. *Sedimentology*, *27*, 63–78.

Sykes, L. R. and Ekström, G. (2012). Earthquakes along Eltanin transform system, SE Pacific Ocean: fault segments characterized by strong and poor seismic coupling and implications for long-term earthquake prediction. *Geophysical Journal International*, *188*(2), 421–434.

Tarling, M. S., Smith, S. A. F., Scott, J. M., Rooney, J. S., Viti, C., and Gordon, K. C. (2019). The internal structure and composition of a plate boundary-scale serpentinite shear zone: The Livingstone Fault, New Zealand. *Solid Earth Discussions*, *10*, 1025–1047.

Tarling, M. S., Smith, S. A. F., Viti, C., and Scott, J. M. (2018). Dynamic earthquake rupture preserved in a creeping serpentinite shear zone. *Nature Communications*, *9*(1), 3552.

Tenthorey, E., Cox, S. F., and Todd, H. F. (2003). Evolution of strength recovery and permeability during fluid-rock reaction in experimental fault zones. *Earth and Planetary Science Letters*, *206*(1), 161–172.

Tesei, T., Collettini, C., Carpenter, B. M., Viti, C., and Marone, C. (2012). Frictional strength and healing behavior of phyllosilicate-rich faults. *Journal of Geophysical Research: Solid Earth*, *117*(B9), 1–13.

Tesei, T., Harbord, C. W. A., De Paola, N., Collettini, C., and Viti, C. (2018). Friction of Mineralogically Controlled Serpentinites and Implications for Fault Weakness. *Journal of Geophysical Research: Solid Earth*, *123*(8), 6976–6991.

Thy, P. (1987). Petrogenetic implications of mineral crystallization trends of Troodos cumulates, Cyprus. *Geological Magazine*, *124*, 1–11.

Townend, J. and Zoback, M. D. (2004). Regional tectonic stress near the San Andreas fault in central and southern California. *Geophysical Research Letters*, *31*(15).

Turcotte, D. L. (1986a). A fractal model for crustal deformation. *Tectonophysics*, *132*, 261–269.

Turcotte, D. L. (1986b). Fractals and fragmentation. *Journal of Geophysical Research*, *91*(B2), 1921–1926.

Turcotte, D. L. (1989). Fractals in Geology and Geophysics. *Pageoph*, *131*(1/2), 171–196.

Turcotte, D. L. and Schubert, G. (2002). *Geodynamics (2nd ed.)*. Cambridge University Press.

Urquhart, E. and Banner, F. T. (1994). Biostratigraphy of the supra-ophiolite sediments of the Troodos Massif, Cyprus: the Cretaceous Perapedhi, Kannaviou, Moni and Kathikas formations. *Geological Magazine*, *131*(4), 499–518.

Van Andel, T. H. (1975). Mesozoic/cenozoic calcite compensation depth and the global distribution of calcareous sediments. *Earth and Planetary Science Letters*, *26*(2), 187–194.

Van Avendonk, H. J. A., Harding, A. J., and Orcutt, J. A. (2001). Contrast in crustal structure across the Clipperton Transform Fault from travel time tomography. *Journal of Geophysical Research*, *106*(B6), 10961–10981.

van den Ende, M. P. A., Chen, J., Niemeijer, A. R., and Ampuero, J. P. (2020). Rheological Transitions Facilitate Fault-Spanning Ruptures on Seismically Active and Creeping Faults. *Journal of Geophysical Research: Solid Earth*, *125*(8), e2019JB019328.

van den Ende, M. P. A. and Niemeijer, A. R. (2019). An investigation into the role of time-dependent cohesion in interseismic fault restrengthening. *Scientific Reports*, *9*(1), 9894.

Van Diggelen, E. W. E., De Bresser, J. H. P., Peach, C. J., and Spiers, C. J. (2010). High shear strain behaviour of synthetic muscovite fault gouges under hydrothermal conditions. *Journal of Structural Geology*, *32*(11), 1685–1700.

van Everdingen, D. A. and Cawood, P. A. (1995). Dyke domains in the Mitsero graben, Troodos ophiolite, Cyprus: an off-axis model for graben formation at a spreading centre. *Journal of the Geological Society*, *152*(6), 923.

Vannucchi, P., Maltman, A., Bettelli, G., and Clennell, B. (2003). On the nature of scaly fabrics and scaly clay. *Journal of Structural Geology*, *25*, 673–688.

Varga, R. J. and Moores, E. M. (1985). Spreading structure of the Troodos ophiolite, Cyprus. *Geology*, *13*(12), 846–850.

Violay, M., Di Toro, G., Gibert, B., Nielsen, S., Spagnuolo, E., Del Gaudio, P., Azais, P., and Scarlato, P. G. (2014). Effect of glass on the frictional

behavior of basalts at seismic slip rates. *Geophysical Research Letters*, *41*(2), 348–355.

Violay, M., Gibert, B., Mainprice, D., Evans, B., Dautria, J.-M., Azais, P., and Pezard, P. (2012). An experimental study of the brittle-ductile transition of basalt at oceanic crust pressure and temperature conditions. *Journal of Geophysical Research: Solid Earth*, *117*(B3).

Viti, C., Collettini, C., Tesei, T., Tarling, M., and Smith, S. (2018). Deformation Processes, Textural Evolution and Weakening in Retrograde Serpentinites. *Minerals*, *8*(6), 1–20.

Viti, C. and Mellini, M. (1998). Mesh textures and bastites in the Elba retrograde serpentinites. *European Journal of Mineralogy*, *10*, 1341–1359.

Wallis, D., Phillips, R. J., and Lloyd, G. E. (2013). Fault weakening across the frictional-viscous transition zone, Karakoram Fault Zone, NW Himalaya. *Tectonics*, *32*(5), 1227–1246.

Wang, C. (2011). High pore pressure, or its absence, in the San Andreas Fault. *Geology*, *39*(11), 1047–1050.

Warren, J. M. and Hirth, G. (2006). Grain size sensitive deformation mechanisms in naturally deformed peridotites. *Earth and Planetary Science Letters*, *248*(1-2), 438–450.

Wassmann, S., Stockhert, B., and Trepmann, C. A. (2011). Dissolution precipitation creep versus crystalline plasticity in high-pressure metamorphic serpentinites. *Geological Society, London, Special Publications*, *360*(1), 129–149.

Wells, D. L. and Coppersmith, K. J. (1994). New empirical relationships among magnitude, rupture length, rupture width, rupture area, and surface displacement. *Bulletin of the Seismolgical Society of America*, *84*(4), 974–1002.

Wesnousky, S. G. (2006). Predicting the endpoints of earthquake ruptures. *Nature*, *444*(7117), 358–360.

Wibberley, C. A. J. (2005). Initiation of basement thrust detachments by fault-zone reaction weakening. *Geological Society Special Publications*, *245*, 347–372.

Wicks, F. J. and Whittaker, E. J. W. (1977). Serpentine textures and serpentinisation. *Canadian Mineralogist*, *15*(459-488), 1025–1047.

Wilson, J. T. (1959). The Geology of the Xeros-Troodos area. *Cyprus Geological Survey Department Memoir No. 1*.

Wilson, J. T. (1965). A New Class of Faults and their Bearing on Continental Drift. *Nature*, *207*(4995), 343–347.

Wintsch, R. P., Christoffersen, R., and Kronenberg, A. K. (1995). Fluid-rock reaction weakening of fault zones. *Journal of Geophysical Research*, *100*(B7), 13021–13032.

Wolfson-Schwehr, M. and Boettcher, M. S. (2019). Global Characteristics of Oceanic Transform Fault Structure and Seismicity. *Transform Plate Boundaries and Fracture Zones, Elsevier*, 21–59.

Wolfson-Schwehr, M., Boettcher, M. S., McGuire, J. J., and Collins, J. A. (2014). The relationship between seismicity and fault structure on the Discovery transform fault, East Pacific Rise. *Geochemistry, Geophysics, Geosystems*, *15*(9), 3698–3712.

Woodcock, N. H. and Mort, K. (2008). Classification of fault breccias and related fault rocks. *Geological Magazine*, *145*(3), 435–440.

Zhang, L., He, C., Liu, Y., and Lin, J. (2017). Frictional properties of the South China Sea oceanic basalt and implications for strength of the Manila subduction seismogenic zone. *Marine Geology*, *394*, 16–29.

Zhong Yan, Z., Yi, W., and Xiao Han, L. (1990). Fractal analysis applied to cataclastic rocks. *Tectonophysics*, *178*(2), 373–377.

Zoback, M. D. (1991). State of Stress and Crustal Deformation along Weak Transform Faults. *Philosophical Transactions: Physical Sciences and Engineering*, *337*(1645), 141–150.

Zoback, M. D., Zoback, M. L., Mount, V. S., Suppe, J., Eaton, J. P., Healy, J. H., Oppenheimer, D., Reasenberg, P., Jones, L., Raleigh, C. B., Wong, I. G., Scotti, O., and Wentworth, C. (1987). New evidence on the state of stress of the San Andreas Fault System. *Science*, *238*, 1105–1111.

Zubtsov, S., Renard, F., Gratier, J.-P., Dysthe, D. K., and Traskine, V. (2005). Single-contact pressure solution creep on calcite monocrystals. *Geological Society, London, Special Publications*, *243*(1), 81.

# Appendix A

# Sample descriptions and locations

**Table A.1:** Brief sample descriptions and locations

| Sample # | Locality | Easting (WGS84 UTM) | Northing (WGS84 UTM) | Sample |
|---|---|---|---|---|
| 17CS01 | C17-002 | 507395 | 3848108 | Massive sepentinite with asthenospheric fabric |
| 17CS02 | C17-013 | 505951 | 3856448 | Foliated fault gouge (sheeted dyke complex) |
| 17CS03 | C17-013 | 505951 | 3856448 | Foliated fault gouge (sheeted dyke complex) with zeolite? Calclite? |
| 17CS04 | C17-013 | 505951 | 3856448 | Foliated fault gouge (sheeted dyke complex) with disseminated min (as above) |
| 17CS05 | C17-013 | 505951 | 3856448 | Foliated fault gouge (sheeted dyke complex) |
| 17CS06 | C17-013 | 505951 | 3856448 | Gossan |
| 17CS07 | C17-015 | 506830 | 3852579 | Tremolite-rich serpentinite? |
| 17CS08 | C17-015 | 506830 | 3852579 | Tremolite-rich serpentinite? (epidote and chlorite? Green) |
| 17CS09 | C17-015 | 506830 | 3852579 | Tremolite-rich serpentinite? |
| 17CS10 | C17-015 | 506830 | 3852579 | Pressure shaddow material (serp.) from serpentinite shear zone |
| 17CS11 | C17-015 | 506830 | 3852579 | Firbous serpentine vein on serpentinite (float) |
| 17CS12 | C17-015 | 506830 | 3852579 | Rodingite |
| 17CS13 | C17-017 | 523605 | 3854799 | Indurated dolerite breccia |
| 17CS14 | C17-003 | 507874 | 3849997 | Massive serpentinite |
| 17CS15 | C17-003 | 507874 | 3849997 | Rodingite |
| 17CS16 | C17-003 | 507874 | 3849997 | Scaly serpentinite |
| 17CS17 | C17-003 | 507897 | 3850164 | Scaly serpentinite |
| 17CS18 | C17-003 | 507892 | 3850153 | Cherty flint-like silica vein in gabbro |
| 17CS19 | C17-003 | 507886 | 3850098 | Scaly-phyllonitic serpentinite |
| 17CS20 | C17-020 | 508316 | 3852733 | Phyllonitic serpentinite |
| 17CS21 | C17-020 | 508316 | 3852733 | Phyllonitic serpentinite |

**Table A.1:** Brief sample descriptions and locations

| Sample # | Locality | Easting (WGS84 UTM) | Northing (WGS84 UTM) | Sample |
|---|---|---|---|---|
| 18CS01 | C18-002 | 507171 | 3847991 | Scaly serpentinite |
| 18CS02 | C18-002 | 507231 | 3848043 | Phyllonitic serpentinite |
| 18CS03 | C18-003 | 507398 | 3848172 | Serpentinite vein in massive serpentinite |
| 18CS04 | C18-003 | 507494 | 3848226 | Massive serpentinite with asthenospheric fabric |
| 18CS05 | C18-003 | 507494 | 3848226 | Massive sepentinite with asthenospheric fabric |
| 18CS06 | C18-003 | 507580 | 3848306 | Phyllonitic serpentinite |
| 18CS07 | C17-003 | 507996 | 3850256 | Tremolite-rich serpentinite? |
| 18CS08 | C17-003 | 507996 | 3850256 | Phyllonitic serpentinite |
| 18CS09 | C17-003 | 507996 | 3850256 | Scaly serpentinite |
| 18CS10 | C18-007 | 508234 | 3850045 | Scaly serpentinite |
| 18CS11 | C17-015 | 506830 | 3852579 | Pressure shaddow material (serp.) from serpentinite shear zone |
| 18CS12 | C18-010 | 506716 | 3852549 | Scaly serpentinite |
| 18CS13 | C18-010 | 506716 | 3852549 | Serpentinite phacoid (scaly serpentinite) |
| 18CS14 | C18-011 | 506665 | 3852578 | Phyllonitic serpentinite |
| 18CS20 | C18-015 | 502501 | 3856069 | Dolerite dyke |
| 18CS21 | C18-015 | 502501 | 3856069 | Indurated dolerite breccia |
| 18CS22 | C18-016 | 502606 | 3855904 | Indurated dolerite breccia |
| 18CS23 | C18-017 | 490381 | 3858910 | Indurated dolerite breccia (with mineralisation) |
| 18CS24 | C18-018 | 499749 | 3851454 | Phyllonitic serpentinite |
| 18CS25 | C18-019 | 504008 | 3856781 | Indurated dolerite breccia |
| 18CS26 | C18-020 | 508232 | 3852312 | Transform sequence dyke-serpentinite contact |
| 18CS27 | C18-020 | 508232 | 3852312 | Serpentinite breccia? |

**Table A.1:** Brief sample descriptions and locations

| Sample # | Locality | Easting (WGS84 UTM) | Northing (WGS84 UTM) | Sample |
|---|---|---|---|---|
| 18CS28 | C18-020 | 508232 | 3852312 | Massive sepentinite |
| 18CS29 | C18-020 | 508165 | 3852358 | Transform sequence dyke-serpentinite contact |
| 18CS30 | C18-021 | 508088 | 3852948 | Scaly serpentinite (with tremolite?) |
| 18CS31 | C18-021 | 508088 | 3852948 | Scaly serpentinite (with tremolite?) |
| 18CS32 | C18-021 | 508088 | 3852948 | Scaly serpentinite (with tremolite?) |
| 18CS33 | C18-021 | 508088 | 3852948 | Phyllonitic serpentinite |
| 18CS46 | C18-027 | 500379 | 3851603 | Scaly serpentinite |
| 18CS47 | C18-027 | 500379 | 3851603 | Phyllonitic serpentinite |
| 18CS48 | C18-028 | 500338 | 3851714 | Tremolite-rich serpentinite? |
| 18CS49 | C18-028 | 500338 | 3851714 | Scaly serpentinite |
| 18CS49a | C18-028 | 500338 | 3851714 | Serpentinite phacoid (scaly serpentinite) |
| 18CS50 | C18-029 | 500361 | 3851914 | Scaly serpentinite |
| 18CS51 | C18-030 | 500787 | 3853352 | Transform sequence gabbro |
| 18CS52 | C18-030 | 500787 | 3853352 | Transform sequence gabbro |
| 18CS53 | C18-030 | 500801 | 3853390 | Serpentinite (contact with transform sequence gabbro) |
| 18CS54 | C18-030 | 500801 | 3853390 | Transform sequence gabbro (contact with serpentinite) |
| 18CS55 | C18-032 | 509972 | 3855907 | Fault breccia in pillow lavas |
| 18CS56 | C17-019 | 524038 | 3855456 | Matrix-rich (dolerite) breccia (sheeted dyke complex) |
| 18CS57 | C18-033 | 500565 | 3852448 | Tremolite-rich serpentinite? |
| 18CS58 | C18-033 | 500565 | 3852448 | Scaly serpentinite (sulphide min.) |
| 18CS59 | C18-033 | 500565 | 3852448 | Scaly serpentinite (sulphide min.) |
| 18CS60 | | 507184 | 3847979 | Serpentinite phacoid (phyllonitic serpentinite) |

**Table A.1:** Brief sample descriptions and locations

| Sample # | Locality | Easting (WGS84 UTM) | Northing (WGS84 UTM) | Sample |
|---|---|---|---|---|
| 18CS61 | | 507243 | 3848072 | Serpentinite phacoid (scaly serpentinite) |
| 18CS62 | C17-001 | 507177 | 3847979 | Phyllonitic serpentinite |
| 18CS63 | | 507576 | 3848300 | Serpentinite phacoid (phyllonitic serpentinite) |
| 18CS64 | | 507576 | 3848300 | Phyllonitic serpentinite |
| 18CS65 | C17-009 | 490035 | 3859267 | Indurated dolerite breccia (with mineralisation) |
| 18CS66 | C18-048 | 510223 | 3852699 | Serpentine overgrowth of serpentinite phacoid (scaly serpentinite) |
| 18CS67 | C18-048 | 510223 | 3852699 | Scaly serpentinite |
| 18CS68 | C18-060b | 490032 | 3859436 | Indurated dolerite breccia (with mineralisation) |
| 18CS69 | C17-005 | 508677 | 3853100 | Phyllonitic serpentinite |
| 18CS70 | C18-075 | 508825 | 3852672 | Serpentinite phacoid (scaly serpentinite) |
| 18CS71 | C18-077 | 502728 | 3851826 | Serpentinite phacoid (phyllonitic serpentinite) |
| 19CS01 | | 506830 | 3852579 | Fractured-scaly serpentinite |
| 19CS02 | | 506716 | 3852549 | Serpentinite phacoid (scaly serpentinite) |
| 19CS03 | | 506716 | 3852549 | Serpentinite phacoid in phyllonitic serpentinite |
| 19CS04 | | 506752 | 3852406 | Scaly serpentinite |
| 19CS05 | C18-009 | 507332 | 3852864 | Scaly-phyllonitic serpentinite (transitional) |
| 19CS06 | | 506984 | 3852528 | Massive serpentinite |
| 19CS07 | | 506984 | 3852528 | Massive serpentinite |
| 19CS08 | ? | ? | ? | Massive serpentinite |
| 19CS09 | C17-016 | 507357 | 3852933 | Serpentinite phacoid (phyllonitic serpentinite) |
| 19CS10 | C17-019 | 524038 | 3855456 | Matrix-rich (dolerite) breccia (sheeted dyke complex) |

**Table A.1:** Brief sample descriptions and locations

| Sample # | Locality | Easting (WGS84 UTM) | Northing (WGS84 UTM) | Sample |
|---|---|---|---|---|
| 19CS11 | C17-013 | 505951 | 3856448 | Foliated fault gouge (sheeted dyke complex) |
| 19CS12 | C17-003 | 507874 | 3849997 | Low strain, fractured serpentinite |
| JC21-77R-9 | | 2°17.814'N | 101°29.684'W | EPR dolerite (Mg#40; MgO 5.6wt%, LOI 1.4wt%) Depth: 3419m |
| JC21-77R-11 | | 2°17.919'N | 101°29.667'W | EPR dolerite (Mg#55; MgO 7.4wt%, LOI 1.5wt%) Depth: 3335m |
| JC21-73R-26 | | 2°15.346'N | 101°33.395'W | EPR dolerite (Mg#57; MgO 7.1wt%, LOI 2.7wt%) Depth: 4745m |

# Appendix B

# Log-normal distributions for fault rock particle size distributions in Chapter 4

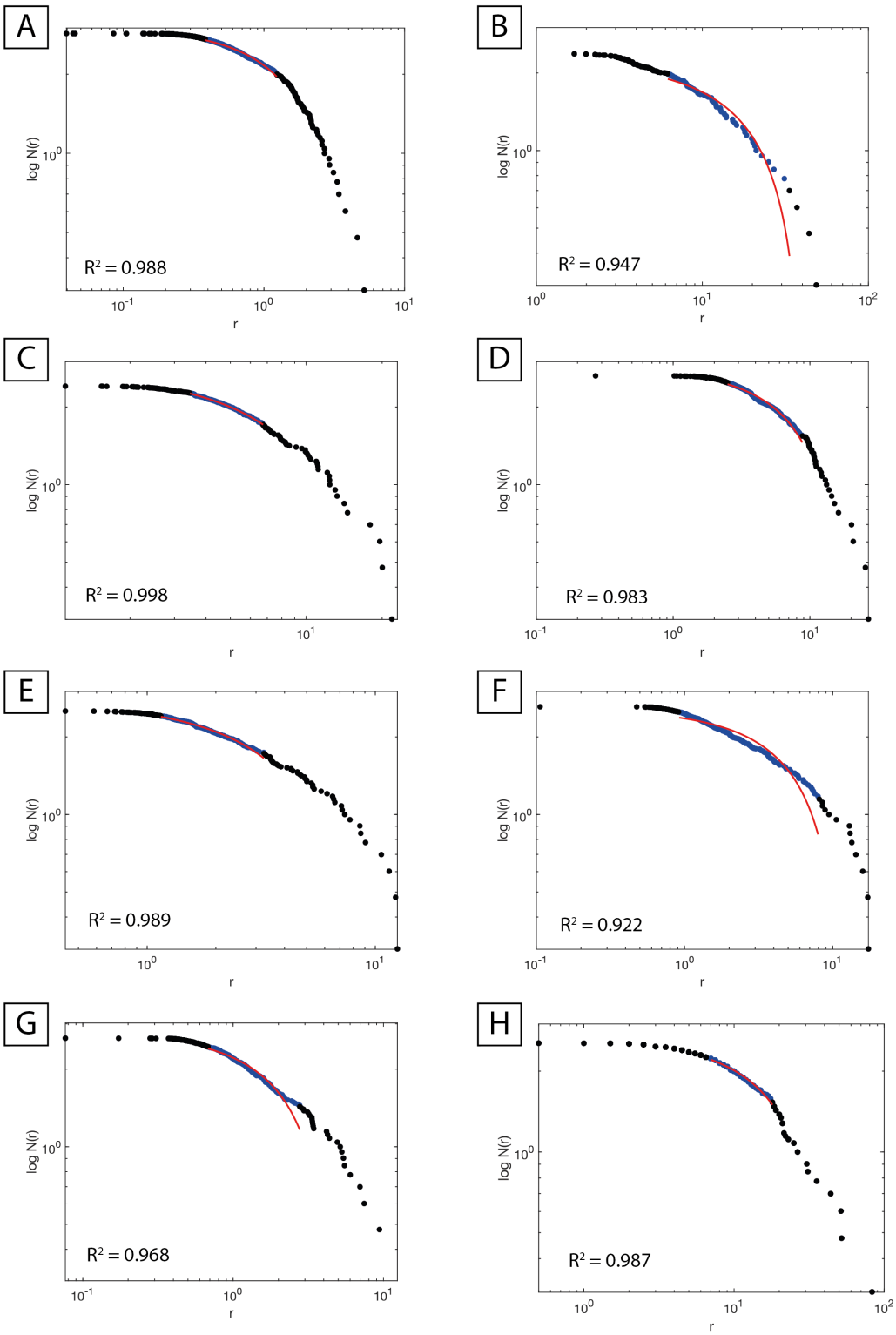


**Figure B.1:** Cumulative clast-size distribution plot showing log $N(r)$ vs. clast size $(r)$. Log-normal distributions (red curve) are fit to the same fractal range (blue data) as used for the power-law distributions (Table 1). $R^2$ values shown reflect the fit of the log-normal distribution to the data. a-o are samples in Table 4.1 and Figure 4.6. i-ix are data from the photomosaic in Figure 4.7.

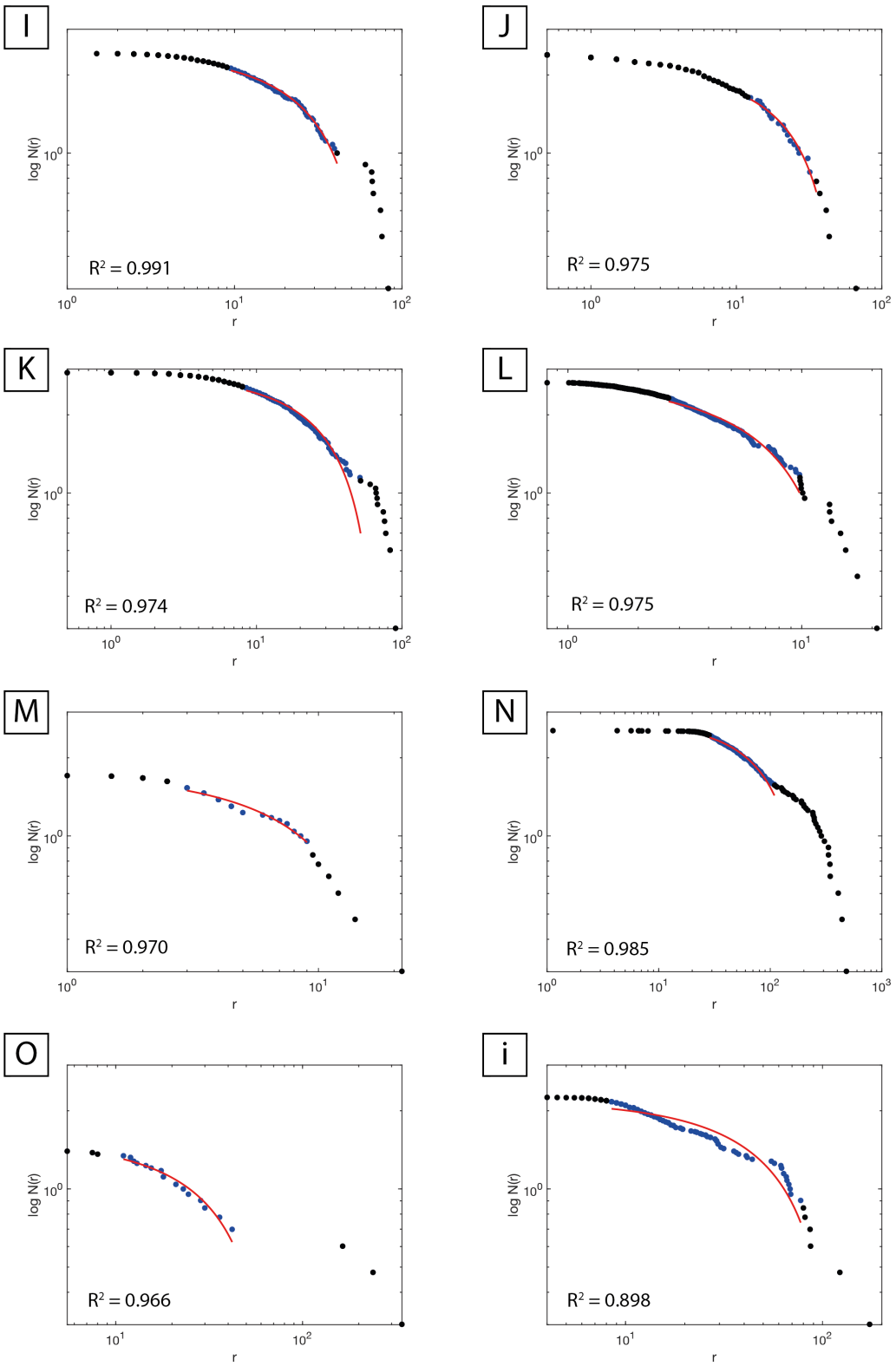


**Figure B.2:** A1 continued from previous page.

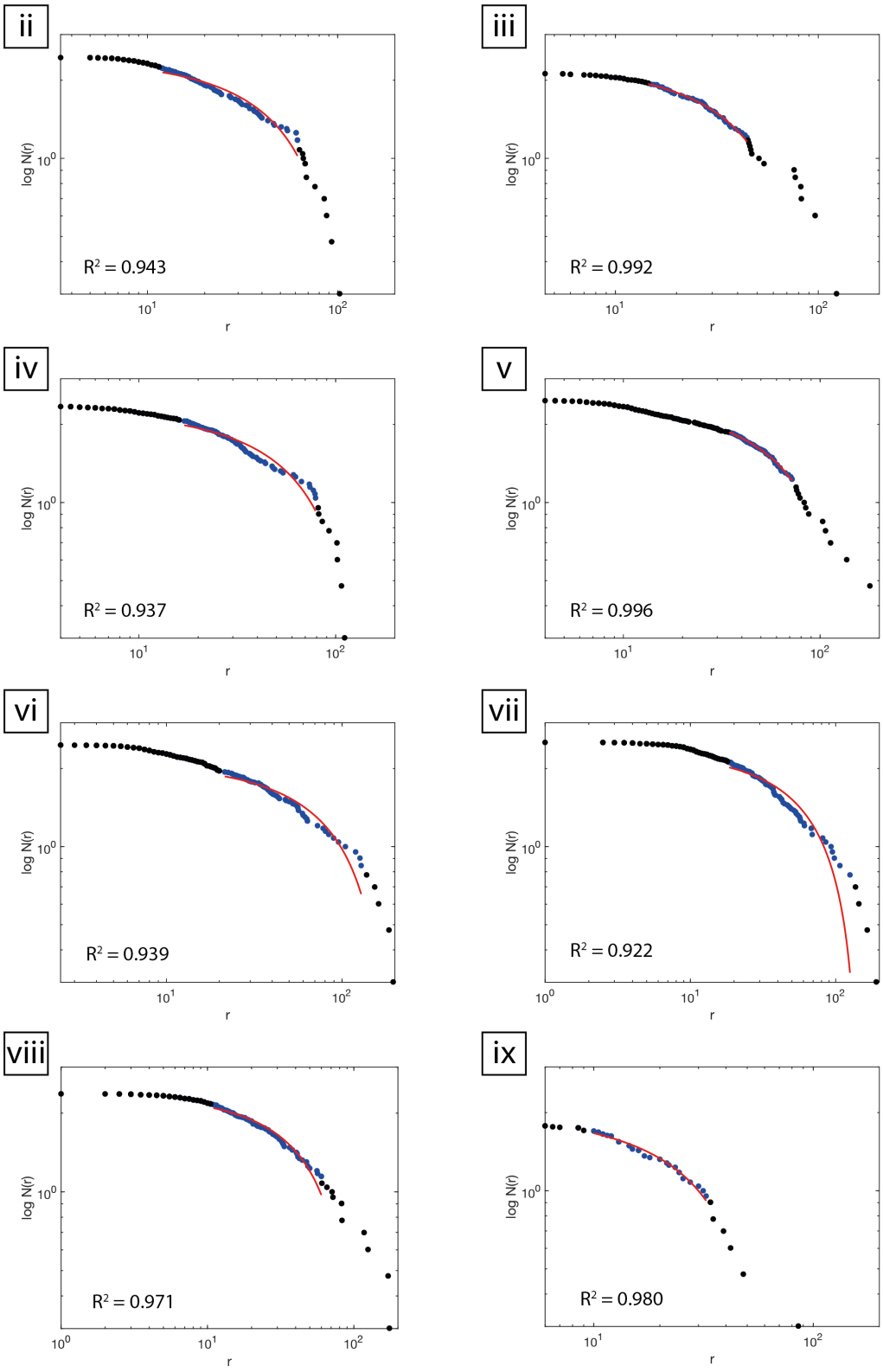


**Figure B.3:** A1 continued from previous page.

# Appendix C

# Rate-and-state friction parameters for experiments presented in Chapter 5

| Experiment | Sample | State | Peak friction coefficient (run-in) | Residual friction coefficient | Effective normal stress (MPa) |
|---|---|---|---|---|---|
| SC_001_G5_JC2177R9_10MPa_shear | Dolerite | Intact | | | 1 |
| SC_002_G5_JC2177R9_10MPa_shear | Dolerite | Intact | 0.88 | 0.85 | 10 |
| SC_003_G5_JC2173R26_10MPa_shear | Fractured dolerite | Intact | 1.96 | 0.76 | 10 |
| SC_004_G1_JC2177R09_10MPa_shear | Dolerite | Powder | 0.74 | 0.69 | 10 |
| SC_005_G5_18CS25_10MPa_shear | Cemented breccia | Intact | 1.62 | 0.79 | 10 |
| SC_006_G1_JC2173R26_10MPa_shear | Fractured dolerite | Powder | 0.52 | 0.52 | 10 |
| SC_010_G1_19CS10_10MPa_shear | Gouge-rich breccia | Intact | 0.53 | 0.48 | 10 |
| SC_011_G4_19CS11_10MPa_shear | Gouge | Intact | 0.37 | 0.30 | 10 |
| SC_012_G1_19CS10_10MPa_shear | Gouge-rich breccia | Powder | 0.37 | 0.35 | 10 |
| SC_013_G4_19CS11_10MPa_shear | Gouge | Powder | 0.31 | 0.25 | 10 |
| SC_017_G4_18CS25_10MPa_shear | Cemented breccia | Powder | 0.69 | 0.63 | 10 |

**Table C.1:** List of direct-shear friction experiments carried out.

**Table C.2:** Rate-and-state friction parameters (ageing law) calculated from velocity step test experiments.

| Experiment | Sample | Vo (mm/s) | V1 (mm/s) | a | b1 | Dc1 | b2 | Dc2 | a-b | std a | std b1 | std Dc1 | std b2 | std Dc2 | std a-b |
|---|---|---|---|---|---|---|---|---|---|---|---|---|---|---|---|
| **002** | dolerite minicore | | | | | | | | | | | | | | |
| **003** | fractured dolerite minicore | 3 | 10 | 0.0047 | 0.0059 | 7.0 | | | -0.0012 | 2.41E-05 | 3.51E-05 | 0.1422 | | | 3.97E-05 |
| | | 10 | 30 | 0.0055 | 0.0057 | 5.0 | | | -0.0002 | 5.74E-05 | 4.64E-05 | 0.1684 | | | 4.21E-05 |
| **004** | dolerite powder | 0.1 | 0.3 | 0.0058 | 0.0050 | 7.5 | 0.0074 | 102.3 | -0.0066 | 5.04E-05 | 5.24E-05 | 0.1083 | 1.20E-04 | 2.32E+00 | 1.02E-04 |
| | | 0.3 | 1 | 0.0066 | 0.0061 | 5.9 | 0.0082 | 90.0 | -0.0077 | 2.54E-05 | 3.36E-05 | 0.1159 | 8.83E-05 | 2.23E+00 | 9.62E-05 |
| | | 1 | 3 | 0.0102 | 0.0081 | 2.8 | 0.0100 | 59.9 | -0.0079 | 2.18E-04 | 1.94E-04 | 0.1259 | 6.71E-05 | 9.36E-01 | 0.00007 |
| | | 3 | 10 | 0.0061 | 0.0053 | 7.3 | 0.0035 | 63.9 | -0.0028 | 2.61E-05 | 4.61E-05 | 0.1432 | 6.09E-05 | 2.60E+00 | 5.16E-05 |
| | | 10 | 30 | 0.0147 | 0.0113 | 1.3 | 0.0047 | 16.8 | -0.0013 | 2.00E-03 | 2.00E-03 | 0.2660 | 5.06E-05 | 3.24E-01 | 2.44E-05 |
| **005** | breccia minicore | 0.1 | 0.3 | | | | | | | | | | | | |
| | | 0.3 | 1 | 0.0083 | 0.0169 | 100.1 | | | -0.0086 | 9.29E-04 | 1.10E-03 | 5.1764 | | | 4.16E-04 |
| | | 1 | 3 | 0.0090 | 0.0055 | 8.1 | 0.0049 | 69.6 | -0.0014 | 1.48E-04 | 1.40E-04 | 0.6929 | 1.94E-04 | 6.60E+00 | 1.57E-04 |
| | | 3 | 10 | 0.0091 | 0.0063 | 13.9 | 0.0122 | 149.6 | -0.0094 | 1.22E-04 | 3.38E-04 | 1.1188 | 3.83E-04 | 1.23E+01 | 4.33E-04 |
| | | 10 | 30 | 0.0113 | 0.0077 | 15.4 | 0.0046 | 170.9 | -0.0009 | 1.02E-04 | 2.28E-04 | 1.1470 | 3.54E-04 | 3.72E+01 | 4.12E-04 |
| **006** | fractured dolerite powder | 0.1 | 0.3 | 0.0060 | 0.0081 | 10.0 | | | -0.0020 | 1.96E-05 | 2.84E-05 | 0.1190 | | | 3.35E-05 |
| | | 0.3 | 1 | 0.0055 | 0.0062 | 12.1 | 0.0064 | 95.4 | -0.0070 | 1.14E-05 | 1.10E-04 | 0.2664 | 1.21E-04 | 4.52E+00 | 1.19E-04 |
| | | 1 | 3 | 0.0064 | 0.0067 | 10.1 | | | -0.0004 | 3.11E-05 | 3.22E-05 | 0.1783 | | | 3.45E-05 |
| | | 3 | 10 | 0.0070 | 0.0057 | 13.3 | 0.0022 | 138.0 | -0.0009 | 2.73E-05 | 1.41E-04 | 0.5303 | 1.85E-04 | 3.08E+01 | 2.14E-04 |
| | | 10 | 30 | 0.0073 | 0.0074 | 15.7 | | | -0.0001 | 3.64E-05 | 5.40E-05 | 0.4597 | | | 6.36E-05 |

**Table C.2 continued from previous page**

| Experiment | Sample | Vo (mm/s) | V1 (mm/s) | a | b1 | Dc1 | b2 | Dc2 | a-b | std a | std b1 | std Dc1 | std b2 | std Dc2 | std a-b |
|---|---|---|---|---|---|---|---|---|---|---|---|---|---|---|---|
| **010** | gouge-rich breccia minicore | 0.1 | 0.3 | 0.0047 | 0.0038 | 42.0 | | | 0.0009 | 8.96E-06 | 4.50E-05 | 1.1428 | | | 4.69E-05 |
| | | 0.3 | 1 | 0.0049 | 0.0049 | 25.8 | -0.0028 | 86.5 | 0.0028 | 9.67E-06 | 4.14E-04 | 1.3523 | 3.83E-04 | 1.24E+01 | 7.36E-05 |
| | | 1 | 3 | 0.0049 | 0.0035 | 23.1 | | | 0.0013 | 8.89E-06 | 2.63E-05 | 0.4066 | | | 2.55E-05 |
| | | 3 | 10 | 0.0054 | 0.0050 | 40.0 | | | 0.0004 | 1.28E-05 | 5.88E-05 | 1.1022 | | | 6.33E-05 |
| | | 10 | 30 | 0.0079 | 0.0030 | 11.5 | 0.0041 | 86.0 | 0.0008 | 1.28E-04 | 9.72E-05 | 1.2276 | 1.15E-04 | 5.03E+00 | 7.02E-05 |
| **011** | gouge minicore | 0.1 | 0.3 | 0.0032 | 0.0037 | 40.0 | -0.0056 | 100.0 | 0.0051 | 6.51E-05 | 7.67E-04 | 4.0170 | 7.69E-04 | 8.54E+00 | 1.08E-04 |
| | | 0.3 | 1 | 0.0032 | 0.0027 | 75.0 | | | 0.0005 | 1.23E-05 | 1.25E-04 | 6.3501 | | | 1.26E-04 |
| | | 1 | 3 | 0.0054 | 0.0039 | 7.1 | | | 0.0015 | 6.79E-05 | 5.98E-05 | 0.2428 | | | 1.81E-05 |
| | | 3 | 10 | 0.0048 | 0.0013 | 48.0 | | | 0.0035 | 6.52E-05 | 7.92E-05 | 3.6584 | | | 4.54E-05 |
| | | 10 | 30 | 0.0066 | 0.0062 | 50.0 | -0.0064 | 27.3 | 0.0067 | 7.44E-05 | 4.40E-03 | 13.4817 | 0.0044 | 27.2749 | 1.08E-04 |
| **012** | gouge-rich breccia powder | 0.1 | 0.3 | 0.0049 | 0.0051 | 7.9 | | | -0.0002 | 1.27E-05 | 1.40E-05 | 0.0853 | | | 1.59E-05 |
| | | 0.3 | 1 | 0.0046 | 0.0036 | 10.4 | | | 0.0009 | 2.56E-05 | 2.98E-05 | 0.3111 | | | 3.24E-05 |
| | | 1 | 3 | 0.0062 | 0.0032 | 2.5 | 0.0029 | 36.9 | 0.0002 | 3.33E-04 | 3.13E-04 | 0.3319 | 3.86E-05 | 1.28E+00 | 3.49E-05 |
| | | 3 | 10 | 0.0047 | 0.0037 | 20.9 | | | 0.0010 | 7.46E-06 | 2.11E-05 | 0.3465 | | | 2.35E-05 |
| | | 10 | 30 | 0.0065 | 0.0062 | 0.3 | 0.0021 | 41.2 | 0.0018 | 1.26E-01 | 1.26E-01 | 0.5855 | 3.57E-05 | 1.89E+00 | 3.42E-05 |
| **013** | gouge powder | 0.1 | 0.3 | 0.0033 | 0.0019 | 12.1 | -0.0023 | 105.2 | 0.0036 | 1.52E-05 | 3.21E-05 | 0.3206 | 3.99E-05 | 4.38E+00 | 3.59E-05 |
| | | 0.3 | 1 | 0.0033 | 0.0013 | 10.6 | 0.0012 | 95.2 | 0.0008 | 1.76E-05 | 4.61E-05 | 0.6744 | 5.70E-05 | 1.14E+01 | 5.49E-05 |
| | | 1 | 3 | 0.0038 | 0.0009 | 7.2 | -0.0008 | 140.0 | 0.0036 | 1.88E-04 | 1.90E-04 | 0.6078 | 7.34E-05 | 3.02E+01 | 8.24E-05 |
| | | 3 | 10 | 0.0045 | 0.0010 | 50.0 | | | 0.0034 | 4.44E-05 | 4.99E-05 | 3.2163 | | | 2.99E-05 |
| | | 10 | 30 | 0.0059 | 0.0002 | 50.0 | | | 0.0057 | 1.98E-04 | 1.69E-04 | 57.2203 | | | 5.70E-05 |

**Table C.2 continued from previous page**

| Experiment | Sample | Vo (mm/s) | V1 (mm/s) | a | b1 | Dc1 | b2 | Dc2 | a-b | std a | std b1 | std Dc1 | std b2 | std Dc2 | std a-b |
|---|---|---|---|---|---|---|---|---|---|---|---|---|---|---|---|
| **017** | breccia powder | 0.1 | 0.3 | 0.0051 | 0.0046 | 6.0 | 0.0042 | 27.3 | -0.0036 | 1.99E-05 | 1.01E-04 | 0.1703 | 1.05E-04 | 9.01E-01 | 3.29E-05 |
| | | 0.3 | 1 | 0.0049 | 0.0035 | 5.5 | 0.0045 | 16.5 | -0.0032 | 3.36E-05 | 2.82E-04 | 0.3688 | 2.93E-04 | 7.79E-01 | 3.20E-05 |
| | | 1 | 3 | 0.0060 | 0.0069 | 6.9 | 0.0029 | 51.4 | -0.0038 | 1.52E-05 | 6.67E-05 | 0.1045 | 7.29E-05 | 2.9417 | 5.59E-05 |
| | | 3 | 10 | 0.0057 | 0.0052 | 6.2 | 0.0040 | 24.3 | -0.0035 | 2.44E-05 | 1.36E-04 | 0.1793 | 1.41E-04 | 9.06E-01 | 3.06E-05 |
| | | 10 | 30 | 0.0070 | 0.0055 | 3.3 | 0.0038 | 30.6 | -0.0023 | 1.21E-04 | 8.30E-05 | 0.1567 | 6.37E-05 | 1.08E+00 | 4.29E-05 |

*std = standard deviation*

**Table C.3:** Rate-and-state friction parameters (slip law) calculated from velocity step test experiments.

| Experiment | Sample | Vo (mm/s) | V1 (mm/s) | a | b1 | Dc1 | b2 | Dc2 | a-b | std a | std b1 | std Dc1 | std b2 | std Dc2 | std a-b |
|---|---|---|---|---|---|---|---|---|---|---|---|---|---|---|---|
| **002** | dolerite minicore | | | | | | | | | | | | | | |
| **003** | fractured dolerite minicore | 3 | 10 | 0.0047 | 0.0059 | 9.9 | | | -0.0012 | 2.43E-05 | 3.28E-05 | 0.2294 | | | 4.11E-05 |
| | | 10 | 30 | 0.0056 | 0.0058 | 6.4 | | | -0.0002 | 6.04E-05 | 4.44E-05 | 0.2457 | | | 4.38E-05 |
| **004** | dolerite powder | 0.1 | 0.3 | | | | | | | | | | | | |
| | | 0.3 | 1 | | | | | | | | | | | | |
| | | 1 | 3 | 0.0145 | 0.0119 | 1.5 | 0.0107 | 85.1 | -0.0081 | 7.77E-04 | 7.62E-04 | 0.1343 | 6.32E-05 | 1.21E+00 | 7.14E-05 |
| | | 3 | 10 | 0.0062 | 0.0051 | 8.7 | 0.0039 | 89.0 | -0.0028 | 3.82E-05 | 6.81E-05 | 0.2998 | 8.05E-05 | 4.89E+00 | 6.18E-05 |
| | | 10 | 30 | 0.0557 | 0.0520 | 0.2 | 0.0050 | 22.8 | -0.0012 | 6.47E-02 | 6.46E-02 | 0.3111 | 4.05E-05 | 4.68E-01 | 2.65E-05 |
| **005** | breccia minicore | 0.1 | 0.3 | | | | | | | | | | | | |
| | | 0.3 | 1 | 0.0095 | 0.0155 | 100.2 | | | -0.0060 | 4.95E-04 | 5.36E-04 | 5.2774 | | | 3.07E-04 |
| | | 1 | 3 | 0.0093 | 0.0054 | 8.5 | 0.0054 | 93.1 | -0.0015 | 2.51E-04 | 1.72E-04 | 1.2256 | 2.31E-04 | 1.10E+01 | 1.78E-04 |
| | | 3 | 10 | 0.0092 | 0.0052 | 13.0 | 0.013 | 179.5 | -0.0090 | 1.24E-04 | 2.64E-04 | 2.2518 | 3.56E-04 | 1.62E+01 | 4.25E-04 |
| | | 10 | 30 | 0.0115 | 0.0078 | 18.8 | 0.0048 | 252.0 | -0.0011 | 1.37E-04 | 3.03E-04 | 1.9338 | 4.17E-04 | 7.78E+01 | 5.61E-04 |
| **006** | fractured dolerite powder | 0.1 | 0.3 | | | | | | | | | | | | |
| | | 0.3 | 1 | 0.0055 | 0.0059 | 17.7 | 0.0069 | 151.0 | -0.0073 | 2.03E-05 | 2.48E-04 | 0.9097 | 2.03E-04 | 1.44E+01 | 2.06E-04 |
| | | 1 | 3 | 0.0064 | 0.0068 | 13.4 | | | -0.0004 | 3.16E-05 | 3.00E-05 | 0.2668 | | | 3.58E-05 |
| | | 3 | 10 | 0.0070 | 0.0057 | 17.6 | 0.0023 | 221.6 | -0.0010 | 3.17E-05 | 1.99E-04 | 1.0884 | 2.28E-04 | 7.80E+01 | 3.14E-04 |
| | | 10 | 30 | 0.0074 | 0.0074 | 20.0 | | | -0.0001 | 4.20E-05 | 4.98E-05 | 0.6621 | | | 6.51E-05 |

**Table C.3 continued from previous page**

| Experiment | Sample | Vo (mm/s) | V1 (mm/s) | a | b1 | Dc1 | b2 | Dc2 | a-b | std a | std b1 | std Dc1 | std b2 | std Dc2 | std a-b |
|---|---|---|---|---|---|---|---|---|---|---|---|---|---|---|---|
| **010** | gouge-rich breccia minicore | 0.1 | 0.3 | 0.0048 | 0.0040 | 60.2 | | | 0.0008 | 9.27E-06 | 4.51E-05 | 1.8132 | | | 4.95E-05 |
| | | 0.3 | 1 | 0.0049 | 0.0525 | 59.0 | -0.0504 | 64.6 | 0.0029 | 1.52E-05 | 1.52E+00 | 77.6554 | 1.52E+00 | 9.12E+01 | 7.06E-05 |
| | | 1 | 3 | 0.0049 | 0.0036 | 31.7 | | | 0.0013 | 6.67E-06 | 2.39E-05 | 0.6091 | | | 2.61E-05 |
| | | 3 | 10 | 0.0054 | 0.0050 | 40.0 | | | 0.0004 | 1.28E-05 | 5.88E-05 | 1.1022 | | | 6.33E-05 |
| | | 10 | 30 | 0.0083 | 0.0030 | 10.0 | 0.0045 | 106.7 | 0.0008 | 3.01E-04 | 2.20E-04 | 1.9842 | 1.18E-04 | 6.92E+00 | 7.45E-05 |
| **011** | gouge minicore | 0.1 | 0.3 | 0.0034 | 0.0042 | 40.0 | -0.0055 | 100.0 | 0.0048 | 2.48E-04 | 2.30E-03 | 9.8816 | 2.30E-03 | 2.59E+01 | 1.19E-04 |
| | | 0.3 | 1 | 0.0032 | 0.0028 | 120.4 | | | 0.0004 | 1.14E-05 | 1.53E-04 | 13.0623 | | | 1.58E-04 |
| | | 1 | 3 | 0.0055 | 0.0040 | 8.6 | | | 0.0015 | 7.15E-05 | 6.18E-05 | 0.3339 | | | 1.89E-05 |
| | | 3 | 10 | 0.0049 | 0.0013 | 62.2 | | | 0.0036 | 9.71E-05 | 1.05E-04 | 5.4001 | | | 4.77E-05 |
| | | 10 | 30 | 0.0071 | 0.0078 | 50.0 | -0.0073 | 100.0 | 0.0066 | 1.84E-04 | 8.90E-03 | 22.8147 | 0.009 | 45.1663 | 1.09E-04 |
| **012** | gouge-rich breccia powder | 0.1 | 0.3 | 0.0050 | 0.0051 | 10.4 | | | -0.0002 | 1.22E-05 | 1.22E-05 | 0.1173 | | | 1.53E-05 |
| | | 0.3 | 1 | 0.0046 | 0.0037 | 15.0 | | | 0.0009 | 2.53E-05 | 2.86E-05 | 0.5001 | | | 3.44E-05 |
| | | 1 | 3 | 0.0077 | 0.0045 | 1.7 | 0.0031 | 50.1 | 0.0001 | 9.30E-04 | 9.17E-04 | 0.4506 | 3.54E-05 | 1.81E+00 | 3.70E-05 |
| | | 3 | 10 | 0.0047 | 0.0038 | 29.7 | | | 0.0010 | 8.25E-06 | 1.99E-05 | 0.5222 | | | 2.33E-05 |
| | | 10 | 30 | 0.0648 | 0.0608 | 0.3 | 0.0022 | 55.4 | 0.0018 | 1.34E-01 | 1.34E-01 | 0.6309 | 4.17E-05 | 3.08E+00 | 3.98E-05 |
| **013** | gouge powder | 0.1 | 0.3 | 0.0031 | 0.0025 | 22.8 | -0.0030 | 103.3 | 0.0035 | 6.50E-05 | 2.25E-04 | 1.1974 | 1.71E-04 | 8.49E+00 | 4.49E-05 |
| | | 0.3 | 1 | 0.0033 | 0.0013 | 14.8 | 0.0013 | 149.7 | 0.0008 | 2.43E-05 | 7.80E-05 | 1.5932 | 7.67E-05 | 3.00E+01 | 7.89E-05 |
| | | 1 | 3 | 0.0037 | 0.0010 | 10.0 | -0.0008 | 140.0 | 0.0035 | 2.09E-04 | 2.22E-04 | 1.2383 | 6.12E-05 | 3.52E+01 | 7.10E-05 |
| | | 3 | 10 | 0.0046 | 0.0011 | 50.0 | | | 0.0035 | 7.32E-05 | 7.36E-05 | 3.4202 | | | 2.49E-05 |
| | | 10 | 30 | 0.0068 | 0.0012 | 29.1 | | | 0.0056 | 8.85E-04 | 8.63E-04 | 11.6923 | | | 3.75E-05 |

**Table C.3 continued from previous page**

| Experiment | Sample | Vo (mm/s) | V1 (mm/s) | a | b1 | Dc1 | b2 | Dc2 | a-b | std a | std b1 | std Dc1 | std b2 | std Dc2 | std a-b |
|---|---|---|---|---|---|---|---|---|---|---|---|---|---|---|---|
| **017** | breccia powder | 0.1 | 0.3 | 0.0051 | 0.0038 | 6.8 | 0.0050 | 36.1 | -0.0036 | 3.46E-05 | 1.47E-04 | 0.4071 | 1.59E-04 | 1.47E+00 | 3.54E-05 |
| | | 0.3 | 1 | 0.0047 | 0.0023 | 7.3 | 0.0055 | 21.8 | -0.0031 | 5.90E-05 | 7.96E-04 | 1.9085 | 8.23E-04 | 2.00E+00 | 3.99E-05 |
| | | 1 | 3 | 0.0060 | 0.0066 | 8.7 | 0.0033 | 71.0 | -0.0033 | 2.12E-05 | 1.04E-04 | 0.2222 | 1.01E-04 | 5.27E+00 | 6.43E-05 |
| | | 3 | 10 | 0.0057 | 0.0046 | 8.0 | 0.0046 | 34.3 | -0.0035 | 3.74E-05 | 2.63E-04 | 0.5052 | 2.73E-04 | 2.09E+00 | 3.93E-05 |
| | | 10 | 30 | 0.0075 | 0.0056 | 3.2 | 0.0042 | 44.9 | -0.0024 | 1.77E-04 | 1.30E-04 | 0.2107 | 6.18E-05 | 1.68E+00 | 4.52E-05 |

*std = standard deviation*